

Design of Scanning Fiber Micro-Cantilever based Catheter for Ultra-Small Endoscopes

**by
Mandeep Kaur**

M.Sc., University of Cassino and Southern Lazio, 2015

B.Sc., University of Cassino and Southern Lazio, 2013

Thesis Submitted in Partial Fulfillment of the
Requirements for the Degree of
Doctor of Philosophy

in the
School of Engineering Science
Faculty of Applied Sciences

© Mandeep Kaur 2022
SIMON FRASER UNIVERSITY
Summer 2022

Copyright in this work is held by the author. Please ensure that any reproduction or re-use is done in accordance with the relevant national copyright legislation.

Declaration of Committee

Name: Mandeep Kaur
Degree: Doctor of Philosophy
Title: Design of Scanning Fiber Micro-Cantilever based Catheter for Ultra-Small Endoscopes

Committee: **Chair: Atousa Hajshirmohammadi**
Lecturer, Engineering Science

Carlo Menon
Co-Supervisor
Adjunct Professor, Engineering Science

Andrew Rawicz
Co-Supervisor
Professor, Engineering Science

Pierre Lane
Committee Member
Associate Professor, Engineering Science

Michael Adachi
Examiner
Assistant Professor, Engineering Science

John Madden
External Examiner
Professor, Electrical and Computer Engineering
University of British Columbia

Abstract

During the past few decades, optical devices are frequently being used in medical applications to image lesions and malignancies, and to assist with surgical procedures. An endoscopic procedure requires the distal end of the scope to be placed close to the imageable target area through an opening such as nose, mouth, etc. Thus, the size of an endoscopic device dictates the area of the body that can be imaged using that device.

The continuous evolution of micro-electro-mechanical systems (MEMSs) along with the development in optics enable the fabrication of flexible endoscopes having diameters just over a millimeter. As a result, medical users are able to image smaller areas of the body that were inaccessible in the past. Thus, lesions and tumors can be detected at preliminary cancerous stages permitting more accurate diagnoses and supporting an increased life expectancy of the patients.

The overarching goal of this work has been to develop a sub-millimeter sized optical scanner that sets the bases for a miniaturized endoscope able to image previously inaccessible luminal organs in real time, at high resolution, in a minimally invasive manner without compromising the comfort of the subject, nor introduce additional risk. Thus, an initial diagnosis can be made, or a small precancerous lesion may be detected, in a small-diameter luminal organ that would not have otherwise been possible.

This work sets out to present an optical-fiber scanner for a scanning fiber endoscope design that has an insertion tube diameter in the sub-millimeter range; small enough to potentially be inserted into the smallest airways of the lung and other small diameter tubes, which may include narrow sections of the pancreatic duct, and the narrowest section at the openings of the fallopian tubes. To attain this goal, a novel approach based on exciting a single mode optical fiber at resonance with the help of an electro-thermal actuator is proposed where an asymmetric conducting element expands due to the Joule effect in presence of an electric current. The actuator provides base excitation motion to a cantilevered based optical fiber whose free end follows a closed line pattern. It has been seen experimentally that the area inside the circle can be scanned by offsetting the excitation frequency from the resonant value to achieve the bi-dimensional scanning. The backscattered reflected light from the target sample is set to be captured using multiple multimode fibers placed at the periphery of the device in a ring shape.

Keywords: Optical fiber scanner; Electro-thermal actuation; Resonance vibration; Imaging; Micro-cantilever beam; MEMS actuators

*T*o my beloved family for their continuous support
through all my life...

Acknowledgements

I would like to thank my senior supervisor, Professor Carlo Menon, for his inspiration, mentorship, attention, guidance, and efforts throughout my graduate studies. Professor Menon's guidance allowed me to become a better researcher allowing me a chance to work on a project that can make difference in the world by improving the lives of many patients.

I would like to express my gratitude to my supervisor Dr. Pierre Lane who provided me continuous guidance throughout the project providing me with invaluable hands-on skills in the field of Optics and imaging. I am also grateful to Geoffrey Hohert for his great support to the project.

I would like to thank my co-supervisor Dr. Andrew Rawicz for his help and valuable suggestions throughout the project. I would like to thank Dr. Ash Parameswaran for sharing some valuable suggestions.

I would also like to thank all the members of MENRVA research group who helped me throughout my research. I would like to especially thank Dr. Carolyn Weeks-Levy for proofreading journal articles. I would also like to thank Yasong Li, Aydin A. Ahrabi for initial equipment trainings. I am also thankful to Thushani De Silva for her help in the clean room. Special thanks are given to the staff of 4D LABS for providing access and training to the laser micromachine.

Last, but not least, I would like to thank my family, and babies Sehajpreet and Mehtaab, for their unconditional love, support, and encouragement.

Table of Contents

Declaration of Committee	ii
Abstract	iii
Dedication	v
Acknowledgements	vi
Table of Contents	vii
List of Tables	xi
List of Figures	xii
List of Acronyms	xviii
Chapter 1. Introduction.....	1
1.1 Motivation	1
1.2 Objectives	3
1.3 Thesis Layout	4
Chapter 2. Literature Review.....	6
2.1 Disclosure	6
2.2 Introduction	6
2.3 Medical Imaging Applications	9
2.3.1 Optical Coherence Tomography	9
2.3.2 Confocal Microscopy	12
2.3.3 Nonlinear Microscopy	15
Multiphoton Microscopy	16
Higher Harmonic Generation Microscopy	17
Raman Scattering Microscopy	19
2.3.4 Photoacoustic Imaging	20
2.4 Overview of optical components used in endoscopes	23
2.4.1 Fiber bundles in endoscopes	25
2.4.2 Single fiber endoscopy	28
2.4.3 Graded index (GRIN) lens scanner	31
2.5 Scanning Directions	32
2.5.1 Side View Imaging	33
2.5.2 Forward View Imaging	34
2.6 Cantilever Beam Mechanics and Scanning Principle	35
2.6.1 Resonant Scanner	39
2.6.2 Non-Resonant Scanner	40
2.6.3 Semi-Resonant Scanner	41
2.7 Scanning patterns	42
2.7.1 Raster scanning	43
2.7.2 Spiral scanning	44
2.7.3 Lissajous scanning	44
2.7.4 Circular scanning	45
2.7.5 Propeller scanning	45

2.8 Concluding Remarks	46
Chapter 3. Actuators in Cantilever-Based Endoscopic Devices	48
3.1 Disclosure	48
3.2 Introduction	48
3.3 Piezoelectric actuators	49
3.3.1 Disc piezoelectric actuator	51
3.3.2 Tubular piezoelectric actuator	53
3.4 Electro-thermal actuators	55
3.4.1 Hot-and-cold Arm actuators	57
3.4.2 Chevron actuators.....	59
3.4.3 Bimorph actuators.....	61
3.5 Electromagnetic actuators	63
3.5.1 Moving magnet configuration	63
3.5.2 Moving coil configuration.....	66
3.5.3 Magnetostrictive actuation	67
3.6 Electrostatic actuators	68
3.6.1 Parallel plate actuator	68
3.6.2 Comb drive actuator	69
3.7 Shape memory alloy actuators	70
3.8 Conclusion	72
Chapter 4. Design and Fabrication of Sub-millimeter sized Optic Fiber Scanner	75
4.1 Disclosure	75
4.2 Introduction	75
4.3 Background.....	75
4.4 Design Overview	77
4.5 Actuator Design	78
4.6 Cantilever Fabrication.....	80
4.7 Packaging	81
Chapter 5. Characterization and Image Reconstruction	84
5.1 Disclosure	84
5.2 Introduction	84
5.3 Resonant Frequency	85
5.4 Simulation for Optimization	86
5.4.1 Fiber-Tip Displacement vs. Time	86
5.4.2 Bridge Temperature vs. Time	88
5.4.3 Temperature vs. Input Current.....	89
5.5 Cantilever Drive Characterization	90
5.6 Scan Characterization	91
5.6.1 Whirling Effect.....	94
5.7 Image Processing.....	96
5.7.1 Imaging Setup	97

5.7.2 Image Acquisition	98
5.7.3 Interpolation	99
5.8 Summary	102
Chapter 6. Fabrication of a stepped optical fiber with minimum power leakage	104
6.1 Disclosure	104
6.2 Introduction	104
6.3 Problem Overview	104
6.3.1 Fabrication of a stepped optical fiber with minimum power leakage	105
6.3.2 Cleavage at the distal end	107
6.3.3 Power Leakage	108
6.4 Chemical Etching	109
6.4.1 Fabrication of a cantilevered section using the chemical etching method	110
6.4.2 Simulation of wet chemical etching	112
6.4.3 Results	114
6.5 Alternative methods.....	116
6.6 Conclusion	117
Chapter 7. Collection of reflected light.....	119
7.1 Disclosure	119
7.2 Introduction	119
7.3 Method	119
7.4 Experimental setup	120
7.5 Results	123
7.6 Discussion.....	125
7.7 Simulation of light collection using Zemax	125
7.8 Conclusions	131
Chapter 8. 2D scanning using single actuator.....	132
8.1 Introduction	132
8.2 Exciting the fiber in two directions.....	134
8.3 Bi-directional motion with nonlinear coupling.....	135
8.4 Bi-directional motion by asymmetric cantilever	136
8.5 Bi-directional motion by an asymmetric actuator.....	139
8.6 Bi-directional motion by an asymmetric actuator and asymmetric cantilever	143
8.6.1 Asymmetric bridge structure	143
Electrothermal Analysis	144
Mechanical Deflection Analysis	147
8.6.2 Design optimization.....	148
Optimization of Design A and Design B	148
Design C	150
Design D	152
8.6.3 Optimized actuator-cantilever setup	154
Design E	156
8.7 2D scan	159

8.8 Conclusions	161
Chapter 9. Fabrication and testing of final assembled device.....	162
9.1 Introduction	162
9.1.1 Optical aspect of the resolution.....	164
9.1.2 Sampling aspect of the resolution	166
9.2 Fabrication and Packaging	167
9.3 Testing Setup	170
9.4 Future Proposed Imaging Setup	171
Chapter 10. Conclusion	172
10.1 Future Work	175
References.....	177

List of Tables

- Table 2.1. Performance of different imaging applications [17].
- Table 2.2. Comparison between system performances of imaging technologies used in endoscopes [73].
- Table 2.3. Comparison between forward and side view scanners [17].
- Table 2.4. Summary table for different scanners [17].
- Table 2.5. Comparison table for different scanning patterns [17].
- Table 3.1. Comparison between different actuation methods used in cantilevered endoscopes [17].
- Table 3.2. Fiber-optic cantilevered scanners developed for endomicroscopy [73].
- Table 7.1. Light transmission properties through the fibers fabricated using the heating and pulling method [229].
- Table 7.2. Light transmission properties through the fibers fabricated using the etching method [229].
- Table 7.3. Optical parameters of skin layers.
- Table 8.1. Parameters of the reference polysilicon micro-actuators.
- Table 9.1. Resonance frequency in Hz as a function of cantilever dimensions.

List of Figures

- Figure 2.1. The schematic diagram of an optical coherence tomography (OCT) scanner [17].
- Figure 2.2. OCT image of the human retina and comparison of macular thickness in a person without Alzheimer's disease (AD), and patient with AD (taken with the permission of [33]).
- Figure 2.3. Schematic diagram of a confocal endoscope [17].
- Figure 2.4. In vivo confocal images: (a) reflectance image of tissue phantom with cervical cells and collagen (taken with permission of [39] © The Optical Society); (b) fluorescence image of an adenoma mucosa (taken with the permission of [43] © 2011 IEEE); (c) fluorescence image of a normal mucosa (taken with the permission of [43] © 2011 IEEE).
- Figure 2.5. Schematic diagram of a nonlinear endoscope [17].
- Figure 2.6. Two-photon exciting fluorescence (TPEF) image of ovarian cancer cells: (a) Fluorescence TPEF image using β -Galactosidase (β -gal) probe; (b) image using Lyso Tracker Red probe; (c) overlay of images a and b; (d) intensity profile (taken from [46] with permission).
- Figure 2.7. Second harmonic generation (SHG) and third harmonic generation (TPEF) images of differentiated neuroblastoma cells (taken with the permission of [50]).
- Figure 2.8. Images of brain metastasis of squamous cell carcinoma: (a) Hematoxylin and eosin-stained sample; (b) TPEF image; (c) Coherent anti-Stokes Raman scattering (CARS) image; (d) combining CARS and TPEF (used with the permission of [52]).
- Figure 2.9. Schematic diagram of a photoacoustic microscope (taken with the permission of [58] CC-By license).
- Figure 2.10. Photoacoustic image of a mouse ear: (a) maximum amplitude image of 1 mm \times 1 mm; (b) image of a small fragment of image a (taken with the permission of [63]).
- Figure 2.11. Block diagram of a confocal micro-endoscope [73].
- Figure 2.12. Fluorescence confocal imaging developed by Pentax: a) schematic design of the endomicroscope; b) an en-face image of rectal mucosa showing the crypt lumens (taken with the permission of [124]).
- Figure 2.13. Schematic diagram of a PARS-OCT probe: a) distal tip; b) circular motion generation by rotating just one lens; c) linear scan by rotation of both lenses (taken with permission of [125]) © The Optical Society.
- Figure 2.14. Endoscopic OCT image of the gill structure of a tadpole: (a) photograph of probe relative to the tadpole; (b, c) OCT images showing gill pockets indicated with g (taken with the permission of [125]). © The Optical Society.
- Figure 2.15. Schematic diagram: (a) side viewing probe; (b) forward viewing probe [17].
- Figure 2.16. Euler–Bernoulli beam and a free body diagram of an element of the beam [73].

- Figure 2.17. Deformation of a cantilever beam at resonance [73].
- Figure 2.18. Mode shapes of a cantilever beam describing the beam shape in vibration at resonance [17].
- Figure 3.1. Piezoelectric bending actuator: a) schematic diagram; b) working principle [73].
- Figure 3.2. Multiple patterns generating fiber scanner: a) schematic diagram of the scanner; b) achieved scanning patterns projected on a USAF target (taken with permission of [162]).
- Figure 3.3. Raster scanning endoscope: a) mechanical assembly; b) developed prototype; c) optical path diagram; d) Fluorescence image of an unstained ex vivo lung tissue (taken with the permission of [150]).
- Figure 3.4. Schematic diagram of a scanning fiber endoscope (taken with permission of [15]).
- Figure 3.5. In vivo images of airways of a pig acquired with: a) conventional Pentax bronchoscope; b) scanning fiber endoscope (taken with permission of [15]).
- Figure 3.6. Nonlinear optical endoscope: a) schematic diagram; b) two-photon and second harmonic generation structural image of a resected mouse liver (taken with permission of [170] CC-By license).
- Figure 3.7. Fourier-plane fiber scanner: a) schematic diagram; b) cross-sectional tomogram of human finger (taken with permissions of [171]).
- Figure 3.8. Electrothermally actuated confocal endo-microscope: a) schematic diagram; b) working principle (taken with permission of [116]).
- Figure 3.9. Cantilevered fiber scanner using Chevron actuator: a) schematic diagram; b) reconstructed image of a resolution target [24].
- Figure 3.10. Schematic diagram of a non-resonant fiber scanner using bimorph electrothermal actuation technique (taken with the permission of [152]).
- Figure 3.11. Forward-viewing OCT probe based on electromagnetic actuation: a) schematic diagram; b) real-time image of conjunctiva (taken with the permission of [196]) © The Optical Society.
- Figure 3.12. Schematic of an electromagnetically driven fiber scanner (taken with the permission of [197] © 2011 IEEE).
- Figure 3.13. Schematic design of a fiber scanner excited at second resonance mode using an electromagnetic actuator (taken with the permission of [115] © 2011 IEEE).
- Figure 3.14. Schematic of a magnetically actuated fiber-based imaging system (reprinted with the permission from [205]).
- Figure 3.15. Electrostatically driven fiber scanner: a) schematic diagram; b) Doppler OCT image of a tadpole heart (taken with permission of [213]) © The Optical Society.
- Figure 3.16. Schematic design of endoscopic tip guided using SMA coils (taken with permission [218] © 2011 IEEE).
- Figure 3.17. Active bending endoscope using SMA coil actuators: a) endoscope design; b) zoomed view of the actuation mechanism (taken with the permission of [220] © 2011 IEEE).

- Figure 4.1. The original proposed design.
- Figure 4.2. The schematic design of the updated packaged assembly.
- Figure 4.3. The laser cutout of the brass foil: a) perpendicular configuration [24], b) parallel configuration.
- Figure 4.4. Fabrication process of the cantilever fiber [229].
- Figure 4.5. Microfabricated SU-8 components: a) upper collars; b) semi-circle pieces; c) collar structures together.
- Figure 4.6. Packaging of the sample: a) actuator flipped on PDMS structure and semi-circle pieces placed in the groove of actuator; b) upper collar structures placed on SMF fiber; d) side view of assembly.
- Figure 4.7. Packaged scanner sample [24].
- Figure 5.1. Resonant frequency in function of the cantilever diameter ($2R$) and length (L) [24].
- Figure 5.2. Dimensions of the device being simulated using ANSYS [163].
- Figure 5.3. Resonance time response of the cantilever fiber measured at the tip, with the damping effect of surrounding air versus no damping. The inset enlarges the displacement profiles between 0.19 s to 0.2 s.
- Figure 5.4. Temperature profile of the aluminum actuating bridge at 0.314 W power input. The inset enlarges the temperature profiles from 0.19 s to 0.2 s [163].
- Figure 5.5. Temperature response of the aluminum bridge at different current levels using an actuation frequency of 3 kHz [163].
- Figure 5.6. Schematic diagram of the experimental setup [24].
- Figure 5.7. The side view of the sample under actuation [24].
- Figure 5.8. Optical setup to capture direct light: a) Ray diagram; b) Experimental setup.
- Figure 5.9. Tip displacements for two different samples using STC-MBE132U3V camera.
- Figure 5.10. Tip displacement using STC-MCA5MUSB3 camera.
- Figure 5.11. Front view of the tip displacement of the cantilever under actuation [24].
- Figure 5.12. The tip displacement in function of current.
- Figure 5.13. SEM image of the distal end of the cantilevered fiber.
- Figure 5.14. Schematic diagram of the complete testing setup [24].
- Figure 5.15. Optical design: a) experimental setup; b) ray diagram.
- Figure 5.16. Timing diagram for image acquisition [24].
- Figure 5.17. Rotating ellipse representing the cantilever's tip displacement [24].
- Figure 5.18. Quarter of ellipse traced in time [24].
- Figure 5.19. Resolution target used as imaging object [24].
- Figure 5.20. Reconstructed image of the resolution target corresponding to 25lp/mm [24].
- Figure 5.21. Acquired image of the resolution target at 30lp/mm [24].

- Figure 6.1. Schematic of fabrication process of the cantilever fiber using the heating and pulling method [229].
- Figure 6.2. The distal end of the cantilevered fiber: a) before process; b) after processing.
- Figure 6.3. The beam of light intensity from the micro-balled tip of the cantilever.
- Figure 6.4. Light leaking at the spliced region.
- Figure 6.5. The schematic of the setup used for etching the optical fibers [229].
- Figure 6.6. The setup used for etching optical fibers at vaporous state [229].
- Figure 6.7. 2D geometry of wet etching assembly with the prescribed boundary conditions [229].
- Figure 6.8. The cross section of the fiber after etching in: a) an open surface; b) presence of an Ecoflex membrane [229].
- Figure 6.9. Fiber diameter in time during etching at 23°C [229].
- Figure 6.10. Etching rate in function of water temperature [229].
- Figure 6.11. Etched fibers: (a) using liquid HF solution; (b) using HF vapor [229].
- Figure 7.1. The schematic design of the test setup described.
- Figure 7.2. The schematic diagram for the capture of reflected light from a mirror [229].
- Figure 7.3. Experimental setup for light collection measurement.
- Figure 7.4. Schematic diagram of a DCFC (taken with the permission of [259] CC-By license).
- Figure 7.5. Optical diagram of the proposed light collection setup [229].
- Figure 7.6. Illumination path of proposed optical system.
- Figure 7.7. Detection path of proposed optical system.
- Figure 7.8. Complete ray fan diagram for tip displacement of $\pm 100 \mu\text{m}$.
- Figure 7.9. Illumination path of the optical setup in non-sequential mode.
- Figure 7.10. Complete optical ray diagram in non-sequential mode.
- Figure 8.1. Schematics showing the proximal scanning with a FORJ (taken with the permission of [263]).
- Figure 8.2. Schematic of the connection between slip rings and brushes (used with the permission of [264] CC BY license from DESIGN WORLD • WTWH Media).
- Figure 8.3. Cantilever-actuator assembly in case of actuation by perpendicular bridges.
- Figure 8.4. The geometry of the cantilever beam under analysis.
- Figure 8.5. Displacement of the tip of the fiber: a) in x direction, b) in y direction.
- Figure 8.6. Packaged sample with asymmetric cantilever fiber.
- Figure 8.7. Front view of performance of sample shown in Figure 6 at different duty cycles: a) 50% duty cycle; b) 25% duty cycle; c) 15% duty cycle.
- Figure 8.8. The non-uniformity of the base excitation
- Figure 8.9. Phase plot of tip displacement using base excitation in Figure 8.8.

- Figure 8.10. Schematic of an asymmetric bridge with cylindrical cantilever assembly.
- Figure 8.11. The displacement of bridge structure: a) zoomed view of bridge structure; b) bridge displacement along X direction; c) bridge displacement in Y direction.
- Figure 8.12. Schematic diagram showing geometry and cantilever alignment in case of an asymmetric bridge configuration.
- Figure 8.13. Time response of cantilever beam tip actuated using asymmetric bridge.
- Figure 8.14. Fiber tip displacement excited by asymmetric bridge in presence of damping.
- Figure 8.15. Front light capture from a sample with configuration shown in Figure 8.12 at a frequency of: a) 1.524 kHz; b) 3.942 kHz; c) 2.007 kHz.
- Figure 8.16. Electrothermal MEMS actuators with a) different arm lengths; b) different cross section.
- Figure 8.17. Temperature distribution along design A electrothermal actuator.
- Figure 8.18. Temperature distribution along design B electrothermal actuator.
- Figure 8.19. Comparison between temperature distribution in design A and design B.
- Figure 8.20. Temperature distribution along design B electrothermal actuator placed on a substrate with an airgap of 2 μm .
- Figure 8.21. Tip deflection versus input voltage for design A (blue stars) and B (red stars).
- Figure 8.22. Variation of tip deflection in function of length ratio between two arms.
- Figure 8.23. Tip deflection of design B in function of length ratio between two arm structures: a) design with 2 μm airgap from substrate; b) design without heat transfer towards substrate.
- Figure 8.24. Schematic diagram of design C.
- Figure 8.25. Performance of design C actuator: a) temperature distribution; b) tip deflection.
- Figure 8.26. Tip deflection of design C in function of length ratio between two arm structures and the wider arm portion in the cold arm.
- Figure 8.27. Tip deflection in function of input voltage of design C compared to designs A and B.
- Figure 8.28. Schematic diagram of design D.
- Figure 8.29. Tip deflection in function of length ratios of hot arm.
- Figure 8.30. Performance of design D actuator compared to other designs: a) temperature distribution; b) tip deflection.
- Figure 8.31. Front light image of the cantilever scan based on bridge having shape of design D.
- Figure 8.32. Tip displacement of the cantilever fiber with frequency change for two samples actuated by a bridge having shape similar to that of design D.
- Figure 8.33. Design E having two cold arms connected at the base: a) schematic diagram; b) laser cut-out of the corresponding actuator.
- Figure 8.34. Sample with design E actuator configuration: a) cantilever-actuator assembly; b) scan performed by the fiber tip in case of asymmetric fiber

facing hot arm; c) scan from fiber tip in case asymmetry towards the cold arm.

Figure 8.35. Modified version of design E having cold arm with a passive fin structure: a) schematic diagram; b) laser cut-out of the corresponding actuator.

Figure 8.36. Sample with modified design E actuator configuration: a) cantilever-actuator assembly; b) scan from fiber tip in case asymmetry towards the cold arm.

Figure 9.1. Material comparison in “Granta: CES Selector” software package based on thermal conductivity vs: a) electrical resistivity; b) thermal expansion coefficient.

Figure 9.2. Front view of actuator-cantilever assembly.

Figure 9.3. Collar structures made from laser cutting of: a) glass coverslip; b) diamond.

List of Acronyms

AC	Alternating Current
AD	Alzheimer's Disease
AlN	Aluminum Nitride
AR-PAM	Acoustic Resolution Photoacoustic Microscopy
β -gal	β -Galactosidase
CARS	Coherent Anti-Stokes Raman Scattering
CCD	Charge-Coupled Device
CFB	Coherent Fiber Bundle
CM	Confocal Microscopy
CMOS	Complementary Metal Oxide Semiconductor
COPD	Chronic Obstructive Pulmonary Disease
CT	Computed Tomography
DAQ	Data Acquisition
DC	Direct Current
DCF	Double Clad Fiber
DCFC	Double Clad Fiber Coupler
DOCT	Doppler OCT
DOF	Degrees of Freedom
ENB	Electromagnetic Navigation Bronchoscopy
ETDRS	Early Treatment Diabetic Retinopathy Study
EUS	Endoscopic Ultrasound
FD	Fourier Domain
FIB	Focused Ion Beam
FORJ	Fiber-Optic-Rotary-Joint
FOV	Field of View
FWHM	Full Width at Half Maximum
GI	Gastrointestinal
GRIN	Graded-Index
HF	Hydrofluoric acid

IR	Infrared
MEMS	Micro-Electro-Mechanical System
MFD	Mode Field Diameter
MMF	Multimode Fiber
NA	Numerical Aperture
NBI	Narrow Band Imaging
NCF	No Core Fiber
NIR	Near-Infrared
OCT	Optical Coherence Tomography
OR-PAM	Optical Resolution Photoacoustic Microscopy
PA	Photoacoustic
PACT	Photoacoustic Computed Tomography
PARS-OCT	Paired-Angle Rotating Scanning OCT
PDE	Partial Differential Equation
PDMS	Polydimethylsiloxane
Pebax	Polyether block amide
PETE	Polyethylene Terephthalate
PMMA	Polymethyl Methacrylate
pRNFL	Peripapillary Retinal Nerve Fiber Layer
PZT	Lead Zirconate Titanate
R-EBUS	Radial Endobronchial Ultrasound
SD	Spectral Domain
SEM	Scanning Electron Microscope
SFE	Scanning Fiber Endoscope
SHG	Second Harmonic Generation
SMA	Shape Memory Alloy
SMF	Single Mode Fiber
SNR	Signal to Noise Ratio
SRS	Stimulated Raman Scattering
SS	Swept-Source
TD	Time Domain

THG	Third Harmonic Generation
TPEF	Two-Photon Exciting Fluorescence
US	Ultrasound
USAF	United States Air Force
VB	Virtual Bronchoscopy
VLS	Visible Light Spectroscopy
WDM	Wavelength Division Multiplexer
WLE	White Light Endoscope

Chapter 1.

Introduction

An endoscope is an imaging device made up of a long and thin tube that can be inserted into the hollow openings of the body to image the inner sections in real time and in a less invasive manner. The advances in fiber optic systems led to the development of flexible endoscopes enabling high resolution images of narrow sections of the body and reducing the number of biopsies required for a specific diagnosis such as cancer detection, microvascular oxygen tension measurement, chronic mesenteric ischemia, sub-cellular molecular interactions, etc. Earlier developed standard white light endoscopes (WLEs) had limited ability to differentiate metaplasia from dysplasia. Such limitations were surpassed by enhancing the image contrast using dyes in chromoendoscopy or applying digital filters in narrow band imaging (NBI) [1, 2]. The increased use of endoscopic devices highly improved the diagnostic rate of cancers by permitting the visualization of early dysplasias which may lead to cancer development [1].

1.1. Motivation

Cancer is the second major cause of deaths around the world. It is estimated that about 9.6 million people died due to cancer in 2018. Among this number, lung cancer is a leading cause of deaths. There were about 2.09 million new cases of lung cancer registered globally each year, while lung cancer is responsible for 1.76 million deaths annually [3].

Chronic obstructive pulmonary diseases (COPDs) are responsible for over 3 million deaths annually around the world, which made up almost 5% of total deaths in 2015. These diseases limit the airflow in the lung which leads to the breathlessness [4].

Similarly, there were over 450 thousand cases diagnosed with pancreatic cancer in 2018, and the number of deaths corresponding to it were about 432 thousand [5]. Similarly, about 300 thousand cases of ovarian cancers were discovered, with around 185 thousand deaths in 2018 [6].

Chest radiography or Low dose computed tomography (CT) are one of the primary screening tests performed to image cancers or COPD at early stages. The sensitivity of these methods is about 78% and 89%, respectively, in the case of the lung cancer [7], between 76%-92% in the case of pancreatic cancer detection using intravenous contrast [8], and about 79% in the case of the ovarian cancer [9]. However, these sensitivities values seem high, the very smaller size tumors or lesions, i.e., early-stage abnormalities, are difficult to screen. Often imaging with an endoscope and biopsy using a fine needle aspiration technique is followed by a CT scan in the case of the suspected malignancy. Depending on the location of the biopsy, there can be other complications related to it; for example in case of transthoracic needle aspiration, there is 15-25% risk of pneumothorax or collapsed lung [10]. Biopsies can be complicated due to abnormal collection of air, or it can lead to inflammation in the case where a biopsy is performed in pancreas. The endoscopic biopsy is feasible but, as the lesion is not being imaged, it's diagnostic yield is small.

To increase the quality of data obtained from a biopsy, several guided bronchoscopy technologies were developed which include electromagnetic navigation bronchoscopy (ENB), virtual bronchoscopy (VB), radial endobronchial ultrasound (R-EBUS), ultrathin bronchoscope, and guide sheath in case of the transbronchial biopsy [11]. Transbronchial biopsy assisted with R-EBUS allows imaging of the sixth- to eighth-generation airways in the lungs, while the traditional bronchoscopes are limited to the fourth-generation airways [11]. The five-year survival rate for patients having COPD is between 40% and 70% depending on its grade, and it is just 18.6% in the case of lung cancer [12].

Endoscopic ultrasound (EUS) is often used to assist the biopsy in cases of pancreatic or ovarian cancer. Ovarian and Pancreatic cancers are the silent killers as the symptoms are noticeable only at an advanced stage of the disease. However, an early-stage cancer also produces some symptoms, but is difficult to detect due to the limitation in the imaging methods. Due to the late detection, the five year survival rate for pancreatic cancer is only 7% [13], while it is 47% for ovarian cancer, which also depends upon the age and stage of the cancer [14].

Thus, the life expectancy is small for all these malignancies discussed above. An early detection, in all these cases can improve the survival rate permitting containment of

the lesion or tumor before it worsens and spreads. The size of an endoscope dictates the body part that can be imaged with it. Currently, the smallest endoscopes available in the market are the scanning fiber type ones and are limited by the size being over 1.2mm [15]. The design of an ultra small endoscope having a smaller diameter would permit the visualization of finer areas of the body allowing for an earlier detection of cancer before metastasizing and providing more time for diagnosis. Smaller endoscopes can increase the survival rates considerably and would provide a higher yield for endoscope assisted biopsies increasing their sensitivity, i.e., reducing the false positives.

This research project consists of the development of a scanning fiber based miniaturized catheter, having a diameter of about 600 μ m, which is the basis for the design of a forward viewing endoscopic head. The proposed ultra-miniaturized endoscope will be small enough to access most airways and areas of the lung (it can nearly reach the terminal bronchiole, i.e., sub-millimeter sized airways of the lung), narrow sections of the pancreatic duct (where most of the times, the pancreatic cancer originates), and the narrowest section at the openings of the fallopian tubes.

The proposed technology has the potential to overcome the limitations of currently available imaging technologies providing an early detection of cancer and COPD having a much smaller size compared to commercially available endoscopes. There are about 35,000 terminal bronchioles having an average diameter of about 0.65 mm that can be made accessible for imaging through the proposed miniaturized endoscope, whereas the current bronchoscopes are limited to visualize the subsegmental bronchi. Thus, the proposed imaging scanner could potentially be deployed through the working channel of an endoscope significantly increasing the diagnostic yield of the transbronchial biopsy and enabling visualization of stage 0 and I cancerous regions (cancer in situ). According to the Canadian Cancer Society report, the low survival rate in many cancers is due to late diagnosis. Non-small cell lung cancer in the United States has a five-year estimated survival rate ranging from 1% to 10% across the substages of stage IV, while it ranges from 68% to 92% for the sub stages of stage I [16].

1.2. Objectives

The final objective of this research project was to develop and assess an apparatus setting the baseline for a technology able to overcome limitations of current available technologies

enabling an early detection of lung diseases, such as COPD and lung cancer, pancreatic and ovarian cancers. The following objectives were proposed in order to obtain the final working prototype of an ultra-miniaturized scanner:

1. Develop and configure a preliminary prototype using a novel thermal actuated cantilever able to meet the desired size requirements.
2. Validate and test the developed prototype through experimentation. Image the tip displacement of the cantilever fiber using an optical setup and reconstruct the radial scan from the light coming out from the tip of the Single Mode Fiber (SMF) cantilever.
3. Fabricate the cantilever fiber minimizing power leakage at the transitional zone between the fixed fiber portion and cantilever.
4. Fabricate the cantilever using a Double Clad Fiber (DCF). Collect the reflected light signal in all cases via inner cladding and compute the signal to noise ratio (SNR).
5. Design a rotary joint supporting optical and electrical signals or find alternative ways to avoid such connections by exciting the cantilever along two axes.
6. Develop the final proposed prototype catheter using a DCF as a cantilever and acquire an image collecting the reflected light within the system itself.

1.3. Thesis Layout

The thesis has the following layout:

Chapter 2, literature review, gives a detailed overview and working principles of optical imaging devices used in medical applications. Moreover, various optical devices along with the scanning principles, directions, and patterns used in endoscopic scanners are analyzed in this chapter.

Chapter 3 further presents different actuators used in cantilever based endoscopic scanners. The working principles, mathematical models, and various applications in medical imaging endoscopic scanners are discussed in here.

Chapter 4 elaborates on the preliminary design and fabrication of a sub-millimeter sized fiber-optic scanner. The working principles of the proposed electro-thermal actuator

along with its early design and fabrication process are presented in this chapter to address OBJECTIVE 1.

Chapter 5 studies the feasibility of the proposed design. In this chapter, the fiber-optic scanner fabricated during the achievement of OBJECTIVE 1, is characterized by linearly actuating the cantilever fiber near its base and evaluating the performance of the sample by imaging the fiber tip. A resolution target is imaged by rotating the target itself showing the completion of OBJECTIVE 2.

Chapter 6 is based on the completion of OBJECTIVE 3 overcoming the problem of light leakage in the heating and pulling method described in Chapter 4. During the fabrication process of the cantilevered fiber, there is some light leaking from the spliced area or a cleaved end. This chapter discusses some of the techniques used to minimize this light leakage.

Chapter 7 consists of the fabrication of the cantilevered fiber using an off-the-shelf available DCF fiber. In this step, the cantilevered fiber samples are fabricated either using the Vytran splicer (heating and pulling method) and Hydrofluoric acid (HF) etching (used in objective 3). The reflected light from a mirror surface is collected using the inner cladding of the DCF. Some Zemax simulations are performed to evaluate the collection of backscattered reflected light from a tissue surface. OBJECTIVE 4 is addressed in this chapter.

Chapter 8 elaborates on OBJECTIVE 5 by developing an alternative design which enables the bi-dimensional scanning of the target sample using a single actuator. The updated actuator is optimized with the help of mathematical models. It enables the fiber tip to move in a circular shaped pattern.

Chapter 9 presents the work performed for OBJECTIVE 6 which describes the fabrication of the final prototype design. The target object is scanned in a 2D manner by changing the actuation frequency in a linear manner allowing the fiber tip to move in a spiral pattern.

Chapter 10 concludes the study of the thesis along with some risk and mitigation strategies for the future testing.

Chapter 2.

Literature Review

2.1. Disclosure

The material presented in this chapter is extracted, reproduced, and modified with permission from the papers listed below which I have co-authored. Eventual modifications may have been introduced for a variety of reasons including clarifying the subject; providing additional information; and ensuring the formatting is consistent with the rest of the thesis.

- Kaur M., Lane P. M., Menon C. Endoscopic Optical Imaging Technologies and Devices for Medical Purposes: State of the Art. *Applied Sciences*, 2020; 10(19), pp. 6865:1-34.
- Kaur M., Lane P. M., Menon C. Scanning and Actuation Techniques for Cantilever-Based Fiber Optic Endoscopic Scanners – A Review. *Sensors*, 2021; 21(1), pp. 251:1-38.

2.2. Introduction

The development of optical components provides the foundation for rapid growth of biomedical imaging techniques. Optical devices have been largely used in medical applications to image and assist with surgical procedures as they allow direct localization of lesions and malignancies reducing the number of biopsies for a specific diagnostic procedure. Some of the largely used non-invasive medical imaging techniques such as X-ray, ultrasound, computed tomography, and magnetic resonance imaging scan large areas of the body and allow to quickly locate abnormalities. However, these techniques only provide structural information and are characterized by poor spatial resolution (~50 μm to 2 mm). Thus, the finer structure details are missed. Alternately, modern optical imaging techniques rely on optical contrast between the area of interest and the surrounding area and provide both the structural and functional information at a finer resolution (in the micrometer range).

Tissues are highly inhomogeneous materials, where light propagation is accompanied by certain absorption, scattering, refraction, or reflection based on different tissue surfaces and the wavelength of the light itself. This interaction between the tissue surface and light allows tissue imaging, which can be performed either using a backscattered or fluorescence light configuration. In the case of backscattering, the diffusely reflected (or backscattered) light from the superficial layers of the tissue is used for imaging purposes. The light photons can be scattered elastically where it changes its direction of propagation or can be scattered inelastically where some of the light photon energy is altered causing the incident and scattering photons to have different frequencies. The elastic scattering provides information about the size distribution of the scatterers. On the other hand, inelastic scattering such as Raman scattering provides information about the chemical composition and molecular structure of the tissue surface [15]. In the case of fluorescence, the incident light is absorbed by the tissue fluorophores causing the molecule/atom's electron to enter an excited state which is not stable and re-emits energy. The emitted energy is typically less than the absorbed energy. Thus, the emitted photons have a longer wavelength than the incident photon. The image contrast is produced by the fluorescence signatures of the different structures and provides detailed information about the tissue molecules. The fluorophore can be endogenous (when naturally contained in the tissue), or exogenous (when the fluorophores are added externally to stain the tissue structures). The latter case is typically used to enhance the image contrast when the background fluorescence is not negligible [15].

The continuous advancement in the optics field leads to the development of various imaging modalities. Among these, Optical Coherence Tomography (OCT) is a frequently used tissue imaging technique where a change in the refractive index of the scattering coefficient alters the intensity of the backscattered light and is used to provide contrast in the image [17]. Photoacoustic (PA) is another imaging technology that images a tissue surface using short pulsed light waves for detection of the ultrasonic waves generated from the optical absorption. It integrates the benefits of high contrast in optical imaging and deep penetration of ultrasonic imaging [18]. Based on imaging depth, PA imaging can be classified into PA microscopy (penetration depth <10mm), PA computed tomography (penetration depth between 10mm and 100mm), and minimally invasive PA imaging (penetration depth \geq 100mm) [19]. Confocal Microscopy (CM) is another imaging technique where the sample is illuminated using a point illumination system, and the out

of focus light is rejected by a pinhole placed at a plane optically conjugate to the object [17]. Nonlinear microscopy is another imaging technique using nonlinear optics [17]. In addition to these techniques, there is visible light spectroscopy (VLS) where the tissue surface is exposed to visible light and the absorbance spectrum provide structural and functional information about the tissue. This technique is largely used to monitor the microvascular hemoglobin oxygen saturation which can be further used to evaluate local ischemia situations by measuring the difference between oxygenated and deoxygenated hemoglobin [20, 21].

The in-vivo imaging of the luminal organs is performed using endoscopes. An endoscope is a long and thin tubular imaging device that can be inserted in the hollow openings of the body, to image the inner structures in a less invasive manner to provide information about early-stage pre-cancerous tissues. The earlier endoscopes were based on the use of white light for imaging that had a limited ability to differentiate between metaplasia and dysplasia. This limitation is overcome by using dyes in chromoendoscopy or using digital band filters in narrow band imaging (NBI) which enhance the imaging contrast [1, 2]. The optical components and the actuation method used in an imaging device dictates its performance. Early video endoscopes were based on the use of coherent fiber bundles (CFBs) which relied on multiple optical fibers to transport light from the light source to the target imaging surface, and charge-coupled devices (CCDs) to collect the reflected light [22]. The resolution of these devices is limited by discrete fiber pixilation. The image resolution is improved by the development of complementary metal oxide semiconductor (CMOS) chips [23]. However, the honeycomb effect generated by the non-imaging area between the fibers and the center-to-center distance between the optical fibers in a CFB limits the resolution due to discrete fiber pixilation [15].

The limited resolution is improved in recently developed flexible endoscopes by scanning laser light at the imaging surface. In such a case, the image is captured on a temporal basis, i.e., acquiring one pixel at a time, instead of a spatial one. In this case, the resolution is still based on the number of fibers present in the bundle but is improved with the help of specific optic lenses. The light beam can be scanned either by actuating the optical fiber at a resonance or non-resonance frequency, actuating a micromirror surface to deviate the light beam, or using a galvanometer scanner at the proximal end. The deviation of the light beam on the imaging target dictates the field of view (FOV) and the resolution of the correspondent image. Scanning and actuation techniques used to excite

a cantilever beam play a critical role in the performance of such a scanning device. In addition, the small size and the distortion-free imaging requirements need to be considered during the design of an endoscopic device for medical purposes as the size of an imaging probe sets the targeted imageable area, and the motion of organs can lead to the generation of artifacts in the image [15, 24, 17].

2.3. Medical Imaging Applications

The different techniques used for tissue and structural imaging are described below and include OCT, CM, nonlinear microscopy, and PA image acquisition.

2.3.1. Optical Coherence Tomography

The working principle of OCT is analogous to that of an ultrasound, with the difference that low coherent light is used instead of sound. Laser light is transmitted to the semi-transparent tissue surface using an optical fiber or other means discussed later in the thesis. The light backscattered from the tissue is monitored to reconstruct a cross-sectional image of the target tissue. The differential backscattered intensity from different tissue interfaces (refractive index changes) provides the contrast in OCT [25].

The speed of light in tissue ($225 \text{ m}/\mu\text{s}$) is about five orders of magnitude larger than the speed of sound in tissue ($150 \times 10^{-5} \text{ m}/\mu\text{s}$). The resolution of an image is directly proportional to the wavelength of the used signal. Smaller wavelength light provides a finer resolution (10 to 100 times) image as compared to that of ultrasound [26]. On the other hand, the time delay between the source signal and the reflected signal is much smaller and cannot be measured directly. Thus, an interference pattern must be measured either using a Michelson or a Mach–Zehnder interferometer [27]. The light coming from the laser source is split into two paths: one going towards the sample (called sample arm), and the other going towards a mirror (reference arm). The backscattered light from the tissue is compared with the light from the reference arm to form an interference pattern if the two light components are within the coherence length of the light source [28]. A schematic diagram of an OCT scanner is shown in Figure 2.1 [17].

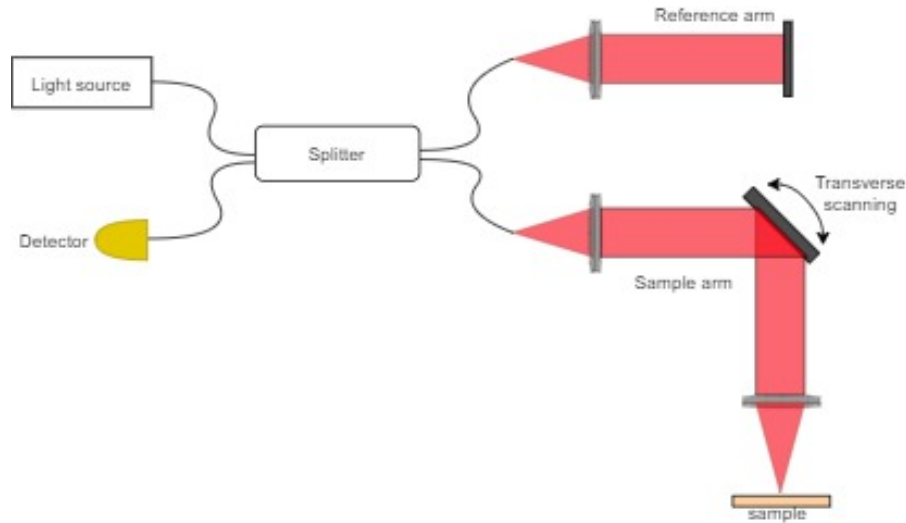


Figure 2.1. The schematic diagram of an optical coherence tomography (OCT) scanner [17].

Scanning can be performed in a time domain (TD) or in a Fourier domain (FD). In TD-OCT, a low-coherence broadband light source provides light to the two arms through an optical splitter. The path length of the reference arm is changed in time by moving the reference mirror in the axial direction. The interference pattern between the reflected light from the reference arm mirror (with distance travelled variable in time) and the backscattered light from sample provides a depth profile of the sample tissue. The two- or three-dimensional structure image is obtained by transversally scanning the light beam along the sample arm [28, 29].

In FD-OCT, the reference arm is static. Axial scanning can be performed in time using a frequency sweep of the light source to cover the broad bandwidth (swept-source OCT, or SS-OCT), or in space using a spectrometer to separate the different wavelengths on the detection side (spectral domain OCT or SD-OCT). Depth information of the sample is obtained using inverse Fourier transformation. In SS-OCT, the light source is a rapidly tunable laser, and the detector is a simple photodiode. In SD-OCT, the light source is a low-coherence laser, and the detector is a line scan camera. The elimination of the mechanically moving mirror in FD-OCT allows the sample to be imaged with higher acquisition speeds, which is the main reason that most of the current OCT systems are FD-OCT [28, 29].

Analogous to ultrasound, it is also possible to use a doppler OCT (DOCT) to measure the velocity of the scattering materials flowing through a channel, such as a blood vessel [28].

In OCT, the lateral resolution depends on the lens system as:

$$(\delta x, \delta y) = 0.56 \frac{\lambda}{NA}, \quad (1)$$

with λ being the central wavelength of the light spectrum, and NA is the numerical aperture. The lateral field of view (FOV) is given by:

$$FOV_{x,y} = \frac{f \tan \theta}{2}, \quad (2)$$

where f is the focal length of the lens, and θ is twice the scanning angle [28].

The axial resolution depends on the light source used by:

$$\delta z = \frac{2 \ln 2 \lambda^2}{\pi \Delta \lambda}, \quad (3)$$

where $\Delta \lambda$ is the full width half maximum of the light spectrum.

The axial FOV or depth of field in the possible image zone is given by:

$$FOV_z = 0.9 \frac{n \lambda}{NA^2}, \quad (4)$$

with n being the index of refraction in the medium [27, 28].

OCT has gone through enormous development since its first appearance in the early 1990s. These improvements comprise the higher imaging resolution (axial resolution in the range of 1–15 μm , lateral resolution in 2–25 μm range), acquisition rate, deep tissue penetration (up to 3 mm), and methods of light transmitted to the target area [30, 28].

OCT is largely used in ophthalmology to image the retina [31, 32]. The cross-sectional OCT image allows the identification of different structure layers in the eye, which can be used as biomarkers in diagnosis. Kim et al. imaged the thickness of the retinal layer using an SD-OCT device and correlated the thickness to the mini-mental state [31]. Cunha et al. determined that patients with Alzheimer's disease (AD) have a thickness reduction of the peripapillary retinal nerve fiber layer (pRNFL) and the internal macular layer. An OCT image of the human retina is shown in Figure 2.2 along with the nine sector Early

Treatment Diabetic Retinopathy Study (ETDRS) grid of the macular area with the average thickness values [33]. Recent development in the optical field utilizes and facilitates miniaturization of the OCT scanners at microscopic ranges enabling in vivo imaging of the blood vessels and hollow cavities in the body, such as the colon, esophagus, urinary tract, and lungs [26, 34, 35]. Various instruments used to transmit, and scan illuminating light on the target tissue sample and collect the backscattered light are discussed later in this chapter.

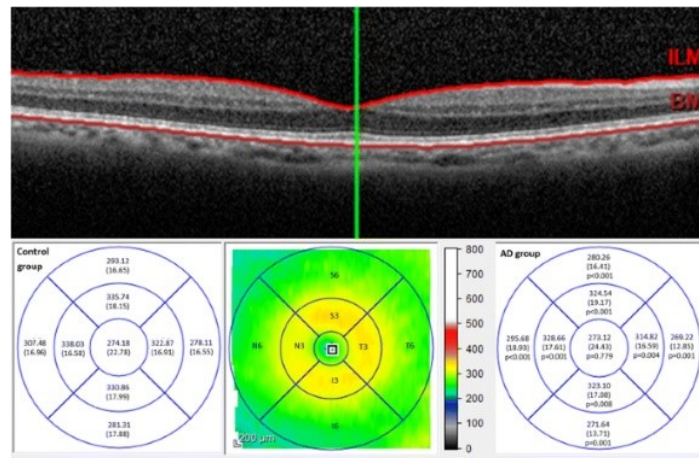


Figure 2.2. OCT image of the human retina and comparison of macular thickness in a person without Alzheimer's disease (AD), and patient with AD (taken with the permission of [33]).

2.3.2. Confocal Microscopy

In a conventional epi-reflectance microscope, the object (specimen) is uniformly illuminated using a light source, and the image is obtained from the reflected light. Biological tissue is a highly light-scattering media. Thus, the scattered photons generated from the out of focus refractive index differences represent noise causing blur in the image. In confocal microscopy (discovered in 1957), the sample is illuminated using a point illumination system, where out-of-focus light is rejected by a pinhole placed at a plane optically conjugate to the object. As a single point of the sample is illuminated at a time, scanning methods are required to generate 2-D or 3-D images using a confocal microscope. For beam scanning, it is possible to use either a single beam for scanning using micro mirrors or other fiber optic techniques discussed later in the chapter, or multiple beam scanning using the spinning Nipkow disks or spectral encoding. The

imaging of thick sections is accomplished using optical sectioning by imaging virtual slices of the sample. The depth of imaging can be changed by refocusing the light [28, 36].

The originally proposed trans-illumination confocal microscope used two objective lenses for illumination and detection of the light passed through a pair of pinholes placed at the light source to create a point source and at the detector to avoid the out-of-focus noise light signal. Thus, the pinholes act as a filter that pass information carrying ballistic photons and reject the scattered out-of-focus photons. Consequently, this configuration generates higher resolution images. The contrast in reflectance-based confocal microscopy is based on the scattering properties of the tissue sample, whereas the contrast in fluorescence-based confocal microscopy is given by the fluorescent properties of the sample. In the latter case, the resolution is increased by staining the sample with fluorophores that increase the contrast and sensitivity of the image [28, 37].

The size of the pinholes affects the lateral and axial resolution of the obtained image and can be measured by placing the point object at the focal point of the objective lens. The resolution can also be described in terms of the Airy pattern, which is the light intensity distribution near the focal point. The Airy pattern in confocal microscopy has a narrower central lobe and attenuated side lobes, providing for high resolution. The transverse resolution is given by Equation (1), while the axial resolution can be described as [28]:

$$\delta z = \frac{0.89\lambda}{n(1-\cos\theta)}, \quad (5)$$

where θ is the angular aperture (half angle of the marginal ray).

The lateral resolution in confocal microscopy is less than 1 μm , and the axial resolution is about 1 μm . In a fluorescence-based system, the resolution depends on the point spread functions of the illumination and detection signals, which differ from each other due to the Stokes shift. In fiber optic confocal microscopy, the fibers used for illumination and detection act as pinholes [28].

Dickensheets and Kino fabricated one of the early fiber optic confocal microscopes, where the single mode fiber illuminates the beam on the target sample, and the beam is scanned along the sample using torsional scanning mirrors [38]. The continuous development in the MEMS field facilitates the miniaturization of devices and

achieving better imaging with higher resolution. Liu et al. developed a 3-D scanning fiber optic confocal microscope, which can scan with a depth of field of over 400 μm . An optical fiber carrying the illuminating light is excited at resonance by an electrothermally actuated MEMS mirror. The scanner can image the tissue surface with a lateral resolution of 1 μm , and an axial resolution of 7 μm [37]. Many different confocal microscopes are reported in the literature and are based on different scanning methods to image different sections of body organs, which are described later in the chapter [39, 40].

In the case of confocal endoscopy, the illumination and collection system are aligned on a single focal plane. The laser light is transported to the distal lens using an optical fiber bundle focused on the tissue sample. The reflected light is refocused through the same lens with a pinhole, which excludes the out-of-focus scattered light, increasing the resolution. Usually, the scanning is made possible by placing the scanning mirrors at the proximal end of the fiber bundle. The systematic design of a confocal endoscope is shown in Figure 2.3 [17].

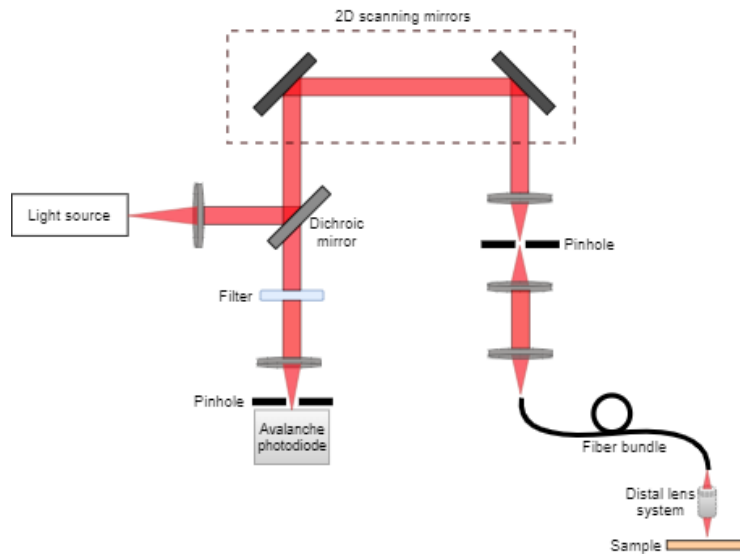


Figure 2.3. Schematic diagram of a confocal endoscope [17].

Cell-viZio developed by Mauna Kea Technologies is one of the most widely used technologies for clinical applications that uses a variety of confocal miniprobes to provide high-quality in vivo tissue imaging [41]. The newly developed Cell-viZio device provides confocal fluorescence microscopy imaging using optical fibers. This technology is named fibered confocal fluorescence microscopy (FCFM). Laemmel et al. tested three different

FCFM probes for microvascular observations and compared the results with intravital fluorescence imaging proving the flexibility, micro-invasiveness, and in vivo imaging of the deep areas over conventional microscopy. The probe with the smallest cross-sectional area has a diameter of 650 μm and provides images with lateral and axial resolutions of 5 and 15 μm , respectively, with a frame rate of 12 Hz [42]. Recently, Wang et al. developed an ultra-small sized confocal endomicroscope. The 2.4-mm-diameter probe (compatible with the 2.8-mm working channels of clinical endoscopes) used by Wang et al. to image the colon of a mouse provides images with a lateral and axial resolution of 1.5 and 12 μm , respectively. The rigid length of the head of an imaging probe is one of the key parameters that dictates the body part that can be imaged. The optical path of the light beam at the fiber tip is folded on-axis using reflecting mirrors to reduce its distal rigid length. The large field of view of 350 $\mu\text{m} \times 350 \mu\text{m}$, the small working distance of 50 μm , and the small diameter make this device compatible in future clinical applications [43]. Figure 2.4a shows an in vivo confocal reflectance image of a tissue phantom containing cervical cells and collagen [39], and Figures 2.4b and 2.4c show confocal images of an adenoma [43] and the normal mucosal surface of the colon of a mouse in fluorescence, respectively [43].

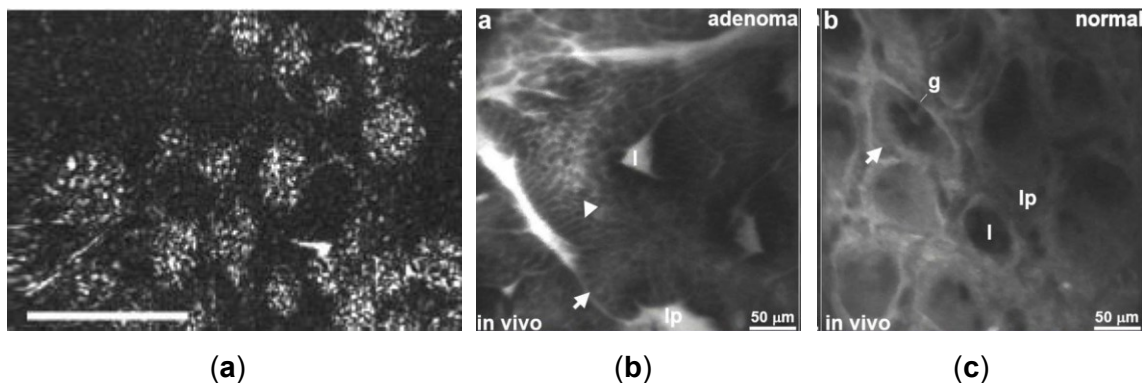


Figure 2.4. In vivo confocal images: (a) reflectance image of tissue phantom with cervical cells and collagen (taken with permission of [39] © The Optical Society); (b) fluorescence image of an adenoma mucosa (taken with the permission of [43] © 2011 IEEE); (c) fluorescence image of a normal mucosa (taken with the permission of [43] © 2011 IEEE).

2.3.3. Nonlinear Microscopy

Nonlinear microscopy is an alternative to conventional confocal microscopy and relies on the use of nonlinear optics, where the relation between the polarization and electric fields is non-linear. In confocal microscopy, a pinhole is used to exclude the out-

of-focus light coming from the sample, but the illumination light still achieves a large excitation volume. The absorption of the illuminating energy by the tissue surface can cause damage to the tissue surface, denoted as phototoxicity. In nonlinear microscopy, high-energy pulses are emitted by a laser source with a low average energy provided to the sample, which reduces the chances of phototoxicity. In this process, the laser light excites the molecule, and its relaxation to ground state produces the fluorescence emission of light [44].

Different technologies using nonlinear optics relying on multiphoton processes, higher harmonic generation, and Raman scattering are briefly discussed below. By scanning a light beam using different technologies, it is possible to generate 2-D or 3-D images, as discussed further in this chapter. Analogous to a microscopic device, it is possible to design a flexible endoscopic probe. The schematic design of such an endoscopic probe with the scanning mechanism at the distal end is shown in Figure 2.5 [17].

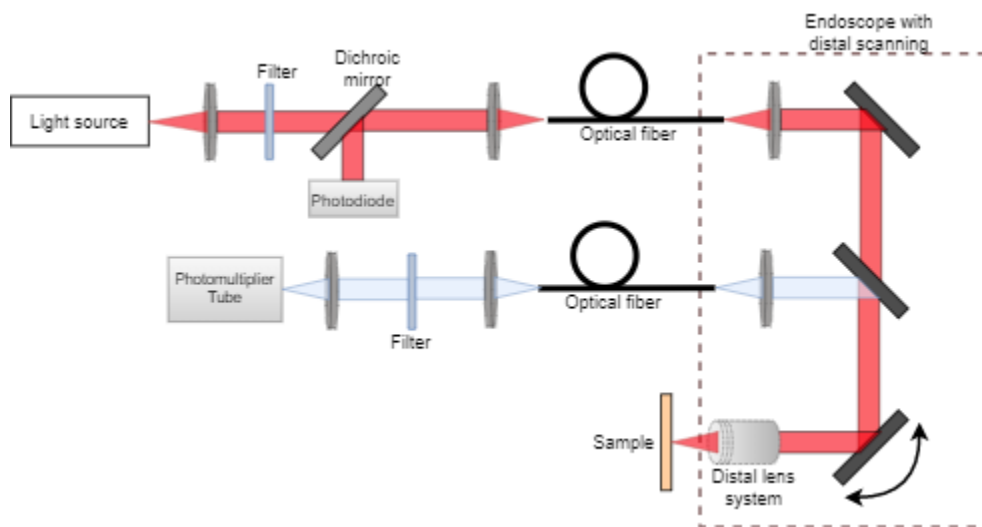


Figure 2.5. Schematic diagram of a nonlinear endoscope [17].

Multiphoton Microscopy

Multiphoton microscopy is based on the use of two or more photons to simultaneously excite a tissue surface. The contributing photons excite the molecules of the sample to its transitional state, which is unstable. The molecule comes to its stable ground state by releasing energy in the form of a fluorescent wave. In two-photon excitation, two photons are simultaneously absorbed in a single event; while in three-photon excitation, three photons are absorbed at the same time. Since the process

requires the simultaneous absorption of more than one photon, absorption is most likely to occur in the focus where the photons' flux is maximized [28].

To excite a molecule with multiple photons, very short (femtosecond to hundreds of femtoseconds) high-energy laser pulses are focused on the sample at a repetition rate of up to 80 MHz [28]. Usually, the excitation of a tissue surface requires ultraviolet radiation to produce fluorescence. Consequently, near-infrared (NIR) light can be used for two-photon microscopy, and infrared (IR) light can be used for three-photon absorption. The longer wavelength light penetrates deeper in the tissue, permitting the possibility of imaging thick sections. Moreover, infrared light causes less scattering compared to employing UV laser light in a single-photon excitation. This characteristic, with no scattering from the out-of-focus zone, gives high contrast in the image without using a pinhole [45].

The resolution of multiphoton microscopy is of the same order as confocal microscopy, but the possibility of a greater penetration depth makes it a popular method for medical imaging. Huang et al. presented a two-photon exciting fluorescence (TPEF) microscope for detection of ovarian cancer [46]. In this case, β -Galactosidase (β -gal) enzyme is used as a biomarker to detect the ovarian cancer cells (Figure 2.6 [46]). Similarly, two-photon microscopes are used for investigating the biological functions and disorders of tumor cells [47] and to image the neural tissues of the brain [48]. Some of the multiphoton-based microscopes presented in the literature are listed by Li et al. in [44].

Higher Harmonic Generation Microscopy

Another kind of nonlinear microscopy method is based on the use of nonlinear scattering from tissue molecules. The laser light interacts with the tissue and causes an electromagnetic field to interact with the tissue's electric cloud, generating oscillating electric dipoles. In non-centro symmetric molecules, the output light beam generated by moving from the transition state to the ground state is a distorted version of the exciting light beam, which creates the harmonics. Analogous to the multiphoton microscopy, the higher energy density required to excite the molecule is possible at the focal point. The harmonic generation is a coherent process, and the electric field radiated by the different molecules interfere with each other. Thus, it requires an ordered tissue structure where the aligned molecules can construct interference [28].

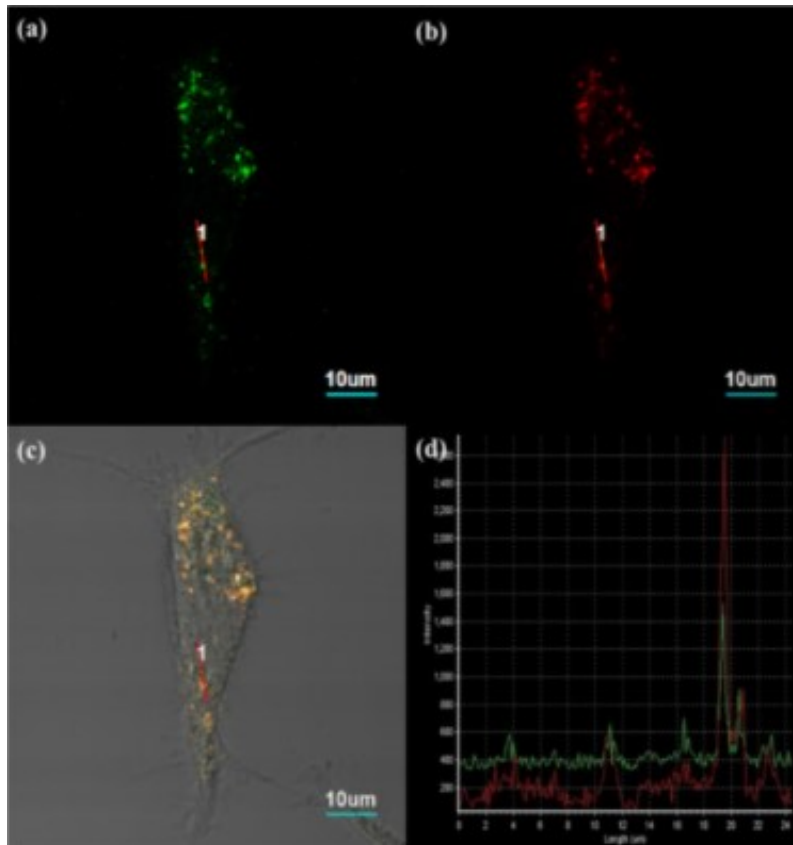


Figure 2.6. Two-photon exciting fluorescence (TPEF) image of ovarian cancer cells: (a) Fluorescence TPEF image using β -Galactosidase (β -gal) probe; (b) image using Lyso Tracker Red probe; (c) overlay of images a and b; (d) intensity profile (taken from [46] with permission).

Like the multiphoton process, harmonic generation comprises second, third, and higher harmonic generation depending on the number of photons exciting the molecules. The energy of the output light beam is given by the sum of the energies of the incoming light beams hitting the tissue surface. In second harmonic generation (SHG), the output photon has a wavelength that is double that of the two hitting photons. In other words, the incoming light from the laser induces a nonlinear polarization in the structure, which then generates a coherent wave with a frequency double that of incoming light. In third harmonic generation (THG), the output wave frequency is three times that of the exciting light beam [28]. The microscopic probe for the harmonic generation process is like that of a multiphoton microscopy. The only difference is the presence of a narrow band-pass filter, in front of the detector and centered at the SHG wavelength to block the residual excitation light [49].

This kind of microscopy is mainly used to image collagen fibers, myosin in muscle fibers, and microtubules in axons because of their ordered tissue structures [44]. Due to the similarity of SHG and TPEF, these techniques are often used together. Many SHG-based nonlinear microscopic devices are presented in the literature for imaging different tissue structures and diagnosis [50, 51]. Campagnola et al. imaged living neuroblastoma cells using both SHG and TPEF techniques. Both techniques provide images with very fine resolution as can be seen in Figure 2.7 [50].

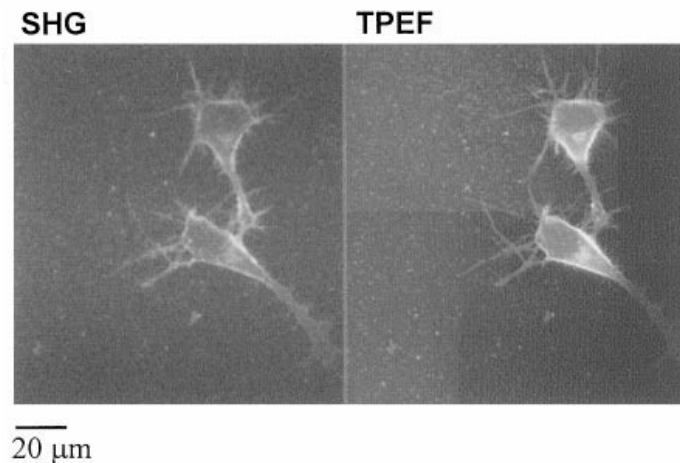


Figure 2.7. Second harmonic generation (SHG) and third harmonic generation (TPEF) images of differentiated neuroblastoma cells (taken with the permission of [50]).

Raman Scattering Microscopy

The Raman effect arises when the incident photon on a molecule interacts with its electric dipole, causing a perturbation and moving it to a virtual vibrational state. The virtual vibrational state is unstable and is followed by a de-excitation state generating a scattered photon. When the initial state of the molecule is at ground level and the final state is characterized by a slightly higher energy, it is referred to as Stokes scatter. The scattered photon in this case has less energy than the exciting photon (also called the red-shifted photon). When the initial state of the molecule is already in an excited virtual state, the incoming photon's interaction with the molecule generates a scattered photon with higher energy than that of the incoming beam. It is called the anti-Stokes or blue-shifted photon [28].

Coherent anti-Stokes Raman scattering (CARS) microscopy is a nonlinear microscopy where a molecule is first excited from the ground state to an intermediate

virtual state with a pump beam at an intermediate wavelength. Using a simultaneous illumination by a second Stokes beam, the molecule is excited into a higher vibrational level. The molecule is unstable at that state and returns to its ground level with higher energy given by the sum of energies of the two beams. In CARS microscopy, this scattered photon is used for imaging the tissue structure [44].

Stimulated Raman scattering (SRS) is another variation of Raman microscopy. It is similar to the Stokes-shifted Raman process, with the difference being that two lasers are coherently used to stimulate the scattering. The scattered signal is higher than that of the spontaneous Stokes shift [28]. A large number of CARS microscopy probes have been designed to image cancer cells [52, 53], as well as SRS microscopy systems to image the distribution of molecules, intracellular particles, proteins, and tumor cells [54, 55]. A list of CARS and SRS microscopy devices is included in [44]. Romeike et al. combined the CARS and TPEF technologies to obtain detailed histomorphological details of the tumor area from a squamous cell carcinoma metastasis, as shown in Figure 2.8 [52].

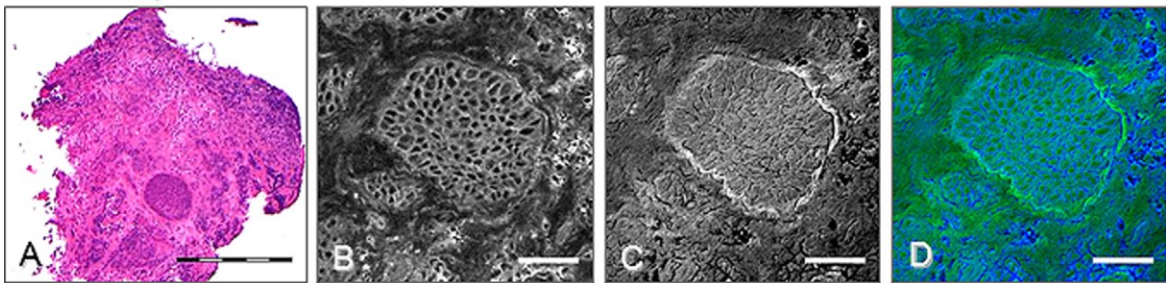


Figure 2.8. Images of brain metastasis of squamous cell carcinoma: (a) Hematoxylin and eosin-stained sample; (b) TPEF image; (c) Coherent anti-Stokes Raman scattering (CARS) image; (d) combining CARS and TPEF (used with the permission of [52]).

2.3.4. Photoacoustic Imaging

Photoacoustic (PA) imaging is a hybrid technology that uses light, which generates sound waves to image a tissue surface. In this technique, a tissue surface to be imaged absorbs the short pulsed high-intensity laser light, causing heating of the local surface, which then emits a high-frequency acoustic wave due to the pressure rise. The emitted ultrasonic signal is very poor as compared to signals from other technologies, and thus requires the use of an acoustic transducer without blocking the optical signal. The PA microscopy provides an absorption contrast with a resolution at a subcellular level and

has a capability to image anatomical, functional, and molecular structures at the same time [56, 57]. A schematic of a photoacoustic system is reported in Figure 2.9 [58].

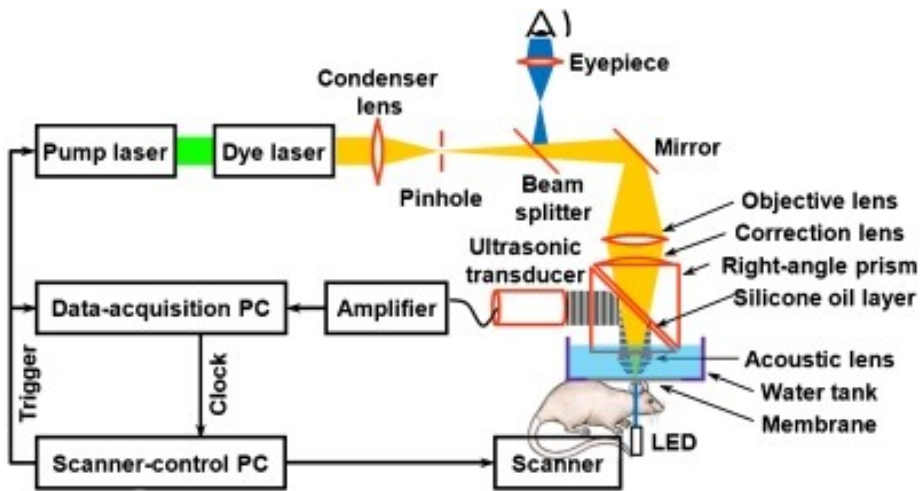


Figure 2.9. Schematic diagram of a photoacoustic microscope (taken with the permission of [58] CC-BY license).

PA microscopy can be classified into optical resolution PA microscopy (OR-PAM) and acoustic resolution PA microscopy (AR-PAM) based on the resolution technique used for imaging. In an OR-PAM device, the optical beam is focused inside the acoustic focus point. On the other hand, in an AR-PAM device, laser light is focused on a tissue surface through an optical system at a tight acoustic focus point. The lateral resolution of the PA microscopic device depends on the size of the focal spot. Since the wavelength of the optical wave is smaller than that of an acoustical wave, a small spot size can be obtained in the former case. Consequently, an OR-PAM system provides a finer resolution (ranges from submicrometer to submillimeter) compared to that of an AR-PAM ($\sim 45 \mu\text{m}$). Conversely, a greater illumination area in AR-PAM allows higher numbers of photons to penetrate deep into the tissue, giving a higher penetration depth [56, 57, 59].

Another imaging technique based on the use of optical and acoustical wave interaction is PA computed tomography (PACT) [58]. It is based on a similar working principle as PA microscopy, with the difference that a reconstruction-based image is formed instead of a focused-based one. Two-dimensional or three-dimensional tissue imaging is possible by scanning the optical and acoustical foci along a tissue surface using appropriate scanning methods. The penetration depth of imaging in this case ranges from a few micrometers to a few millimeters.

PA-based microscope catheters are largely used to image the bladder [60] and neurovascular systems [61], characterize microvascular parameters [58], and detect breast cancer [62]. Many devices based on PA microscopy are described in [30]. OR-PAM devices can achieve lateral and axial resolution as small as ~ 0.5 and $10 \mu\text{m}$, respectively [63]. Maslov et al. imaged a large FOV image of the mouse ear using this technique. They were able to image the ear capillaries with finer resolution even at a depth of $150 \mu\text{m}$ as can be seen in Figure 2.10 [63]. It is possible to get an even finer resolution image using a high-frequency signal, but the higher attenuation of the acoustical wave limits the penetration depth at this point. Thus, there is a trade-off between the resolution and imaging depth, with the penetration depth:resolution ratio being about 200 [64]. The penetration depth also depends on the PA modality used for imaging and on the nature of the transducer used for signal detection [65]. Using NIR light, the penetration depth can reach up to 7 cm [64].

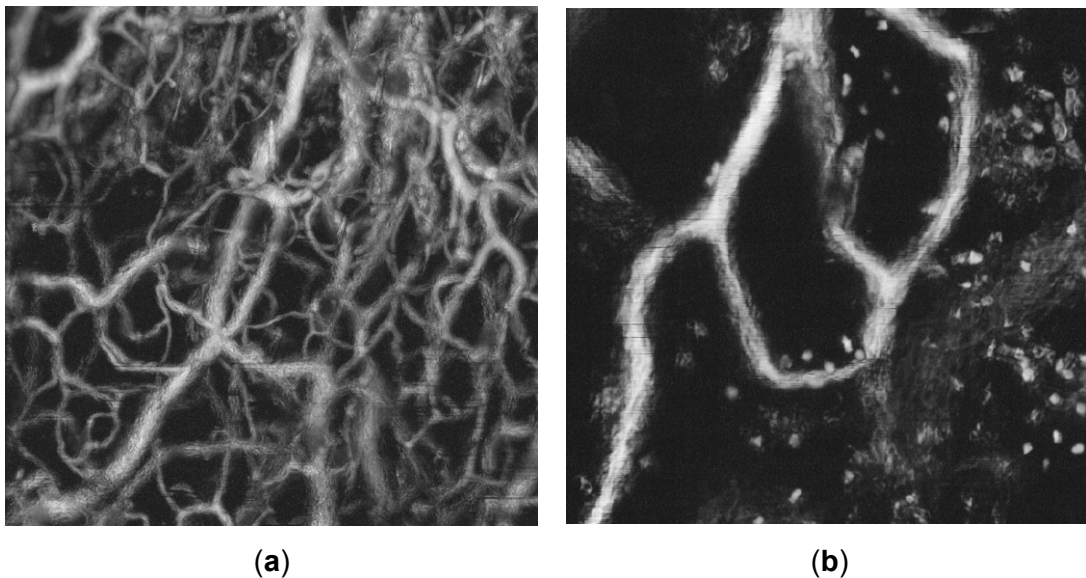


Figure 2.10. Photoacoustic image of a mouse ear: (a) maximum amplitude image of $1 \text{ mm} \times 1 \text{ mm}$; (b) image of a small fragment of image a (taken with the permission of [63]).

It is possible to use more than one technology to image the surface under consideration as every modality shows different aspects of the surface. The performance of different imaging techniques is compared in Table 2.1 [17].

Table 2.1. Performance of different imaging applications [17].

	OCT	CM	Nonlinear Microscopy			Photoacoustic Imaging		
			Multiphoton	Harmonic Generation	Raman Scattering	OR-PAM	AR-PAM	PACT
Lateral resolution	2–25 μm [30, 28]	1 μm [28, 37]	$\approx 0.2 \mu\text{m}$ [66]	4.9 μm [67]	300 nm [68]	$\sim 0.5\text{--}10 \mu\text{m}$ [63, 64]	45 μm [60, 64]	70–720 μm [60, 64]
Axial resolution	1–15 μm [30, 28]	7 μm [37]	$\approx 0.6 \mu\text{m}$ [66]	3.1 μm [67]	1.6 μm [68]	10 μm [63]	15 μm [60, 64]	25–640 μm [60, 64]
Penetration depth	1–3 mm [30, 15, 28]	>400 μm [44]	>200 μm [66]	100–300 μm [69]	$\sim 130 \mu\text{m}$ [70]	$\sim 1 \text{ mm}$ [64]	$\sim 3\text{--}5 \text{ mm}$ [64]	70 mm [64]
FOV	2–5 mm [30]	0.25–1 mm [30]	200–500 μm [30]	170 μm [69]	205 $\mu\text{m} \times 205 \mu\text{m}$ [55]	1–2 mm [30]	upto 36 mm \times 80 mm [71]	$\sim 40 \text{ mm}$ [71]
Orientation	Cross-section [28]	en face [28]	en face [28]			Cross-section [60]		
wavelength	Near IR	Visible or Near IR	Near IR			Near IR or IR		
Source	Low coherence [28]	Continuous wave or pulsed [28]	Pulsed [28]			Pulsed [60]		
Frame rate	>60 Hz [30]	>15 Hz [30]	>5 Hz [30]			$\sim 10 \text{ Hz}$ (depends on scanning area) [30]		
Advantages	High sensitivity, high imaging speed, deep tissue penetration, independent of source spectrum	High contrast due to rejection of out-of-focus scattered photons, isotropic and fine resolution, ability to control depth of field, ability to change magnification by changing the scanned area	Label free technology, High spatial resolution, less phototoxicity, and photobleaching due to exciting event taking place at focus point			High spatial resolution, High contrast, High imaging speed, and deep tissue penetration		
Disadvantages	Expensive detector, depth resolution dependent on NA, small dynamic range	Two or more nearby fluorescence signals can overlap	Expensive laser source, needs dispersion compensation			Expensive transducers required to detect the poor acoustic signal, Signal to noise ratio decreases with the tissue penetration		

2.4. Overview of optical components used in endoscopes

The key element used in cantilever-based endoscopic devices is an optical fiber acting as a waveguide through which light is transmitted using the principle of total internal reflection at the interface of two different dielectric media. The inner cylindrical portion is

called the core, while the outer region is named the cladding. Both materials are characterized by a slight change in refractive index; this is from which comes the name of step-index fibers. There are different classifications of optical fibers available based on normalized wave number V , defined as:

$$V = (2\pi a NA)/\lambda \quad (6)$$

where a is the core radius, λ is the wavelength of the light, and NA is the numerical aperture of the fiber [72]. NA is calculated from the refractive index of the core and cladding material of the fiber as [72]:

$$NA = \sqrt{n_{core}^2 - n_{clad}^2} \quad (7)$$

The V -parameter determines the number of spatial modes of the electromagnetic wave that can propagate within the fiber. An optical fiber is defined as a single mode fiber (SMF) if $V < 2.405$.

For a large V -parameter, the total number of allowed modes N through the fiber can be approximated as [72]:

$$N \approx V^2/2 \quad (8)$$

Such fibers are called multimode fibers (MMFs).

Other than simple step-index fibers, there are other fibers having different refractive index profiles varying with radius and increasingly find use in communication fields to avoid dispersion of optical waves during propagation. Among these fibers, the most used ones are fibers having a double step shaped profile or a nearly parabolic variation of index, designated double clad fibers (DCF) and gradient-index (GRIN) fibers, respectively. In GRIN fibers, light propagates due to the profile of the refractive index instead of the total internal reflection and follows a sinusoidal path [72].

Different kinds of optical imaging modalities used in endoscopic imaging devices are described below in detail in this section. These technologies are compared with the CCD/CMOS camera in Table 2.2 [73]. Following the definitions in [15], pixel density for the CFB, CCD and CMOS technologies is the number of imaging elements (pixels or fibers) per square millimeter that can be achieved in practice, while image resolution is the number of these elements in a 1mm diameter. Pixel density and image resolution for a

Scanning Fiber Endoscope (SFE) assumes use of a single mode fiber and is based on specific sampling considerations [15].

Table 2.2. Comparison between system performances of imaging technologies used in endoscopes [73].

Imaging modality	Pixel density (pixels/mm ²)	Image resolution (Pixels)	Pixel size	Advantages	Disadvantages
CFB	113k	30.0k/64.0k	2 μ m \emptyset	Small form factor, low cost	Cross coupling and honeycomb effect degrade image resolution. Aging effect results in non-working pixels due to fractured fibers within the bundle
CCD	238k	95.0k	0.5 μ m x 0.5 μ m	Small pixel size, low cost, no aging effect	Rectangular geometry limits the usable area, low dynamic range, poor light collection in low illumination area
CMOS	476k	190k	1.45 μ m x 1.45 μ m	Higher image resolution, low cost	Rectangular geometry limits the usable area, poor resolution in devices with diameter <1mm
SFE	345k	282k	Dependent on scanning pattern and sampling rate	Higher sampling rate and resolution in sub-millimeter sized devices	Performance dependent on actuation method and sampling rate. Spatial point spread dependent on objective lens at the tip and illumination properties.

2.4.1. Fiber bundles in endoscopes

Fiber bundles comprise thousands of step-index (or GRIN) fibers contained within a very small area ranging from a few micrometers to millimeters in range. A fiber bundle is used to carry the illumination light from the proximal end to the distal end, and vice versa, of a device. In a coherent fiber bundle, fibers at both ends are placed at the same relative position, so that the image is transmitted from one end to the other without any distortion. In miniaturized scanners, a coherent fiber bundle is predominantly used due to the perfect alignment of fibers, which facilitates the decoding of the signal [74]. As the light intensity information is transmitted from one end of the fiber bundle to the other, it is possible to place the scanning mechanism at the proximal end of the device, which is a major advantage of such devices.

Every core of the step-index fiber in the bundle acts as a pixel of the imaged data. Thus, the resolution of the image captured using a fiber bundle depends on the core size of the fiber and the core-to-core distance between the fibers [75]. For a coherent fiber

bundle with the core separation distance among adjacent fibers represented by Δ_{core} , the cross-sectional core density or pixel density is given by [15]:

$$Core\ density = \frac{2}{\sqrt{3}} \left(\frac{1}{\Delta_{core}} \right)^2 \quad (9)$$

From the core density and the active area covered by the fibers A_{cfb} , neglecting the space occupied by outer protective jacket and sheath, the image resolution can be obtained as [15]:

$$Image\ resolution = core\ density * A_{cfb} \quad (10)$$

This equation indicates a major drawback of using fiber bundles for miniaturized devices as the resolution will be poor due to the honeycomb effect generated by the space between the consecutive fiber cores representing the non-imaged area [15].

Another disadvantage of using fiber bundles is the crosstalk phenomenon. The cladding of the step-index fibers constituting the bundle is rendered to a thin layer around the core during the fabrication of a flexible fiber bundle. A very thin cladding surface enables the leakage of the light as it travels through the core reducing the contrast and the resolution of the image generated. It is possible to reduce the effect of crosstalk by increasing the thickness of the cladding section, enlarging contrast between the refractive indices of the core and cladding material, and/or by reducing the number of modes propagating through the fiber. However, these approaches make the device rigid, and the honeycomb effect will be more intensified, thus degrading the resolution [76, 77].

It is possible to refine the resolution of the obtained images by post-processing the data using certain algorithms. Using specific transformation models based on the point spread function of the cores of each fiber from the bundle, it is possible to smooth the light gradient reducing the pixilation effect produced by the honeycomb pattern [78-80]. The limitation of these transformation methods to be able to improve the resolution due to under-sampling is alleviated using pixel super-resolution techniques. In such methods, the source/image probe is shifted slightly several times for the acquisition of different images, and these images are further combined to enhance the resolution of the image [81].

In endoscopes that use fiber bundles, a pair of mirrors placed at the proximal end of the device permit the illumination of a single fiber from the bundle at a time. The fast-axis scanning (axis with high scanning frequency) is performed using the resonant

scanner (mirror surface vibrated at resonance using one of the actuators described later in this chapter), while a galvo scanner (optical mirror scanned using a galvanometer-based motor) is used for the slow-axis scanning. A schematic diagram of a confocal micro-endoscope developed using such a technique is shown in Figure 2.11 [73].

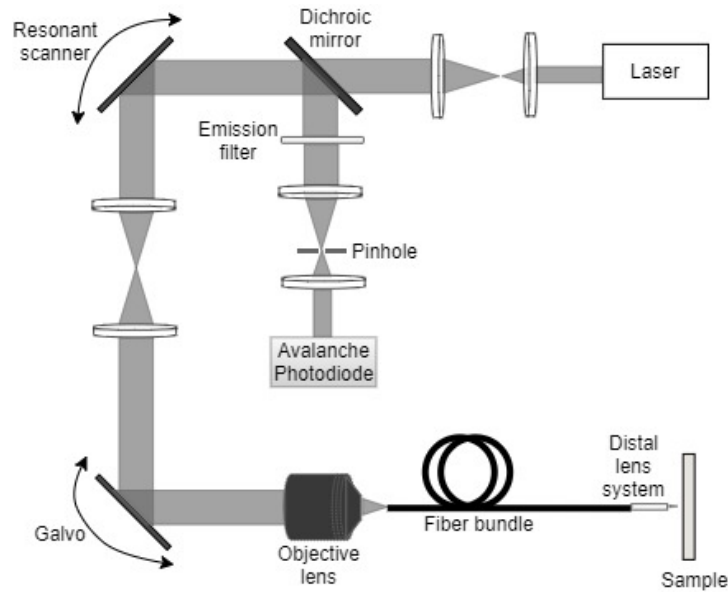


Figure 2.11. Block diagram of a confocal micro-endoscope [73].

Sung et al. developed an early fiber-optic based confocal reflectance microscope to image epithelial cells and tissues in real time showing the cell morphology and tissue architecture without the use of any fluorescent stains. The image guide contained 30,000 fibers and the device had an overall diameter of 7mm, and rigid length of 22mm to image the human tissue with a lateral and axial resolution (smallest resolvable feature) of $2\mu\text{m}$ and $10\mu\text{m}$, respectively [82]. Knittel et al. developed a similar confocal endoscope where tissue images with a lateral and axial resolution of $3.1\mu\text{m}$ and $16.6\mu\text{m}$, respectively, were obtained using a similar fiber bundle contained in a diameter of 1mm [83]. Lane et al. developed a similar endoscopic probe for imaging bronchial epithelium having a diameter and length of 1.27mm and 10mm, respectively. This probe had a lateral resolution of $1.4\mu\text{m}$ and an axial resolution of $16\text{-}26\mu\text{m}$ [84]. A commercially available endoscope based on this technique was developed by Mauna Kea Technologies [41, 85].

2.4.2. Single fiber endoscopy

A single mode fiber (SMF), characterized by having a step-shaped index of refraction change from the core of the fiber to the cladding surface permits the propagation of only one mode of light through the fiber. A single spatial mode enables a diffraction-limited spot to be projected on the sample plane resulting in a high-resolution image with the use of a SMF. Due to this property and high flexibility, such fibers find use in miniaturized optical scanners.

A SMF may find a use in a scanning fiber optic microscope, acting as a spatial filter [86] or as a pinhole detector [87]. The same fiber is used for laser light illumination and the collection of the reflected light [86]. An SMF serves as a pinhole in a confocal system and is used in spectrally encoded confocal microscopes [88, 89]. By moving the fiber in a plane perpendicular to its axis using mechanical systems or a galvanometer, it is possible to get a 2D image.

The SFE described earlier uses a SMF vibrated in resonance to scan the light beam across the target tissue surface, and a peripheric ring of fibers detect the time-multiplexed backscattered light. In this case, the sample resolution depends on the scanning motion and sampling rate which are not fixed a priori during fabrication. In an SFE, the smallest resolvable feature is determined by its point spread function. A wider tip displacement will provide a higher FOV and higher image resolution in terms of numbers of pixels in the scanned area as described in Table 2.2 [73].

In contrast to an SMF, a multimode fiber can transmit many spatial modes at the same time. These fibers have core sizes much bigger than the single mode fibers; usually in the range of $50\mu\text{m}$ - $2000\mu\text{m}$. Multimode fibers can be classified into step-index multimode fibers and graded-index (GRIN) multimode fibers based on the change of refractive index from the core to the cladding, which can be sharp or gradual, respectively [90].

A multimode fiber can be considered as an alternative to a fiber bundle and supports the miniaturization of optical devices. As each fiber in the fiber bundle represents a pixel for the acquired image, each pixel can be represented by a propagating mode in the fiber. Thus, it is possible to increase the pixel density of a device up to 1-2 orders of magnitude by replacing the fiber bundle with a multimode fiber [91]. A side-viewing

endoscopic probe for PA and ultrasound (US) imaging was developed using a MMF to deliver laser pulses to the target tissue, and a coaxial US transducer detects the PA and US echo signals. The light and acoustic signal is deflected 45° by a scanning mirror placed at the distal end of the probe which is rotated by magnets or a micromotor to provide a rotational scanning [92, 93].

The main limitation of using a multimode fiber in an imaging device is modal dispersion, which causes multipath artifacts. Several methods have been explored to provide an image without image artifacts. For example, Papadopoulos et al. used a digital phase conjugation technique to generate a sharp focus point. In this technique, the phase of the distorted wavefront was calculated, and an unmodulated beam of this phase was propagated in a backward direction to cancel out the distortions and to generate the original signal [94]. Some other groups proposed wave-front shaping methods to focus the light passing through a multimode fiber. Even though these methods successfully focused the light, they required continuous recalculation of the optimal wave due to the fiber motion [91, 94]. These methods do not work in the case of reflection mode detection of objects. In reflection mode imaging, the transmission matrix describing the response between the modes at the input and output planes can be used to overcome the distortion [91].

The modal dispersion effect is avoided using GRIN fibers where the refractive index change along the section of the fiber equalizes the travel time of the different modes. Thus, different spatial modes propagate at similar velocities. Sato et al. used a GRIN fiber for the fabrication of a single fiber endoscope used for reflectance imaging. However, this device had some problems related to nonuniform image quality, background distortion, etc. [95]. High-quality photoacoustic images using a GRIN fiber are reported in [96] where the light focusing property of the GRIN fibers permitted the propagation of spatially distributed Gaussian beams through the fiber that enhanced the focusing of the spot at the output. This, in turn, permitted high-resolution imaging [96].

Double clad fibers consisting of a central core and two outer cladding layers are another type of frequently used fiber in endoscopes. These fibers provide the unique feature of allowing the propagation of both single mode and multimode light through the fiber. The single mode light travels through the central core, while the multimode light is transmitted through the inner cladding material. Such a fiber is principally used in fluorescence imaging devices having single-mode illumination and multimode signal

collection. Thus, the advantages of single mode illumination and multimode collection are combined in these fibers [97-99].

It is possible to combine OCT and fluorescence imaging in a single endoscope using a DCF. In this case, OCT illumination and fluorescence excitation light is projected on the sample through the core of the DCF. The backscattered OCT signal is collected through the core, and the fluorescence emission from the sample is collected through the inner cladding of the fiber. The OCT source light and fluorescence excitation light are combined using a wavelength division multiplexer (WDM) before sending it through the core of DCF. The recollected light is separated using a DCF coupler where the recollected OCT signal from the core of the DCF is submitted to a SMF, while the fluorescence signal from inner cladding is forwarded to an MMF [100, 101].

Buenconsejo et al. developed a device that combined narrowband reflectance, OCT, and autofluorescence imaging in a single fiber endoscope using a DCF. This device worked analogously to other OCT devices except for the difference that the red/green/blue (RGB) light was emitted from the central core, while the collection of the reflected light was performed through the inner cladding. The separation of the various light signals from three modalities was done using an additional WDM [102].

In a single fiber-based micro-endoscope, the light beam can be steered at either the proximal or distal tip of the fiber. The possibility of scanning a light beam at the proximal end of an endoscopic device enables the separation of large sized beam scanning devices from the distal end. Thus, it is possible to come up with small sized endoscopic devices that can image the deep tissue systems within the body. Proximal scanning is usually performed using side-viewing imaging probes where a drive mechanism rotates the fiber to scan the light beam along the circumference of the target sample [35]. On the other hand, distal scanning is preferentially used in cantilevered-based single fiber endoscopes where the fiber tip is displaced mechanically using a variety of actuators. Usually the fibers are excited at resonance to obtain high tip displacements using piezo-electric [103-111], electrostatic [112, 113], electro-magnetic [114, 115], electro-thermal [116-118], micro-motor mirror [119-121], or shape memory alloy [122] actuators. The working principle of these actuators will be discussed in detail later in this thesis. Pan et al. developed a fiber-optic scanner where the beam was steered at the distal end using a pair of micro-mirrors [123]. The only commercially available single fiber endoscope was developed by Pentax

to image the upper and lower gastrointestinal (GI) tract. The optical scheme of this device is shown in Figure 2.12a [124]. In this case, the confocal images showing the subcellular and cellular structures of the upper and lower-GI tract are imaged after the administration of the contrast agent. An in-vivo confocal image of rectal mucosa in human colon collected using the Pentax endoscope is shown in Figure 2.12b where crypt lumens can be clearly identified [124].

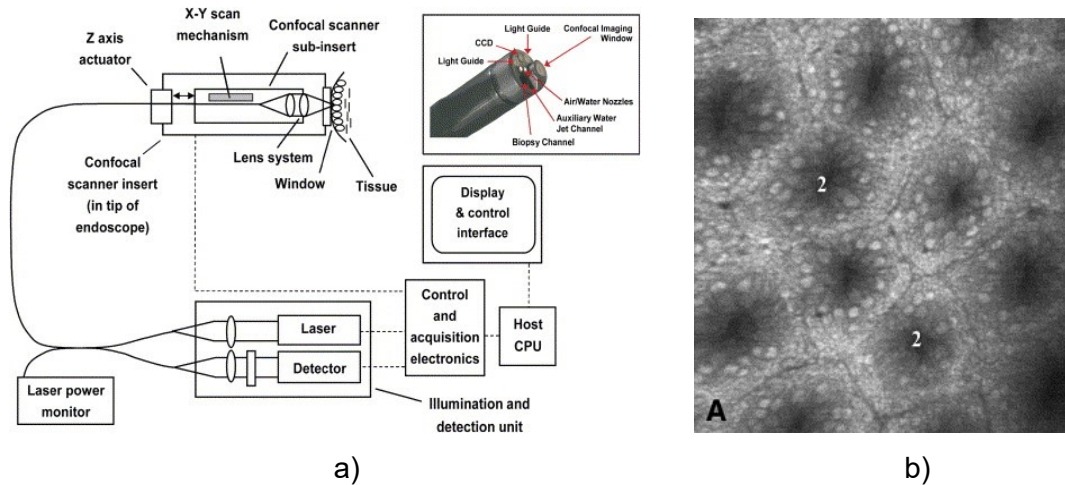


Figure 2.12. Fluorescence confocal imaging developed by Pentax: a) schematic design of the endomicroscope; b) an en-face image of rectal mucosa showing the crypt lumens (taken with the permission of [124]).

2.4.3. Graded index (GRIN) lens scanner

In lens scanners, light is deflected due to a non-planar interface between the air and the lens. The lateral motion of the lens perpendicular to the direction of the incident beam in these scanners cause variation in the refraction angle allowing light scanning.

Wu et al. developed a paired-angle rotating scanning OCT (PARS-OCT) probe to image the gill structure of a *Xenopus laevis* tadpole, where the beam steering the distal end of the probe was obtained by the rotary motion of the two angle polished GRIN lenses. A schematic diagram of this system is shown in Figure 2.13 [125]. The OCT images of the gill structure of a tadpole obtained using this device are shown in Figure 2.14. The photograph of an OCT probe relative to the tadpole is shown in Figure 2.14a, while the OCT images in Figures 2.14b and 2.14c clearly identify the gill pockets [125]. Sarunic et al. integrated a gear-based linear scan mechanism with the PARS-OCT device to control

the rotational speed of inner and outer GRIN lenses. They were able to identify vitreous, retina, and choroid surfaces in the OCT images of an ex vivo porcine retina [126].

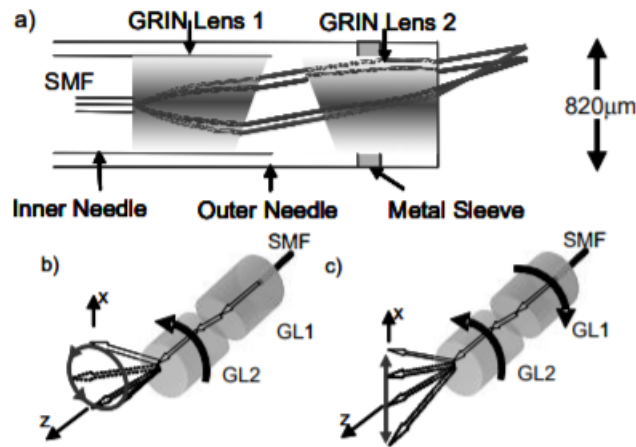


Figure 2.13. Schematic diagram of a PARS-OCT probe: a) distal tip; b) circular motion generation by rotating just one lens; c) linear scan by rotation of both lenses (taken with permission of [125]) © The Optical Society.

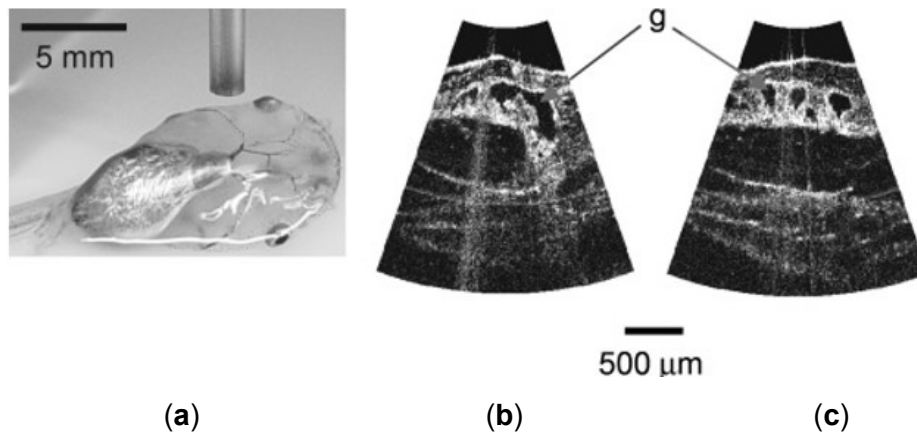


Figure 2.14. Endoscopic OCT image of the gill structure of a tadpole: (a) photograph of probe relative to the tadpole; (b, c) OCT images showing gill pockets indicated with g (taken with the permission of [125]). © The Optical Society.

2.5. Scanning Directions

Considering the basis of the scanning mode and the light illumination direction, optical scanner probes can be divided into two groups: side-view imaging and forward-view imaging. Side imaging probes generate circumferential images by scanning the target area from the side of the probe. By moving the probe linearly along the axis while

scanning, the beam will generate a cylindrical 2-D image area [127]. In the case of distal scanning, such devices can be as small as 1.65 mm [128]. On the other hand, forward imaging probes evaluate the target tissue surface image from the front. By scanning the light beam, 2-D images are generated. By moving the probe along the axis, it is possible to get 3-D images. Such devices are characterized by a high scan speed and can be used as a guide for medical devices used during surgery and other endoscopic procedures. However, these devices have a much larger size as their miniaturization is limited by the scanning elements. The smallest forward view imaging probe with the distal scanning method has a diameter of 2.4 mm [129]. It is possible to get more compact-sized probes using proximal scanning. The diameter of the probe can be reduced up to 250 μm [130]. Further details about these devices are described below in this chapter.

2.5.1. Side View Imaging

In side-view transverse scanning, the light beam coming from an optical fiber is deflected at a certain angle by the presence of a prism, mirror, or a reflecting surface. The deflected light passes through a transparent optical window on the side of the probe. The optical fiber with the optics components attached to its distal end is rotated to scan the light beam in a circumferential pattern. In the first side-viewing OCT probe [34], a graded-index (GRIN) lens was attached to a single mode fiber (SMF) with a core diameter of 9 μm . A right-angle microprism was attached to the GRIN lens, which deviated the light beam perpendicularly to the catheter axis. The distal end can be rotated using a drive motor [34, 131, 132] or a rotational stage [127] and scans the beam circumferentially. It is possible to deflect the light beam avoiding the prism by polishing the optical fiber at a certain angle and coating the surface with a reflecting material like aluminum or gold [132]. Even though such a design is easier to fabricate, it has a poor resolution. This limitation can be surpassed by splicing the GRIN lens and having no core fiber (NCF) at the tip of the SMF. NCF polished at a certain angle and coated with a reflecting metal layer gives a deflected beam with a Gaussian-shaped beam profile [133]. Yang et al. used a polished ball-lens at the distal tip of an SMF to deflect and focus the light beam through an optical window. The rotation of the fiber is performed using a linear scanner [134].

Some of the image artifacts related to the rotation of the fiber and the attached components are eliminated by rotating the microprism at the distal tip of the probe. In such a case, the prism is separated from the GRIN lens and actuated using a micromotor placed

at the distal end [128, 135], providing the images with a finer resolution. The schematic of a catheter-based side viewing endoscope is shown in Figure 2.15a [17]. More recent side viewing imaging probes rely on the use of parabolic or cone-shaped mirrors at the distal tip. Such mirrors permit the incoming light from the fiber to be reflected in all directions, giving an omnidirectional side view. Such devices, called catadioptric probes, provide a panoramic field of view, obviating the need for rotation of the probe components [136].

2.5.2. Forward View Imaging

Forward view imaging techniques provide images of the area in front of the probe. A laser beam coming in from the optical fiber is scanned laterally to cover the 2-D imaging area as in Figure 2.15b [17]. A large number of these probes use piezoelectric [34, 129, 137, 138], electromagnetic [114, 139, 115], electrothermal [24, 116, 117], shape memory alloy [122], or electroactive ionic polymer [140] actuators to excite an SMF acting as a cantilever beam in the desired scan pattern.

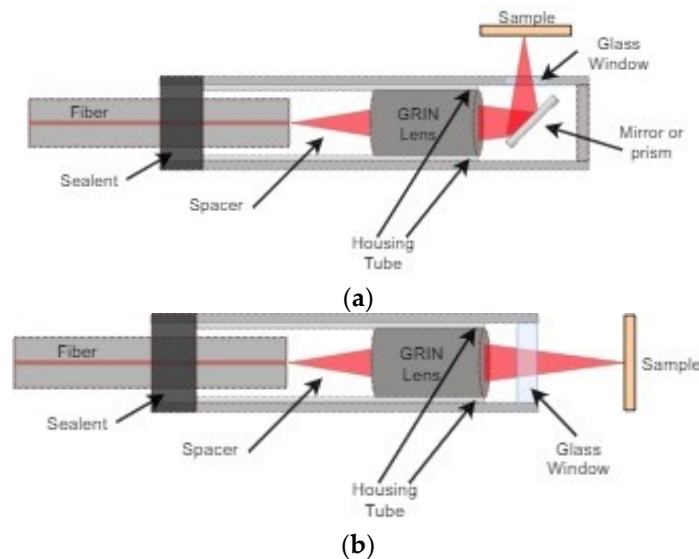


Figure 2.15. Schematic diagram: (a) side viewing probe; (b) forward viewing probe [17].

Another group of forward-viewing imaging probes use a scanning mirror at the distal end of the probe to deflect the light beam while scanning it. These mirrors can be actuated using an electrostatic actuator [113], electro-thermal bimorph actuator [123], piezoelectric actuation method [141], or servo motor [142].

Some of the forward viewing devices use a coherent fiber bundle (CFB) to shine the light on a target sample. Such devices permit the scanning mechanism to be employed at the proximal end [75]. Another type of forward-viewing device utilizes a pair of GRIN lenses rotating in opposite directions to deflect the beam in a fan-shaped scan [126, 125].

The features of the scanners based on these two kinds of imaging modalities are compared in Table 2.3 [17].

Table 2.3. Comparison between forward and side view scanners [17].

	Forward View	Side View	References
Probe diameter	>250 μm (proximal scanning) >1.65 mm (distal scanning)	>250 μm (proximal scanning) >2.4 mm (distal scanning)	[128, 130, 125]
Rigid length	>9 mm	>11 mm	[138, 143]
FOV	50–400 μm	~3–4 mm	[42, 127, 142]
Image orientation	en face	Peripheral surface	
Advantages	Can be used for image guidance to relocate and control the position of the medical devices, can directly image the extent of the malignancy and cancerous surface	Can image the finer cavities of the body, gives information about the wall/section of tissue layer involved in the malignancy, higher field of view, less expensive	
Disadvantages	Limited field of view, limitation of miniaturization limits the ability to image the narrower sections	Difficult to guide the probe in the body due to lack of guidance	

2.6. Cantilever Beam Mechanics and Scanning Principle

In small cantilevered optical scanners, the image is obtained by scanning the light beam at the distal end of the device, as stated earlier. In most of the earlier endoscopes using CFBs to transport the light to the tissue surface, the beam is scanned using micromirrors placed at the proximal end of the device. In these so-called proximal scanners, the large-dimensional scanning components can be separated from the distal end of the endoscopic device. Thus, it is possible to fabricate very compact-sized scanning devices. However, as the beam sweeps light across the CFB, a portion of the light enters through the cladding of the fibers as well, which results in poor contrast in the image. On the other hand, the scanning device is placed at the distal end of the endoscopic scanner to illuminate the light on the target sample in distal scanners. These single-fiber-based endoscopes require distal scanning to sweep the light across the target sample [77].

The cantilever-based endoscopic scanners belong to the category of forward-view imaging devices. In such devices, an optical fiber is fixed at a distance of a few millimeters from its distal end. The free end of the fiber acts as a cantilever beam, which is vibrated, using certain actuators described later in the thesis, to illuminate the target tissue area. The backscattered reflected light is used to reconstruct the image of the area using certain image processing algorithms. These cantilevered optical fibers can be vibrated in resonance, or at a frequency different from their resonant frequency.

Almost all cantilevered-fiber optic endoscopes can be considered as cylindrical-shaped beams. The first resonant frequency (also called natural frequency) of a cylindrical-shaped cantilevered beam (where one side is rigidly blocked for any movement and the other end is free to move) is given by:

$$f_n = \frac{1.875^2}{4\pi} \sqrt{\frac{E R}{\rho L^2}} \quad (11)$$

with E , ρ , R , and L being the Young's modulus, density, radius, and length of the cantilever beam, respectively [144]. From this equation, the driving frequency in resonant scanners depends on the inherent properties and dimensions of the optical fiber acting as the cantilever beam. In nearly all such scanners, the fiber is a standard 125 μm diameter fiber. Thus, the resonant and driving frequencies can be adjusted by changing the length of the cantilevered section.

The deflection of a cantilevered beam in the transverse direction can be obtained considering the Euler–Bernoulli beam. The Euler–Bernoulli beam theory describes the relationship between the beam deflection $w(x,t)$ and the applied load $f(x,t)$, assuming small deformations in the beam such that the planes perpendicular to the x - y axis do not bend after the deformation. The equation describing the deflection $w(x,t)$ of the beam in the y direction, in time (t) and along the length (x), can be derived considering the force and moment equilibrium of an infinitesimal element dx of the beam as in Figure 2.16 [73]. The equilibrium of forces in the y direction yields:

$$\left(V(x,t) + \frac{\partial V(x,t)}{\partial x} dx \right) - V(x,t) + f(x,t) dx = \rho A(x) dx \frac{\partial^2 w(x,t)}{\partial t^2} \quad (12)$$

where $V(x,t)$ is the shear force and $f(x,t)$ the total applied external force per unit length, while the term on the right-hand side describes the inertial force of the element, with $A(x)$ being the cross-section of the beam. Similarly, the equilibrium of moment acting on the element can be written as:

$$\left[M(x,t) + \frac{\partial M(x,t)}{\partial x} dx \right] - M(x,t) + \left[V(x,t) + \frac{\partial V(x,t)}{\partial x} dx \right] dx + [f(x,t) dx] \frac{dx}{2} = 0 \quad (13)$$

with $M(x,t)$ being the bending moment related to beam deflection $w(x,t)$ and flexural stiffness $EI(x)$ of the cantilever beam, where E is the Young's modulus, and $I(x)$ is the cross-sectional area moment of inertia [144]. $M(x,t)$ is given by:

$$M(x,t) = EI(x) \frac{\partial^2 w(x,t)}{\partial x^2} \quad (14)$$

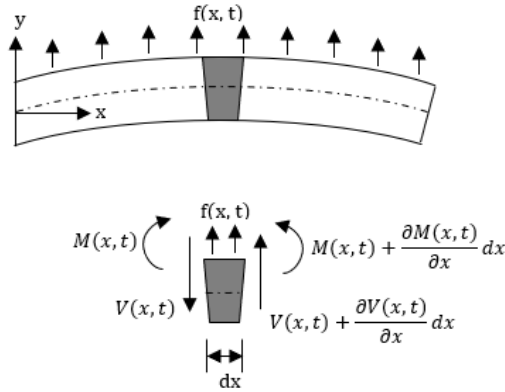


Figure 2.16. Euler–Bernoulli beam and a free body diagram of an element of the beam [73].

Simplifying and neglecting higher order terms in Equation (13), and combining it with (12) and (14), gives:

$$\rho A(x) \frac{\partial^2 w(x,t)}{\partial t^2} + \frac{\partial^2}{\partial x^2} \left[EI(x) \frac{\partial^2 w(x,t)}{\partial x^2} \right] = f(x,t) \quad (15)$$

The beam deformation under free vibration can be attained by considering $f(x,t) = 0$. For beams with a uniform cross-section, Equation (15) can be further simplified by having $A(x) = A$, and $I(x) = I$. Thus,

$$\frac{\partial^2 w(x,t)}{\partial t^2} + \frac{EI}{\rho A} \frac{\partial^4 w(x,t)}{\partial x^4} = 0 \quad (16)$$

The beam deflection can be solved using this equation with four boundary conditions and two initial conditions. The initial conditions are the specified initial deflection $w_0(x)$ and velocity $\dot{w}_0(x)$ profiles causing the motion:

$$w(x, 0) = w_0(x) \quad \text{and} \quad w_t(x, 0) = \dot{w}_0(x) \quad (17)$$

For a cantilever beam, the boundary conditions are the zero bending moment and the shear force at the free end, and no deflection and slope at the fixed end. In other words,

$$w(0, t) = 0 \quad (18)$$

$$\frac{\partial w(0, t)}{\partial x} = 0 \quad (19)$$

$$EI \frac{\partial^2 w(0, t)}{\partial x^2} = 0 \quad (20)$$

$$\frac{\partial}{\partial x} \left[EI \frac{\partial^2 w(0, t)}{\partial x^2} \right] = 0 \quad (21)$$

Equation (16) can be solved by separating variables as in $w(x, t) = X(x)T(t)$. This approach permits the separation of Equation (16) into two sub-equations, which can be solved separately to yield temporal and spatial results. The total solution can be obtained by combining the two results. As stated above, the temporal solution depends upon the initial conditions, which vary from case to case. Given the boundary conditions, the spatial part yields:

$$X(x) = \cosh(\beta_n x) + \cos(\beta_n x) + \sigma_n [\sinh(\beta_n x) + \sin(\beta_n x)] \quad (22)$$

where β_n and σ_n are the coefficients depending on the mode considered. For the first resonant mode, $\beta_n l$ is 1.875, while σ_n is 0.7341 [144]. The first mode shape of a cantilevered beam actuated at resonance is shown in Figure 2.17 along with the beam in an initial state [73].

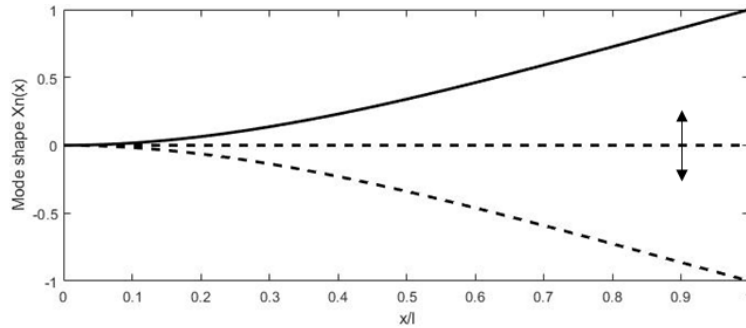


Figure 2.17. Deformation of a cantilever beam at resonance [73].

Optical scanners for medical imaging predominantly are scanning fiber endoscopes (SFEs). In these devices, an optical fiber is vibrated to shine light on a target tissue, and the reflected light is captured using one of the modalities described earlier. The main reason for the large demand of SFEs comes from the fact that the resolution in these devices is not limited by pixel elements in the image sensor but by the peak-to-peak displacement of the fiber tip and core diameter of the fiber. The optical fibers can be vibrated in resonant, non-resonant mode, or using an intermediate frequency to scan the light beam across the target tissue sample. The resonance actuation is used in cases where high-frequency operation and a high amplitude of the scanning fiber are required. The non-resonant scanners are preferred in cases when very different scan frequencies in two directions is a prerequisite. It is possible to avoid the drawbacks of both methods and keep the higher flexibility using a semi-resonant scanning mode.

2.6.1. Resonant Scanner

The distal tip of the fiber can achieve higher displacement when it is vibrated at resonance. In other words, the amplitude of the scanning beam and the obtainable resolution can be maximized by exciting the distal free end of the optical fiber at its natural (first resonant) frequency. Many scanning fiber endoscopes are based on the first mode of resonance to scan the light. The proximal end of the fiber is usually excited at resonant frequency using piezoelectric [30, 31, 32, 35], electromagnetic [34, 36, 37], electrothermal [38-40], shape memory alloy [44], or electroactive ionic polymer [45] actuators. The distal end follows the mode shape shown in Figure 2.18 [17]. Various resonant scanners in the literature are compared in [145].

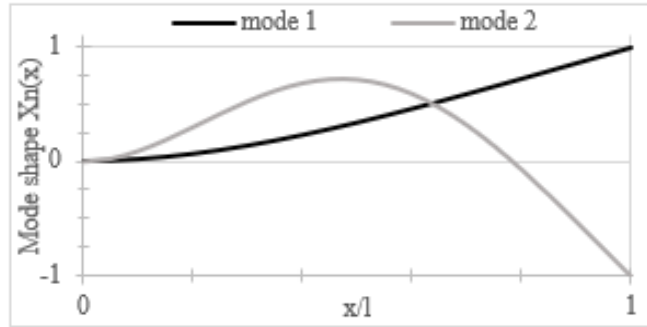


Figure 2.18. Mode shapes of a cantilever beam describing the beam shape in vibration at resonance [17].

In most cases, the cantilevered fiber scanners are characterized by having a symmetrical cylindrical section. In cases when the beam structure is excited with large displacements near its resonance frequency, the cross-coupling of the motion between the planes perpendicular to the beam axis leads to a whirling phenomenon. This nonlinear tip response of the excited fiber is highly unstable. In very small frequency ranges, a stable whirling motion can be produced, which allows the fiber to trace an elliptical shape pattern. The equation of motion describing the whirling phenomenon was studied by Haight and King in [146], and further developed by Hyer in the case of a cantilever beam [147].

It is possible to avoid the undesired whirling motion by changing the shape of the optical fiber beam or finding the two eigendirections on the beam where the excitation can cancel the whirling effect [148]. It is even seen that the whirling effect can be positively exploited for 2-D scanning using a single actuator. It is experimentally shown in [149] that exciting the cantilevered fiber at a second mode of resonance gives a stable circular-shaped pattern by tip displacement. Thus, it can be beneficially used for scanning the target area by sweeping the circular area by continuously increasing the driving voltage of the exciting actuator [149].

2.6.2. Non-Resonant Scanner

Resonant fiber scanners provide a large scan area for a given input power. However, it is difficult to get a resonant fiber scanner for an application requiring low-frequency scanning [145]. From Equation (11), it is clear that very long and slender beams are required to get a small resonant frequency. Moreover, the resonant scanners do not provide the flexibility in offsetting the center of the image field from the optical axis. It is

possible to offset the center using additional deflectors, which, on the other hand, make the scanner more complex and bulkier.

Such problems can be partially solved by exciting the scanning fiber at a frequency away from its natural frequency. In this case, the tip displacement of the fiber, given the excitation power, will be much smaller. There are some non-resonant scanners available using a bimorph piezo bender actuator [150], and electro-magnetic actuators [151]. As stated earlier, these scanners use a high amount of power to produce the desired tip displacement, which can cause safety issues in such devices.

In such scanners, the deflection of the distal tip of the fiber (δ_{tip}) is related to the displacement of the actuator exciting the vibration (δ_s) by:

$$\delta_{tip} = \delta_s \left[1 + \frac{3(1-a)}{2a} \right] + \frac{qgL^4}{8EI} \quad (23)$$

with L, a, q, E, I, g being the length of the cantilevered portion of the fiber, length ratio of the fixed end, mass per unit length of the fiber, Young's modulus, the moment of the inertia of the fiber, and acceleration of the gravity, respectively [152].

Park et al. developed a MEMS scanner for the design of an endoscopic OCT probe. In this case, a 40-mm-long fiber is actuated using a 3 V drive voltage [153]. Naono et al. designed a non-resonant thin-film piezoelectric actuated scanner for an OCT application [154].

Non-resonant scanners can be miniaturized by decreasing the length of the cantilevered portion and increasing the tip deflection using the leverage method. Sawinski and Denk used a double-lever method to amplify the tip displacement of the optical fiber. In this case, a piezo-bender actuator was connected to the fiber at the cross point of the leverage. Such an optical scanner provides a tip deflection comparable to that obtained in resonant scanners, with the possibility of shifting the center of the image [155].

2.6.3. Semi-Resonant Scanner

As seen above, the resonance operation mode limits the shifting of the center of the image and is operable in high-frequency scanning fields. The resonant scanner is also sensitive to the working conditions. A slight offset from the peak frequency can generate

instability in the motion of the fiber. Conversely, a non-resonant scanner operates at a low-frequency range but requires high power consumption or longer fiber tips to cover a certain scanning area.

These problems can be circumvented using a semi-resonant scanning mode of operation. Such a scanner is proposed by Moon et al., where the cantilevered optical fiber is excited at an intermediate frequency, which is far from the resonance peak but provides some amplitude gain. An OCT endoscope designed based on this method prevents the sensitivity and nonlinear whirling problems related to resonant scanners [156].

A representative table highlighting the performance of three kinds of scanners described above is reported in Table 2.4 where the number of check marks indicates qualitatively the value of the parameter [17].

Table 2.4. Summary table for different scanners [17].

	Resonant Scanner	Semi-Resonant Scanner	Non-Resonant Scanner
Scan area	✓✓✓	✓✓	✓
Power consumption	✓	✓✓	✓✓✓
Operating frequency	High	Intermediate	Low
Advantages	Large displacement amplitude, low power consumption	Large scanning amplitude than non-resonant scanners, variable imaging field, stable working conditions	Operable at very low frequencies, stable to small variations of operating conditions, image field is variable
Disadvantages	Offsetting the image field requires complex systems, Instability can lead to whirling motion	Performance highly depending on the working frequency	Small scanning amplitude, high power consumption

2.7. Scanning patterns

In MEMS scanning mirrors or fiber optic scanners, the laser beam is scanned along two perpendicular axes to reconstruct the image of the target sample. The scan along the two directions can be implemented either using separate actuation methods or by a single actuation device. The resolution of the image obtained depends upon the scanning method used to scan the laser beam across the sample [157]. The different scanning methods used by the optical scanners are reported below in the detail.

2.7.1. Raster scanning

Raster scanning (also called serpentine scanning) is a commonly used scanning pattern. In this case, the scanning image is subdivided into scan lines in one direction. The beam sweeps the sample in one direction along a line, comes back to other side and again starts scanning along a line. Thus, it follows a rectangular scan pattern. The axis of the line scan is called the fast axis (scanned rapidly), while the other axis is called the slow axis (scanned slowly). Usually, the fast axis is driven by oscillating the light beam at resonance, while the slow-axis scan is performed using a non-resonant scan [157].

Typically, the raster scan pattern is obtained using gimbal mounted micromirrors or optical fiber scanners. The number of pixels along the fast axis is:

$$N_h = \frac{\theta_{opt} D}{a\lambda} \quad (24)$$

where θ_{opt} is the total optical scan angle, D is the diameter of the scanning mirror, a is the shape factor depending on the spot size, and λ is the system wavelength. The number of the pixels along the slow axis is:

$$N_v = \frac{f_h K_{ub} K_{rt}}{F_r} \quad (25)$$

with f_h , K_{rt} , F_r being the scan frequency, fraction of time for retrace the scanner, and the scanner speed, respectively. K_{ub} is a constant ($K_{ub} = 1$ for unidirectional scanning, $K_{ub} = 2$ for bidirectional scanning) [145].

The scanning beam passes on the surface of the target object at different times. Thus, each pixel on the reconstructed image corresponds to a different time point. This kind of scanning in time leads to in-frame and inter-frame motion artifacts. The former among these takes place in the case where there is a displacement or movement of the sample within the acquisition time. The inter-frame artifacts occur due to motion occurring between the successive frames or image sequences. The in-frame motion artifact can be reduced by changing the motion path or using image processing algorithms. The inter-frame distortions can be reduced by increasing the scanning speed by implementing a bidirectional scan [158]. Duma et al. tested triangular, sinusoidal, and sawtooth scanning profiles and demonstrated that the triangular profile provides artifact-free images. The other two profiles display image distortion at the margins [159].

The raster scanners require high operating voltages to get slow axis scans and have difficulties incorporating them in small spaces, which make them less usable in clinical devices [160].

2.7.2. Spiral scanning

A spiral scan pattern is generated using a 2D actuation method by employing the same actuation frequency along the two axes. In other words, the spiral pattern is obtained by driving the light beam at the same frequency with increasing amplitude along two directions with a phase shift of 90° [160].

The phase shift between the two signals, and the amplitude variation in the driving signal affect the circularity of the obtained spiral. Such scanning patterns are obtained with resonant fiber-optic scanner. These scanners are activated with increasing actuation amplitude until they reach the maximum radius (r_{\max}) followed by a breaking time to reset the fiber at its rest position, which then repeats the scan and moves to the next frame [15].

The motion of the fiber tip in time during the spiral scan in polar coordinates can be described by:

$$r(t) = r_0 + v_r t \quad (26)$$

$$\phi(t) = \phi_0 + \beta t \quad (27)$$

where v_r , and β are the constant radial and angular velocities, respectively. The angular motion is fast with respect to the radial motion. The scanning pattern is smooth and is used in fiber-optic endoscopic scanners [15, 109]. A higher frame rate can be achieved using a larger amplitude compared to a raster scanner. However, the illumination beam density is variable within the scanned image and is higher at the center compared to the outer surface [160].

2.7.3. Lissajous scanning

A Lissajous scanning pattern is another 2D scanning pattern obtained with variable frequencies (ω_x , ω_y), and the phases (ϕ_x , ϕ_y) along the two axes. The scanning pattern is governed by independent oscillatory equations along the two axes [161]:

$$x = A_x \sin(\omega_x t + \phi_x) \quad (28)$$

$$y = A_y \sin(\omega_y t + \phi_y) \quad (29)$$

One of the main parameters characterizing the scanning pattern is its fill factor defined as the ratio of scanned area vs total pixel area in the image. Fill factor depends on the ratio of the frequencies along the two axes. For a higher fill factor, a high ratio between the two scanning frequencies is desired [145]. The scanning pattern is quasi-random and non-repetitive in time. The scanning beam is uniformly spread on the scanned surface, is highly smooth, and requires low power consumption [161]. Such patterns are not very useful for high quality displays, however, are largely used in resonant fiber scanners [117, 105].

2.7.4. Circular scanning

A circular section optical fiber is characterized by having the same fundamental frequency along two directions. It is possible to get a circular shape pattern from the fiber tip by exciting it in the two directions with a 90° phase shift [162]. As stated earlier, it is also possible to get a circular shaped pattern from the fiber tip by exciting it in a single direction at a second mode of resonance due to nonlinear coupling with longitudinal inertia [149].

By changing the amplitude of the driving signal, it is possible to sweep the area inside the circular shape like the spiral shape pattern. Wu et al. developed an imaging fiber optic catheter, where the 2D scan is obtained using a concentric circle scan pattern with the help of a triangle amplitude modulated sinusoidal actuation wave [149]. Like the spiral shaped pattern, the light density is higher in the center and decreases moving toward the outer circle.



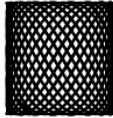


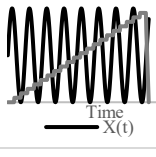
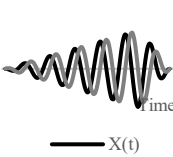
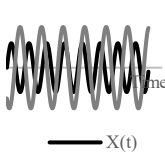
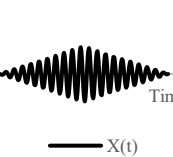
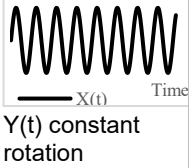
2.7.5. Propeller scanning

Propeller scanning consists of generating a line scan by actuating the optical fiber in one direction or steering the beam using a mirror device. The line pattern is then rotated to generate a circular shaped 2D pattern [163]. The rotation motion can be transmitted from the proximal end to the distal end using torque cables, while the optical connection between the steady and rotating parts can be applied using fiber optic rotary joints.

The line scan direction represents the fast axis, while the rotation represents the slow axis. The light intensity is not uniform and is higher in the center compared to the edges. The rotation speed affects the resolution of the obtained image. Kaur et al. used a propeller scanning pattern to get a 2D scan pattern using a single direction actuation of a cantilevered fiber. The fast axis scan is obtained by using an electrothermal actuator, while the slow axis scan is performed by rotating the target sample [24].

Scanning patterns and the actuation power provided to the two actuators to get the corresponding 2D pattern is shown in Table 2.5 along with its advantages and disadvantages [17].

Table 2.5. Comparison table for different scanning patterns [17].

	Raster	Spiral	Lissajous	Circular	Propeller
Scanning pattern					
Actuation pattern					
Advantages	Uniform light intensity	Easy to get, area is swept by changing the driving voltage	Uniform light intensity, most used	Possible to get circular pattern with 1D actuation, area is swept by changing the driving voltage	Easy to generate
Disadvantages	Points are scanned at different times can lead to motion artifacts	Light intensity is higher in center	Fill factor highly depends on the frequency ratio, quasi-random pattern	Light intensity is higher in center	Non uniform light intensity, the rotation of miniaturized structure requires complex and expensive devices

2.8. Concluding Remarks

The continuous growth of microfabrication techniques and optical components make the latest imaging devices much smaller, allowing visualization of narrower sections of the body and imaging of target areas with a very fine resolution. The smaller an imaging

device is, the further it can be advanced into the body, enabling an improved detection of lesion/tumor surfaces.

In medical applications, OCT is a frequently used imaging modality to image tissue structures due to the smaller size of the probe device; among this type, FD-OCT is widely used. Among the other imaging modalities, nonlinear microscopy can generate images with a finer resolution, while photoacoustic imaging can image deeper into the tissue. Many imaging probes have been developed using electrostatic actuation due to the ease of fabrication and fast scanning speed.

The advancement of MEMSs and small-sized optical components enable the fabrication of imaging devices with promising performance as compared to traditional medical devices. Such devices enable the detection of lesions/tumors at an earlier stage and act as a guide during surgical procedures, increasing diagnostic capabilities.

It has been analyzed that SFEs enable the development of high-resolution sub-millimeter sized endoscopes for small airway scanning where the pixel size is dependent on the vibration and scanning motion of the fiber itself. It has also been discussed that the distal end of a SFE achieves the highest tip displacement for a given power when excited at resonance. These considerations are considered for the development of the proposed imaging scanner.

Chapter 3.

Actuators in Cantilever-Based Endoscopic Devices

3.1. Disclosure

The material presented in this chapter is extracted, reproduced, and modified with permission from the papers listed below which I have co-authored. Eventual modifications may have been introduced for a variety of reasons including clarify the subject; to provide additional information; and ensure the formatting is consistent with the rest of the thesis.

- Kaur M., Lane P. M., Menon C. Endoscopic Optical Imaging Technologies and Devices for Medical Purposes: State of the Art. *Applied Sciences*, 2020; 10(19), pp. 6865:1-34.
- Kaur M., Lane P. M., Menon C. Scanning and Actuation Techniques for Cantilever-Based Fiber Optic Endoscopic Scanners – A Review. *Sensors*, 2021; 21(1), pp. 251:1-38.

3.2. Introduction

This Chapter describes the various actuation methods used to excite the miniaturized optical cantilever beams along with their working principles and applications in optical imaging devices.

The miniature size of MEMS devices along with their light weight and stable performance characteristics make them attractive for micro and nano applications among which are endoscopic optical devices. Based on the working principle, MEMS actuators can be subdivided into piezoelectric, electrostatic, electrothermal, electromagnetic, and shape memory alloy actuators. The piezoelectric actuators are widely used in endoscopic catheter design due to their compact size, low power consumption, and large output force. On the other hand, the actuation displacement is limited in such devices. Electrostatic actuators are the second most used actuation method in medical scanning devices due to their fast response, and ease of fabrication. However, it is hard to produce such devices at very small dimensions, which limits its use in systems requiring a distal actuation. Electrothermal actuators generate high actuation displacement and force, but the elevated

working temperature and low working frequency limit their use in some cases. Electromagnetic and shape memory alloy actuators find limited applications in cantilevered fiber-optic endoscopic scanners [164]. All these actuation methods are described in this section at detail and compared in Table 3.1 where the number of ticks qualitatively indicates the intensity of a certain pattern [17].

Table 3.1. Comparison between different actuation methods used in cantilevered endoscopes [17].

	Electrostatic	Electro-thermal	Piezoelectric	Electromagnetic	Shape memory alloy
Force	✓	✓	✓✓✓	✓✓	✓✓✓
Displacement amplitude	✓✓	✓✓✓	✓	✓✓✓	✓✓
Compactness	✓✓✓	✓✓✓	✓✓	✓	✓✓
Power consumption	✓✓	✓	✓	✓✓✓	✓✓✓
Working principle	Electrostatic force	Thermal expansion	Piezoelectric effect	Magnetization effect	Material deformation
Motion range	1D/2D	1D/2D	2D	1D	1D
Scanning pattern	Spiral	Lissajous	Spiral	Linear	Linear
Advantages	Fast response, low voltage required, easy fabrication, and no hysteresis	Large displacement, low operating voltage, small dimensions	Large force generated, wide operating frequency range, low power consumption	Large displacement obtained, quick and linear response, easy to control	Flexibility, large frequency response
Disadvantages	Large device dimensions, pull-in problem, complicated circuit	High working temperature, not operable at very high frequencies	Limited displacement	Large device dimensions, difficult to manufacture	Slow response speed

3.3. Piezoelectric actuators

The working principle of piezoelectric actuators is based on the so-called piezoelectric effect. Piezoelectric materials can change the material polarization in the presence of a mechanical stress, and conversely generate strain or force in the presence of an external electric field. Among the various crystalline, ceramic, and polymeric materials, aluminum nitride (AlN) and lead zirconate titanate (PZT) are most frequently

used in MEMS devices [165]. Piezoelectric actuators are characterized by providing fast response, low driving voltage, and low power consumption [166].

The relationship between the electric field applied to the material and the mechanical deformation exhibited by the material is non-linear due to the presence of hysteresis and drift. For a small variation in electric field, the material behavior is almost linear, and can be described by:

$$\varepsilon = Ed + c^{-1}\sigma \quad (1)$$

where ε is the strain tensor, E is electric field vector, σ is the stress tensor, d is the piezoelectric tensor (vector of strain coefficients), and c is the elastic tensor. In the case of no external force, the second component on the right-hand side of equation (1) becomes zero. The piezoelectric strain depends upon the direction of the mechanical and electrical fields [167].

Piezoelectric materials often show a non-linear hysteresis behavior, which causes the relationship curve between the displacement exhibited by the material and the applied electric field to be different in ascending and descending directions. Various models have been proposed to describe this hysteresis phenomena. Bahadur and Mills proposed a hysteresis model to characterize the symmetric and asymmetric rate-dependent hysteresis. The output charge (q) is related to the endpoint displacement (x) and the applied voltage (V_p) by:

$$q = C_0V_p + T_{em}x \quad (2)$$

with C_0 and T_{em} being the capacitance of the piezoelectric element and the electromechanical coupling factor, respectively [168].

Normally, piezoelectric devices are restricted for 1D operation with force/displacement occurring along the axis defined by the electric field. In these so-called longitudinally translating piezo chips, the electric field is applied parallel to the polarization direction of the material which causes the displacement in the same direction of the field normal to the surface of the electrodes. In shear piezo elements, the polarization is obtained in the direction perpendicular to the field direction. Thus, there is an orthogonal relationship between the direction of the displacement and that of the electric field [169].

Piezoelectric actuators are available in single disc/plate and tubular configurations. These configurations are described below in detail.

3.3.1. Disc piezoelectric actuator

Flat disc piezoelectric actuators can be constructed using a single piezo element (unimorph actuators) or using two different piezo elements (bimorph actuators). In either case, piezo elements are connected to a base material. There is an expansion or contraction of the piezo material in the presence of an electric current which provides the bending motion of the actuator. The schematic diagram showing the working principle of a piezo bending actuator is shown in Figure 3.1 [73]. When a positive voltage is applied to the piezoelectric ceramic layer, it elongates in the x direction, while the base material does not change its length resulting in convex bending of actuator towards the conductive layer as in Figure 3.1b [73]. Similarly, bending in the opposite direction occurs by applying a negative voltage to the piezoelectric sheet. Li et al. fabricated a scanning fiber probe for an OCT endoscope, where an optical fiber was placed in middle of the two piezoelectric plates with a common copper substrate element. The bending of the fiber tip in the vertical direction was obtained by exciting the two piezo elements with the same voltage, i.e., the structure will bend along the positive or negative directions by elongating or contracting both elements. On the other side, the motion of the tip along the horizontal axis was obtained by applying an opposite polarity voltage to the two elements. A two-dimensional Lissajous scanning pattern was obtained by the fiber tip by controlling the voltages on the two layers [107].

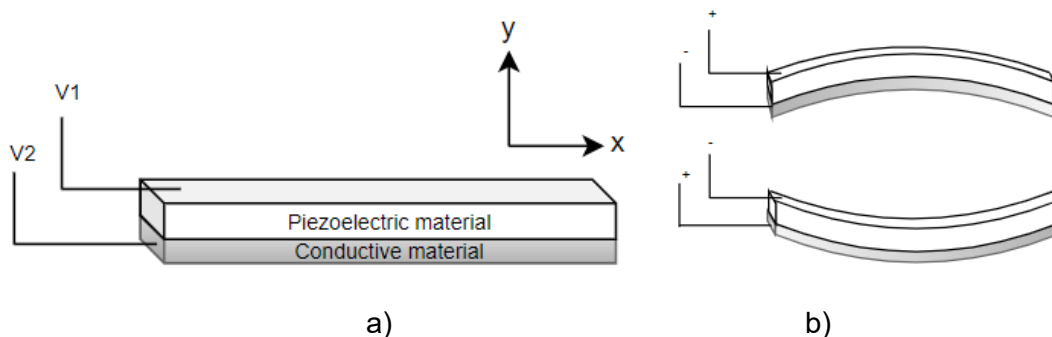


Figure 3.1. Piezoelectric bending actuator: a) schematic diagram; b) working principle [73].

Tekpinar et al. developed a piezoelectric fiber scanner where two planar piezo bimorph cantilever actuators were placed perpendicular to each other to generate the 2D motion of an optical fiber connected to them. In this case, the dimensions of the cantilevered fiber and the mode optimization allowed the fiber tip to interchangeably follow a raster, spiral, or Lissajous scanning pattern by simply changing the actuation parameters. A schematic diagram of such a model is shown in Figure 3.2a [162]. The different scanning patterns were projected on a United States Air Force (USAF) resolution target to evaluate the image uniformity. From Figure 3.2b, a raster scan provides a uniform illumination on the target, while the spiral one is characterized by decreasing illumination along the radius. The illumination in case of a Lissajous scan is highly dependent on the fill factor [162].

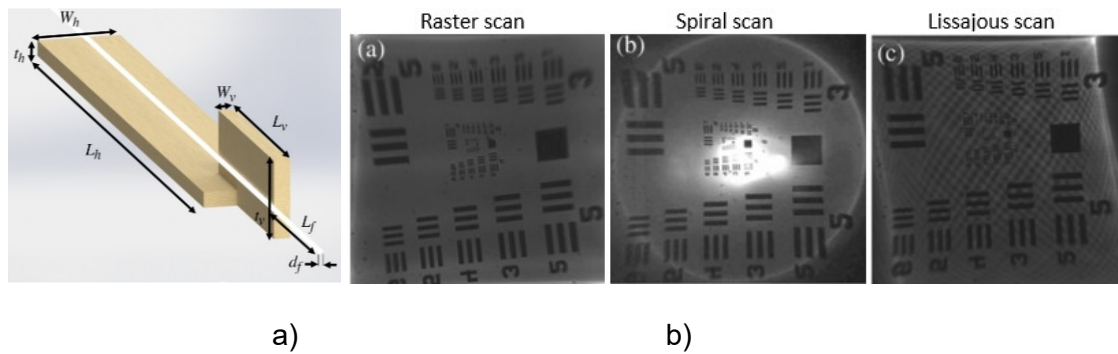


Figure 3.2. Multiple patterns generating fiber scanner: a) schematic diagram of the scanner; b) achieved scanning patterns projected on a USAF target (taken with permission of [162]).

Rivera et al. developed a compact multiphoton endoscope (with an outer diameter of 3mm) where two bimorph piezoelectric actuators were used to excite a DCF. Two bimorph structures were placed in such a configuration to have perpendicular bending axes. A raster scanning pattern was generated by exciting the fiber in two directions. The fast-scanning motion was obtained by exciting one of the actuators at the resonant frequency of the extending cantilevered DCF, and slow axis scanning was performed by exciting the other actuator at a frequency much lower than resonance frequency. The mechanical assembly of the described endoscope is illustrated in Figure 3.3a [150]. The developed prototype and the optical path diagram inside the endoscopic tip are shown in Figures 3.3b, and 3.3c [150]. Using the developed probes, the authors were able to obtain the fluorescence images of an ex vivo mouse lung tissue at depths comparable to a commercial multiphoton microscope. The finer resolution (lateral and axial resolution of

0.8 μm and 9.4 μm , respectively) enabled the probe to clearly identify the alveolar walls and lumens in the unstained lung tissue, as in Figure 3.3d [150].

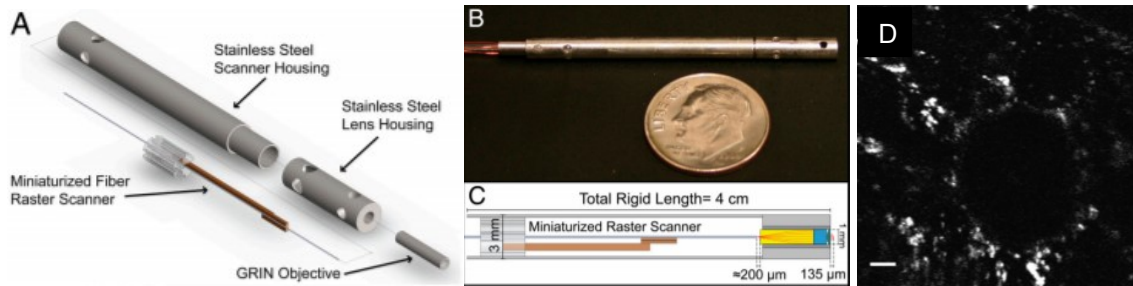


Figure 3.3. Raster scanning endoscope: a) mechanical assembly; b) developed prototype; c) optical path diagram; d) Fluorescence image of an unstained ex vivo lung tissue (taken with the permission of [150]).

It is possible to enhance the cantilever fiber deflection with low power consumption by using very thin piezoelectric ceramic layers. Recent developments in the field showed the ability to form piezoelectric layers with thicknesses at submicron levels. A variety of methods were implemented to deposit the thin film of these materials. Such methods included arc discharged reactive ion-plating, epitaxial process, sol-gel spin-coating, and sputtering [166].

3.3.2. Tubular piezoelectric actuator

In the tubular structure, a thin ceramic sheet is bent into a cylindrical shape, and can experience axial, radial, or bending motions. The tube shrinks radially and axially in the presence of a voltage difference between the inner and outer electrodes of the tube. In these actuators, the load can be either mounted on the curved surface for radial displacement, or on the rims for axial displacement. These devices are very rapidly responsive, but the generated force is limited. Usually, the displacement produced by a piezoelectric device is very small. Thus, it is possible to stack up various piezoelectric disks or tubes to amplify the generated displacement [165].

As described earlier, piezoelectric actuators are most used in cantilevered based endoscopic probes, especially the tubular piezoelectric actuators. In this case, the tube structure is divided into four electrodes, and placed near the blocked end of the cantilever fiber. The base excitation of the fiber along a certain direction is obtained by applying voltage to two opposite electrodes. Seibel et al. used this configuration to obtain a 2D

displacement of the fiber tip. In this small sized endoscope, the drive voltage at two pairs of electrodes had an increasing amplitude and a phase shift of 90° , which resulted in a spiral pattern followed by the fiber tip [19, 20]. The schematic diagram of the scanning fiber endoscope is shown in Figure 3.4 along with the zoomed view of the scanning portion showing the cantilevered fiber's connection with the tubular actuator [15]. Some in-vivo testing images of airways of a live pig taken with this endoscope (Figure 3.5b) were compared with the corresponding images from a conventional Pentax bronchoscope (Figure 3.5a). The two devices showed comparable images in terms of resolution and field of view [15].

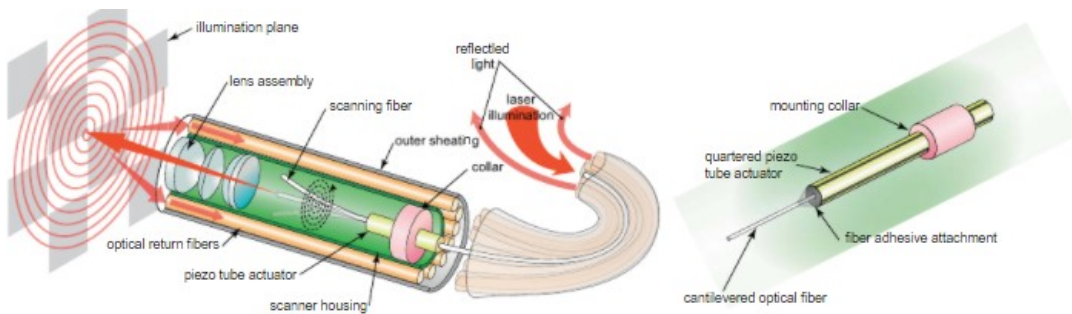


Figure 3.4. Schematic diagram of a scanning fiber endoscope (taken with permission of [15]).

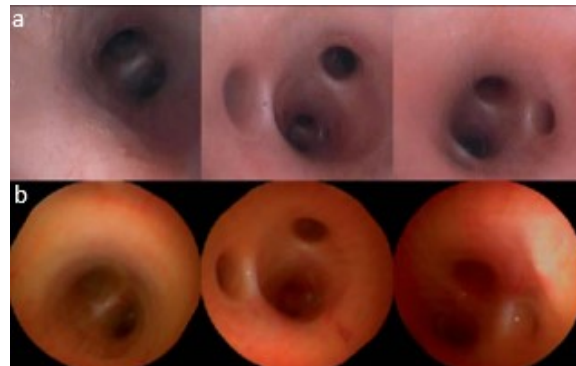


Figure 3.5. In vivo images of airways of a pig acquired with: a) conventional Pentax bronchoscope; b) scanning fiber endoscope (taken with permission of [15]).

A similar fiber optic scanner using a tubular piezoelectric actuator, packaged within a 2 mm housing tube, was developed by Liang et al. as a two-photon and second harmonic endoscope. This novel endo-microscope enabled label-free histological imaging of tissue structures with sub-cellular resolution. The schematic diagram of the developed two-photon endoscope is illustrated in Figure 3.6a [170]. An overlaid two-photon and second

harmonic generation image of a mouse liver acquired with such endoscope is shown in Figure 3.6b where the collagen fibers (in red), and vitamin A granules (in bright green) dispersed in the cytoplasm (dark green) can be clearly identified [170].

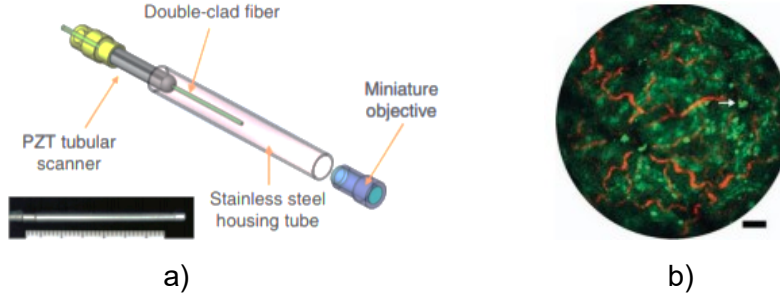


Figure 3.6. Nonlinear optical endoscope: a) schematic diagram; b) two-photon and second harmonic generation structural image of a resected mouse liver (taken with permission of [170] CC-BY license).

Vilches et al. developed a fiber scanner for OCT where a piezoelectric tubular actuator provided the base excitation motion to an optical fiber having a GRIN lens attached to its free end. In this configuration, schematized in Figure 3.7a, the beam scanning was attained by rotating the angle of the collimated beam which provided high resolution imaging while avoiding optical aberrations [171]. The cross-sectional tomogram of a human finger obtained with this scanner is shown in Figure 3.7b [171].

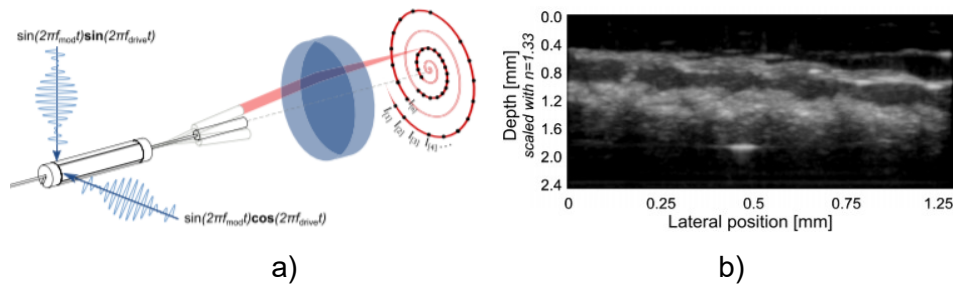


Figure 3.7. Fourier-plane fiber scanner: a) schematic diagram; b) cross-sectional tomogram of human finger (taken with permissions of [171]).

3.4. Electro-thermal actuators

The working principle of an electrothermal actuator is based on the Joule effect. The electric resistivity causes an increase in temperature in the presence of current flowing through the actuator. The amount of heat generated in a material is directly

proportional to the material's resistivity, current, and length of the actuator; while it is inversely proportional to the cross-sectional area of the device. Generated heat causes thermal expansion and consequently the deformation of the material.

In electrothermal actuators, the cross section is usually much smaller than the length of the actuator to make it more resistive and, consequently, causes higher temperature variations for a given input power. Thus, the temperature along the actuator can be calculated using a one-dimensional model. A correction factor can be included in the equation to consider this approximation. The nonlinear partial differential equation describing the temperature variation (T) in space and time can be obtained using the conservation of energy [172]. In the case of a rectangular section bar (with width w, and height h), the partial differential equation (PDE) describing the heat transfer along the length x becomes:

$$\rho c_p \frac{\partial T}{\partial t} dx = J^2 \rho_r dx - \left[\frac{d}{dx} \left(-k_p \frac{dT}{dx} \right) dx + (T - T_p) \left(\frac{S}{h R_T} \right) dx + \left(\frac{2h_{cs}}{w} + \frac{\lambda h_{cf}}{h} \right) (T - T_a) dx + \frac{\lambda \epsilon_x \sigma}{h} (T^4 - T_a^4) dx \right] \quad (3)$$

with ρ , c_p , ρ_r , k_p being the density, specific heat, resistivity, and the thermal conductivity of the material characterizing the actuator, respectively. h_{cs} and h_{cf} are the convection coefficients for the side walls and the faces of the actuator element, respectively. λ is the coefficient describing the heat loss. ϵ_x and σ are the surface emissivity and the Stefan-Boltzmann constant for radiation heat transfer, respectively, while T_p and T_a are the substrate, and ambient temperature, respectively. R_T is the thermal resistance between the actuator surface and the substrate material. J is the current density along the actuator given by the current passing through it per unit section of the actuator material. S is the shape factor and is a function of total heat flux defined as:

$$S = \frac{h}{w} \left(\frac{2t_v}{h} + 1 \right) + 1 \quad (4)$$

where t_v is the air gap between the actuator material and the substrate [172, 173].

The heat transfer through convection and radiation is evident at very high temperatures. In electrothermal actuators, the operable temperature is limited to avoid damage to the material. Thus, the corresponding terms in equation (3) can be neglected [172, 174]. Therefore, equation (3) can be simplified to:

$$\rho c_p \frac{\partial T}{\partial t} = J^2 \rho_r + k_p \frac{d^2 T}{dx^2} - (T - T_p) \left(\frac{S}{h R_T} \right) \quad (5)$$

The temperature profile along the actuator can be determined knowing the initial temperature of the actuator and the two boundary conditions.

Based on configuration, electro-thermal actuators can be divided into Hot-and-Cold Arm, Chevron, and Bimorph actuators.

3.4.1. Hot-and-cold Arm actuators

These actuators are also called U-shaped actuators, folded beam actuators, heatuators, or pseudo bimorph actuators. As the name implies, the structure of the actuator is made up of at least one hot arm and one cold arm. The actuator is usually made up of a homogenous material with folded arms in a U-shaped pattern that are constrained by anchors. Usually, the anchor surfaces are characterized by having a large surface area required to ensure heat dissipation. Two arms of the actuator characterized by different cross sections are connected in series to an electric circuit. The current flows through the structure with different current densities within the two arms. Therefore, more heat is produced within the thin arm through the Joule heating principle compared to that of the wide arm. This differential thermal expansion of the material causes the thin arm to expand more and bend towards the wide section generating the bending moment [164, 175].

At the base of the cold arm, there is a thin section flexure arm which helps the bending deflection at the tip of the actuator in the shape of an arc in the actuator plane. The length of the flexure arm plays an important role on the value of the tip deflection. In the original model proposed by Guckel et al., the length of the flexure arm and the wide arm were equal to half of the length of the thin arm [176]. Huang and Lee developed the mathematical model describing the tip displacement of the actuator tip with respect to the function of the air gap between the two arms and the geometry of the arm structures. The smaller gap between the two arms led to a higher tip displacement, and the optimal length for the flexure arm was around 14%-18% of the total length of thin arm [177].

The temperature along the beam can be obtained by unfolding the beam and applying equation (5). In the case of no external load acting on the tip, the lateral deflection of the tip at the free end of these actuators can be described by:

$$\delta y = \frac{1}{2} \frac{(a^4 - a^2 + 2a) A r \alpha \Delta T_{net} L^2}{5a^4 I + a^4 r^2 A - 2a^3 I + 5a I + r^2 a A + I + a^5 I - 2a^2 I} \quad (6)$$

where L , a , A , r , α , I are the actuator length, ratio of flexure arm length to hot arm length, cross section area of the flexure and hot arm, center gap between the hot arm and the flexure component, coefficient of thermal expansion, and the moment of inertia of the hot arm (flexure arm), respectively. ΔT_{net} is the net temperature difference defined as the temperature which would cause the expansion of the hot arm alone and is the same as the net expansion in the real actuator case where a small expansion of the cold arm corresponds to a decrease in the flexure component and results in a decrease in the net expansion between the two arms [178].

Hot-and-Cold Arm actuators are used widely in MEMS devices. There are large variations in the geometry of the actuators to achieve asymmetric thermal expansion. It is possible to get the in-plane deflection by changing the length of the arms instead of the cross-section [179], or use a combination of both the difference in the length and cross section [180], or connecting the two arms of the actuator in parallel instead of series enabling higher current density in the thick arm causing the tip deflection towards the thin arm [181], or changing the resistivity of one arm by selectively doping it.

Lara-Castro et al. designed an array of four electrothermal actuators based on the hot-and-cold arm configuration to get out-of-plane displacement. Four actuators are used to control the rotation of a MEMS mirror for endoscopic OCT purposes [182]. Some other changes in the geometry of the actuator includes using two hot arms [117, 183]. Seo et al. used this kind of double hot arm electrothermal actuator to get lateral in-plane displacement of the optical fiber for endoscopic purposes [184, 117]. An optical fiber was firmly connected to the linking bridge connecting the two hot arms and the cold arm. The differential thermal expansion between hot and cold arms allowed the cantilevered fiber to move in a lateral direction (in-plane motion), while the thermal expansion between the actuator surface and the fiber gave the vertical motion causing the fiber tip to follow a Lissajous scanning pattern [117]. The schematic diagram of a 1.65mm diameter confocal endo-microscope catheter developed using this type of actuator is shown in Figure 3.8 [116].

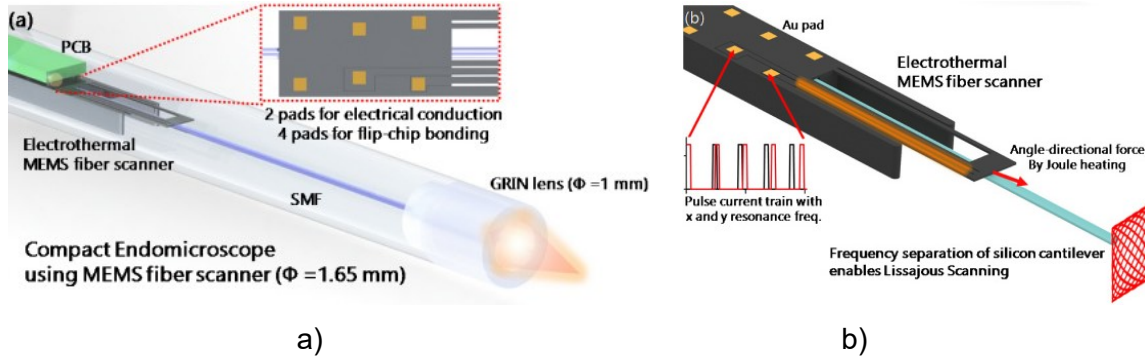


Figure 3.8. Electrothermally actuated confocal endo-microscope: a) schematic diagram; b) working principle (taken with permission of [116]).

3.4.2. Chevron actuators

Chevron actuators are also called bent-beam actuators or V-shaped actuators and are the other type of in-plane electrothermal actuators with a slightly different working principle. In this case, the in-plane displacement of the tip of the actuator is obtained from the total thermal expansion of the components instead of a differential expansion [164].

In a V-shaped electrothermal actuator, two symmetrical slanted beams are connected at a certain angle to a central shuttle beam at the apex of the base with anchors. The current passing through the actuator causes the thermal expansion of both slanted beams due to the Joule heating principle. As the movement of the beam is constrained by the anchors and the central shuttle, the thermal expansion causes a compression force and a bending moment, which gives rise to the lateral displacement of the shuttle beam [185].

Like the U-shaped beams, the temperature distribution along the arms of the actuator can be obtained using equation (5). Enikov et al. described the analytical model for V-shaped thermal actuators. The analysis of the beam deformation was considered by considering the buckling effect in the beam due to the axial thermal load and transversely applied force, if any. The numerical solution of the thermoelastic buckling model of the beam led to tip deflection of the beam or the central shuttle beam [185]. However, Sinclair presented a simplified model describing the tip displacement to be:

$$\delta = [l^2 + 2(l)l' - l \cos^2(\theta)]^{1/2} - l \sin(\theta) \quad (7)$$

where θ is the initial tilt angle of the arm beam, l is the length of the single actuator arm, and l' is the elongation due to thermal expansion [186].

These actuators provide certain advantages over the bent-beam actuators described earlier, such as rectilinear displacement, larger exhibited force at the tip, and lower power consumption [164]. The displacement of the central tip of the actuator can be increased by using longer arm components, or reducing the bending angle θ . The opposite changes increase the exhibited force. Moreover, it is possible to amplify the motion of the shuttle beam by connecting the two bent beam actuators in cascade. In the cascaded configuration, two V-shaped electrothermal actuators are anchored to the substrate and connected with secondary V-shaped beams. The current can be passed either through the primary units only or through all the structural components [187]. Similarly, it is possible to increase the output force without changing the displacement from the device by placing multiple V-shaped actuators in parallel [188]. It is even possible to combine the parallel and cascade configurations to obtain the desired displacement and force outputs [189].

Another variation in Chevron actuators consists of changing the geometry of the actuator to get a wide range of output properties. Among these, the most frequently used are the electrothermal actuators with Z-shaped patterned arms. In this configuration, the thermal expansion of the beams is blocked due to symmetry constraints leading to the bending of the beams, and thus the in-plane displacement of the central shuttle element. Z-shaped actuators permit smaller feature sizes, and larger displacement compared to the V-shaped electrothermal actuators [164, 190]. Another alternative in chevron actuators is a combination of straight and bent beams, or the so-called kink actuator. This kind of actuator consists primarily of straight arms which undergo thermal expansion by the Joule effect, while the small kink in the middle serves to guide the motion of the actuator. Kink actuators provide higher displacement at lower power levels as compared to V-shaped actuators [191].

Chevron actuators find use in some cantilever-based optical scanners. A sub-millimeter sized cantilevered fiber optical scanner is developed in this thesis that can find use as a forward-viewing endoscopic probe. In the initial proposed design presented later in detail, shown in Figure 3.9a [24], an electrothermal chevron actuator made with two parallel legs excite an SMF at resonance. In this case, the total thermal expansion of the

actuating material provides a base excitation motion to the cantilevered fiber [24]. A resolution target image captured with this scanner is provided in Figure 3.9b [24].

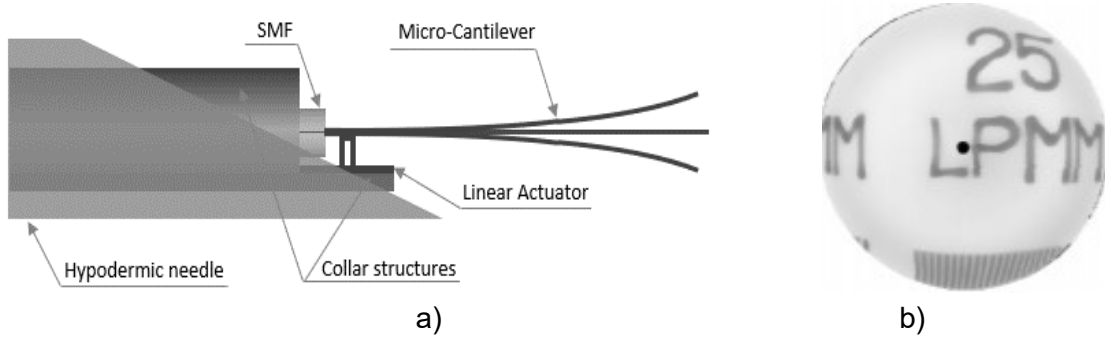


Figure 3.9. Cantilevered fiber scanner using Chevron actuator: a) schematic diagram; b) reconstructed image of a resolution target [24].

3.4.3. Bimorph actuators

A third class of electrothermal MEMS actuators are bimorph or bi-material type actuators. In this kind of actuator, two or more materials with different thermal expansion coefficients are stacked on top of each other. The different thermal expansion causes the actuator to bend or curl due to the induced strain generated by Joule heating during actuation, which results in an out-of-plane motion [175].

The basic design of a bimorph electrothermal actuator consists of a cantilever shaped micro-actuator fabricated using two layers of different materials connected to each other. The bending direction of the actuator tip during actuation will be dictated by the material with the higher thermal expansion coefficient compared to the one with the lower thermal expansion coefficient. The mathematical model for the tip deflection of such a micro-actuator is described by Chu et al. [192]. Assuming a constant curvature, the deflection at the free end of a cantilevered bi-material actuator is given by:

$$\delta = kL^2/2 \quad (8)$$

with L being the length of the cantilevered bi-metallic beam, and k being the curvature which is:

$$k = \frac{1}{r} = \frac{6b_1b_2E_1E_2t_1t_2(t_1+t_2)(\alpha_2-\alpha_1)\Delta T}{(b_1E_1t_1^2)^2+(b_2E_2t_2^2)^2+2b_1b_2E_1E_2t_1t_2(2t_1^2+3t_1t_2+2t_2^2)} \quad (9)$$

where r is the radius of curvature, b , t , E , α are the width, thickness, Young's modulus of elasticity, and the thermal expansion coefficient, respectively, of the two materials characterizing the actuator. ΔT is the change in temperature due to Joule heating [192].

Like other electrothermal actuators, it is possible to place the different bimorph actuators in a cascaded configuration to amplify the obtainable tip displacement. In such structures, the various bimorphs are placed together in a serpentine direction which causes the tip deflection from each bimorph to be added in series yielding the higher overall tip displacement. It is possible to use different geometries for the bimorph structures to adapt according to the required spacing limitations in the microdevices. Large numbers of bimorph structures can be connected in a vertical cascaded form to generate a large out of plane displacement. Many bimorph structures can also be placed in parallel to lift the high load mirror surface [193].

Bimorph actuators are the most frequently used electrothermal actuators and find use in many scanning mirror MEMS devices. Zhang et al. developed a cantilevered fiber scanner excited non-resonantly using a MEMS stage. This platform, placed at a certain distance from the fixed end of the fiber, was connected to the fixed surface using three-segment bimorph actuators at four edges. Three segments of the Al-SiO₂ bimorph actuators were placed in a configuration, shown in the schematic of Figure 3.10, to cancel out the lateral motion generating large vertical motion at the fiber tip [152]. Such a device along with imaging optics was packaged in a 5.5mm probe to use as an endoscopic OCT probe [153].

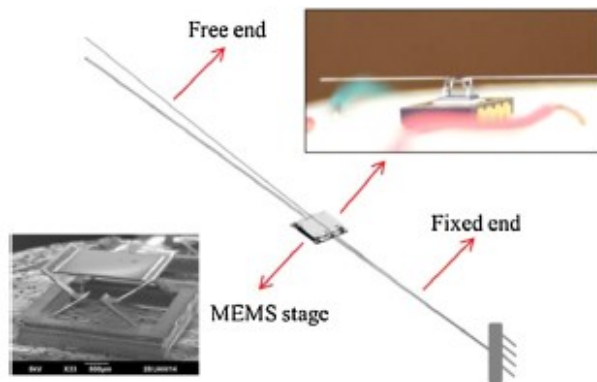


Figure 3.10. Schematic diagram of a non-resonant fiber scanner using bimorph electrothermal actuation technique (taken with the permission of [152]).

3.5. Electromagnetic actuators

The working principle that governs the motion in these actuators is the so-called electromagnetic principle where the conversion from electric/magnetic energy to mechanical energy takes place by means of a magnetic field. Like an electrostatic actuator, there are stationary and moving parts named the stator and the rotor, respectively. Depending on whether the magnetic field is generated by the stator or rotor component, there are two different configurations available for these actuators. Both configurations are described below in detail.

3.5.1. Moving magnet configuration

In this configuration of MEMS electromagnetic actuators, a bulk magnet is placed inside an electric coil. When the current flows inside the wire coil, it generates a magnetic field. The intensity of the generated magnetic field depends upon the current passing through the coil, the radius of the coil surface and the distance from the coil. For a circular coil, the generated magnetic field is given by the Biot-Savart equation:

$$\mathbf{H}(z) = \frac{\mu_0 N I r^2}{2(r^2+z^2)^{3/2}} \quad (10)$$

where μ_0 is the permeability constant, N is the number of turns, I is the current, r is the mean radius, and z is the distance along central axis [194].

In the moving magnet configuration, a permanent magnet with net magnetization vector \mathbf{M} is placed inside an external magnetic field \mathbf{H}_{ext} created by one or more electric coils at angle α . The external field applies a torque on the moveable magnet given by:

$$T_H = |V_{mag} \mathbf{M} \times \mathbf{H}_{ext}| = V_{mag} M H_{ext} \sin(\alpha) \quad (11)$$

with V_{mag} being the magnetic volume. Using a soft-magnetic material, the generated torque T_H rotates \mathbf{M} moving it away from the equilibrium position (easy axis) by an angle θ . An anisotropy magnetic torque T_a will be generated inside the magnet tending to realign it to its initial position.

$$T_a = -K_a \sin(2\theta) \quad (12)$$

K_a is the magnetic-anisotropy constant. An opposite torque - \mathbf{T}_a is exerted on the easy axis, and thus on the magnet itself [115]. If the direction of \mathbf{H}_{ext} remains constant at an angle γ ($\alpha = \gamma$ at the beginning) from the easy axis, the torque becomes:

$$\mathbf{T}_H = V_{mag} M H_{ext} \sin(\gamma - \theta) \quad (13)$$

In a permanent magnet, $M = M_s$ (saturated magnetization), and $\theta = 0$. The magnetization of soft magnets changes with the applied external magnetic field and M_s .

The external magnetization vector acting along the direction of \mathbf{M} is:

$$H_a = H_{ext} \cos(\gamma - \theta) \quad (14)$$

Thus, the change in \mathbf{M} induces the poles at the end of magnet which generates a demagnetized field \mathbf{H}_d in the opposite direction of \mathbf{H}_a :

$$H_d = -N_M M / \mu_0 \quad (15)$$

where N_M is the shape anisotropy coefficient. The net field (\mathbf{H}_i) inside the sample changes to the sum of the applied and demagnetized field. The sample moves to reduce \mathbf{H}_i , and make the magnetization vector to be:

$$M = \min \left[\frac{\mu_0 H_{ext} \cos(\gamma - \theta)}{N_M}, M_s \right] \quad (16)$$

In equilibrium, the field torque \mathbf{T}_H rotates \mathbf{M} from easy axis, and is balanced by the anisotropy torque \mathbf{T}_a and tends to align M and vibrate the magnetic component [195].

Joos et al. developed an OCT probe for imaging based on this technique. In this probe, an electromagnetic coil was placed at the outer surface in the center in which a magnet was placed carrying a thin-walled 28-gauge tube. An SMF fiber was contained in an "S" shaped 34-gauge stainless-steel tube placed within the 28-gauge tube, as in the schematic shown in Figure 3.11a. In the presence of an electric current at the coil, the electromagnetic force generated the sliding motion of the 28-gauge tube along the curved part of the inner S-shaped tube allowing the fiber to move in the lateral direction [196]. The performance of the device was tested by imaging ocular tissue structures. A real time OCT image of the ocular conjunctiva is shown in Figure 3.11b where different tenons and sclera layers can be clearly identified [196].

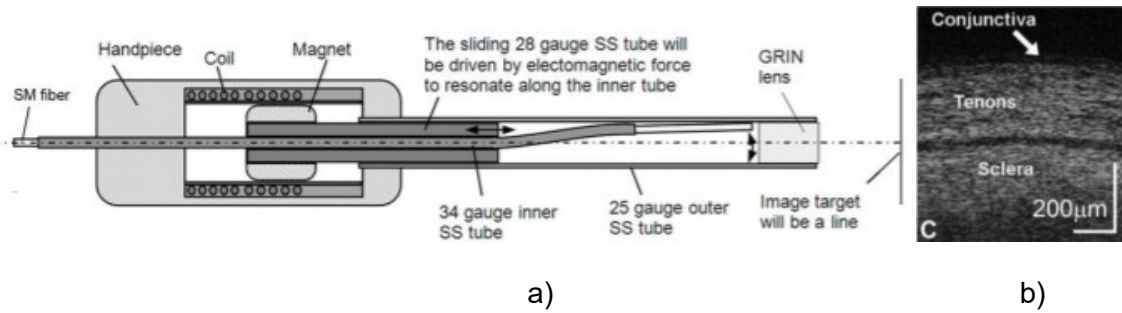


Figure 3.11. Forward-viewing OCT probe based on electromagnetic actuation: a) schematic diagram; b) real-time image of conjunctiva (taken with the permission of [196]) © The Optical Society.

Sun et al. developed a cantilevered fiber scanner for medical endoscopic applications where an SMF with a collimating lens was excited at resonance using an electromagnetic actuator working on this principle. The researchers fixed a soft cylindrical magnet to an optical fiber using a 1mm diameter polyimide pipe, and a tilted coil was fabricated using a microfabrication lithography technique [197]. The schematic of the design is illustrated in Figure 3.12. In the presence of an Alternating Current (AC) applied to the coil, a magnetic field was generated within the coil and vibrated the magnet fixed to the fiber resulting in excitation of the fiber [197]. Two tilted coils can be used to drive the fiber in two directions to get a 2D image [198].

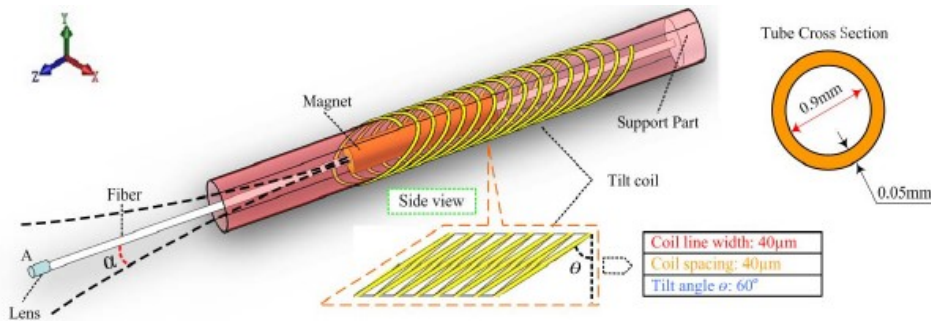


Figure 3.12. Schematic of an electromagnetically driven fiber scanner (taken with the permission of [197]) © 2011 IEEE).

A similar probe, schematized in Figure 3.13, was recently developed by Yao et al. where a cantilevered fiber containing a mass element and a lens at its tip was excited at a second resonance mode using a pair of flexible driving coils. The geometry of the cantilevered portion generated a 2D elliptical motion with a larger scan angle at the fiber tip in the presence of a magnetic force generated by the soft magnet in the presence of a magnetic field [115].

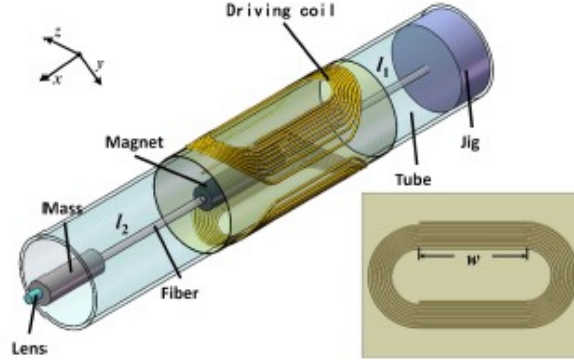


Figure 3.13. Schematic design of a fiber scanner excited at second resonance mode using an electromagnetic actuator (taken with the permission of [115] © 2011 IEEE).

3.5.2. Moving coil configuration

In the moving coil configuration, an electric coil is fabricated on the scanner and is placed inside a static magnetic field created by external magnets. When the current flows through the coil in the presence of an external magnetic field, a force is exerted on the coil designated as the Lorentz force. The force generated on the coil is given by:

$$F = |IL \times \mathbf{B}| = BIL \sin(\theta) \quad (17)$$

where \mathbf{B} is the external magnetic field, I is the current, L is the length of the conductor, and θ is the angle between the direction of the current and magnetic field [199]. The force produced can be written in terms of equation (10) as well. Usually, the conductor is placed perpendicular to the magnetic field to get the maximum exerted force. The equation (17) will be simplified to:

$$F = BIL \quad (18)$$

In the case of a coil with N turns, the generated magnetic torque on the coil is:

$$T_{mag} = 2 \sum_{n=1}^N BILr_n \quad (19)$$

with r_n being the distance of the n^{th} coil turn from the center [145].

As in the previous case, the actuator (coil surface) deforms due to the generated torque, and a restorative torque will arise in the coil to bring it to its initial state causing the vibration of the moving coil. This technique is frequently used to actuate micro-mirror surfaces [200, 201] and finds limited use in cantilevered fiber scanners.

3.5.3. Magnetostrictive actuation

Magnetic materials are characterized by a special property which allows them to change their dimensions in the presence of a magnetic field. This effect is called magnetostriction. The material can undergo a change in dimension until it reaches the value of saturation magnetostriction, which depends on the magnetization and, therefore, on the applied magnetic field [202].

Bourouina et al. developed a 2D optical scanner based on the magnetostrictive effect. In this case, a silicon cantilever was coated with a magnetostrictive film. Due to the uniaxial nature of the magnetostrictive material, bending and torsion vibrations were generated simultaneously in the presence of an AC magnetic field generated by the electric coils placed in its surroundings. Later, a piezoresistive detector was incorporated in the device to measure the bending and torsional vibrations [203, 204].

A slightly different fiber-optic scanner was developed by a group of researchers from the University of Texas. In this design, an optical fiber was coated with a ferromagnetic gel which experienced a bending motion in presence of an external magnetic field generated by a magnet placed at the outer surface. The schematic configuration of such device is shown in Figure 3.14 [205].

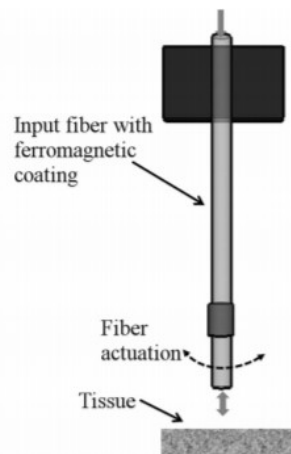


Figure 3.14. Schematic of a magnetically actuated fiber-based imaging system (reprinted with the permission from [205]).

3.6. Electrostatic actuators

An electrostatic actuator includes at least two pairs of electrodes attached to two plates separated by a gap. One of these plates is fixed by anchors, and is named the stator, while the other plate can move and is designated the shuttle. In the presence of a voltage difference between the two plates, an attractive electrostatic force generates between them causing the movement of the shuttle plate towards the stator. The amount of the electrostatic force generated between the two components depends on the gap and the dielectric constant of the media separating the two plates. The generated electrostatic force is given by:

$$F_{es} = \frac{A\varepsilon V^4}{2g^2} \quad (20)$$

where A is the electrode area, ε is the dielectric constant of the air, V is the total voltage difference applied to the plates, and g is the air-gap distance [206]. The maximum voltage that can be applied to a pair of electrostatic electrodes is delimited by the pull-in voltage. The electrostatic force increases with the applied voltage until the point when the force causes the two plates to collapse together. The maximum applicable voltage without causing this phenomenon is called pull-in point voltage. The electrostatic actuators can be classified into parallel plate and comb drive, which are described below.

3.6.1. Parallel plate actuator

In a parallel plate configuration, two electrodes are placed parallel to each other in an interdigitated finger configuration. In optical scanners, the moving electrode is mostly represented by a polysilicon mirror used to deflect the light.

Another variation of a parallel plate actuator is a system where the moving electrode has a rotational degree of freedom. The voltage application to the electrodes in this case causes the rotation of the moving electrode with a tilt angle obtained from the equilibrium between the electrostatic torque generated by the electrostatic force and the restoring torque. The large deflection angle in this case requires a large air gap between the electrodes. The maximum deflection of the rotating electrode should be less than one third of the air gap to avoid the pull-in phenomenon [207].

Most of the torsional electrostatic actuators are divided into small sized scanner arrays causing large tilting angles with small air gaps. There are some systems developed with tapered electrodes to allow large tilting angles.

One of the main drawbacks of the electrostatic actuators is that a large driving voltage is required to get moderate deflection angles. It is possible to partially overcome this by using tapered electrodes instead of the parallel shaped ones [208].

3.6.2. Comb drive actuator

In electrostatic comb actuators, multiple plates are connected to make interdigitated static and mobile rows. Such a configuration enables an increase of the interaction area between the two electrodes, and, consequently, high electrostatic forces are generated. As in the parallel plate configuration, the out of plane motion of the mobile mirror structure can be obtained by making a vertical offset between the torsional support and the driving arm [207].

In vertical comb drives, the moving comb motion is out of plane with the motion of the fixed comb, which avoids the pull-in phenomenon. Moreover, the deflecting mirror can be decoupled from the actuating part permitting a large possible deflection of the mirror itself. The higher electrostatic torque generated by the comb structure leads to the possibility of higher driving frequencies and thus a higher scan speed [209].

Vertical comb drives are used frequently to actuate micromirrors [210, 157, 211]. It is possible to place the moving comb structures at a certain angle with respect to the fixed ones to get an angular vertical comb drive. The initial angle between the comb structures determines the obtainable maximum angle rotation of the mirror connected to it [112].

A group of researchers at Fraunhofer university studied the design optimization for comb drive micro-actuators. It was more convenient to place the electrodes in a star shaped pattern to get a higher deflection of the mirror surface [212].

Both types of actuators are mainly used to actuate micromirrors [166]. Munce et al. developed an electrostatically driven fiber-optic scanner (shown in Figure 3.15a) where a single mode fiber was placed in a platinum coil. The packaged probe had a diameter of

2.2mm. There were two insulated wires placed around the optical fiber which acted as electrodes. An electrostatic force was generated around the fiber in the presence of a potential difference between the two electrodes which allowed the fiber tip to vibrate [213]. An in-vivo Doppler OCT image of the heart of a *Xenopus laevis* tadpole, taken with this device (Figure 3.15b) enabled the clear visualization of left and right aortic arches [213].

3.7. Shape memory alloy actuators

Shape memory alloys (SMAs) are unique metallic alloys having the ability to return to its original shape after being deformed plastically. The deformation recovery is usually obtained by increasing the temperature of the material which releases the state of stress.

SMA material is either available in a wire or a sheet shape. Frequently used SMA actuators come in the form of a coil structure as they can provide a larger stroke as compared to a straight wire per unit length. The shear modulus and the spring constant of a SMA coil/spring depend on composition, temperature, strain, and shape memory treatment applied to the material. In the design of a SMA actuator, the material is deformed at a low temperature and thermally treated to remember its shape. The shape recovery of the coil is obtained by increasing the temperature via the Joule effect by passing a current through the wire [214].

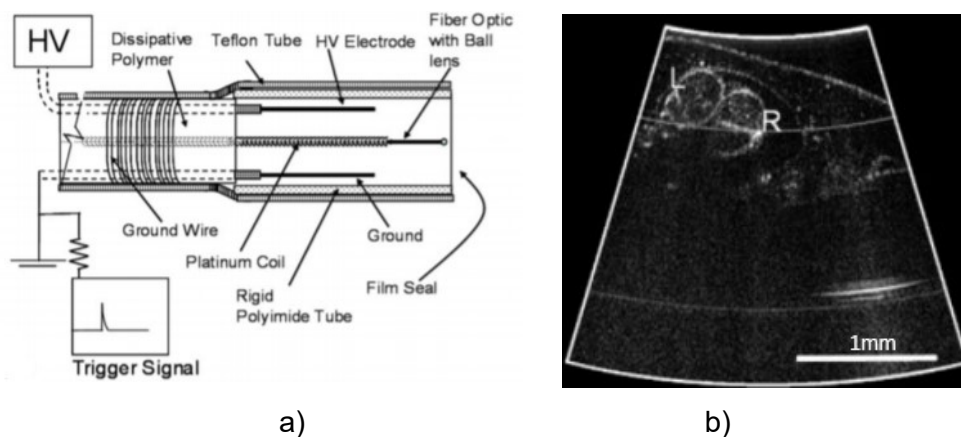


Figure 3.15. Electrostatically driven fiber scanner: a) schematic diagram; b) Doppler OCT image of a tadpole heart (taken with permission of [213]) © The Optical Society.

Although SMA actuators generate large forces and displacements, their response time is slow. Currently, these actuators find limited use in applications requiring cyclic performance at frequency of over 1 Hz [215, 216].

The SMA coil actuators show a one-way shape memory effect. Thus, a bias spring or a second SMA coil spring is combined with a SMA coil actuator to get two-way actuation. When current is passed through the SMA coil, it tends to return to its original shape, which exerts a force on the second spring/coil permitting motion in one direction. When the current is stopped, the SMA coil cools down and it is re-deformed by the force applied by a bias spring or by activating the second coil [217].

SMA coils are used in endoscopes to bend their distal tip for a long time. Maeda et al. fabricated a 2mm diameter endoscope head where an actuation ring connected to two SMA springs guided the bending motion of the endoscope tip, which contained the optical guide fibers, by pulling or releasing the pull wire connected to it. The schematic diagram showing the structure of the described design is shown in Figure 3.16 [218]. When an SMA coil spring (1) is heated, it tends to recover its shape and rotates the actuation ring to the right which in turn pulls the wire causing the bending motion of the tip. By stopping the current in that coil and heating the other coil, the tip returns to its original position [218].

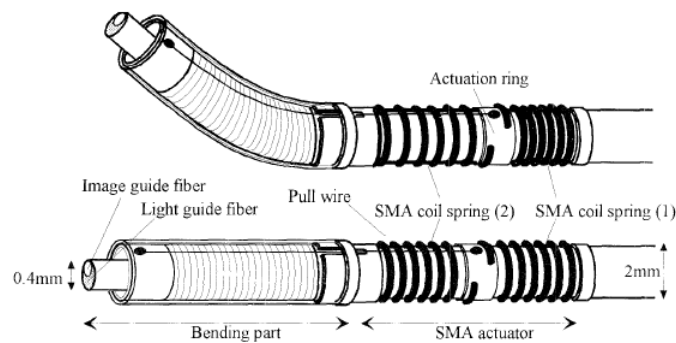


Figure 3.16. Schematic design of endoscopic tip guided using SMA coils (taken with permission [218] © 2011 IEEE).

Haga et al. used three SMA coils actuators at equilateral triangle locations between two links to form a joint. The bending motion generated by these actuators allowed the snake like movement of the central working channel of the endoscope, i.e., guided the endoscope [219].

A similar endoscope was designed by Makishi et al. where an active bending motion of the endoscopic tip, containing a CCD imager, was obtained using three SMA coil actuators [220]. The endoscope design showing the structure of the device is illustrated in Figure 3.17 [220]. Another similar endoscope was developed by Kobayashi et al. where the bending motion of the endoscopic central channel containing a CMOS imager and three LEDs was obtained using three SMA wires and a stopper coil. In this case, a large bending angle was obtained at low cost by allowing the SMA wires to follow an arc shaped deformation [122].

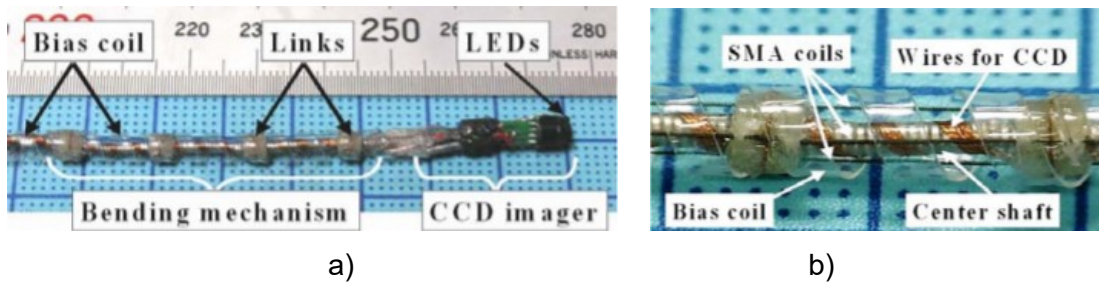


Figure 3.17. Active bending endoscope using SMA coil actuators: a) endoscope design; b) zoomed view of the actuation mechanism (taken with the permission of [220] © 2011 IEEE).

3.8. Conclusion

Frequently used MEMS actuators in fiber-optic endoscopic devices comprise piezoelectric, electrothermal, electromagnetic, electrostatic and shape memory alloy actuators. Piezoelectric actuators are available in plate or tubular structure, among which the latter one is largely used as it provides the base excitation to the fiber held in the center along two directions. By linearly increasing the amplitude of sinusoidal voltages at two pairs of electrodes with a 180° phase shift, one can obtain a spiral scanning pattern.

Electrothermal actuators are available in three different types including hot-and-cold arm, chevron, and bimorph actuators. In a hot-and-cold arm actuator, the different geometries of the two legs produce an asymmetric heat generation and, consequently, an asymmetric thermal expansion generating a bending motion at the actuator tip. Similarly, in bimorph actuators, the different material properties cause the bending of actuator tip. These techniques can be combined with other actuation methods to obtain a 2D Lissajous scanning pattern. Chevron actuators have symmetrical legs and provide linear 1D motion at its tip.

Electrostatic actuators are available in parallel plate and comb drive configurations. These actuators find limited use in fiberoptic scanners due to their large dimensions but are highly used in scanners having proximal scanning devices such as mirrors.

The shape recovery property of shape memory alloy materials makes them an excellent alternative for providing a large actuation force in compact dimensions.

Various imaging endoscopic devices using these actuators are described in this chapter. The performance of some recently developed fiber-optic cantilever-based scanners is summarized and compared with the clinically available endoscopes in Table 3.2 [73].

The size of an actuator is an important factor in a cantilevered endoscopic device. The developments in the MEMS field permit the mass production of small sized actuators enabling the fabrication of small sized imaging probes. The endoscopic technology is aiming towards the design of low-cost disposable imaging devices as the reprocessing and sanitation of an endoscopic device is a complex and expensive process. The fabrication of small sized actuation mechanisms helps cut down the price of the device. Moreover, small sized probes can be advanced deeper to image the small body cavities enabling an earlier detection of pre-cancerous surfaces and help the diagnostic procedure to control the lesion at a preliminary stage.

The current small sized endoscopes are based on the use of the piezoelectric actuators which can produce motion at very high frequency (over 10 kHz) but are arguably limited to produce meaningful strain required for the actuation of the scanning fibers. Thus, a high amount of input power and a stack of material are needed in these devices. SMAs are largely used in some biomedical devices due to their large deformation and high work density but are still in the early development phase for their use in high frequency vibrating cantilevers due to the low thermodynamic efficiency at macro-scale applications. On the other hand, electrothermal actuators can produce high displacement at a limited power consumption and small dimensions. However, their response time and operating temperatures are highly dependent on the material used, which has prevented their use in very high frequency operating devices to date.

The sub-millimeter sized dimensions and operating conditions of the proposed scanner make electrothermal actuators the preferred choice for the design due to their compactness, high strain and limited power requirement.

Table 3.2. Fiber-optic cantilevered scanners developed for endomicroscopy [73].

Actuation principle	Imaging modality	Scanning direction	Resolution	FOV	Frequency	Driving voltage	Frame rate	Scanner dimensions	Scanning pattern	Cantilever fiber	Refs.
Piezoelectric bimorph	Multiphoton	Forward	0.8 μ m(lateral), 10 μ m(axial)	110 μ m x 110 μ m	1.05kHz (fast axis), 4.1Hz	50Vpp (resonant bimorph) 200Vp (non-resonant)	4.1 fps (512 x 512pixels)	3mm (diameter) 40mm (rigid length)	Raster scan	DCF	[150]
Piezoelectric tube	Two-photon	Forward	0.61 μ m+1.10 μ m (from center of FOV to peripheric zone)	160 μ m	3.1kHz	48Vpp	6fps	~2mm (diameter)	Spiral	DCF with GRIN lens	[221]
Piezoelectric tube	Two-Photon	Forward	10 μ m	70°	5kHz	25V	15fps	1.6mm (diameter)	Spiral	SMF	[138]
Piezoelectric thin film	E-OCT	Side-view	5 μ m (axial)	152°	394Hz	1.3Vpp	-	3.4mm x 2.5mm	radial	-	[154]
Electrothermal	Confocal endomicroscope	Forward	~1.7 μ m	378 μ m x 439 μ m	239Hz (x-axis) 207Hz (y-axis)	16Vpp	1fps	1.65mm (diameter) 28mm (rigid length)	Lissajous	SMF	[116]
Electrothermal	OCT (A-scan)	Forward	~17 μ m (lateral) ~9 μ m (axial)	~3mm (beam scanning)	~100Hz	3Vac_p p. 1.5V DC offset	200fps	5.5mm (diameter) 55mm (rigid length)	raster	-	[153]
Electromagnetic	OCT (B-scan)	Forward	4-6 μ m (axial) 25-35 μ m (lateral)	2mm	5Hz	\pm 10V (triangle wave)	-	0.51mm (diameter)	Linear	SMF	[196]
Micromotor	PA and US endoscopy	Side-view	~58 μ m (PA radial) ~30 μ m (US radial) ~100 μ m (PA transvers) ~120 μ m (US transverse)	~310°	~4Hz	~3.2V DC	4 fps	2.5mm (diameter) ~35mm (Rigid length_	Radial	MMF	[92]
Electromagnetic	Confocal	Forward	0.8 μ m (lateral)	390 μ m x 390 μ m	700 Hz (fast scan) 1- 2Hz (slow scan)	-	1fps	8mm (diameter)	Raster	SMF	[222]
Cellvizio	Confocal	Forward	5-15 μ m (axial) 2-5 μ m (lateral)	600 μ m x 500 μ m	-	-	12fps	2.5mm	-	-	[85]

Chapter 4.

Design and Fabrication of Sub-millimeter sized Optic Fiber Scanner

4.1. Disclosure

The material presented in this chapter is extracted, reproduced, and modified with permission from the papers listed below which I have co-authored. Eventual modifications may have been introduced for a variety of reasons including clarify the subject; provide additional information; and ensure the formatting is consistent with the rest of the thesis.

- Kaur M., Brown M., Lane P. M., Menon C. An Electro-Thermally Actuated Micro-Cantilever-Based Fiber Optic Scanner. *IEEE Sensors Journal*, 2020; 20(17), pp.9877-9885.
- Kaur M., Hohert G., Lane P. M., Menon C. Fabrication of a stepped optical fiber tip for miniaturized scanners. *Optical Fiber Technology*, 2021; 61, pp. 102436:1-8.

4.2. Introduction

This chapter elaborates on the working principle, design, and fabrication processes of the proposed miniaturized optical scanner. The scanner is composed of a single-mode optical fiber (SMF) with a cantilevered section at its distal tip. The fiber cantilever is electro-thermally actuated near its base in a single direction and excited at resonance to obtain large deflections at the tip of the fiber.

This chapter aims to describe achievement of OBJECTIVE 1 of thesis: “Development and Fabrication of the preliminary packaged prototype”.

4.3. Background

As stated in the previous chapter, the scanning fiber endoscopes permit miniaturization of the distal tip size of an endoscope, which resulted in relatively high-fidelity endoscopes that are only about 1.2+ mm [15]. The main factors that prevent the

further miniaturization of the endoscope's design consist of their actuation method and collection fibers to capture the reflected light (which are the fibers placed on the outer edge of the material surrounding the cantilever fiber). Conventional piezoelectric actuators produce a very small amount of displacement ranging from few nm to sub-micrometer range under very high excitation voltages (up to several hundred volts), so it requires a certain number of the elements stacked together to produce the desired base excitation [223]. To overcome these limitations of the current smallest endoscope, a new design for the endoscope head is proposed consisting in the usage of an electro-thermal actuator to achieve the desired vibratory motion, and a single mode dual clad optical fiber as the cantilever permitting the collection of the reflected light within the inner clad. Despite having a slower response time in the macro-scale and a higher power consumption compared to the piezoelectric actuators, electrothermal actuators can produce high output forces and large displacements at a low excitation voltage [223]. Thus, it is possible to have a very small sized electrothermal actuator able to produce the desired displacement.

As stated earlier, the proposed imaging device with sub-millimeter dimensions (~ 600 μm in diameter) is set to overcome the limitations of currently available imaging technologies to provide an earlier detection of cancer and COPD. There are about 35000 terminal bronchioles having an average diameter of about 0.65 mm that can be made accessible for imaging through the proposed miniaturized endoscope whereas the current bronchoscopes are limited to visualization of the subsegmental bronchi. Thus, the proposed imaging scanner could potentially dramatically improve the diagnostic yield of a transbronchial biopsy. Such a device would enable visualization of the terminal airways for the first time providing imaging of cancerous lesions at an earlier stage.

In the proposed design, the single mode dual clad fiber acts as a cantilever which is driven at resonance by exciting it at the base using an electro-thermal actuator. The dynamic response of a micro-cantilever optical fiber vibrating at resonance due to the base excitation caused by the Joule heating of the actuator is presented in [224, 225]. The natural frequency of a micro-cantilever decreases as the density of the surrounding material increases [224]. The tip displacement, i.e., the displacement at the distal end, of the micro-cantilever also depends on the surrounding medium. As the density of the fluid medium increases, the vibratory response has a small transient period, and tip displacement at steady state is small due to a damping effect caused by the surrounding media [226, 227]. The actuator length in the case of electro-thermal actuator dictates the

base excitation applied to the fiber based micro-cantilever for the given inputs. For a given input power and increasing the actuator length, increases the temperature and therefore the deformation of the actuator. This change, depending on the material of the actuator itself, will continue up to a certain point after which it reaches stabilization at a particular value [227, 228].

However, the analytical and finite element models of the resonantly vibrating cantilevers presented in [224-228] were based on certain assumptions. For example, the assumption of considering the actuating wires in contact with a heat sink at constant temperature is not always true, given the small size of the structures and high frequency of the current supplied. Another assumption consists of the fact that the excitation is provided at the base of fixed end of the cantilevered end, which is not exactly the case, as there is some gap between the fixed end and the actuation portion of the cantilever.

4.4. Design Overview

This project consists in the design of a novel, ultrathin, electro-thermally actuated 1D fiber optic scanner vibrating at resonant frequency, which can be packaged within a $\sim 500\mu\text{m}$ diameter housing. The proposed scanner provides the potential for a sub-millimeter sized forward-viewing endoscopic catheter which is small enough to access the submillimeter sized airways of the lung, pancreatic duct, and fallopian tubes for early cancer screening.

In the original proposed design, shown in Figure 4.1, the cantilever beam is made up of a double clad optical fiber having a diameter reduced to about $12\ \mu\text{m}$ (shown in red), which is excited near the base using an electro-thermal at resonant frequency. The fiber is supposed to align parallel to the actuation wire to minimize the blockage of the reflected light coming towards the inner cladding of the fiber. In this design, the 1D actuation of the cantilevered fiber enables its distal end to follow a 1D line scan. The entire micro-cantilever assembly is proposed to be rotated to cover a circular area. The emitted light from the inner core of the cantilever is then collimated by a lens and projected through a lens on a target sample, and the reflected light is captured by the inner cladding of the DCF to reconstruct the image.

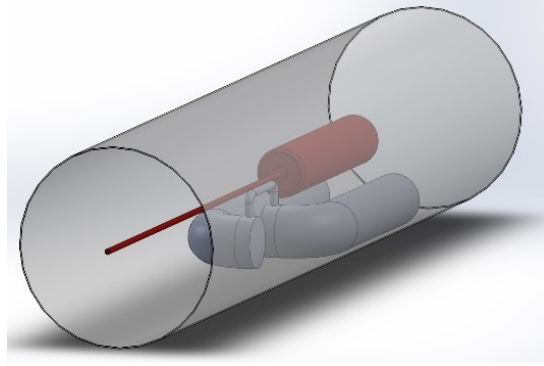


Figure 4.1. The original proposed design.

4.5. Actuator Design

In the original design, the actuator was represented by a fine (20 μm) aluminum wire (as high electrical resistance and temperature variation is required) bent in a U-shape in connection with large conduction copper wires which act as a heat sink for the actuator wires. The material selection for the actuating and conducting wires was based on the fact that the actuating wires can heat up and cool down more quickly than the conducting wires for a given input current (aluminum is about 40% more resistive than copper). Since thermal conduction is the main heat transfer method at the given dimensions, the conductive wires act as a heat sink allowing the actuating wire to cool down in a very small fraction of time (copper is about 50% more thermally conductive than aluminum). The fine aluminum wire is continuously heated up and cooled down by passing a periodic sinusoidal current at frequency equal to the natural frequency of the cantilevered fiber.

The original design showed some difficulties from the manufacturing and assembly point of view. First, it requires everything to be assembled outside as the alignment in the hypodermal needle is not possible due to limited space (internal diameter of the needle $\sim 400 \mu\text{m}$). Additionally, copper and aluminum in the proposed model are difficult to join at this scale due to different types of materials. Moreover, the bending process of the actuator wire, keeping its side wall perfectly vertical, is also difficult as aluminum is a very ductile material. In addition, the alignment of the fiber (cylindrical shaped) parallel to the actuation wire (cylindrical shape) is difficult as it tends to slide easily.

To overcome these difficulties, the actuator design was modified through the usage of a thin metallic foil which is cut down into a pattern similar to the earlier design; i.e., the

actuator part having the thin cross section in contact with a wider conduction surface. The thin bridge like structure is manually lifted 90° and the fiber is placed on that. With this method, the actuation portion had a rectangular cross section (25µm X 25µm), and it was easier to place the fiber on it. The schematic representation of the design of the proposed assembly is shown in Figure 4.2.

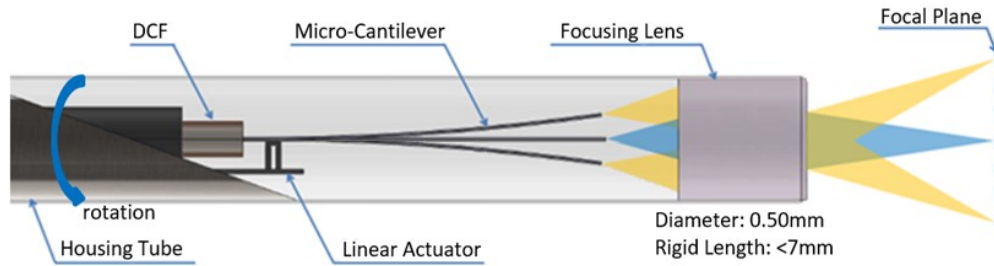


Figure 4.2. The schematic design of the updated packaged assembly.

Excitation provided by the electro-thermal actuator was based on thermal expansion and contraction of the material when the current is turned on or off. Many MEMS electrothermal actuators were composed of silicon as the core material for the device fabrication. However, the principal properties considered for an electrothermal actuator material selection for the current proposed device were electrical resistivity, thermal conductivity, coefficient of linear thermal expansion, and Young's modulus as described in [163]. From the selection process discussed in [163], brass (having an electric and thermal conductivity of about $\frac{1}{4}$ of that of copper) and aluminum were selected as candidate materials. These metals have a much higher thermal expansion coefficient and thermal conductivity compared to silicon. Brass was used in the samples tested for this thesis as it was easier to work with and permitted easy connection with copper conducting wires.

The metallic actuator was made from 25 µm thin brass foil. The bridge shaped pattern was laser cut using a laser micromachining workstation (IX-280-ML, IPG photonics). The bridge-shaped part was then manually lifted perpendicular to the rest of the foil. This bridge section was very small, being 150 µm tall with a cross section of about 25 µm by 25 µm. The resistance of this section was therefore higher than the rest of foil, which acted as a heat conductor and helps the bridge cool while current was off. The terminal parts of the foil piece were attached to copper wires to connect the actuator with the circuit and help conduct heat. The rectangular bridge-shaped pattern was made in two

different configurations, as shown in Figure 4.3. One was made with the bridge perpendicular to the cantilever fiber (Figure 4.3a [24]). The other had the bridge's upright edge placed parallel along the fiber (Figure 4.3b). The first configuration was easier to work with as the fiber was easily placed on the actuator bridge. The second had an advantage in that the reflected light from the tissue surface was minimally obstructed by the bridge when entering the inner clad of the fiber. Both setups were tested in the samples, but the second configuration was preferred.

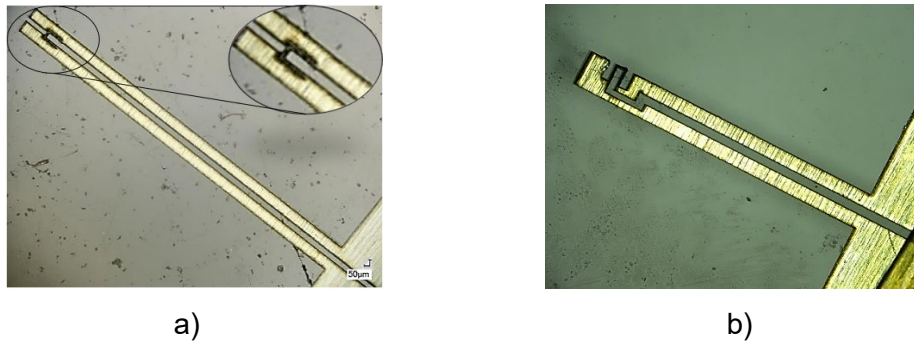


Figure 4.3. The laser cutout of the brass foil: a) perpendicular configuration [24], b) parallel configuration.

4.6. Cantilever Fabrication

One of the main key components in the prototype design was the Double Clad Fiber (DCF), where the illuminating light was carried along its core, and the reflected light from the tissue surface in our case, was collected through the inner cladding. Cantilevers were fabricated using the heat and pull method, typically employed to taper optical fibers for the fabrication of couplers, facilitated with a Vytran GPX-3000 glass processing platform.

The DCF with the desired core and cladding dimensions for the proposed wavelength of 446nm was not available off-the-shelf and needed to be fabricated as a custom order. Thus, to verify the proposed model, the microcantilever based catheter presented in the thesis was fabricated using SMF and a multimode fiber (MMF). In the preliminary design, a 125 μm Multi-Mode Fiber (MMF) with a 25 μm core mode diameter (FG025LJA Thorlabs) was tapered down to 12.5 μm to obtain a core mode diameter of about 2.5 μm , which matched the SMF core size. Fiber tapering was achieved by heating the fiber to its glass transition temperature and pulling one end of the fiber at a velocity of

about 1.00 mm/s. The filament power, delay, and pulling velocity made a precise tension profile providing the desired diameter of the tapered section.

This tapered fiber was then cleaved off with precision diamond blade scribing technology. The tension and scribe technology provided a quasi-flat, perpendicular cleave with mirror-quality end face finishes. The tapered fiber was then aligned with the SMF core by connecting the proximal end of the SMF to a laser and monitoring the maximum relative power transmitted through the aligned fibers. The fibers were then spliced once the cores were perfectly aligned in a two-step splicing method. In the first step, the fiber tips were slightly melted to connect them together. Second, more power was applied to strengthen the connection optically and mechanically. The overall fabrication process for the cantilevered tip of the fiber is shown in Figure 4.4 [229].

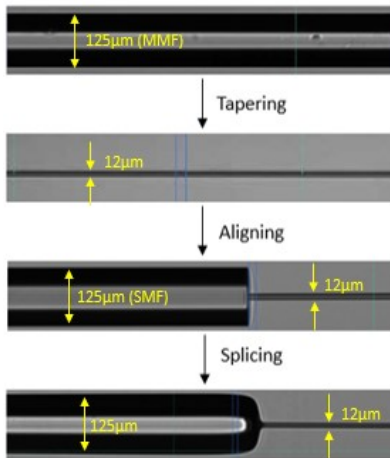


Figure 4.4. Fabrication process of the cantilever fiber [229].

4.7. Packaging

The metallic actuator and micro-cantilever fiber were assembled outside their 500 µm nitinol hypodermic needle housing. To fix each component in place, a series of Polymethyl methacrylate (PMMA) acrylic collars and semi-circular structures, having a thickness of 100 µm, were manufactured with soft lithography using epoxy-based negative photoresist SU-8 (SU-8 3050, MicroChem). Figure 4.5 shows the SU-8 structures placed on a silicon wafer. The semi-circle SU-8 piece in Figure 4.5b provided a flat base for the actuator, while the upper collar in Figure 4.5a went on top of the 125 µm optical fiber section.

The bridge pattern on the actuator was lifted manually, and the actuator was placed on a Polydimethylsiloxane (PDMS) block facing the bridge downwards. SU-8 semi-circular pieces were placed in the groove of the metal foil actuator as in Figure 4.6a. The upper collar structures were then aligned on the optical fiber as in Figure 4.6b. A thin layer of epoxy (5 Minute epoxy, Devcon) was applied to both structures to fix the collar structures altogether on the corresponding piece. These two components having the SU-8 structures were glued together with the help of epoxy.

Once the first epoxy was cured, heat-cured epoxy (EP17 HTND-CCM, MasterBond) was applied in excess to the assembly and pushed inside the needle. Figure 4.6d shows the top view of the packaged assembly. This epoxy acted as a filler for spaces within the assembly structure and needle. It also affixed the assembly inside the needle.

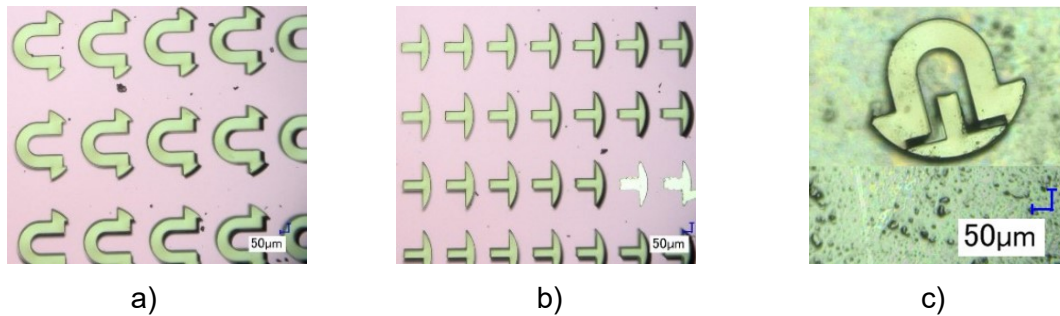


Figure 4.5. Microfabricated SU-8 components: a) upper collars; b) semi-circle pieces; c) collar structures together.

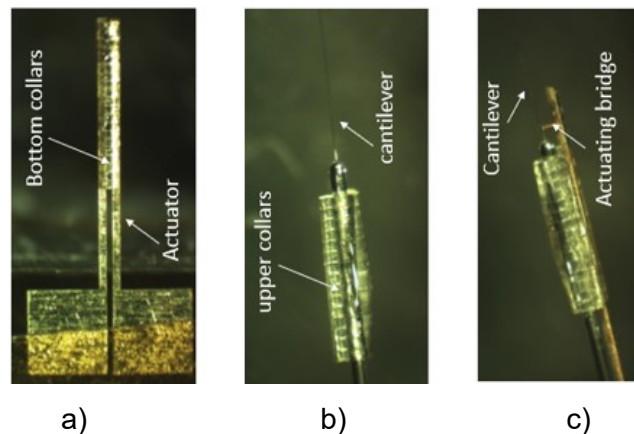


Figure 4.6. Packaging of the sample: a) actuator flipped on PDMS structure and semi-circle pieces placed in the groove of actuator; b) upper collar structures placed on SMF fiber; d) side view of assembly.

The epoxy used in the packaging heavily effects performance of the sample. As discussed in [163], glue that was not fully hardened significantly dampened cantilever vibration. Additionally, improper curing led to epoxy degradation at high operating temperatures. Improper curing can cause epoxy cracking or separation of the assembled device from the needle, further dampening motion. A fully packaged assembly with the fiber placed perpendicularly to the bridge is shown in Figure 4.7 [24].

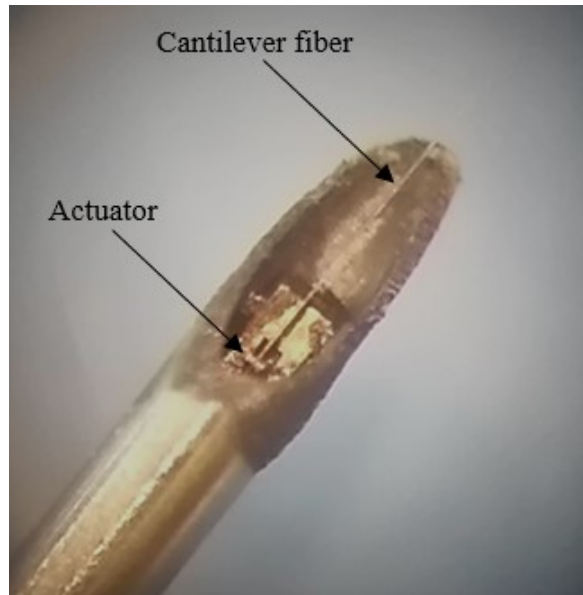


Figure 4.7. Packaged scanner sample [24].

Chapter 5.

Characterization and Image Reconstruction

5.1. Disclosure

The material presented in this chapter is extracted, reproduced, and modified with permission from the papers listed below which I have co-authored. Eventual modifications may have been introduced for a variety of reasons including clarifying the subject; providing additional information; and ensuring the formatting was consistent with the rest of the thesis.

- Ahrabi A., Kaur M., Li Y., Lane P., Menon C. An Electro-Thermal Actuation Method for Resonance Vibration of a Miniaturized Optical-Fiber Scanner for Future Scanning Fiber Endoscope Design. *Actuators*, 2019; 8(21), pp. 1-18.
- Kaur M., Brown M., Lane P. M., Menon C. An Electro-Thermally Actuated Micro-Cantilever-Based Fiber Optic Scanner. *IEEE Sensors Journal*, 2020; 20(17), pp.9877-9885.

5.2. Introduction

This chapter describes the characterization of the scanner designed and fabricated in Chapter 4. The fiber-optic micro-cantilever was linearly actuated near its base by the metallic bridge actuator. The performance of the prototype was first simulated using the finite element analysis using COMSOL Multiphysics, and ANSYS Workbench. Then, 1D scan performance was assessed by vibrating the fiber at resonance and imaging the distal tip of the sample under the microscope. In the later instance, the 2D image of an object was demonstrated by simultaneously rotating the object while scanning across its diameter.

This chapter is directed towards the fulfillment of OBJECTIVE 2 of thesis: “Imaging the tip displacement and reconstruct 2D image”.

5.3. Resonant Frequency

As stated earlier, the micro-cantilever was linearly actuated near its base by the metallic bridge. By matching the frequency of the current passing through the bridge to the resonant frequency of the micro-cantilever, a greater tip displacement was obtained. The first resonant (natural) frequency of a cantilever beam with a round cross section is given by:

$$F = \frac{(1.875)^2}{2\pi} \sqrt{\frac{EI}{\rho AL^4}} = 1.194^2 \frac{\pi\sqrt{E}}{16\sqrt{\rho}} \frac{R}{L^2} \quad (1)$$

where ρ , E , L and R are the density, Young's modulus, length and radius of the cantilever, respectively [144].

The natural frequency as function of these parameters is plotted in Figure 5.1 [24]. Each line in this figure corresponds to a given length of the cantilever indicated on each line in μm .

As each sample was manually fabricated, there were variations among them, including: position of the bridge along the micro-cantilever's length, epoxy amount, curing time/procedure, fiber dimensions, fiber alignment accuracy with respect to the bridge, etc. Therefore, each sample's resonant frequency was different and was obtained by testing frequencies around $\pm 500\text{Hz}$ of the expected value and measuring for maximum cantilever tip displacement.

From the length and diameter of the cantilevered fiber measured under the microscope, the theoretical resonant frequency was calculated, which was considered as the starting test value for the resonant frequency. The exact resonant frequency was obtained by sweeping the frequency nearby the theoretical value and measuring the amplitude of tip displacement until it reached the maximum value.

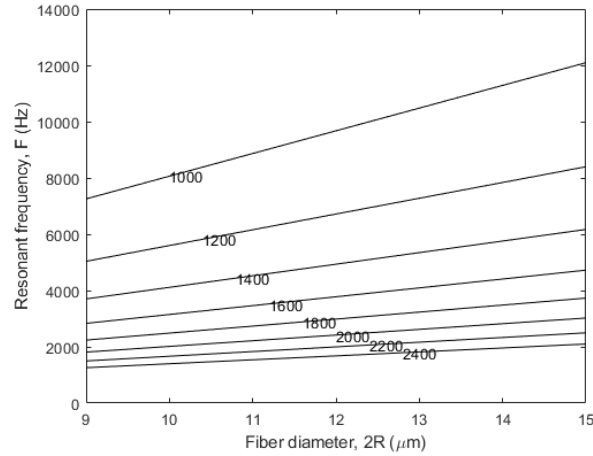


Figure 5.1. Resonant frequency in function of the cantilever diameter (2R) and length (L) [24].

5.4. Simulation for Optimization

Finite element analysis of the exact model (Figure 5.2 [163]) used in the actuator system was performed to predict the response of the system and provide suggestions for optimization of its performance, specifically fiber-tip displacement and temperature at the vibrating bridge. The simulations were performed in four parts using ANSYS (Version 18.2, ANSYS Inc., Canonsburg, Pennsylvania, USA), and COMSOL Multiphysics (Version 5.4, COMSOL AB, Stockholm, Sweden).

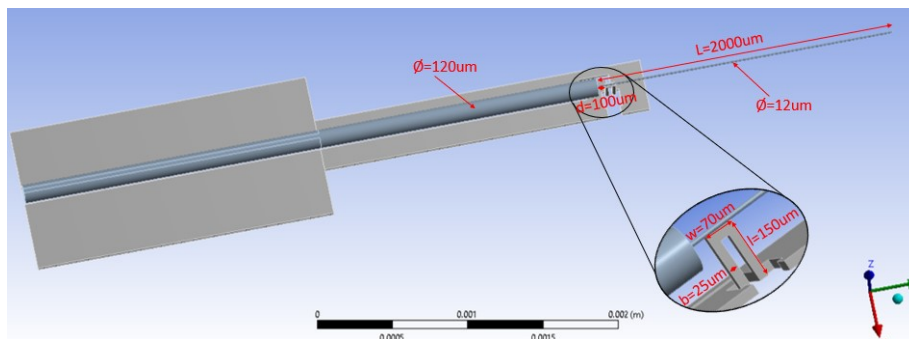


Figure 5.2. Dimensions of the device being simulated using ANSYS [163].

5.4.1. Fiber-Tip Displacement vs. Time

Fiber-tip displacement was simulated at resonance frequency of the optical fiber using COMSOL Multiphysics. Modal analysis determined the resonance frequency of the optical fiber, which was set as an input for the simulation. To simulate the damping effect,

air surrounded the device. In the actual case, there was some transient time range when the bridge continued to heat up and reached a state where the average temperature remained constant, and temperature fluctuations were present around that value due to the periodic heating and cooling. The cantilever fiber tip displacement response to a steady state temperature variation was analyzed in this case to reduce the computation time, and the response curves are shown in Figure 5.3 where the inset enlarges the displacement profiles between 0.19 s to 0.2 s.

Aluminum 6061 was used as the actuator (bridge) material and was set 100 μm tall. In a specific instance of the simulation, a signal in the form of a square wave cycle at 1370.916 Hz with a current value of 1.04 A ran through the structure. The length of the cantilever fiber was about 1.85 mm and the diameter was 11 μm ; the distance between the vibrating bridge and the junction of large and small fiber was 100 μm . The fiber-tip displacement in the above set-up was estimated to peak and settle at $\sim 80 \mu\text{m}$ unlike the undamped response.

In the case where the square wave is considered as the sum of odd harmonics following the Fourier series, it was possible to observe the beating effect in the tip displacement curve when the excitation frequency considered in the model was slightly offset from the resonant frequency. However, such behaviour was not present in the case where a single square wave with some slope (due to response time of the circuit) was used in the model.

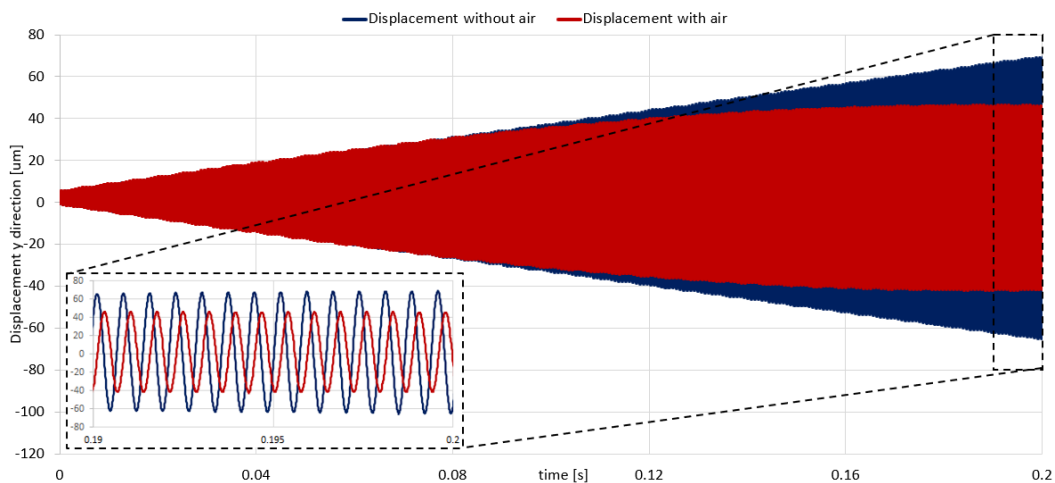


Figure 5.3. Resonance time response of the cantilever fiber measured at the tip, with the damping effect of surrounding air versus no damping. The inset enlarges the displacement profiles between 0.19 s to 0.2 s.

5.4.2. Bridge Temperature vs. Time

As an electro-thermal actuator, at steady state, the higher and lower bounds of the temperature of the actuating bridge dictate how much it will expand and contract, which in turn dictates how well it oscillates the optical fiber placed on top of it. Furthermore, at elevated temperatures, prolonged use of the device can heat up the surrounding environment which can quickly soften and degrade the quality of adhesive, which in turn impairs the mechanical integrity of the entire device (less rigid) and lowers performance because of the increased damping on the “fixed” end of the system. Thus, it is imperative to know how hot the actuator gets and how its temperature fluctuates. The temperature variations of the actuator due to an electric pulse were studied with respect to time. Figure 5.4 shows the simulation of temperature of an aluminum 6061 actuating bridge with an average input power of 0.314 W and a square signal at 2 kHz, at a room temperature of 20 °C, and at body temperature of 37 °C [163]. The temperature quickly settled at ~53 °C and ~70 °C, respectively, in 0.12 s. Temperature fluctuated within ~3 °C (see inset of Figure 5.4) because of the cyclic current passing through the actuating bridge which was essentially a resistive load. The temperature fluctuations were contained within ~3 °C in the simulated period. The time for the temperature to reach steady state was roughly the same as the time for the settlement of the tip displacement (see Figure 5.3). The system response was generally the same for a higher electric current input, albeit with a higher steady-state temperature.

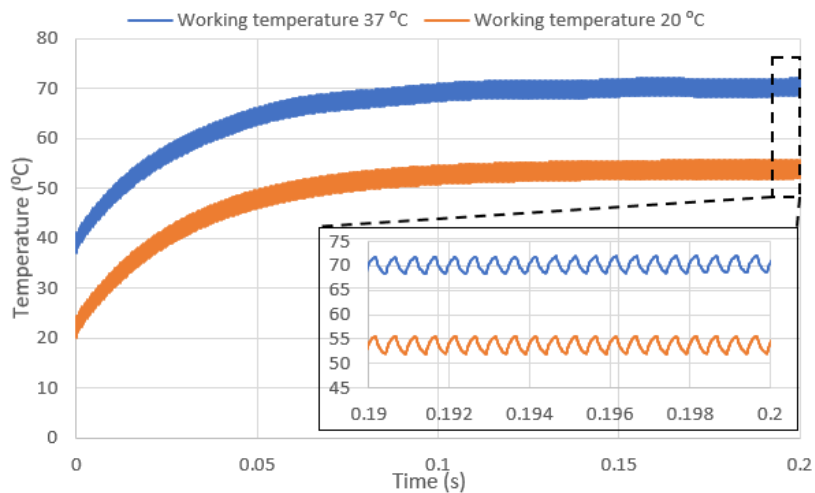


Figure 5.4. Temperature profile of the aluminum actuating bridge at 0.314 W power input. The inset enlarges the temperature profiles from 0.19 s to 0.2 s [163].

5.4.3. Temperature vs. Input Current

With a higher input current, more energy flows through the actuating bridge and causes a higher bridge temperature and larger thermal expansion. The bridge temperature under various power inputs was simulated to determine if the temperature rose to a high enough degree that it might compromise the structural integrity of the system and damage any of the components. Figure 5.5 shows the simulated aluminum bridge temperature at different current levels using ANSYS [163]. The frequency of electric pulses given to the bridge was 3 kHz. Literature shows that the Young's modulus decreased from ~4 GPa to ~2.5 GPa when SU-8 was heated up to 50 °C from room temperature (25 °C); the Young's modulus further decreased to ~1 GPa when SU-8 was heated to 100 °C [230]. The temperature increased to 80 °C when it was given a high current input (1.4 A), which could possibly cause the collar section to soften. The collar section was intended to keep the fiber and metal foil in place, so that the fiber can achieve the desired oscillation performance. Soft collars may cause undesirable damping effects which can decrease the amount of lateral tip displacement of the oscillating fiber. For all previous simulations, the electric pulse given to the metal bridge was a square wave with a 50% duty cycle. Decreasing the duty cycle, i.e., giving the bridge more time to cool down during the off cycles, provides a solution to lower the risk of mechanical damping effect due to rising temperature.

It was also observed from the simulation that the higher the current level, the larger the temperature fluctuation at steady state was observed. The temperature fluctuation increased from ~0.5 °C to ~4 °C for a current level of 0.47 A to 1.41 A (Figure 5.5 [163]), and the temperature differential was higher at higher power levels.

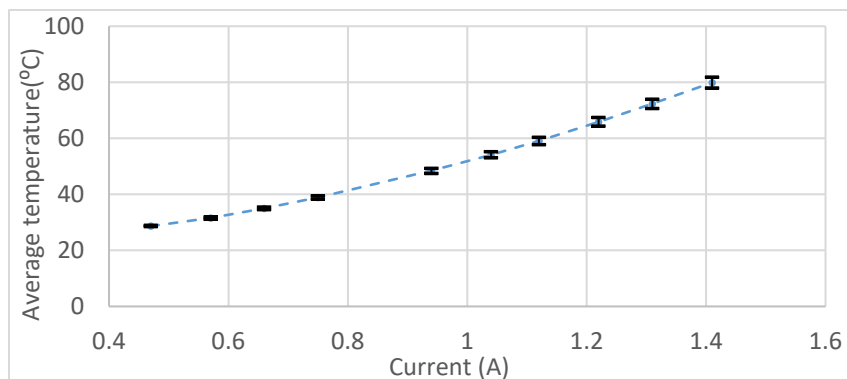


Figure 5.5. Temperature response of the aluminum bridge at different current levels using an actuation frequency of 3 kHz [163].

5.5. Cantilever Drive Characterization

The actuator was driven with a square wave in order to obtain a periodic expansion and contraction of the bridge with a corresponding excitation near the cantilever fiber base. The frequency of the driver signal was given by the natural frequency of the cantilevered fiber, as stated above. The resistance of the actuator varied by a very small amount (5% -7%) during the active cycle time (given by the change of resistivity with the temperature). Thus, the power dissipated in the actuating bridge structure was mainly controlled by the current passing through it.

The duty cycle of the square wave is an important parameter that influences the performance of the sample. At the beginning of a test, a duty cycle of 50% was used to quickly determine the resonant frequency. The actuator bridge was heated up during the on-cycle and was cooled down via conduction in the off cycle of the periodic signal because heat dissipation is an important factor limiting the performance the device. In other terms, the average temperature of the structure will continuously be increasing if the device did not have enough time to cool down. By decreasing the duty-cycle, it was possible to give the device more time to cool down. It was experimentally shown in [163] that for a given average power, it was possible to get higher tip displacements with smaller duty-cycles.

By decreasing the duty cycle from 50% to 25%, the amplitude of the tip displacement increases (more than double) for a given amount of average power passed through the bridge. After various attempts using different duty cycles, a smaller duty cycle of 6% was used as a standard value for the further tests. Thus, the current was passed through the sample for 6% of the period related to the resonant frequency, and 94% of the time was left without current to allow the heat dissipation from the thin actuator. This also permitted the usage of a higher current within the sample without damaging it. Thus, it was possible to excite the actuator using a 25V peak-to-peak pulse train, with a 0.44A current passing through it. It was possible to drive the samples with even smaller duty cycles, but the required excitation voltage was much higher for the desired tip displacement, which can be unsafe for the actuator itself given its small dimensions.

A schematic diagram of the test setup is depicted in Figure 5.6 [24]. The data acquisition (DAQ) board, or a function generator (Tektronix AFG1062) sends a square

wave signal to the driver circuit, which is powered by an external direct current (DC) supply. The output of the circuit is connected to the conduction wires of the metal actuator foil which are non-polar.

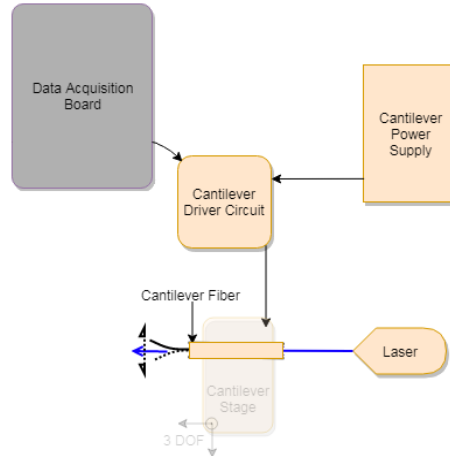


Figure 5.6. Schematic diagram of the experimental setup [24].

5.6. Scan Characterization

First, the performance of the vibrating cantilevered fiber in response to the periodic input current was analyzed under the microscope. Most of the fabricated samples used brass material as it was easy to work with, and the micro-cantilevers were placed on the actuator so that the gap between the base and actuator is about 100 μm .

The actuator foil was directly attached to the glass slide using heat cure epoxy. The conduction wires were then connected to the driver circuit, and frequency was swept around the theoretical resonant frequency to obtain the exact natural frequency. As described previously, the duty cycle was then decreased, and the max current was slightly increased to get a higher tip displacement. The side view image of the cantilever fiber in actuation under the microscope (VHX-2000, Keyence) is shown in Figure 5.7 [24].

To capture the image of the light emitted by the vibrating cantilever fiber on the tissue surface, a CMOS camera sensor was placed in the front plane of the distal end of vibrating cantilever while the other end of the optical fiber was connected to the 450 nm blue laser (LP450-SF15, Thorlabs). The wavelength of the laser light was selected based on the optical fiber properties so that the fiber acts as single mode at that wavelength, and the light was propagated through the fiber with minimum losses.



Figure 5.7. The side view of the sample under actuation [24].

An optical setup, equivalent to the GRIN lens assembly in the proposed design, was designed using off-the-shelf available catalog components which permitted the acquisition of the image of the line scanned by the laser light coming out of the fiber's tip. The CMOS camera used in the imaging process was either a 1.3MP Monochrome Sentec (STC_MBE132U3V) characterized by having a pixel size of $5.3 \mu\text{m} \times 5.3 \mu\text{m}$, or a 5MP Sentec (STC-MCA5MUSB3 model) camera characterized by a pixel size of $2.2 \mu\text{m} \times 2.2 \mu\text{m}$. The schematic design and the actual assembled setup are represented in Figure 5.8 where the sample is mounted on a three degrees of freedom (DOF) stage, allowing its alignment with the optical lenses. The theoretical magnification of the optical system was 18.18x, and the actual magnification of the system measured knowing the size of the line on USAF resolution target and the pixel size of the CMOS camera was 18.25x.

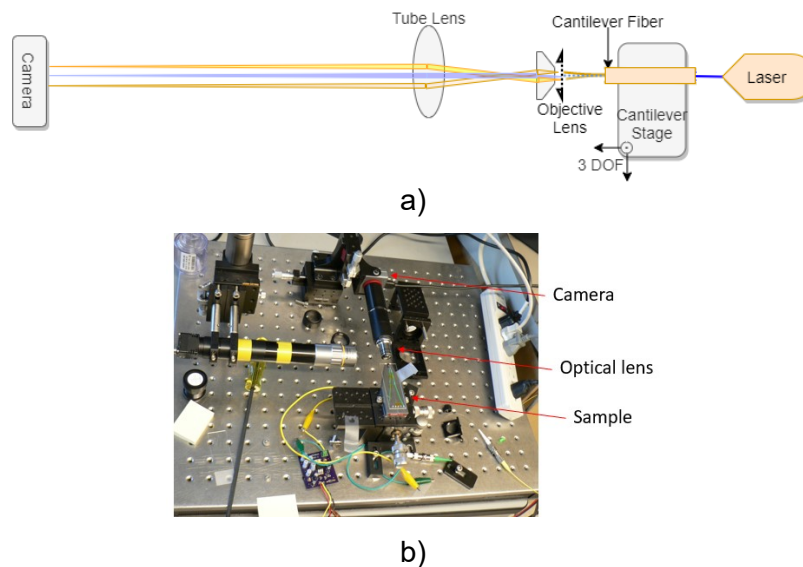


Figure 5.8. Optical setup to capture direct light: a) Ray diagram; b) Experimental setup.

The in-plane line scan representing the tip displacement, in the case of two different samples, taken from the front (using STC-MBE132U3V camera) is shown in Figure 5.9, while the tip displacement of another sample measured using STC-MCA5MUSB3 is shown in Figure 5.10.

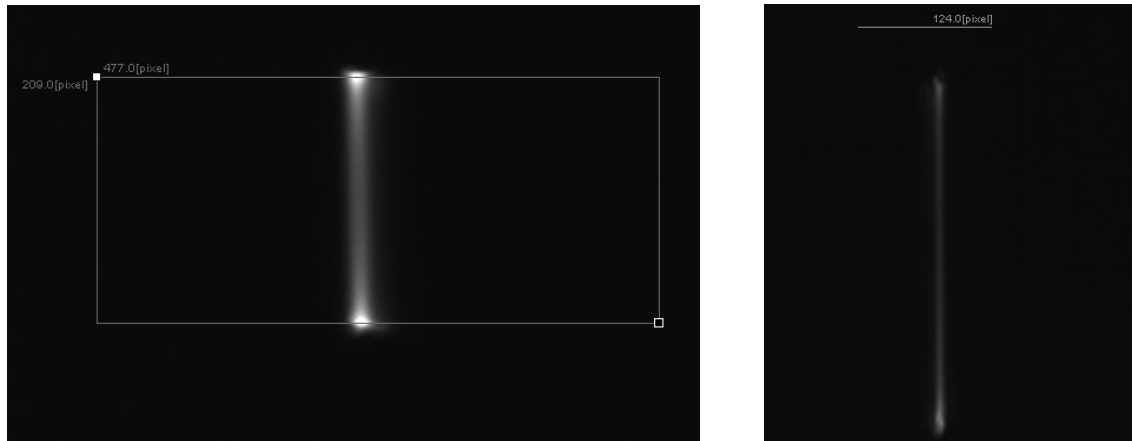


Figure 5.9. Tip displacements for two different samples using STC-MBE132U3V camera.

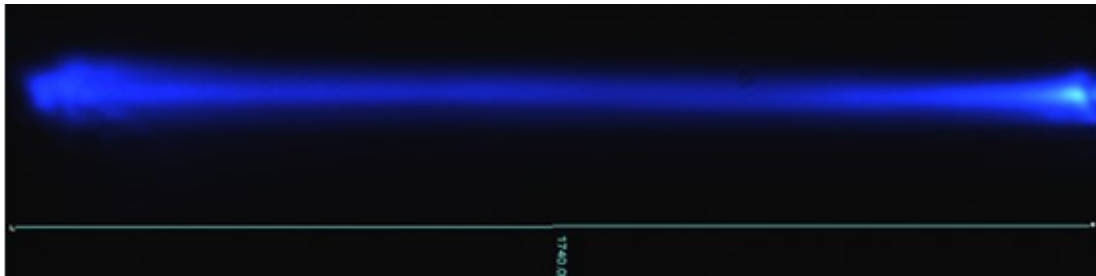


Figure 5.10. Tip displacement using STC-MCA5MUSB3 camera.

In most of the cases, the tip displacement was a straight line, especially when the cantilever fiber was actuated at small excitations, i.e., using a small amount of current provided to it. As the current increased at resonant frequency, the fiber tip started to whirl, i.e., it presented an elliptical shape pattern instead of a line. The image of such a shape pattern is shown in Figure 5.11 [24], while the change in the fiber tip displacement in function of current supplied is reported in Figure 5.12.

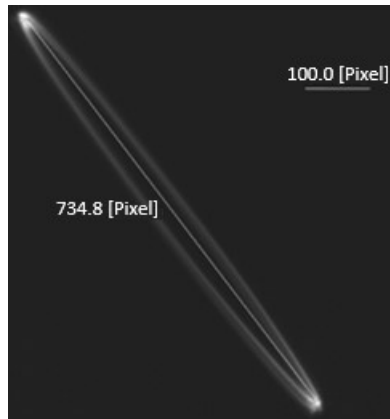


Figure 5.11. Front view of the tip displacement of the cantilever under actuation [24].

The non-linear performance of the fiber tip may be due to reasons such as: asymmetry of the bridge and/or cantilevered fiber, pretension in the cantilever, etc. These deviations from the ideal can generate a whirling motion in the fiber, i.e., the path of light was elliptical instead of a line [146, 147, 149].

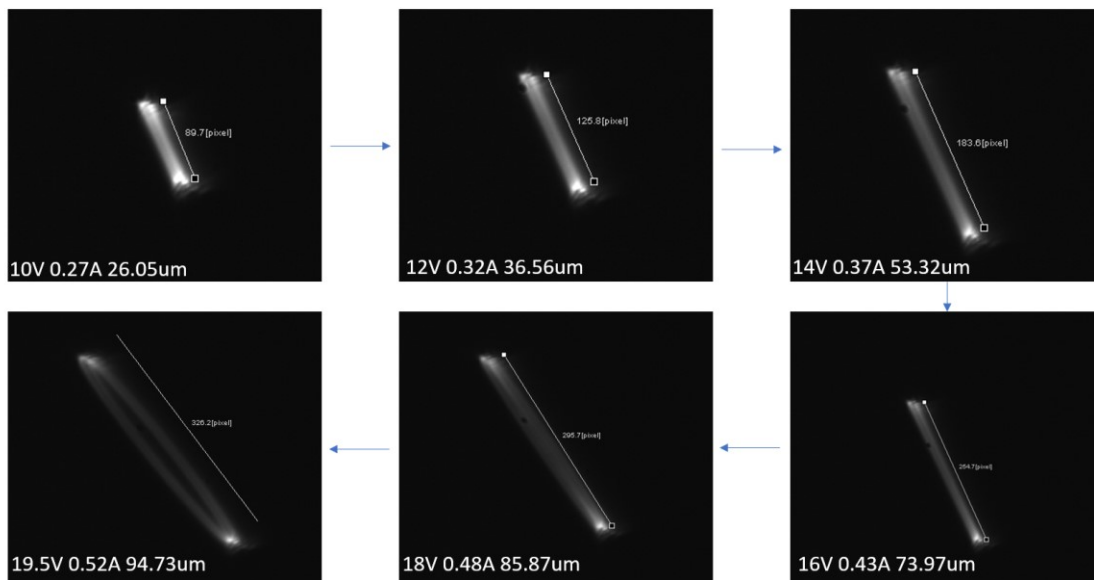


Figure 5.12. The tip displacement in function of current.

5.6.1. Whirling Effect

The nonlinearities in the motion of the base excited cantilevered beam may be due to the asymmetry in the geometry of the beam, or asymmetric excitation from the base. To verify if there was any asymmetry in the cantilever's cross section, the beam was

analyzed under the SEM and there was no asymmetry visible in there as shown in Figure 5.13.

The bridge structure actuating the cantilever had two leg structures of the same dimensions. Thus, the current density and the corresponding thermal expansion of the two legs were equal, giving an actuation in a purely vertical direction. Furthermore, as the fiber was placed in a parallel or in a perpendicular direction to the bridge shaped actuator, the contact was linear (or on point in case of the pre-stress in fiber) between the cylinder beam and the rectangular actuator. Therefore, there are less chances of the asymmetry in load.

The non-linearity of the line scanned by the cantilevered fiber's tip excited unidirectionally by the electro-thermal actuator placed near the base of the cantilever was caused by the nonlinear coupling between the motion of the two planes. Haight and King, in [146], studied the equations of motion showing that a cylindrical beam excited harmonically at the base becomes unstable and tends to move in the plane normal to the cross section of the beam tracing an elliptical shape pattern. This nonlinearity of the fiber tip's response can be avoided by changing the natural frequency ratios in two planes, and by adding damping in motion [146].

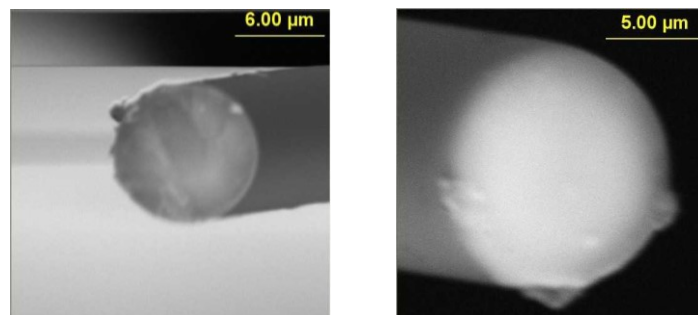


Figure 5.13. SEM image of the distal end of the cantilevered fiber.

Similarly, Hyer studied the whirling motion in the case of a cantilever beam excited linearly at the base in [147]. In this case, the whirling was associated with the tension varying along the beam due to the axial constraint applied at the fixed support of the cantilevered beam. As the beam was moving in resonance, it produced large displacements; thus, the variation of the tension along the cantilever cannot be neglected and cause the nonlinear response of its free end. The whirling motion was stable within a range of the excitation frequency close to the resonant frequency while it was unstable at

the resonance. The nonlinearity in displacement can be omitted by moving the excitation frequency away from the natural frequency [147].

Wu et. Al. studied and analyzed in [149] that a cantilevered beam excited at base in resonance presents an elliptical shaped pattern by tip displacement at higher base excitation. In the case the excitation frequency was matched to the second resonant frequency, it was possible to obtain a circular shaped pattern. This method would be quite useful as it permits obtaining a 2D scan pattern just by applying a linear excitation, but it was not practical in our case. One of the main reasons for that consists of the fact that the tip displacement in the second resonant mode is way less than the first mode tip displacement (almost 1/4). Thus, the corresponding field of view in this case would be very small. Moreover, the frequency at second mode in our case will be of the order of 15-20kHz. The heat dissipation at this small period will be ineffective requiring the use of small currents provided, further reducing the tip displacement.

Thus, as there was a small ellipticity in the pattern followed by the tip displacement of the fiber, which was due to axial inertia; one of the possible ways to reduce it, that was implemented in our case, was the usage of small duty cycle. This permitted a longer period of time for the actuator to cool down and permitted the use of higher power in short period of time providing higher values of the tip displacements. The small ellipticity in the tip displacement was measured and considered in the image processing process.

5.7. Image processing

Once the 1D image of the light transmitted by the cantilevered fiber under excitation was obtained, the next step consisted of the rotation of the assembly to get a 2D image from it. Since all the samples at this stage were made using a Single Mode Fiber, the reflected light was captured using the photodetector and external optical setup. The calibration target was considered as the reflecting surface. 2D imaging was obtained using our 1D fiber scanner by scanning a laser spot over a rotating object and interpolating the reflected light to reconstruct an image.

5.7.1. Imaging Setup

Light from the fiber cantilever was projected onto the object to be imaged by an objective lens ($f=16.5\text{mm}$) and scan lens ($f=150\text{mm}$) as shown in Figure 5.14 [24]. Back reflected light from the object was collected by the scan lens and refocused by a tube lens ($f=150\text{mm}$) on a photo detector (PDA100A2, Thorlabs). The experimental setup showing optical components is reported in Figure 5.15a along with the ray diagram (Figure 5.15b).

Light from the fiber was collimated as it passed through the objective lens. Half of the light was focused on the object by the scan lens after passing through a 50/50 beam splitter. The light reflected from the object passed back through the scan lens and was projected on the photo detector. The output of the detector was connected to a DAQ board (USB X Series 6341, National Instruments). The DAQ board collected the analog intensity data from the photodetector to be processed into the scanned image.

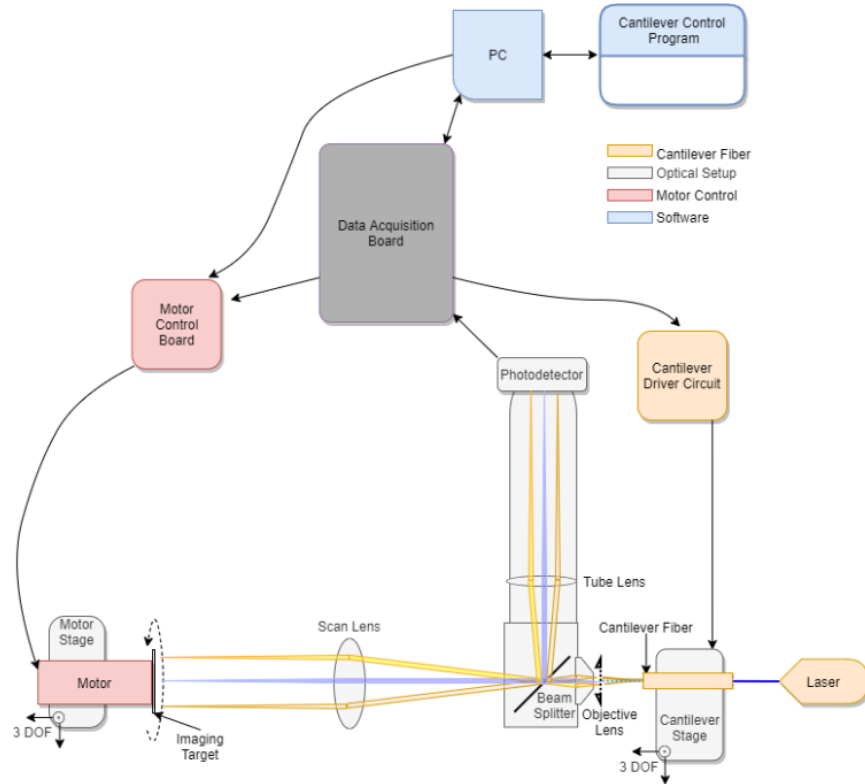


Figure 5.14. Schematic diagram of the complete testing setup [24].

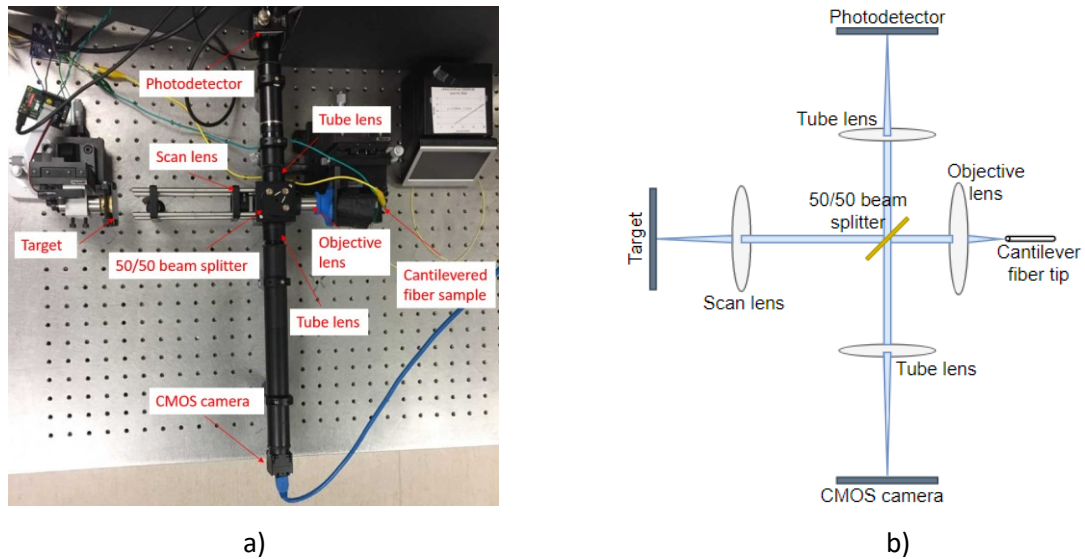


Figure 5.15. Optical design: a) experimental setup; b) ray diagram.

5.7.2. Image Acquisition

A polar scanning geometry was used to create a two-dimensional image. The cantilever scanned across the object to be imaged (fast axis of the scan) while the object rotated (slow axis of the scan). The frequency of rotation can be increased for higher frame rate or decreased for better resolution. For example, a fiber with a diameter of $12\mu\text{m}$ and length of about 2mm (having a resonant frequency of 2.5 kHz) at 30 frames per second will have ~ 166 fast-axis scans per frame. At half the frame rate twice as many fast-axis scans occur.

A schematic diagram of the imaging setup is shown in Figure 5.14. A variable frequency resolution target (Variable Frequency Target 5-200 lp/mm, Edmund Optics) was used as the object to be imaged. The resolution target was attached to the shaft of a stepper motor using a 3D-printed holder. The motor carrying the resolution target was mounted on a three degrees-of-freedom stage, allowing the alignment of the center of the rotating target with the incoming light beam.

The DAQ board was programmed to provide the timing signals for the system. The same computer program also interpolated the sampled data and displayed images in real time. The cantilever resonant frequency, duty cycle, cantilever tip phase offset, number of samples per line, and the number of lines per rotation were configured through the program. The DAQmx board generated the timing signals required for the cantilever drive

circuit and the motor. Rotation of the motor was synchronized with the cantilever. The light intensity was sampled by an analog-to-digital convertor. The line timing is illustrated in Figure 5.16 [24].

The Cantilever Drive signal was generated by the DAQmx board using the resonant frequency of the cantilever and a desired duty cycle. Digitization of scanline intensity was triggered by the Cantilever Sync signal which was delayed in time from the rising edge of Cantilever Drive to account for the phase shift (ψ_{offset}) between the drive waveform and the actual cantilever tip position. The scanline intensity was sampled by the Sample Clock signal.

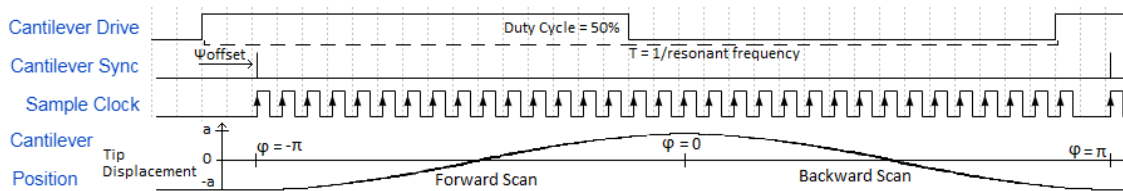


Figure 5.16. Timing diagram for image acquisition [24].

5.7.3. Interpolation

We assumed the cantilever tip followed a sinusoidal pattern in time so that the tip displacement in spatial coordinates (x, y) can be modeled as an ellipse with major axis $2a$ and minor axis $2b$. As illustrated in Figure 5.17 [24], the cantilever tip traced out one complete elliptical cycle as $-\pi < \varphi \leq \pi$.

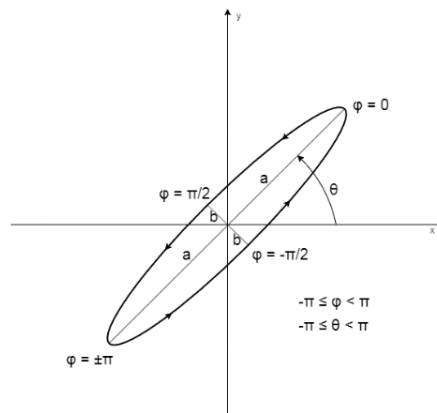


Figure 5.17. Rotating ellipse representing the cantilever's tip displacement [24].

Consequently, the tip position (x, y) of a cantilever rotated through an angle θ can be represented as the product of a rotation matrix and a position matrix parameterized by φ ,

$$\begin{bmatrix} x \\ y \end{bmatrix} = \begin{bmatrix} \cos \theta & -\sin \theta \\ \sin \theta & \cos \theta \end{bmatrix} \begin{bmatrix} a \cos \varphi \\ b \sin \varphi \end{bmatrix} \quad \begin{array}{l} -\pi \leq \varphi < \pi \\ -\pi \leq \theta < \pi \end{array} \quad (2)$$

Equation 2 can therefore be used to describe cantilever tip position (x, y) as the cantilever scans (elliptically) in the radial direction $(-\pi < \varphi \leq \pi)$ and the object being imaged (or the scanner assembly) rotates in the azimuthal direction $(-\pi < \theta \leq \pi)$.

The image intensity is sampled uniformly in (φ, θ) space and must be interpolated for uniform sampling in (x, y) space. In general, inverting Equation 2 and solving for (φ, θ) in terms of (x, y) provides 4 solutions. One solution is:

$$\begin{aligned} \theta &= \arctan \frac{bx\sqrt{a^2 - r^2} - ay\sqrt{-b^2 + r^2}}{-by\sqrt{a^2 - r^2} - ax\sqrt{-b^2 + r^2}} \\ \varphi &= \arctan \sqrt{-\frac{a^2 - r^2}{b^2 - r^2}} \end{aligned} \quad (3)$$

where we have defined $r^2 = x^2 + y^2$. This solution corresponds to a radial forward scan and includes sample points such that $-\pi \leq \varphi < -\frac{\pi}{2}$ and $-\pi \leq \theta < \pi$, illustrated in Figure 5.18 by the red arm of the ellipse [24]. The other three solutions correspond to the other half of the forward scan and the backward scan. When the cantilever scan is linear ($b = 0$), Equation 3 simplifies to $\theta = \tan^{-1} \frac{y}{x}$ and $\varphi = \cos^{-1} \frac{r}{a}$.

An M-by-N pixel interpolation table is constructed, where $m = 0, 1, \dots, M - 1$, $n = 0, 1, \dots, N - 1$, M is the width of the image, and N is the height. Discrete pixel (m, n) is related to continuous position (x, y) using:

$$x = a \left(\frac{2m}{M} - 1 \right) \quad y = a \left(\frac{2n}{N} - 1 \right) \quad (4)$$

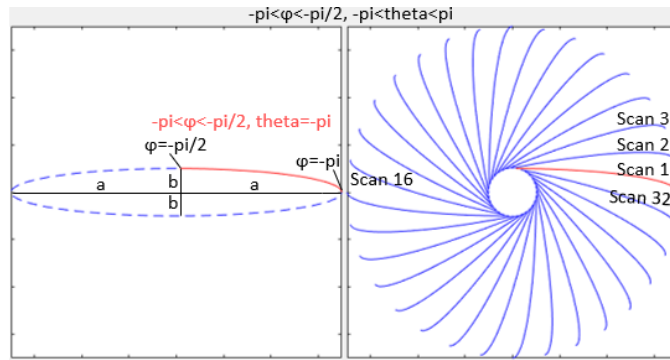


Figure 5.18. Quarter of ellipse traced in time [24].

The (φ, θ) elements for the interpolation table are then calculated using Equations 3 and 4.

The resolution target is shown in Figure 5.19 [24]. An image of the resolution target acquired with the cantilever fiber placed perpendicularly to the brass foil bridge is shown in Figures 5.20 [24], and 5.21 [24]. As discussed earlier, the cantilever tip traced an elliptical scan and the 2D scan was obtained by rotating the elliptical pattern, which led to no image data being available in its center (within a circle of radius b , seen as a black circle in Figure 5.20 and white circle in Figure 5.21). The imaged section of the resolution target shown in Figure 5.20 corresponds to a 25lp/mm area. Figure 5.21 shows the lines pattern and the numbers written in the nearby space corresponding to 30lp/mm features. This means that the smallest resolvable line feature had a width of $16.67\mu\text{m}$. Due to the higher density of data points near the center, the image was much sharper in that area.

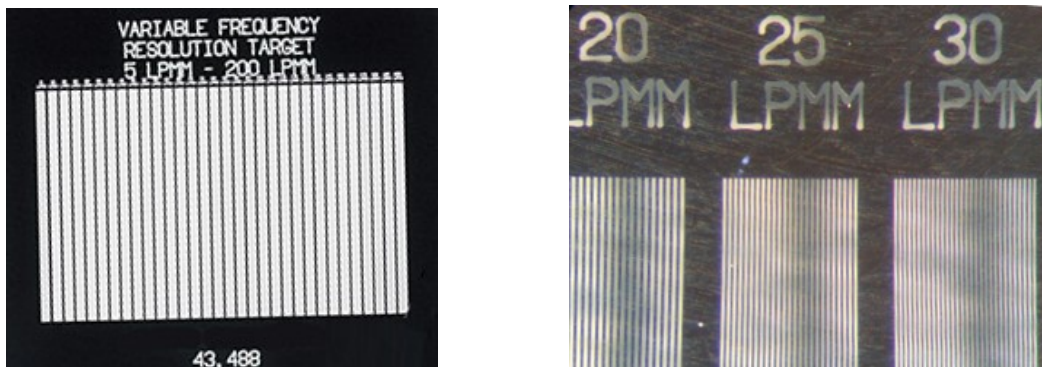


Figure 5.19. Resolution target used as imaging object [24].



Figure 5.20. Reconstructed image of the resolution target corresponding to 25lp/mm [24].



Figure 5.21. Acquired image of the resolution target at 30lp/mm [24].

5.8. Summary

The performance of the bench top models of the proposed submillimeter sized imaging scanner have been analyzed proving the desired performance of the device. The experimental results show the promising performance of the proposed optical scanner. The peak tip displacement of the cantilevered fiber increased linearly with the current supplied to the actuator and showed an elliptical shaped pattern due to the whirling effect at higher power. The ellipticity and the voltage at which it became prominent depended

highly on the sample. Some samples showed the ellipse pattern at about 10V while others showed a near-linear pattern even at 22V. The ellipticity was reduced by offsetting the actuation frequency from resonant frequency, or lowering power, but the overall displacement of the scanning fiber decreased as well. Duty cycle also affected the performance of the sample. A smaller duty cycle allowed more time for heat dissipation. For a given average power, it meant that more power can be used in the shorter on phase, causing greater tip displacement. However, the high peak temperature reached with small duty cycles led to damage to the bridge and the sample itself. A 6% duty cycle was used for testing the samples as it permitted the desired tip displacement without damaging the sample.

There were some variations among the samples during their fabrication processes. As stated earlier, these differences caused the resonant frequency and performance of the sample to be different. The fabrication process can be optimized to produce the similar sample. Etching permitted the batch fabrication of the cantilevered fibers. Thus, similar fibers can be generated by etching many fibers at the same time. Moreover, the fiber position with respect to the actuator can be controlled by using step shoulders.

Current samples were mounted on glass slides for ease of handling, which limited direct rotation to get 2D images from 1D actuation. In future samples, the glass slide will be omitted. This will permit rotation of the cantilevered assembly instead of the image target. In that case, the current scanner can be potentially used as endoscopic catheter having sub-millimeter dimensions. The image obtained from the device is highly affected by optical parts used for imaging. For endoscopic purposes, the currently used lens system will be replaced by a much smaller grin lens. The optical fiber itself will then be replaced by a double clad fiber (DCF) where reflected light will be captured by its inner cladding. The reflected light signal will be separated from the core signal using a Double Clad Fiber Coupler (DCFC) before reaching the detector for processing.

The elliptical shape of the fiber tip's motion meant there was no data available from the central image area. This area can be reduced by exciting the fiber at lower frequencies. The reconstructed images showed a small distortion at the bottom. The reconstruction algorithm can be slightly updated by recalibrating it to avoid such distortions and make the images clearer and sharper.

Chapter 6.

Fabrication of a stepped optical fiber with minimum power leakage

6.1. Disclosure

The material presented in this chapter is extracted, reproduced, and modified with permission from the papers listed below which I have co-authored. Eventual modifications may have been introduced for a variety of reasons including clarifying the subject; providing additional information; and ensuring the formatting is consistent with the rest of the thesis.

- Kaur M., Hohert G., Lane P. M., Menon C. Fabrication of a stepped optical fiber tip for miniaturized scanners. *Optical Fiber Technology*, 2021; 61, pp. 102436:1-8.

6.2. Introduction

The optical fibers used in the vibrating cantilever were fabricated using the heating and pulling method as described in Chapter 3. However, as will be described in the next section, there was some light leaking at the spliced area or a cleaved end. This chapter discusses some of the techniques used to minimize this light leakage.

This chapter is directed towards the OBJECTIVE 3 of the thesis: “Fabrication of cantilevered fiber with minimum power leakage”.

6.3. Problem Overview

As stated earlier, various small sized optical scanning probes have been recently developed by vibrating the distal tip of a single mode optical fiber at resonance using an actuator placed a few millimeters away from the free end [231, 149, 198, 184, 115, 153, 137]. The vibrating fiber shines light on the target sample, and the reflected light signal is captured by a charged-coupled device (CCD)/complementary metal oxide semiconductor (CMOS) camera using an optical lens system [137], or external optical fibers placed at the

periphery of the central vibrating fiber [231, 17]. Analogous to the latter method, it is possible to miniaturize an optical scanning device by using a double clad fiber (DCF) where the central core of the fiber is used to shine the light on the target sample and the backscattered reflected light is collected through the inner cladding of the fiber, which is then used to reconstruct the image of the scanned object [232, 163]. The scan area is dictated by the tip displacement of the distal end of the fiber, and the natural frequency of a cantilevered fiber can be increased by reducing the diameter of the vibrating portion to make it compatible with the driving frequency offered by micro-actuators [24].

As seen previously in the proposed design, the distal end of the DCF was reduced in diameter and was vibrated at resonance. The purpose of diameter reduction was to get adequate resonant frequency as discussed in the previous chapters. Moreover, it was also mentioned in chapter 4 that the central core of the DCF was used to transmit and shine light on the target surface while the inner cladding was used to capture the backscattered reflected light. Consequently, the fabrication of such a small sized cantilever requires that the distal end of the inner cladding surface be perpendicular to the illumination path to capture the maximum amount of the incoming light.

The heating and pulling method is a commonly used technique to reduce the diameter of an optical fiber. In this process, a large amount of heat, generated by a flame, electric arc, or a high-power laser, is applied to the fiber to locally increase the temperature until it reaches its glass transition temperature. At the same time, the fiber is pulled axially to reduce the section. The tapered fiber generated with this method conserves its geometrical aspect, as the core and cladding are both reduced in dimension at the same rate [233]. However, this technique leads to a longer tapered area and cannot be directly used as the reflected light will be reflected back from the tapered area.

This technique was modified by adding some more steps to get the stepped transition area in correspondence with reduction of cross section. The process was described in detail in Chapter 4 and is summarized below.

6.3.1. Fabrication of a cantilevered section using the heating and pulling method

In the heating and pulling method, the reduction in the cross section of an optical fiber is performed by heating the fiber and pulling it apart at the same time. The schematic

diagram showing an overall fabrication process for the cantilevered tip of the fiber is illustrated in Figure 6.1 [229]. First, the plastic protective jackets on the fibers were stripped away. A 125 μm Multi-Mode Fiber (MMF) with 105 μm core (MM-S105/125-22A, Nufern) was tapered down to a 12 μm outer diameter to obtain a core diameter of about 10 μm (assuming the ratio between the outer diameter and the core diameter remains same after tapering process), which closely matched the core size of a DCF fiber (outer diameter of 125 μm , and core of 9 μm). The schematic of this step is shown in Figure 6.1a. Fiber tapering was achieved by heating the fiber to its glass transition temperature ($\sim 2000^\circ\text{C}$), then pulling one end at a velocity of ~ 1.00 mm/s, performed automatically by a Vytran glass processing station (GPX-3000, ThorLabs). The filament power (36.0W), delay (2.00s), and pulling velocity (1.00mm/s) provided a precise tension profile, generating the desired diameter for the tapered section.

The tapered fiber was then cleaved off with a precision diamond blade scribe providing a quasi-flat and perpendicular glass end face, as in Figure 6.1b. The tapered fiber was then aligned with the DCF core by connecting the proximal end of the DCF to a laser and monitoring the maximum relative power transmitted through the aligned fiber cores, as schematized in Figure 6.1c. Usually, the maximum transmitted light varied from 60% to 90% of the incoming light, depending on fabrication imperfections. The fibers were then spliced using a two-step splicing method aligning their cores. In the first step, the fiber tips were slightly melted and connected with a hot push of 8.0 μm and 47.0W of filament power for 2.00 seconds. Secondly, more power was applied to strengthen the connection optically and mechanically by applying a filament power of 50.0W with no hot push. The spliced MMF was then cleaved off at the desired length (2.00mm in our case) from the spliced region (Figure 6.1d). The two-step splicing process allowed a firm connection minimizing distortion at the splice joint.

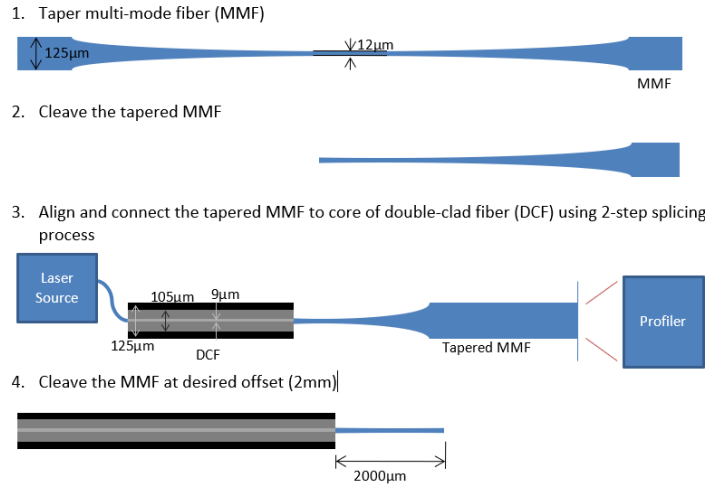


Figure 6.1. Schematic of fabrication process of the cantilever fiber using the heating and pulling method [229].

6.3.2. Cleavage at the distal end

Cleavage is the last step performed in the cantilever fabrication method discussed above. It was performed by applying tension in the fiber and creating a fracture in it using a diamond knife shaped tool. The cleavage did not provide a perfect plane cut surface at the distal end of the cantilevered beam. Thus, the light coming out from the fiber tip did not follow a Gaussian kind distribution of emitted light and was hard to focus on the target features. In addition, the corresponding image formed by it had a bad contrast. Thus, to overcome these effects, the distal end of the fiber was slightly melted. The scope of this process was to create a lens like structure at the tip of the fiber so that the emitted light will follow a Gaussian shaped profile. Figure 6.2 shows the distal end of the cantilevered fiber before and after micro-balling process. The plot of the intensity of light exiting the cantilever tip is reported in Figure 6.3 showing the approximate Gaussian profile of the light intensity in two directions.

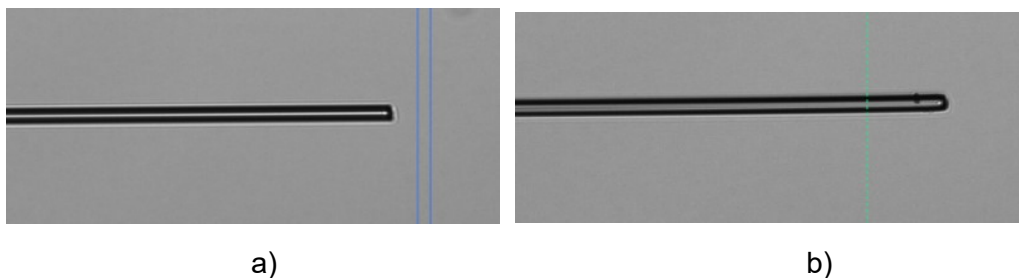


Figure 6.2. The distal end of the cantilevered fiber: a) before process; b) after processing.

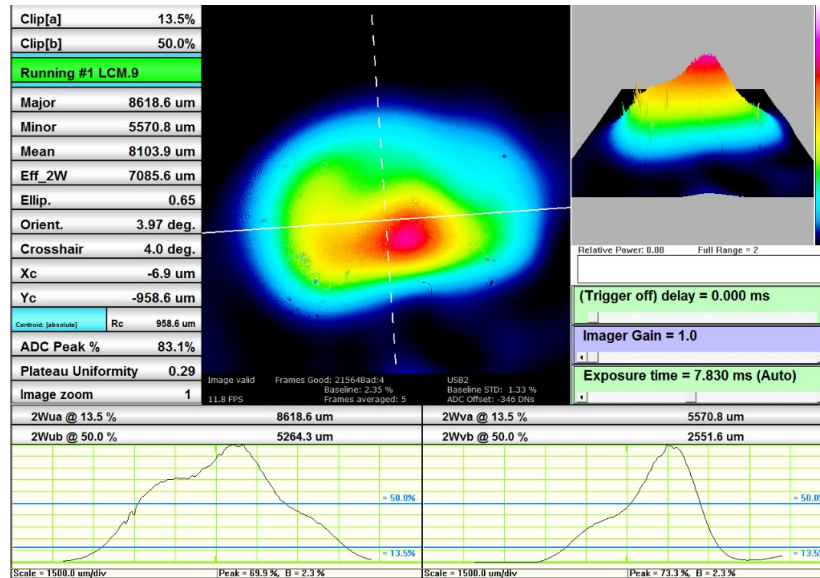


Figure 6.3. The beam of light intensity from the micro-balled tip of the cantilever.

6.3.3. Power Leakage

One of the flaws in this fabrication process for the cantilevered fiber which causes reduction of image contrast was in the joint between larger portion of fiber representing the fixed end (125 μm) and the cantilevered portion (12.5 μm). The cores of the fibers were attempted to be aligned and then heated and pushed together in the two-step splice process. During this operation, it was hard to keep the perfectly aligned connection. Hence, in the cantilevered fiber samples, the light transmitted to the cantilever end, in the best case, was only about one third of the light intensity coming from the laser. Thus, about two third of the light was leaked through the spliced area. A large amount of light intensity should be provided to the proximal end of the fiber to shine on the desired tissue surface. When the light coming from the cantilever tip was focused on the target, this leaked light caused a blur in the image and reduced its contrast. As a very small amount of the light was transmitted through the distal end, a large amount of laser light that was leaking, was emitted to tissue. The light leakage at the interface area is clearly seen in Figure 6.4. Thus, a higher light intensity was required to illuminate the target, and the leaked light added to the background noise in the target sample.

In the final design, the reflected light was supposed to be collected from the inner clad of the fiber, and the leaked light acted as a noise signal. Thus, it was problematic in

that case as the signal representing the reflected light signal was very weak with respect to this leaked light and would be hard to separate between them.

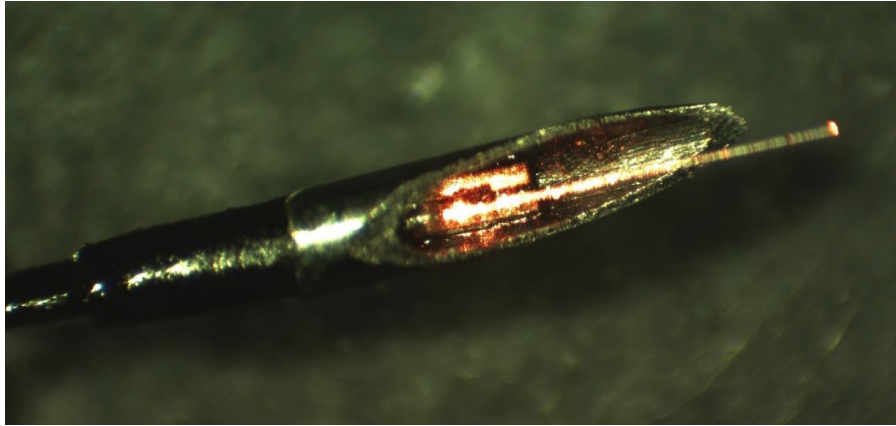


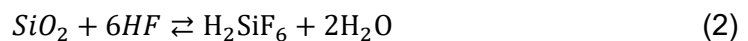
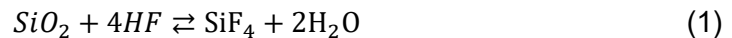
Figure 6.4. Light leaking at the spliced region.

It is reported in the literature that the reheating of the silica fibers leads to the reduction in strength of the fibers by adhesion of solid particles to the fiber's surface causing residual stresses in the spliced area [234, 235]. In the Vytran splicing setup used in this study, a high-purity Argon gas flowed over the fibers during fusion step to enable a clean spliced region without degrading the mechanical strength of the joint [236].

6.4. Chemical Etching

Another alternative way to reduce the cross section of a glass fiber is through the use of chemical etching using hydrofluoric acid (HF) solution. Commonly this method is used for tapering the glass fiber to generate nanometric scale tips permitting to visualize and monitor cell surfaces or used in nanoscopic sensors or photonic micro-devices [237, 238].

In the chemical etching method, the fiber was submerged in an etchant solution until it reached the desired dimensions. The geometrical aspect of the fiber was changed by dissolving only the outer cladding surface. The reaction between HF and the fiber surface is characterized by one of the following reactions (1) or (2).



The first reaction is dominant in diluted HF solutions, while the second one prevails in concentrated etchant solutions [239]. The surface etching reactions described above are a simplification of the actual reactions occurring in the solution. The chemistry behind the actual etching process is more broadly described in literature [240-244]. One of the key points of the glass dissolution chemistry is that the HF solution is dissociated into various species; among which HF and HF_2^- mainly control the surface etching [240, 245]. Both reactions are characterized by a negative reaction enthalpy. Thus, the etching reaction is a slightly exothermic reaction. For wet etching, a Buffered HF solution with a stabilized HF activity (Buffer HF Improved or Buffer Oxide Etchant) is often used due to the toxicity of HF. In most etchant solutions, ammonium fluoride (NH_4F) acts as a buffering agent and controls the pH of the solution maintaining the HF concentration described by the following reaction [246]:



Etching is highly dependent on the temperature and concentration of the etchant solution. A high temperature and/or concentration of the etchant leads to the rapid dissolution of the glass surface. Moreover, stirring or agitation of the etchant solution also enhances the reduction of the cross section by promoting diffusion of the reactant to the fiber surface and removal of by-products. The etching rate is approximately double with a 10°C increase in temperature at a given concentration of the solution [247]. However, high temperature, concentration, and presence of agitation in the etchant solution increases the evaporation rate of the solution making it hazardous to work with.

6.4.1. Fabrication of a cantilevered section using the chemical etching method

The buffered solution used in experiments was a mixture of NH_4F (40%) and HF (49%), combined in a volumetric ratio of 6:1. The solution had an HF concentration of 3.25M and a pH of ~ 4 [247]. The small concentration of HF solution caused the etching process to be slow as compared to the heating and pulling method, but it allowed the generation of a stepped fiber tip with the continuity of the fiber core in addition to the desired change in the cross section. Additionally, it was possible to fabricate multiple cantilevered fibers at the same time allowing batch fabrication. The buffered solution had a vapor pressure and boiling temperature like that of water enabling the use of an etchant solution in an open system with limited evaporation. Furthermore, the presence of a

floating plastic tray, as will be seen later, reduced the open surface by a considerable amount. Thus, the amount of etchant evaporated during the etching process was very small and did not have any impact on the process.

With chemical etching, a tapered region ($\sim 600\ \mu\text{m}$ axially) is often formed at the transition zone of the fiber. This tapering process occurs due to the capillary (meniscus) effect causing a slight rise of the HF solution with respect to the surface of the liquid along the optical fiber dipped in it. The HF that rises along the sidewalls of the fiber reduces its diameter, causing the tapered section [248]. Thus, the capillary effect can be blocked by preventing the presence of the etchant solution in contact with areas above the liquid interface of the dipped fibers. To accomplish this, a thin membrane of Ecoflex silicone rubber (Ecoflex 00-20, Smooth-On) was attached to a small plastic tray that floated on the surface of the HF. Small holes were drilled in the tray and the flexible membrane. The plastic protective coating on the fibers was stripped, and the fibers were passed through these holes, protruding $\sim 2\ \text{mm}$ into the HF solution. The flexible membrane closed the hole around the sidewalls of the fiber during the etching process, which prevented the solution from rising along the walls, and thus preventing the tapered region.

Figure 6.5 shows the schematic of the setup used for the etching process. The buffered HF solution was held in a plastic container carrying the floating plastic tray with the fibers. This setup was placed inside a container of water and was then placed on top of a hotplate, which guaranteed the uniform temperature of the solution during the etching process. Fibers were then taken out of the solution individually at specific time intervals and examined under the microscope to characterize their diameters [229].

As stated earlier, the etching process is greatly affected by the temperature of the etchant solution. To account for this variation, etching was repeated at different temperatures (from 23°C to 35°C) by heating the water and the etchant solution using a hotplate. The water temperature was measured at regular intervals with a thermometer. As stated earlier, the etching reaction was slightly exothermic, but due to the large amount of the etchant solution and water, the temperature change during the process was very small ($<1^\circ\text{C}$).

It is also possible to etch an optical fiber using an etchant solution in a vaporous state [238]. The overall etching reaction was the same as the one described earlier, with

the difference being that there was condensation of the etchant vapour on the fiber surface, followed by the etching reaction, and evaporation of the by-product [249].

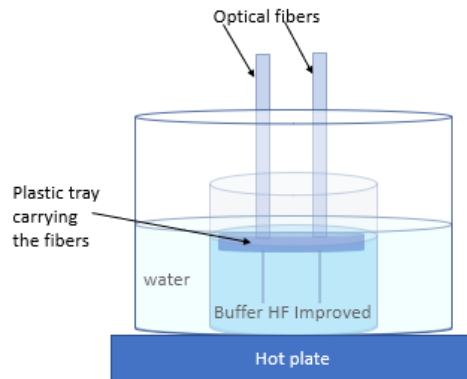


Figure 6.5. The schematic of the setup used for etching the optical fibers [229].

As described earlier, the buffered solution is characterized with a small vapor pressure. Thus, the vapors generated at room temperature will be available in a small amount. A high concentration HF (48%) solution was used to create the vapor etchant and was heated up to 35°C. The elevated temperature and high concentration of the etchant caused rapid vaporization, and a high etch rate. An Ecoflex membrane was attached to the bottom of the container's lid, and fibers were inserted in the HF vapor via holes in the lid and membrane. The schematic diagram of the test setup is shown in Figure 6.6 [229].

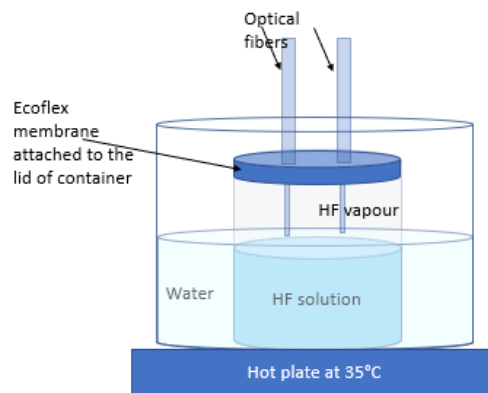


Figure 6.6. The setup used for etching optical fibers at vaporous state [229].

6.4.2. Simulation of wet chemical etching

The etching process can be analytically modeled as a diffusion-controlled or a reaction-controlled process based on the reaction rate. Usually, the etching reaction is

quite fast, and the process is controlled by the diffusion of the reactant species to the surface. The etchant flow impacts the process as well. Thus, convection needs to be considered in the calculations in the case where the etchant is not stationary. In our case, the etching process occurred in a stationary etchant solution, and no convection needed to be considered, which simplified the calculations.

The mathematical model describing the etching process can be either formulated using a moving grid approach [250, 251] where the moving boundary tracks the etching process by change in shape, or a fixed grid approach [252, 253]. In the latter case, the total concentration of the etchant solution given by the sum of reacted and unreacted portion is considered constant. The reacted concentration changes as the etching proceeds and allows for calculation of the etch front surface [254].

The governing equation describing the etching process is the mass diffusion equation described below:

$$\frac{\partial c}{\partial t} = D\nabla^2 c \quad (4)$$

where c is the concentration of HF solution, and D is the diffusion coefficient [238].

The velocity of the moving interface is given by:

$$v = -\frac{RM_{sub}}{m\rho_{sub}} \quad (5)$$

with R being the reaction rate at interface, M_{sub} , and ρ_{sub} being the molecular weight and the density of the optical fiber, respectively, and m is the stoichiometric reaction parameter from equations (1) or (2) [238].

The etching process at the interface of fiber-etchant solution was simulated in COMSOL Multiphysics ambient using a moving boundary approach. It was possible to model the etching process as a 2D case due to the axial symmetry of the geometry. A zoomed version of the model geometry showing the optical fiber in an etchant solution schematized in Figure 6.5 is shown in Figure 6.7. The etchant solution surface in contact with the plastic tray was modelled as a surface with zero normal displacement. The white portion in Figure 6.7 represents the section the fiber under the etching process and the etched surface was considered as the deforming boundary [229]. It was considered that

the concentration of the etchant solution was constant and equal to its initial value at the bottom surface of the etchant solution.

The diffusion of the etchant solution around the fiber interface was modelled using Transport of Diluted Species (chds) physics. In addition, the deformed geometry module described the moving geometry at the interface with velocity v . The diffusion coefficient for HF and HF_2^- is $3 \times 10^{-9} \text{ m}^2/\text{s}$ [255].

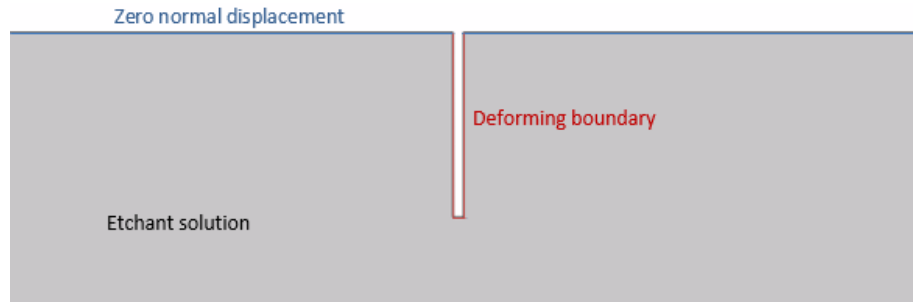


Figure 6.7. 2D geometry of wet etching assembly with the prescribed boundary conditions [229].

6.4.3. Results

In the chemical etching process, the fiber was dipped into a buffer etchant solution. In an open container, etchant solution rose along the fiber at the open interface surface due to capillary action and caused the tapering of the cross section as can be seen in Figure 6.8a. The tapered region created by the etching solution at ambient temperature was $\sim 600 \mu\text{m}$. The flat interface was generated using an Ecoflex membrane to prevent the rise of solution up the sides of the fiber. It provided a quasi-flat interface surface as can be seen in Figure 6.8b where the tapered region was less than $90 \mu\text{m}$ [229].

The wet etching process was evaluated at different temperatures within the 23°C - 35°C range. The simulation results at 23°C are compared with the experimental results in Figure 6.9 [229]. The etching process was repeated multiple times to evaluate the reproducibility of the process and check the variance of results. Some of test results performed at the same conditions are shown in Figure 6.9 as test 1 to test 4 and compared with theoretical simulation results showing the compatibility between the results.

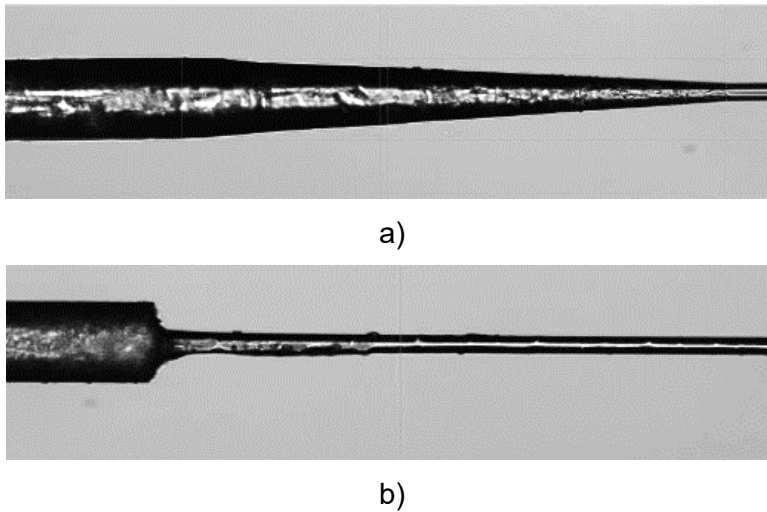


Figure 6.8. The cross section of the fiber after etching in: a) an open surface; b) presence of an Ecoflex membrane [229].

The etching of optical fibers was repeated at different temperatures within the prescribed range, and an etching curve like Figure 6.9 was obtained in each case. The trend of each curve defining the fiber diameter in time represents its etching rate and is recorded as a point in Figure 6.10, which described the etching rate as a function of temperature. As the temperature of the etchant solution increased, the etching rate continued to increase with a parabolic trend as can be seen in Figure 6.10 [229]. The etched fiber obtained with this method as shown in Figure 6.11a, had a quasi-smooth and linear surface.

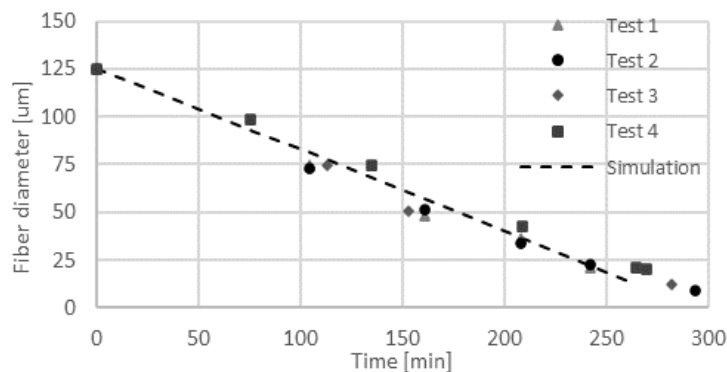


Figure 6.9. Fiber diameter in time during etching at 23°C [229].

In the case of fiber etching using HF in a vapor state, the concentration of the vapor decreased as the distance from the liquid surface increased. Thus, the fiber was etched more towards the free end, and the fiber was semi-linearly tapered as shown in Figure

6.11b. Thus, etching using a vaporous state did not yield the desired stepped structure and was not further investigated [229].

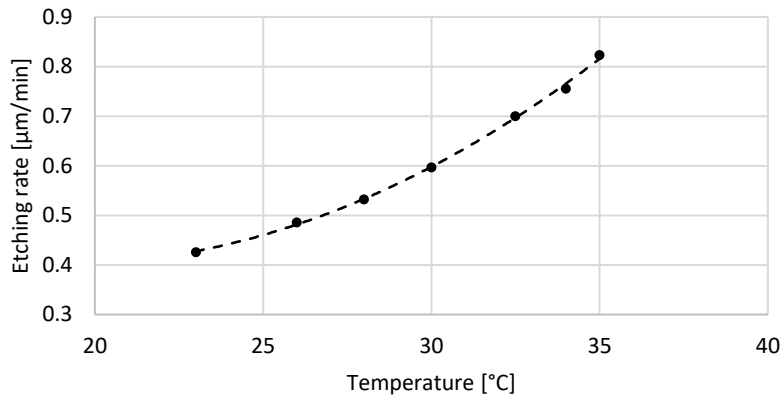


Figure 6.10. Etching rate in function of water temperature [229].

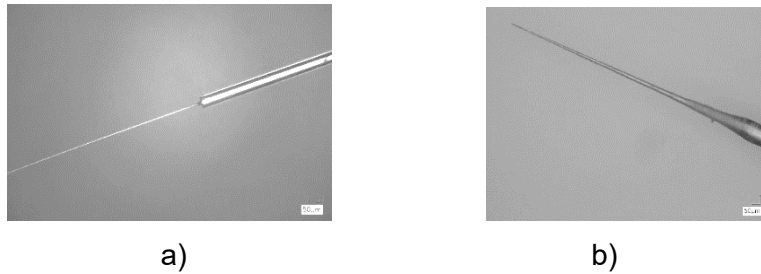


Figure 6.11. Etched fibers: (a) using liquid HF solution; (b) using HF vapor [229].

6.5. Alternative methods

Other possible methods to create the microstructures in the glass surface are the use of laser micromachining [256], and focused ion beam (FIB) [257].

In case of the laser micromachining, a material is cut down by locally heating the material using the high intensity laser beam. The glass fibers are characterized by having a high thermal conductivity, so a high amount of the heat created by the laser beams is required to create a cut using the laser micromachining device. Moreover, the fiber should be spinning during the cutting process to reduce the dimensions of the fiber along the radius. The FIB technique uses focused beam of ions (often gallium) to locally mill or sputter the surface of a sample. During the cutting process, secondary electrons are produced which are used to reconstruct the scanning electron microscope (SEM) image. In both cases, a very small amount of the material is removed in one pass. Thus, the

process requires a long processing time, and higher costs to create the desired shape pattern for the cantilever surface.

6.6. Conclusion

The fabrication processes to make micrometer sized double clad fiber tips with a step reduction of the cross section using the heating-pulling and the chemical etching methods are shown in this chapter. Such fibers can be used as a resonant scanner by fixing the larger section and exciting the thin section of the fiber with a micro-actuator. In the first fabrication process, an MMF was tapered down and spliced to a DCF. In the second technique, a buffered etchant solution with stabilized HF activity was used to etch the fibers. To get a flat transition, a flexible membrane was attached on the bottom surface of a plastic tray holding the fibers. The flexibility of the membrane caused the continuous closure of the membrane around the fiber and prevented the formation of a meniscus that caused tapering in the fiber. Wet etching was performed using the etchant solution at vaporous and liquid states, with the latter one allowing the fabrication of smooth surfaced stepped fibers.

Some of the advantages of using chemical etching over the heating and pulling method are:

- Continuity of the core at the transition zone. Thus, the light coming from the laser is nearly 100% transmitted to the distal end of the fiber.
- No light leakage at the interface section causing less power needed to illuminate the target sample.
- Possibility of batch fabrication of the fiber samples, i.e., many fibers can be produced at the same time.
- The cantilever portion can be made as large as desired by dipping a large portion of the fiber inside the etching solution. However, in the heating and pulling method, the thin sections are limited to a length of a few millimeters due to mechanical resistance.
- Very thin section fibers can be fabricated as compared to the heating and pulling method.
- Consistency of geometry among the different samples.

Notwithstanding, HF is a volatile chemical to work with; although this drawback can be eliminated by using a less concentrated or buffered etching solution.

Moreover, in the case of the heating and pulling method, the properties of the fibers depended on the age of the heating element causing variability among the samples. In addition, depending on the fusion conditions, heating of an optical fiber can degrade its mechanical strength, while the etching using HF does not affect its strength.

To conclude, wet etching is preferred over the heating and pulling method to fabricate the micrometer sized stepped fiber tips with a flat interface surface, which can find use in sub-micrometer sized optical scanners and sensors.

Chapter 7.

Collection of reflected light

7.1. Disclosure

The material presented in this chapter is extracted, reproduced, and modified with permission from the papers listed below which I have co-authored. Eventual modifications may have been introduced for a variety of reasons including clarifying the subject; providing additional information; and ensuring the formatting is consistent with the rest of the thesis.

- Kaur M., Hohert G., Lane P. M., Menon C. Fabrication of a stepped optical fiber tip for miniaturized scanners. *Optical Fiber Technology*, 2021; 61, pp. 102436:1-8.

7.2. Introduction

Once different methods to fabricate the cantilevered fiber were explored, the next step consisted of the fabrication of the cantilevered fiber using an off-the-shelf available DCF fiber. At this step, an off-the-shelf available DCF (SM-9/105/125-20A, Coherent) was used. This fiber was characterized by having a 9 μm single mode core, and the first cladding has a diameter of 105 μm .

In this step, the cantilevered fiber samples were fabricated either using the Vytran splicer (used in objective 1 and 2), and HF etching (used in objective 3). The next step consisted of the collection of the reflected light from the inner cladding of the DCF fiber while shining the light through the inner core.

This chapter is aimed to fulfill the OBJECTIVE 4 of the thesis: "Collection of reflected light in DCF fiber cantilever, and measure signal to noise ratio (SNR)".

7.3. Method

The light collection efficiency of the cantilevered fibers fabricated following the methods described in Chapter 6 was characterized by transmitting light through the core

of the DCF towards a reflecting surface and collecting the reflected light through the inner cladding of the fiber. A double clad fiber coupler (DCFC) was used to separate the light transmitted through the core of the fiber and the reflected signal passing through the cladding.

In the testing the collection of light using the inner clad, first the light was shone through the fiber's core without hitting any target, and the background noise was measured. This noise was generated by the outside light, and the leaked/reflected light from the interface in correspondence with the transitional section of the cantilevered fiber. In the next step, the same process was repeated but in the presence of a reflecting surface.

The light reflected by the tissue surface is a diffuse reflection, i.e., the incident light is scattered back into many angles instead of just a particular direction and depends upon the incidence angle. If the light is hitting vertically on the tissue surface, the reflectance for epithelial layer and upper submucosa can be assumed to be 10% [258]. A sintered Teflon sheet can be used as a reflecting surface to quantify the amount of light backscattered from the tissue surfaces. In the preliminary design, a mirror was used as a reflecting target. The generic schematic design of the described process is shown in Figure 7.1. However, to focus the light at the interface surface an objective lens was added in the design described in detail in the next section. The SNR was calculated from the detected signal and the noise measurements.

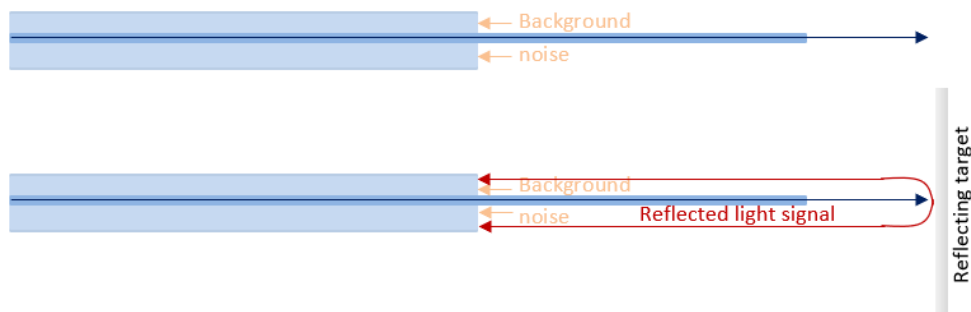


Figure 7.1. The schematic design of the test setup described.

7.4. Experimental setup

The light collection efficiency of a stepped DCF can be characterized by sending light through the core of the fiber and capturing the reflected light from a target surface in

front of the fiber. In the case of an irregular interface surface at the etched region, some of the incoming light will be further reflected or scattered away.

The schematic diagram of the setup used to quantify these light intensities is shown in Figure 7.2, where P0, P1, and P2 represent the laser power incident on the mirror, power backscattered from the transitional interface, and overall reflected light measured from the detector, respectively [229]. The experimental setup following the schematics is shown in Figure 7.3. There was no noise signal generated by the presence of ambient light. P0 was measured by placing the detector in the mirror position. The backscattered light from the transition zone was the power detected by an optical power meter, as in the setup of Figure 7.2, by blocking the light beam between the objective lens and mirror. Thus, the power reflected by the mirror, P3, can be calculated as:

$$\text{Power reflected by mirror (P3)} = P2 - P1 \quad (1)$$

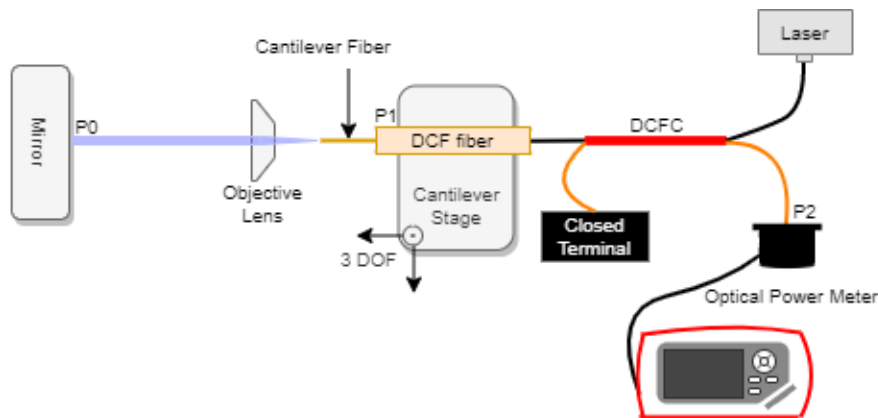


Figure 7.2. The schematic diagram for the capture of reflected light from a mirror [229].

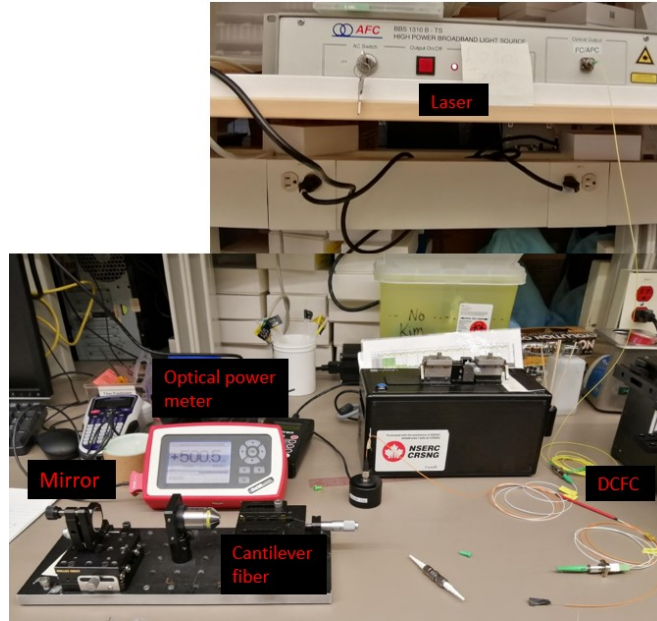


Figure 7.3. Experimental setup for light collection measurement.

A laser compatible with the used DCF ($\lambda=1310$ nm) was connected to the proximal end of the fiber with the help of a DCFC (DC1300LEFA, Thorlabs). The DCFC was designed to have the inner cladding of the DCF fused with a 200 μm core of a parallel MMF to siphon off power in the inner cladding towards the detector. The schematic diagram of the internal structure of a DCFC is shown in Figure 7.4 (taken with the permission of [259]). The light in the single mode core was transmitted with no loss, while the multimode transfer had a ratio of output (port B) to input (port S) signal of $\geq 60\%$ [259]. The optical diagram, illustrated in Figure 7.5, depicts the illumination and detection path of the light.

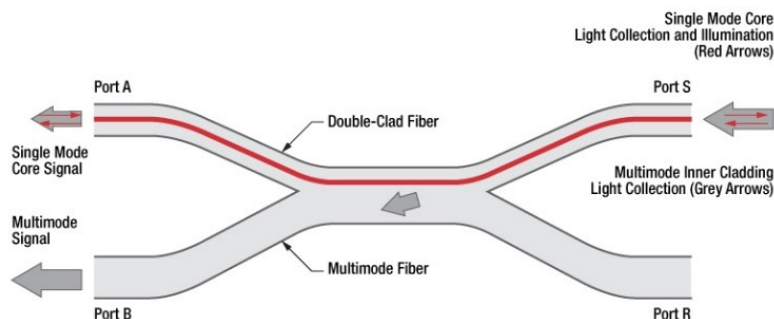


Figure 7.4. Schematic diagram of a DCFC (taken with the permission of [259] CC-BY license).

The objective lens was initially placed at the focal length (~16.5mm) away from the fiber tip and collimated the incoming light to the mirror surface. The transmitted and reflected light from the mirror surface followed the same path if the incident beam is perpendicular to the mirror. To direct the reflected light on the fiber cladding surface, the mirror was slightly tilted and the fiber tip was moved slightly offset from the focal length of the lens using 3D stage at a position where optical power meter showed a maximum reading of the reflected light.

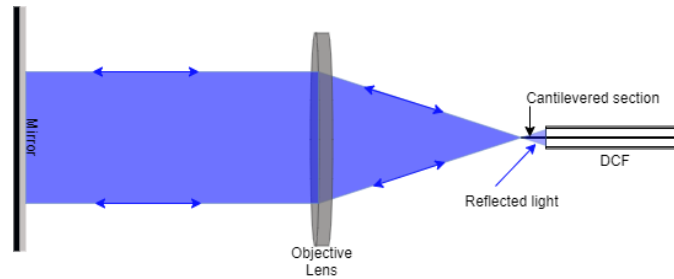


Figure 7.5. Optical diagram of the proposed light collection setup [229].

Thus, the efficiency of the DCF system is defined as:

$$\eta = \frac{P_2 - P_1}{P_0} \quad (2)$$

Due to the flat or irregular interface surface, some of the light was back reflected at the interface region. Back reflection, or optical return, is an undesirable effect in the fibers and is characterized by the contrast between the amount of light reflected by the mirror (P_3) and the back-reflected light measured by blocking the light towards the mirror (P_1):

$$\text{Contrast} = \frac{P_3}{P_1} \quad (3)$$

7.5. Results

The amount of light intensity collected by the cladding of cantilevered fiber samples is considered following the schematic of Figure 7.5 [229]. In the case of a cleaved DCF with no cantilevered portion, the light incoming from the core of the DCF was 12.35 mW, while the measured reflected light was 7.41 mW, and the optical return was 72.1 μ W. Thus, the efficiency (η) was ~59.33%, while the contrast was 101.78.

In the case of the spliced fiber, the light incoming from the laser was 3.425mW, but there was some power leakage at the spliced region due to imperfect alignment of the cores. The light intensity at the fiber tip was much smaller and varied among the samples depending on the light transmission at the transient section. The parameters characterizing the collection of reflected light for three different cantilevered fibers are reported in Table 7.1 [229].

Table 7.1. Light transmission properties through the fibers fabricated using the heating and pulling method [229].

Sample number	Transmission in spliced section	Light intensity at fiber tip (P0)	Measured reflected light (P2)	Optical return (P1)	η	Contrast
1	86.26%	2.96mW	0.154mW	0.007mW	4.95%	20.68
2	64.82%	2.22mW	0.213mW	0.031mW	8.21%	5.96
3	89.17%	3.05mW	0.148mW	0.007mW	4.64%	21.49

Similar data obtained for the chemically etched fibers is summarized in Table 7.2 [229]. In this case, no light leakage occurred in the transition zone due to etching of just the cladding surface. Thus, the light intensity at the fiber tip was much higher compared to the heating and pulling method.

Table 7.2. Light transmission properties through the fibers fabricated using the etching method [229].

Sample number	Light Intensity at fiber tip (P0)	Measured reflected light (P2)	Optical return (P1)	η	Contrast
1	11.58mW	1.252mW	0.243mW	8.71%	4.15
2	11.58mW	0.463mW	0.034mW	3.70%	12.67
3	11.58mW	1.882mW	0.041mW	15.89%	44.45

From the measured data, it can be summarized that the efficiency and the contrast of the samples were highly variable among the samples fabricated using both methods. In the case of the heating and pulling method, it was mainly a function of the filament power, the alignment of the DCF fiber, and the taper of the MMF fiber.

In chemically etched fibers, the flatness at the interface surface was highly dependent on the straightness of the fiber in the plastic tray. The variability among the samples was avoided by placing the fibers perpendicular to the etchant surface, which also resulted in a nice flat stepped interface.

7.6. Discussion

From the light collection efficiency values shown in the tables of the previous section, it can be seen that a very small fraction (<20%) of the reflected light was captured by the inner cladding of the DCF. These values were obtained using the mirror as a reflecting object which had a 100% reflectance. However, as mentioned above, the actual tissue surfaces (the final imaging target of the device) had a very small reflectance. Thus, the actual efficiency of the system to collect the backscattered reflected light from the tissue surface will be even much smaller.

Moreover, tissue surfaces are characterized by having a diffuse reflectance compared to the specular reflectance of the mirror surface. This allows the reflected light to hit the interface surface in a direction not perfectly perpendicular to the interface surface. The light hitting from the different angles can be back reflected from the interface region thereby reducing the amount of light reaching the detector surface through the inner cladding. Thus, the SNR in the actual working conditions will be very poor (<1%).

As stated in chapter 4, the actual proposed design required miniature optical components compatible with the imaging probe design. One of the possible options makes use of a GRIN lens at its distal end of the device to collimate the light exiting the catheter on the target sample since the diameter of a GRIN lens can be reduced to as small as few hundred micrometers. The next steps encompassed the use of an off-the-shelf available GRIN lens and measurement of the light intensity and SNR in the presence of such a lens.

7.7. Simulation of light collection using Zemax

The simulation of the optical system at the distal end of the catheter system was performed using Zemax software. Some off-the-shelf GRIN lenses compatible with the device dimensions were considered. A 350 μm diameter GRIN lens from GRIN Tech (GT-IFRL-035-005-50-570) was used as objective lens. It is an imaging focusing rod lens

having a diameter of 350 μm , and lens length of 790 μm . The numerical aperture (NA) of such a lens is 0.5, and it carries a coating compatible with a working wavelength of 570 nm. Another similar lens was used at the fiber tip is a 500 μm diameter GRIN lens from GRIN Tech (GT-IFRL-050-005-50-570) which has a lens length of 1.19 mm, and NA and coating like the other lens.

The optical design of the illumination path using such lenses is shown in Figure 7.6. The different coloured rays show the fan of rays when the cantilever's tip is at center, and when it is displaced by 50 μm and 100 μm . A grin lens GT-IFRL-035-005-50-570 (described above) characterized by an object plane working distance (the distance between the object plane and the lens surface facing towards the object) of 55 μm , and the image working distance (the distance between the other surface of the lens and the plane where the light is focused) of 1.25 mm provided a FOV of about 38 degrees for the vibrating tip displacement of ± 100 μm . On the other hand, GT-IFRL-050-005-50-570 had the same image working distance of 1.25 mm required an object working distance of 120 μm . For a similar tip displacement of ± 100 μm , it provided a FOV of about 26 degrees. Since the first lens (GT-IFRL-035-005-50-570) permitted the device to generate a high FOV, it was used for further analyses performed below.

In the case of a hypothetical surface where the rays of light are retro-reflected from a tissue-like surface with diffuse scattering properties, the incoming rays from the surface will follow the optical path shown in Figure 7.7 where they are collected through the inner cladding of DCF. To evaluate the reflected light from mirror surface, and collected through the inner cladding of the DCF, a detector surface having a diameter of 105 μm was placed 2 mm away from the illumination point. The complete ray fan diagram showing the tip displacement of ± 100 μm with a detector surface is reported in Figure 7.8. In this case of a perfect reflecting surface, the light collected by the detector can be approximated considering the uniform light distribution at light collection surface. The light collection efficiency was approximately equal to the ratio of detector surface area (area in correspondence of cladding surface – area of the cantilever section) compared to the overall area of the light cone at that plane, which was about 0.6% of the incident light at image plane.

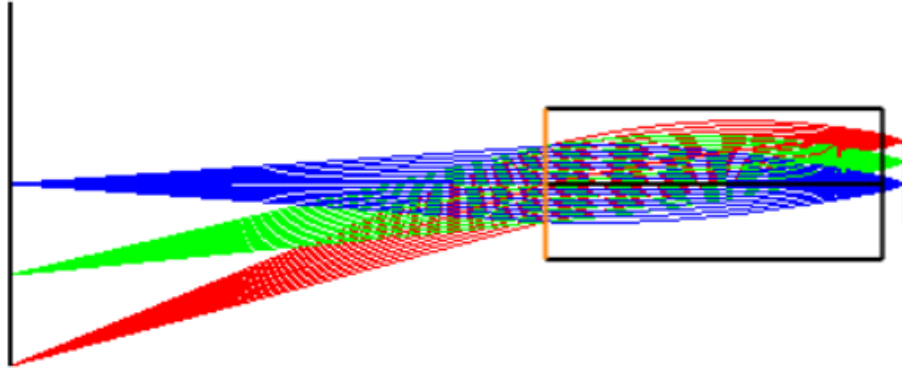


Figure 7.6. Illumination path of proposed optical system.

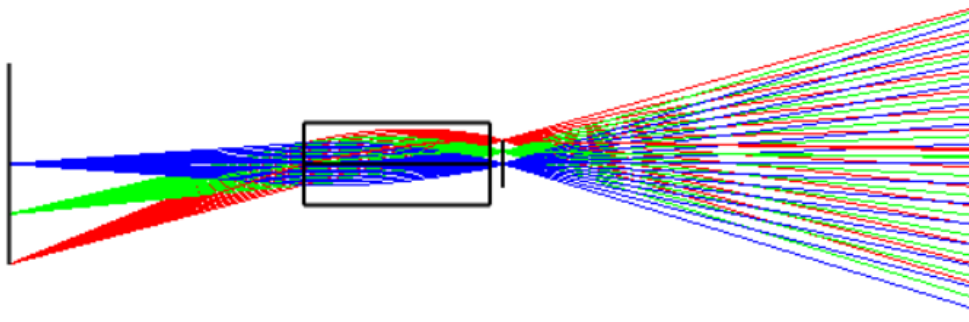


Figure 7.7. Detection path of proposed optical system.

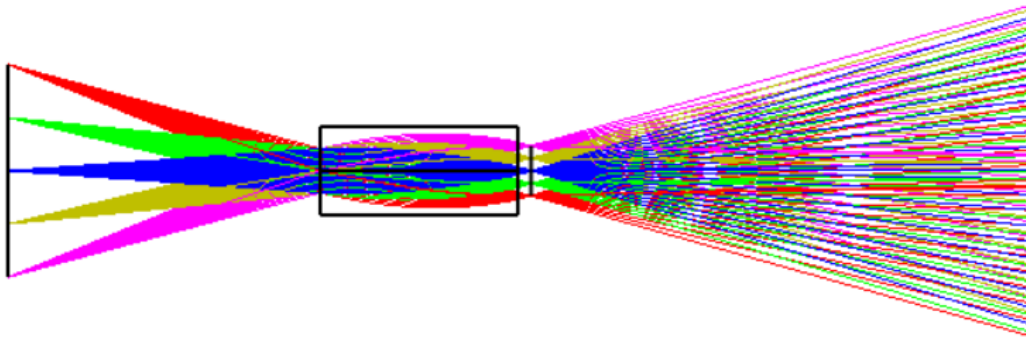


Figure 7.8. Complete ray fan diagram for tip displacement of $\pm 100 \mu\text{m}$.

However, as stated previously, a tissue surface reflects the light diffusively, and the reflectance is about 10% or less. Thus, to consider the tissue reflectance in the Zemax model, the non-sequential simulation was performed.

First, the cantilever portion's bending angle was calculated at the displacement of $\pm 100 \mu\text{m}$. Given the nominal length of the cantilever portion to be 2 mm, and the distal end displacement of $\pm 100 \mu\text{m}$, the bending angle was calculated to be $\pm 2.86^\circ$.

The tissue surface is made up of many skin layers. Since the primary goal of this simulation was to evaluate the amount of light reflected back from the tissue surface and not scattered by the tissue, only a single layer of the tissue system was analyzed. Specifically, living epidermis layer is modeled in this analysis [260]. Henyey-Greenstein distribution function is often used to simulate the light scattering in a biological tissue media. The primary factor controlling the scattering in the model is anisotropy factor, g . The angular distribution of light scattering according to this model is given by:

$$p(\theta) = \frac{1}{4\pi} \frac{1-g^2}{(1+g^2-2g \cos\theta)^{3/2}} \quad (4)$$

This model is included in the non-sequential mode of the Zemax OpticStudio, and the input parameters required for this model are Mean Path, Transmission factor, and anisotropy factor. Mean path and Transmission factors are related to tissue absorption coefficient (μ_a) and scattering coefficient (μ_s) by [261]:

$$\text{Mean Path} = \frac{1}{\mu_a + \mu_s} \quad (5)$$

$$\text{Transmission} = \frac{\mu_s}{\mu_a + \mu_s} \quad (6)$$

The refractive index, absorption and scattering coefficients, and the anisotropy factor for the modeled skin layer are given in Table 7.3.

Table 7.3. Optical parameters of skin layers.

Skin Layer	μ_a [1/mm]	μ_s [1/mm]	g [-]	N @ 575 nm
Living epidermis	1	20	0.79	1.45

Considering the tilt angle of the cantilever, and the optical parameters of the GRIN lens used in previous analysis, the illumination path of light in a non-sequential mode of analysis is shown in Figure 7.9. The reflected light in the proposed system was collected at the base of cantilever by a 105 μm sized cladding surface with no detection at the center area in correspondence with the cantilever section. The light collection was modeled by placing an absorbing detector at the base of cantilever, and measuring the light intensity detected by that surface compared to the light intensity emitted by the source beams. The scattered light path is shown in Figure 7.10.

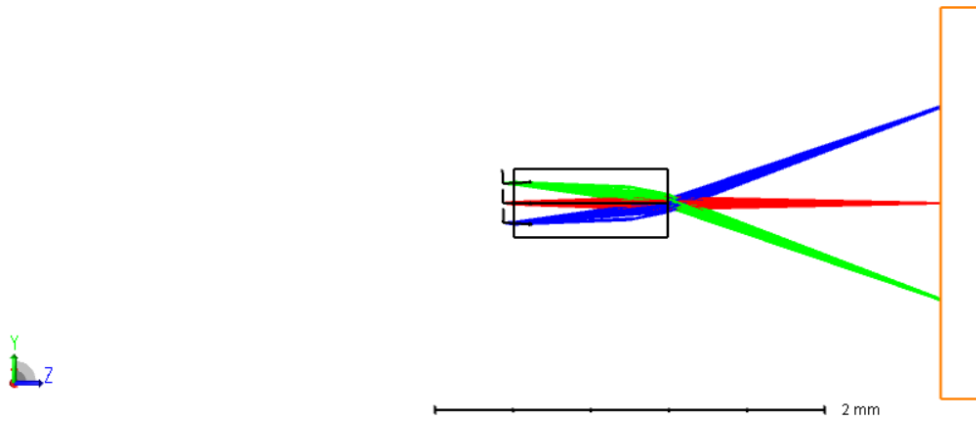


Figure 7.9. Illumination path of the optical setup in non-sequential mode.

The amount of the light varies on the detector plane and if the detector surface is placed on the axis or off-axis. A rectangular detector having an area equal to that in correspondence of the cladding surface reduced by the cantilever section is placed on the axis at 2 mm away from the fiber tip surface. The total power collected by the detector surface is considered for the further calculations. Thus, from the ray tracing analysis, the light collected by the detector placed axially is about 0.5% of the light emitted by the source beams.

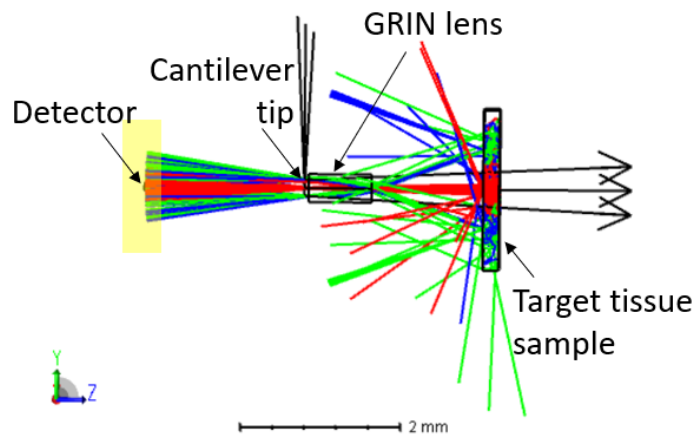


Figure 7.10. Complete optical ray diagram in non-sequential mode.

In a real sample, the amount of the light that reaches the detecting surface will be even smaller than the calculated value due to the presence of the metallic actuator in front of the inner cladding surface blocking some portion of the backscattered light. Thus, the amount of light reaching the detector surface will be of same order of the noise signal and it would be hard to separate the imaging signal from the noise. Therefore, some other

alternative measure needed to be considered to capture high amount of scattered light signal from the target tissue surface.

It has been studied in the literature that it is possible to use non-confocal light collection using external collection fibers to get a higher amount of reflected light signal (collection efficiency can be 40x greater than that of a confocal detection method). The amount of the light collected in such a case depends on the size, number, and the position of the collection fibers [262]. Thus, it is a possibility to use a ring of multimode fibers placed at the periphery of the vibrating cantilever fiber [138]. However, it will result in an increased probe diameter. One way to reduce the overall probe diameter is to decrease the diameter of the stationary portion of the light carrying cantilever beam. It can be done by means of chemical etching or changing the 250 μm DCF fiber to a small diameter SMF.

As discussed earlier, the light collection efficiency in these cases depends upon position, number and diameter of the fibers used for light collection. In the case where 50 μm diameter fibers are used for light collection, it is possible to place 25 of these fibers at the periphery of the device. Using Zemax simulations, it was shown that it was possible to capture about 15.5% of the reflected light when these fibers were placed at about 680 μm away from the lens surface towards the target sample. The optical ray diagram with one of these collection fibers is shown in Figure 7.11.

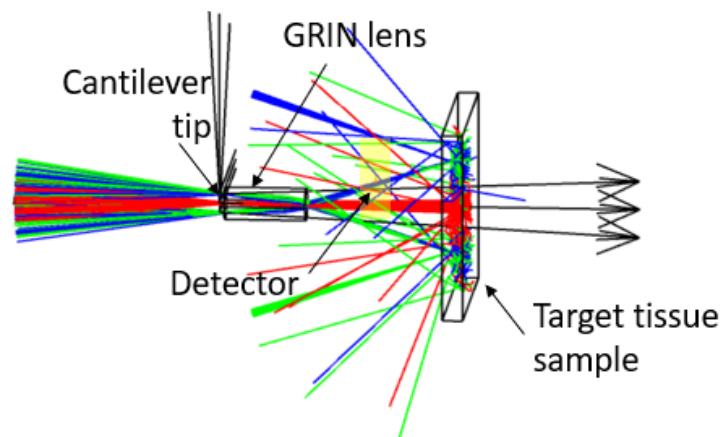


Figure 7.11. Optical ray diagram of the optical system with a collection fiber at periphery.

It is also possible to further increase the reflected light signal by combining the light collected through the inner cladding of the DCF fiber and that collected by the peripheral ring of multimode fibers. Moreover, the scanning of the smaller areas can help maintain

the higher scanning rate allowing each tissue point to be exposed for longer illumination times.

7.8. Conclusions

From the above analysis, the actual light collected by the detecting surface was very small compared to the light emitted by the light source. In the actual system, the spot size of the incoming light was much bigger, and the aberrations introduced by the lens further decreased the amount of light collected by the detector. Moreover, the presence of the metallic actuator occluded some of the inner cladding area to collect the reflected light reducing the overall light that passed through the cladding surface. Furthermore, the light that leaked in the case of cantilever fabricated using the spliced method, or non-perfect flat interface in the case of the etched cantilever reduced the actual amount of light captured via cladding.

In case the light leaking at the fiber is not considered in the analysis, another loss of light happens in correspondence of the light interaction with the tissue surface. In the case of a tissue surface, only about 10% of the transmitted light was back reflected from the surface. Thus, a very small amount of light reached the fiber clad surface and further propagated with some losses to the photodetector element. The sensitivity of a photodetector element depends directly on the light intensity hitting at its surface. It was possible to generate a smooth image by decreasing the frame rate and increasing the light intensity hitting the tissue surface. Since the amount of light that can be transmitted to a tissue surface without creating any damage was limited, improvement of the efficiency of the light collection system was required.

Thus, the amount of the light captured by the cladding surface was much smaller than the background signal noise as discussed earlier in this chapter. In addition, from the light transmission phenomena considered above, it can be deduced that the light collection through the inner cladding was not enough to make an image of the tissue surface, and further light collection techniques needs to be considered. It was found that by using a non-confocal collection via multimode fibers placed at the periphery of the device, it was possible to collect high amount of backscattered light to reconstruct the image.

Chapter 8.

2D scanning using single actuator

The original proposed design was based on exciting the optical fiber cantilever at its base along the radial direction using an electro-thermal actuator. This actuation permitted 1D motion of the fiber in ideal cases without any whirling, and the entire assembly needed to be rotated to acquire a 2D scan. However, it seemed feasible to rotate the entire assembly within the given dimensions, but there are some challenges related to this approach as will be discussed later in this chapter. Some other plausible techniques to obtain two-dimensional image using single actuator are presented in this chapter.

This chapter addresses OBJECTIVE 5 of the thesis: “Design of rotary joint with optical and electrical connection, or alternatives to avoid rotation”.

8.1. Introduction

Usually in OCT scanners, the circumferential scanning is performed using a Fiber-Optic-Rotary-Joint (FORJ). A FORJ is a device used to transmit optical signals across the rotating interfaces. Other than the free rotation of one side of the connection, FORJ should permit a low insertion loss (defined as ratio of input power to the output power in the connection) and a high return loss (amount of input signal to the signal reflected by the discontinuity). FORJ uses a pair of air-coupled lenses to allow the continuity of the optical connection between a rotating optical fiber and a stationary one. The schematic of a FORJ is shown in Figure 8.1 [263]. The lens on the stationary side is fixed in the space and is used to collimate the light from source fiber, while the other lens is mounted in a ball bearing (often rotated using a DC motor) and focuses the collimated light from the other lens to the endoscopic distal end fiber [263].

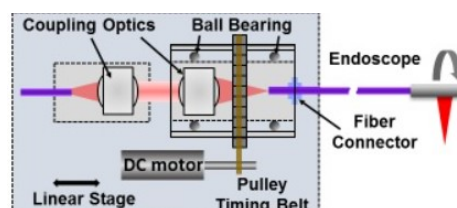


Figure 8.1. Schematics showing the proximal scanning with a FORJ (taken with the permission of [263]).

On the other side of the FORJ, the continuity of an electrical connection between a rotating and stationary component is permitted by a slip ring. In this connection, one of the surfaces contains graphite or metal brushes, while the other surface is made of a metal ring. During the rotary connection, the brushes rub against the metal ring allowing the continuity of the flow of electricity. A schematic of the slip ring and brush connection is reported in Figure 8.2 [264].

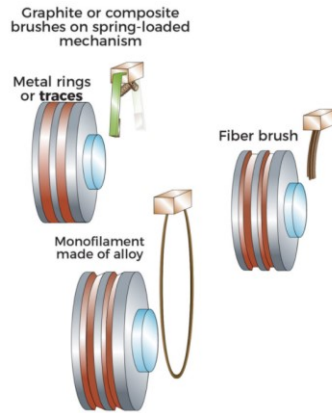


Figure 8.2. Schematic of the connection between slip rings and brushes (used with the permission of [264] CC BY license from DESIGN WORLD • WTWH Media).

In the proposed design of rotating the vibrating fiber-actuator assembly, the continuity of both electrical and optical connections among the rotating and stationary portions is required. One of the possibilities to meet this requirement consists in the combination of the FORJ and slip rings [265, 266]. There are some hybrid FORJ available in the market for the single/multimode fiber, but they are mostly over 3 cm in diameter. However, in our case we have a DCF fiber, and the submillimeter sized diameter restrictions with such a connection are challenging.

Furthermore, torque drive cables/wires are normally used to transmit the torque applied at one end to the other end of the FORJ. This will add surrounding components around the assembly increasing the dimensions of the final device. Moreover, the presence of electrical wires and the optical fiber within the 500 μm hypodermic needle along with such torque cables make the connection even more challenging.

To simplify the design of the catheter and get a bidimensional scan from the distal end, another possibility consisted in the variation of the actuator and/or cantilever design

such that the fiber tip was vibrating in the 2D plane. Such design alterations avoided the use of FORJ and slip rings and are discussed in detail below in following sections.

8.2. Exciting the fiber in two directions

Many endoscopic catheters perform bi-directional scans of an optical fiber by exciting it in two perpendicular directions. Such devices are either based on the use of tubular piezoelectric actuators with split electrodes, or a combination of other actuation principles such as differential thermal expansion and bimorph effect. The cantilever fiber follows a spiral pattern in the first case, while a Lissajous pattern is normally generated in the latter case [17].

A possible alteration to the design can be the use of two actuators placed perpendicular to each other. Such excitation of the cantilever can be achieved if another bridge structure is added on the actuator foil surface perpendicularly to the previous one. A schematic diagram of such an actuator assembly is shown in Figure 8.3. In this case, the driving signal for two bridges can be altered to obtain a spiral pattern from the fiber tip.

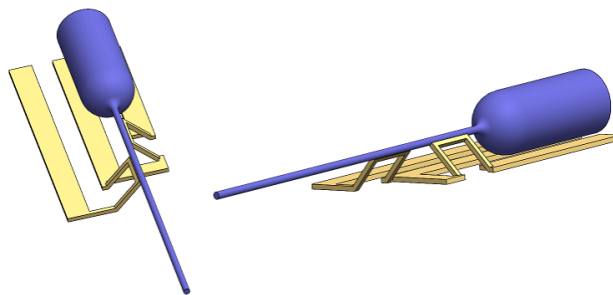


Figure 8.3. Cantilever-actuator assembly in case of actuation by perpendicular bridges.

This design seems feasible, but it includes some complications. First, the original design consists of the use of a DCF as the cantilevered fiber where the illumination light is sent through the vibrating cantilever, and the reflected light is collected through the inner cladding. As seen in previous chapter, a very small amount of the reflected light reached the inner clad surface. A new design configuration with two perpendicular bridge structures would further block some of this incoming reflected light due to the presence of another actuator.

In addition, the presence of another bridge foil structure would have spatial issues related the space available within the needle. Given the dimensions available for the metal foil actuator, the presence of another bridge divides the foil structures in three portions which will be much thinner than the structures in the case of single actuator. Thus, the heat dissipation problem will be worst than the one in the case of two foil surfaces. Moreover, the reflected light from the tissue surface will be blocked by two bridge structures reducing the signal for the image processing.

As all the samples are handmade at this step, keeping the two foil structures perfectly vertical and in place to avoid the connection between these foils and the needle will be difficult. The bridge structures become easier to break at the bridge area given the small size of heat sink portions and requirement of partially bending the foil to get two perpendicular bridges from a planar foil.

Thus, this idea of using two bridge structures has been abandoned given said manufacturing difficulties.

8.3. Bi-directional motion with nonlinear coupling

As stated in chapter 5, the single direction actuation of a symmetric beam can lead to the cross-coupling of motion in the plane. When the excitation frequency is close to the resonant frequency, the planar motion instability generates an out-of-plane motion. Thus, the free end of the cantilever beam excited at resonance at its base tends to follow an elliptical path.

Wu et. Al. discovered that the elliptical shape pattern described by the fiber tip can be converted into a circular shape pattern when the excitation frequency matches the second resonant frequency of the cantilever [149]. If such motion is obtained, then the complete 2D scan can performed following a circular shaped pattern and sweeping the area inside the circle by varying the excitation power.

This method seems quite useful as permits the generation of a 2D scan pattern just by applying a linear excitation; however, it is not practical in the current design of catheter. One of the main reasons for this is the fact that tip displacement in the second resonant mode is much less than the first mode tip displacement (almost 1/4). Thus, the corresponding field of view in this case would be very small or a higher excitation power

would be required to obtain a noticeable displacement, which in case of a sub-millimeter sized electrothermal actuator can lead to the fusion of very thin parts due to high temperatures.

Moreover, the frequency at the second resonance mode in the given case will be in the order of 15-20 kHz. The heat dissipation at this small period will be ineffective in the current sub-millimeter sized actuator. Thus, it requires the use of a very small input power, further reducing the tip displacement.

8.4. Bi-directional motion by an asymmetric cantilever

Another approach to obtain an out of plane motion from a single linear actuation is the use of an asymmetric cantilever. A small asymmetry in the cross section of the vibrating beam can lead the beam to vibrate in the plane perpendicular to its axial direction. This effect of a slight asymmetry in the cross section of the cantilevered beam is analyzed computationally using ANSYS. The geometry of the analyzed cantilevered beam is shown in Figure 8.4, which is fixed at one end. This proximal end of the cantilevered beam is harmonically excited linearly in one direction at the value close to excitation by a thermal actuator. The slight asymmetry causes the tip of the cantilevered fiber to move in the plane perpendicular to the axial direction of fiber itself as shown in Figure 8.5.

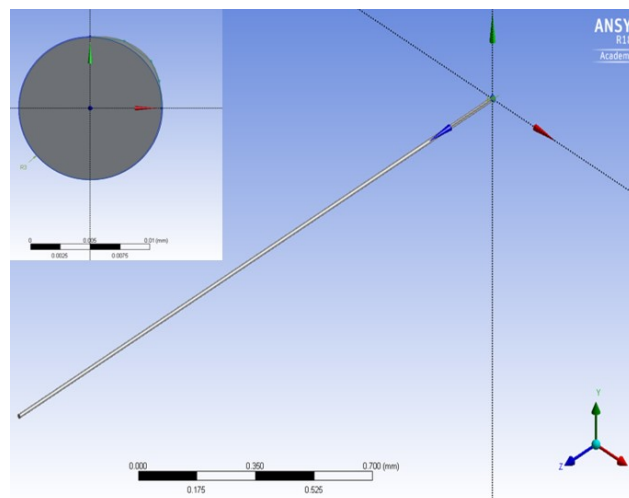


Figure 8.4. The geometry of the cantilever beam under analysis.

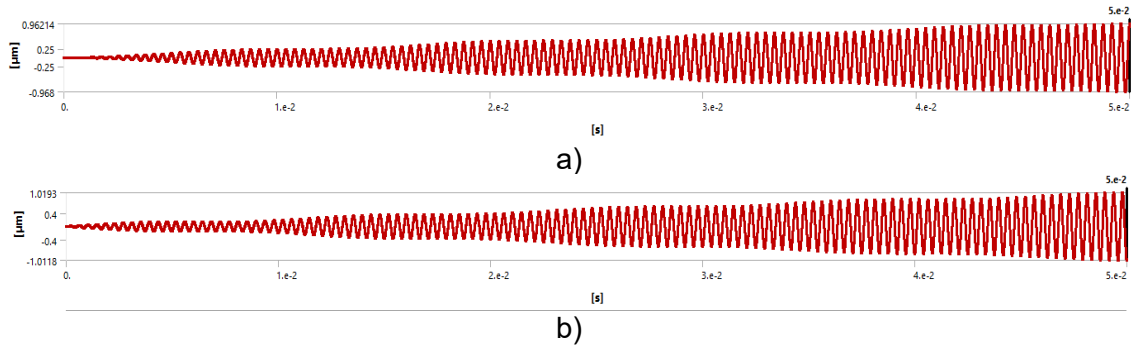


Figure 8.5. Displacement of the tip of the fiber: a) in x direction, b) in y direction.

An asymmetry of the vibrating cantilever is beneficially used in [111] to produce 2D motion of the cantilevered beam by exciting it at the base in one direction. In this case, a protruding rod is attached parallel to the actual cantilever beam near its base with the help of a stiffening rod. The linear force applied by the base excitation actuator can be divided into two perpendicular components with each component having different beam geometry. On one side, the beam has a cylindrical geometry, while from a perpendicular direction, it has different geometry given by the combination of the actual beam and additional components. Thus, the beam has a different resonant frequency in each direction. By combining these frequencies and providing a corresponding driving signal, the fiber tip is allowed to follow a Lissajous scanning pattern [111].

As seen in the fabrication process described in chapters 4 and 6, the splicer usage in the heating and pulling method allowed the fabrication of cylindrical shaped cantilevered fibers. Similarly, the chemical etching provided a cylindrical shape. However, it was possible to create an asymmetric region in the fiber by controlling the etching until a certain point, and then cover one side of fiber with a polymeric coating and continue etching.

Another approach to make the cantilever asymmetric is to add additional mass on one side of the cantilever. Some samples were tested based on the design of a previously described electro-thermal actuator and asymmetrical cantilever. In most of these samples, an additional piece of 12 μm fiber is attached to one side of cantilever fiber with the help of epoxy. Since the operating temperatures of the considered electro-thermal actuators were high (analyzed in chapter 5), a heat resistant epoxy (EP17 HTND-CCM, Masterbond) was preferably used in such samples. One of these samples is shown in Figure 8.6.



Figure 8.6. Packaged sample with asymmetric cantilever fiber.

These samples still show an elliptical shaped pattern at the distal end when actuated linearly. However, the out of plane motion was slightly increased as shown in Figure 8.7. It can also be seen that a smaller duty cycle with given average power only increased the motion along the excitation direction, while the motion in other direction remained almost the same.

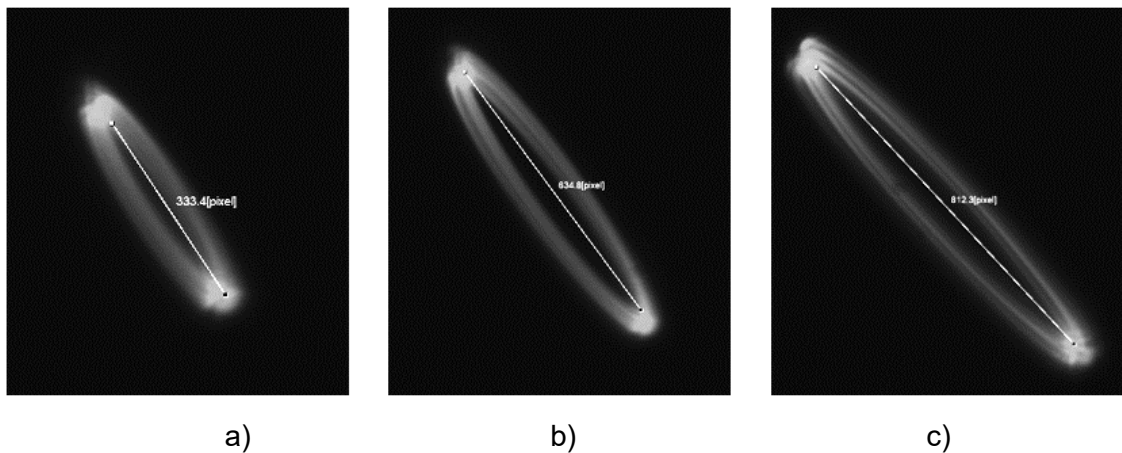


Figure 8.7. Front view of performance of sample shown in Figure 6 at different duty cycles: a) 50% duty cycle; b) 25% duty cycle; c) 15% duty cycle.

From the analysis of such samples, the out of plane motion was still insufficient to create a complete 2D scan without rotating the whole assembly. Thus, another alternative approach needs to be considered to increase the motion along the shorter axis of the ellipse.

8.5. Bi-directional motion by an asymmetric actuator

As stated earlier in section 8.2., it was possible to get a bi-dimensional motion from the fiber tip by exciting the cantilever fiber in two directions. However, the use of a second actuator was not feasible in the current design due to the previously mentioned reasons. Nevertheless, it was possible to generate an asymmetric/nonlinear excitation from a single actuator. It was produced using an ANSYS simulation that showed the nonlinearity in the tip displacement can also be obtained by the non-uniformity of the excitation at the base. If a small out of plane excitation is included in the design, as in Figure 8.8, the fiber tip showed a corresponding out of plane motion. Thus, the fiber tip followed an elliptical pattern at steady state as shown in the phase plot of the tip displacement in Figure 8.9.

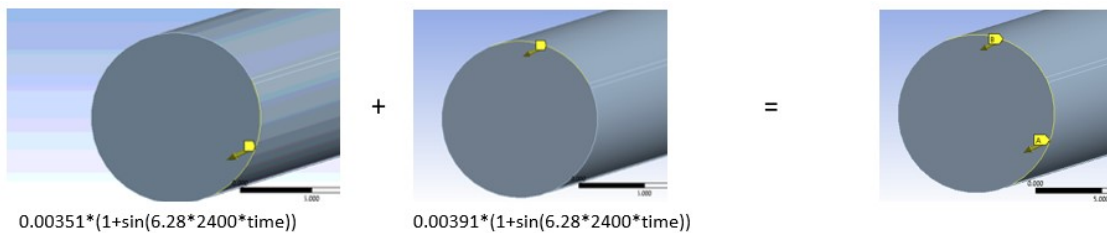


Figure 8.8. The non-uniformity of the base excitation

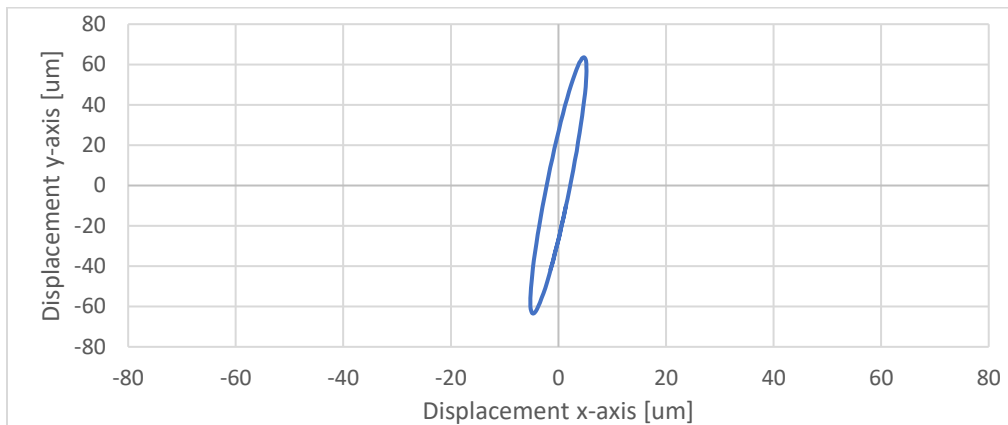


Figure 8.9. Phase plot of tip displacement using base excitation in Figure 8.8.

Based on an asymmetric bridge structure having one leg 25 μm wide and the other 35 μm wide, a more detailed simulation of the actuator-fiber assembly was performed in COMSOL Multiphysics. The schematic diagram of the design is shown in Figure 8.10. In such a design, the actuator bridge provided a vertical motion and a horizontal motion

towards the wider leg of the bridge. The intensity of the bridge displacement depended upon the position along the bridge as in Figure 8.11.

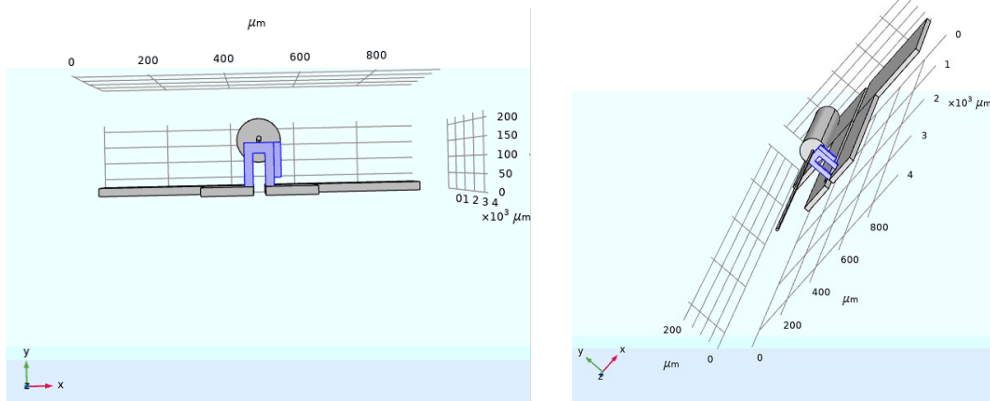


Figure 8.10. Schematic of an asymmetric bridge with cylindrical cantilever assembly.

Figure 8.11b shows the bridge deformation along vertical X direction for different values of parameter “a” shown in Figure 8.11a, while Figure 8.11c shows the displacement along horizontal Y direction. As can be seen from Figure 8.11, the maximum vertical excitation corresponded to the center of bridge while the maximum horizontal displacement occurred at the edges of the bridge. Thus, to obtain a noticeable bridge displacement along both directions, it was better to place the cantilever at an off-centered position ($\frac{1}{4}$ or $\frac{3}{4}$ length of the bridge arc length shown as red line).

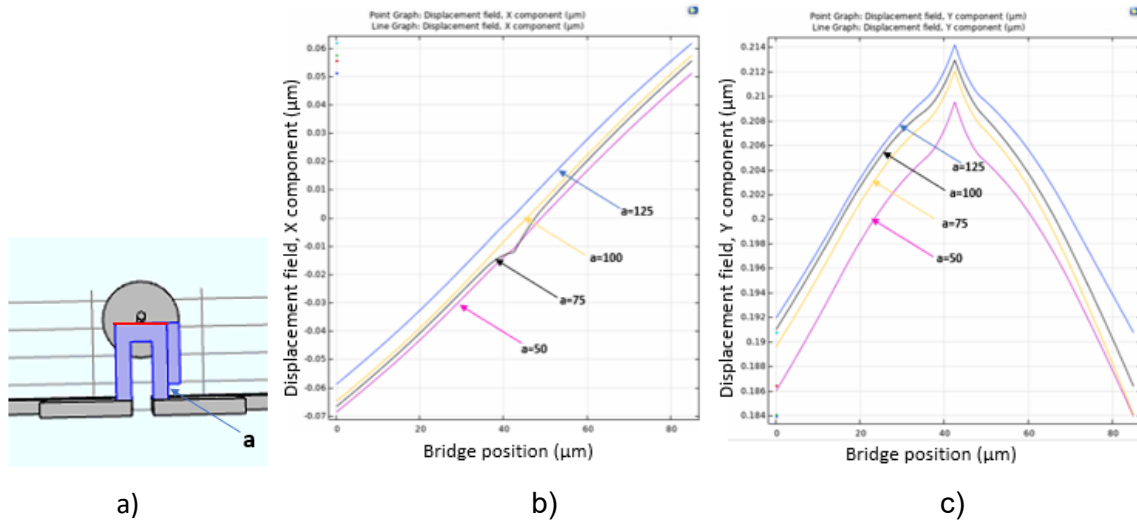


Figure 8.11. The displacement of bridge structure: a) zoomed view of bridge structure; b) bridge displacement along X direction; c) bridge displacement in Y direction.

In the case where the fiber is placed at $\frac{1}{4}$ of the arc length of the bridge, as shown in Figure 8.12, the system's performance is shown in Figure 8.13. In this Figure, the blue curve shows the fiber tip displacement along X direction, while the orange curve corresponds to the displacement along Y direction. The continuous increase in the tip displacement was due to the no damping effect considered in this analysis. When the damping effect was considered in the simulation, both displacements reached steady state, and the phase plot of Figure 8.14 shows that the tip follows a Lissajous scanning pattern. It can also be seen that the scan needed to run for about 27 periods of the excitation signal to cover the full 2D area.

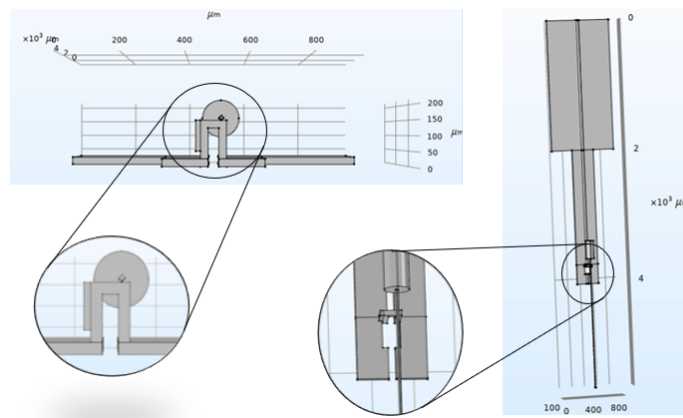


Figure 8.12. Schematic diagram showing geometry and cantilever alignment in case of an asymmetric bridge configuration.

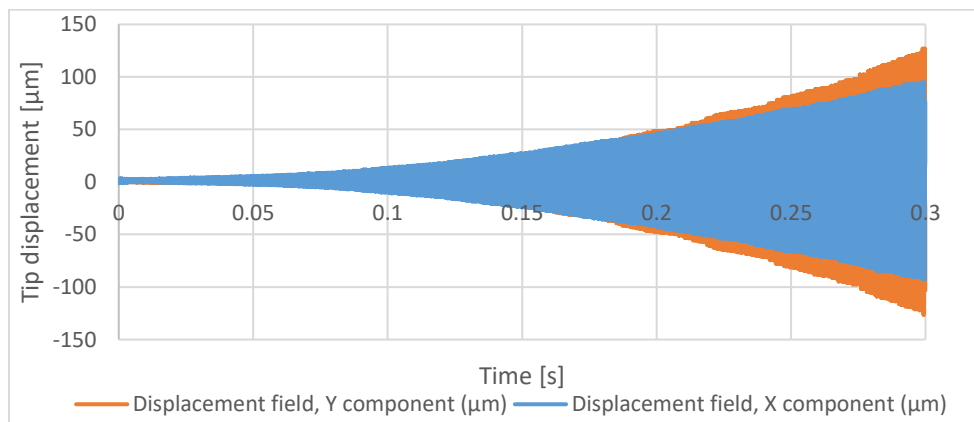


Figure 8.13. Time response of cantilever beam tip actuated using asymmetric bridge.

Some samples were made using an asymmetric bridge configuration and placing the cantilever fiber shifted towards the thinner leg of the bridge. The front light captured

from this kind of sample is shown in Figure 8.15. The sample was first vibrated at a small max current (0.95A) and a 50% duty cycle to detect the resonant frequency. It showed a perfectly vertical performance at 1.524 kHz (Figure 8.15a), and a perfectly horizontal pattern at 3.942 kHz (Figure 8.15b). Thus, the Lissajous pattern frequency must be within these two frequencies which was detected to be around 2.007 kHz. However, the scanning intensity was very small. To better evaluate the pattern, the system was run at a 20% duty cycle with a higher max current value. As seen in Figure 8.15c, the displacement amplitude of the scanning Lissajous pattern was still small with respect to the desired tip displacements in two directions.

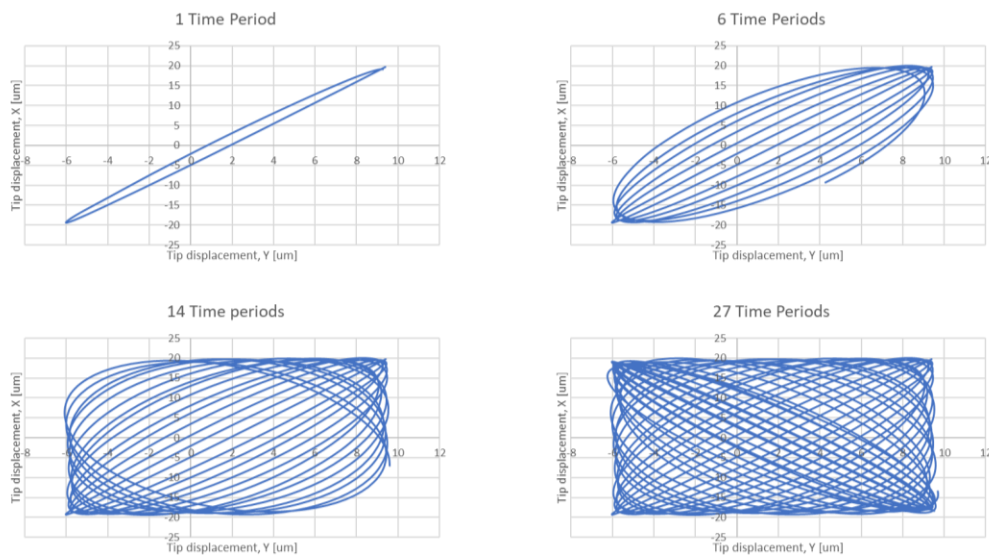


Figure 8.14. Fiber tip displacement excited by asymmetric bridge in presence of damping.

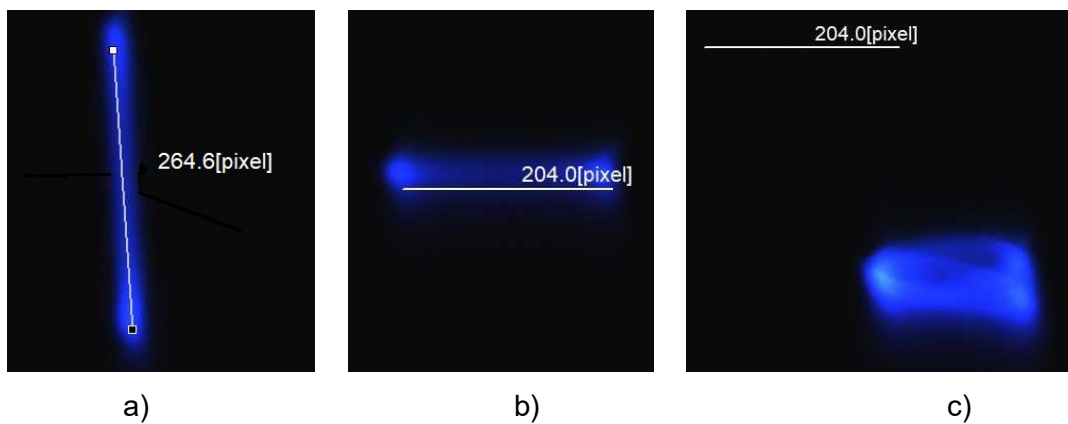


Figure 8.15. Front light capture from a sample with configuration shown in Figure 8.12 at a frequency of: a) 1.524 kHz; b) 3.942 kHz; c) 2.007 kHz.

8.6. Bi-directional motion by an asymmetric actuator and asymmetric cantilever

From the analysis shown in Sections 8.4. and 8.5., it was possible to obtain a bi-dimensional motion of the cantilever tip using either an asymmetric cantilever or actuator. However, it generated a very small tip displacement of the cantilever tip in one of the vibrating directions or along both directions, respectively. Thus, the combination of the two cases using an asymmetric bridge with an asymmetric cantilever was considered.

8.6.1. Asymmetric bridge structure

The main structure in the actuator that dictated the response of the cantilever fiber is the bridge, which is initially composed of two parallel rectangular legs giving primarily single direction base excitation to the cantilevered fiber. To get the maximum bi-directional base excitation, the bridge needs to be optimized, which is performed both analytically and using the simulation in COMSOL Multiphysics environment.

The bridge is analogous to MEMS electrothermal actuators which are primarily made up of two arms. The most commonly used U-shaped electrothermal micro-actuators for an in-plane bidirectional motion are either made of different beam/arm lengths [267] or different cross section of the two beams [177] as shown in Figures 8.16a and 8.16b, respectively. The working principle of these actuators consist of an asymmetric temperature and consequent asymmetric thermal expansion between the two arm structures [73]. The asymmetric thermal expansion in the first case (Figure 8.16a) is obtained by different beam lengths. The average temperature in the longer arm is higher than the shorter arm and will be shown later in this chapter. Thus, the longer arm tends to expand more than the shorter arm due to the higher average temperature and length. This asymmetric thermal expansion allows the free end of the actuator to bend towards the shorter arm.

In the case of an electrothermal actuator characterized with a different cross section, one arm is wider than the other (Figure 8.16b). The wider arm (also called cold arm) is usually connected to the connection anchors with a small thinner beam section called the flexure enabling the movement of the colder arm [268]. In another configuration, the flexure arm is directly connected to the hot thinner arm while the colder arm is

connected towards one of the anchors [269]. In these actuators, the asymmetric cross section of the two beams causes different current densities in the two sections. Therefore, more heat will be generated in the thinner arm due to Joule heating causing an asymmetry in the temperature between two arms. Consequently, the different thermal expansion causes the thin arm to bend towards the cold arm generating a bending moment [73].

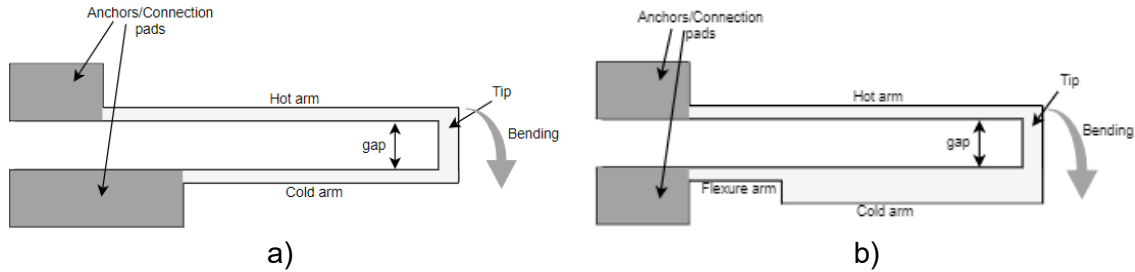


Figure 8.16. Electrothermal MEMS actuators with a) different arm lengths; b) different cross section.

Electrothermal Analysis

Steady state analytical models were developed for both cases considering the dimensions of similar polysilicon micro-actuators developed in the literature to compare the results and validate the model. An electrothermal actuator with different arm lengths (design A) considered as the reference is the one developed by Pan and Hsu in [267], while the micro-actuator with different cross sections (design B) considered as the reference is the one developed by Huang and Lee in [177]. The material properties and dimensional parameters of both micro-actuators are summarized in Table 8.1.

Table 8.1. Parameters of the reference polysilicon micro-actuators.

	Design A [267]	Design B [177]
Material properties		
Young's modulus	150 e9 Pa	150 e9 Pa
Poisson's ratio	0.066	0.066
Thermal conductivity	41 W/ (m °C)	30 W/ (m °C)
Thermal expansion coeff.	2.7 e-6 °C	2.7 e-6 °C
Resistivity	5 e-4 Ω m	1.1 e-5 Ω m

	Design A [267]	Design B [177]
Geometric dimensions		
Gap between beams	$\geq 5 \mu\text{m}$	$3 \mu\text{m}$
Length of hot arm	$500\text{-}750 \mu\text{m}$	$200 \mu\text{m}$
Length of the cold arm	$100\text{-}500 \mu\text{m}$	$162 \mu\text{m}$
Width of beams	$1\text{-}3 \mu\text{m}$	$14 \mu\text{m}$ (cold arm); $2.5 \mu\text{m}$ (hot arm)
Thickness of beams	$2\text{-}3 \mu\text{m}$	$1\text{-}4 \mu\text{m}$

The mathematical equations showing the electro-thermal model for design A are mostly described in the literature [267, 270]. A similar approach is used to analyze the temperature distribution along the actuator. The actuator is long and slender, which means that the heat flows primarily in the longitudinal direction. Since convection and radiation are negligible at the given dimensions of the structure, a one-dimensional conduction heat transfer model gives reasonable results [178]. Mathematical equations developed for this actuator were solved in MATLAB. A similar model was simulated in COMSOL Multiphysics, and the temperature distribution from both analyses are reported in Figure 8.17 along with the 1D model of the design A actuator.

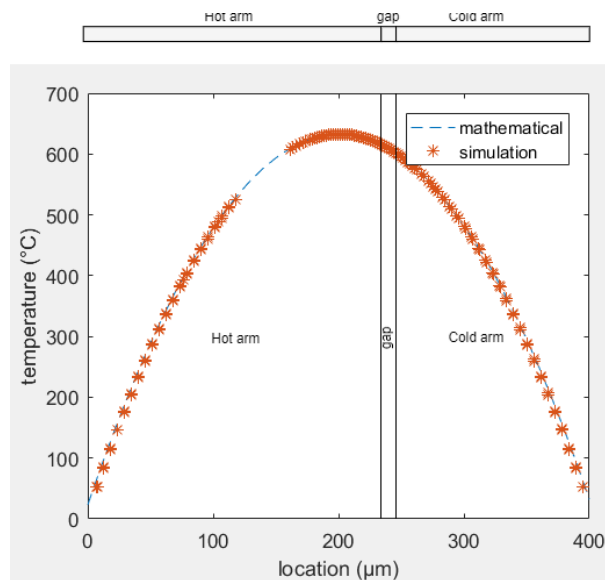


Figure 8.17. Temperature distribution along design A electrothermal actuator.

Analogous to electro-thermal analysis of design A, similar mathematical equations were developed for design B electrothermal actuator (actuator having arms of different cross section and a flexure arm). A similar model was developed in COMSOL Multiphysics, and the results of both analyses are shown in Figure 8.18. The mathematical model results matched perfectly with the simulation results. The temperature curves from both models are compared in Figure 8.19 where average temperature difference between the two arms was higher in case B.

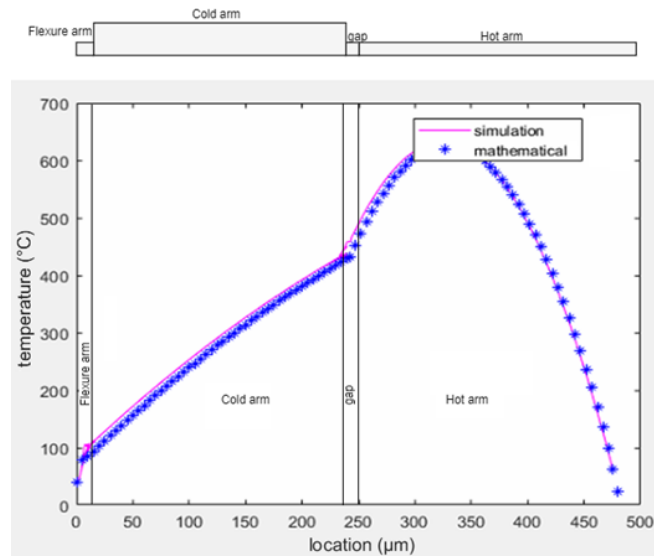


Figure 8.18. Temperature distribution along design B electrothermal actuator.

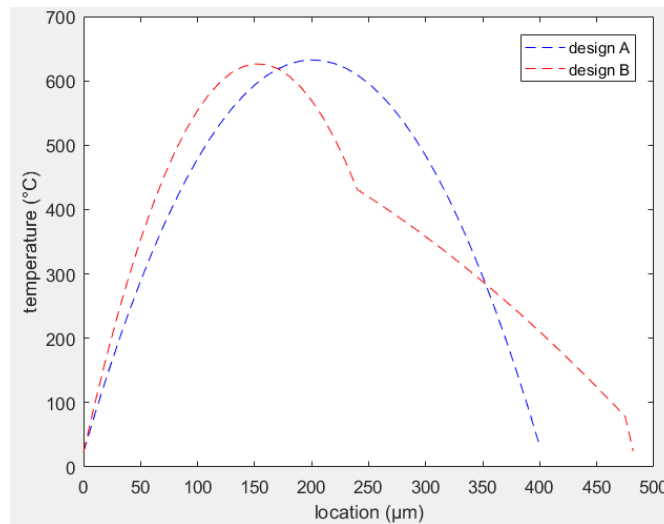


Figure 8.19. Comparison between temperature distribution in design A and design B.

In some cases, a MEMS electrothermal actuator is connected to a silicon substrate at a very small gap of few microns [178, 177]. In this kind of configuration, the conduction from the actuator to the substrate through the airgap needs to be included in the design. As shown in the temperature profile in Figure 8.20 (obtained using mathematical equations with actuator dimensions considered in [177]), the heat dissipation in this case is more effective than the previous case resulting in even higher average temperature difference between two arms.

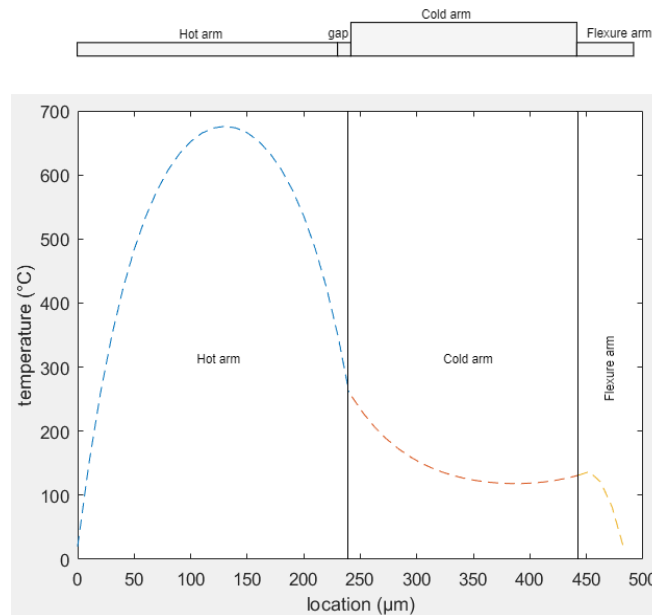


Figure 8.20. Temperature distribution along design B electrothermal actuator placed on a substrate with an airgap of 2 μm .

Mechanical Deflection Analysis

The mechanical deflection analysis of an electrothermal MEMS actuator is initiated with the calculation of the thermal expansion for each arm from the temperature distribution shown in the previous section. For the mechanical deflection analysis, the actuator can be considered as a plane frame fixed at both ends. The analytical model for both designs is developed using the force method. Considering the dimensional parameters of the actuators similar to the reference actuators in both designs reported above, the performance of actuators was analyzed in function of the input voltage. To compare the results of two designs, the same material properties were used in this analysis. Tip deflection curves for both designs with respect to the input current are shown

in Figure 8.21. From the tip deflection curves, it was noted that design B generated a larger tip deflection as compared to design A for a given input voltage.

8.6.2. Design optimization

Apart from the different material used in the two designs, the previous section highlighted that the temperature difference between the two arm structures was greater in design B than in design A. Thus, design B showed higher tip deflection as in Figure 8.21. In this section, these designs were optimized, and additional changes were introduced in the structure to get an even higher tip displacement.

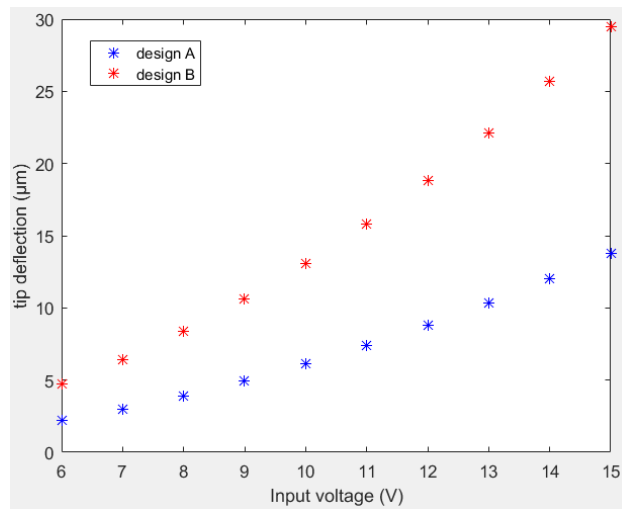


Figure 8.21. Tip deflection versus input voltage for design A (blue stars) and B (red stars).

Optimization of Design A and Design B

An electrothermal actuator with a higher tip deflection is a desired structure so that one can get the desired motion using a lower amount of input power. The temperature difference between the two arms and the corresponding tip displacement of the free end of the actuator are directly related to the length of two arm structures. The tip deflection for design A as a function of length ratio between the two arms is shown in Figure 8.22 where L_c is the length of cold arm and L_h is the length of the hot arm. All the other dimensional and mechanical properties of the actuator were the same as its reference structure. The optimal design length of cold arm is 0.52 times the length of the hot arm to get the maximum tip displacement at given input power.

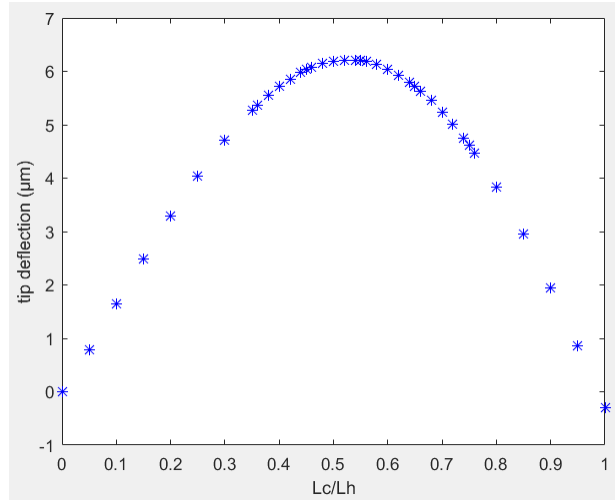


Figure 8.22. Variation of tip deflection in function of length ratio between two arms.

In design B, the performance also depends on the width of the cold arm structure. For a given dimensions of the hot arm, the longer is the wider section of the cold arm, the higher is the heat dissipation in the cold arm, and the higher is the tip displacement. However, a longer cold arm portion determines a smaller flexure arm. Consequently, the flexural rigidity of the cold arm to the bending of the flexure arm and the wider cold arm increases as well. In the case of design B placed on a substrate with a small airgap, the tip deflection as a function of length ratio between the two arms (L_c/L_h) is reported in Figure 8.23a. For a given width of the cold arm, there will be an optimal length ratio of 0.96 that gives the maximum tip displacement.

In the proposed design of actuator, the bridge structure looking similar to these micro-actuators is lifted perpendicular to the surface. So, in the actual proposed design, there will be no heat transfer via conduction towards the substrate. Thus, the design B to be considered here will be the one with no heat transfer towards the substrate. The temperature distribution of such a structure is shown in Figure 8.18, and the tip deflection curves as a function of length ratio is reported in Figure 8.23b for an input voltage of 10V. It can be noticed that even in this case, the optimal length ratio between the wider area of cold arm and hot arm is 0.96.

Similarly, the width of cold arm plays an important role in the tip displacement. A wider cold arm will have a smaller average temperature in that section due to a smaller current density and higher heat dissipation. Thus, a wider cold arm shows a higher tip

displacement compared to a narrower one as in Figure 8.23. In case the width of two arms is the same (i.e., $w_c=w_h$), the two arms expand at the same length, and there will be zero bending moment.

Analogous to this, it is also possible to check the effect of other parameters such as length and width of the hot arm. The longer the hot arm, the higher the average temperature and tip displacement. However, the maximum of the hot arm length is limited by the fact that for very long actuators, the maximum temperature can be very high causing the local melting of the arm itself. Similarly, the higher the width or thickness of the hot arm, the smaller the current density and average temperature resulting in a small tip deflection.

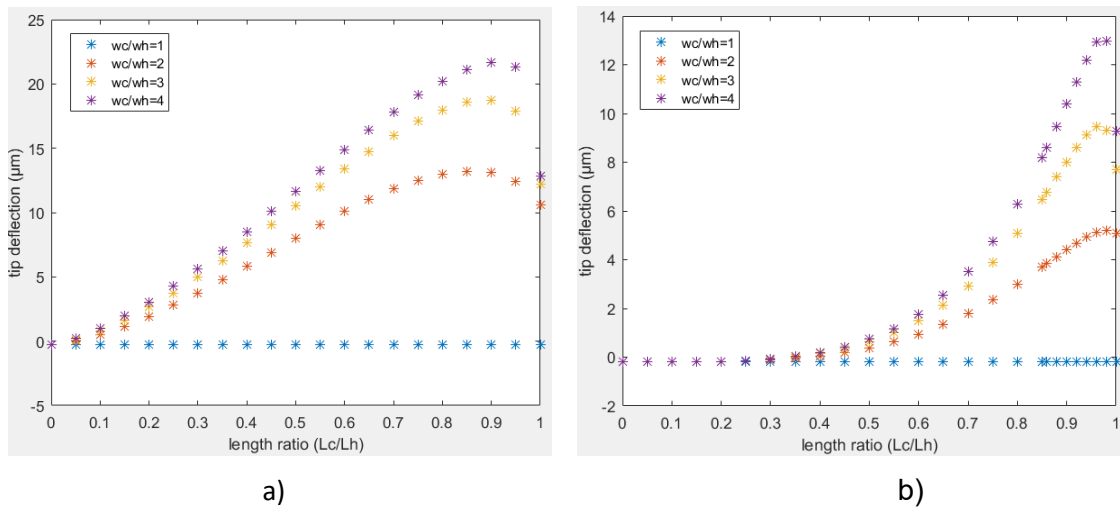


Figure 8.23. Tip deflection of design B in function of length ratio between two arm structures: a) design with 2 μm airgap from substrate; b) design without heat transfer towards substrate.

Design C

In the previous sections, it was noted that the electrothermal actuators are based on the asymmetric thermal expansion to get bending of the free end of the actuator. This asymmetry in the temperature distribution between the two arm structures was due to different lengths of the arms in design A, and due to different widths of the two arms. Design C is the combination of design A and design B, where the uneven thermal expansion of the two arm structures is obtained via both different length and width of the two arms. The schematic diagram of such structure is shown in Figure 8.24.

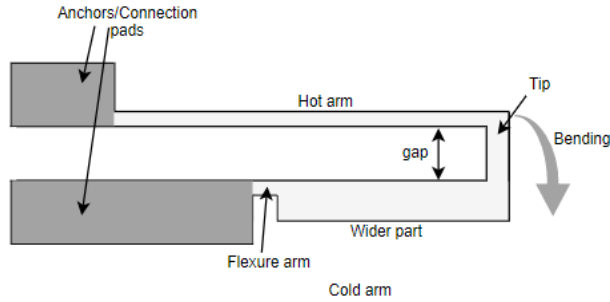


Figure 8.24. Schematic diagram of design C.

The optimal dimensions between the two arm structures, obtained in the previous section, were considered as the starting point of this analysis (i.e., length of smaller arm is 0.52 times the length of longer arm, and in the smaller arm, the length of the wider portion is 0.96 times the overall length of that section). The temperature distribution along the structure is shown in Figure 8.25a. The beam deflection as a function of input voltage is shown in Figure 8.25b.

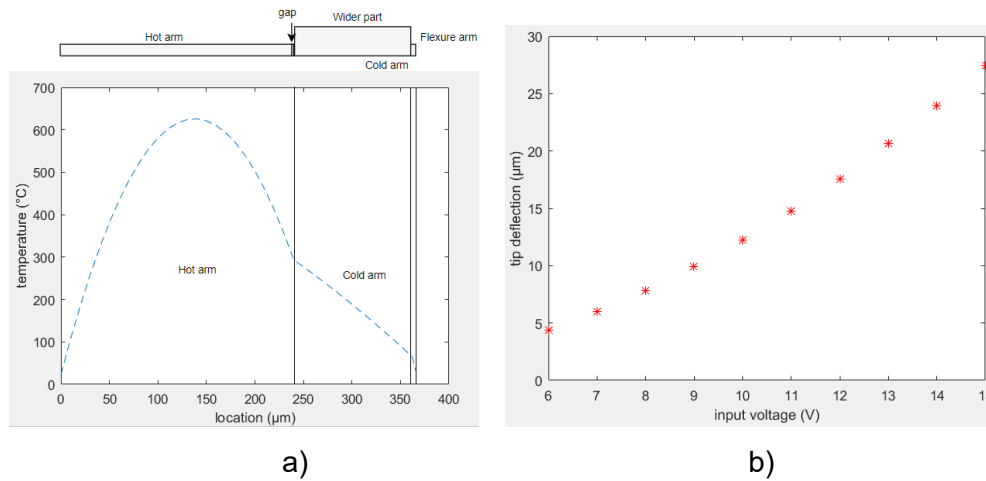


Figure 8.25. Performance of design C actuator: a) temperature distribution; b) tip deflection.

Analogous to previous cases, the dimension of the actuator needs to be optimized. First the performance of the design C actuator was obtained as a function of the overall length of cold arm with respect to hot arm length, and the portion of the wider arm inside the cold arm. From Figure 8.26, the maximum tip displacement obtained in the case of L_c/L_h is equal to 0.79 and when the wider part is about 0.96 times the overall length of the cold arm. It can also be noted that if the wider part was longer than 0.96 times, the displacement decreased as the effect of flexural rigidity became more evident.

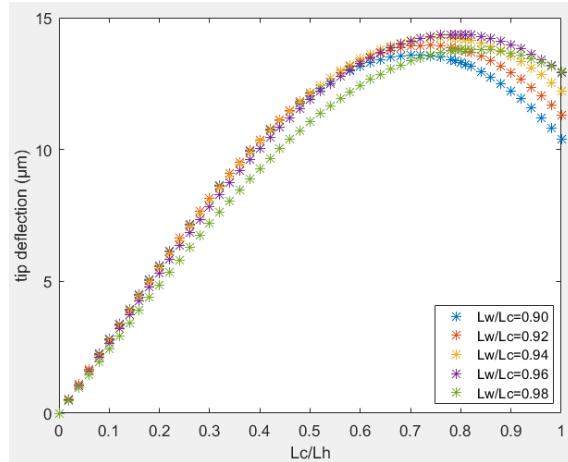


Figure 8.26. Tip deflection of design C in function of length ratio between two arm structures and the wider arm portion in the cold arm.

A comparison between the tip deflection of optimized design C with designs A and B is reported in Figure 8.27. It can be noticed that design C had an increase in tip deflection of about 10% with respect to design B and over 130% compared to design A.

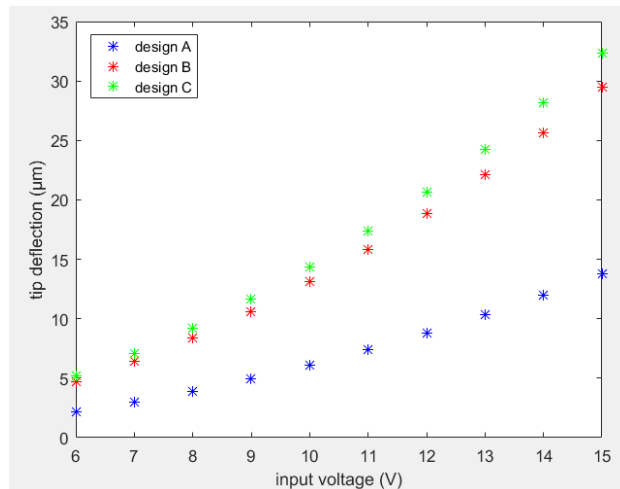


Figure 8.27. Tip deflection in function of input voltage of design C compared to designs A and B.

Design D

In the previous analyses, no changes were made in the hot arm structure. It can be noted that the width of the hot arm also played an important role in the overall tip deflection of the free end of the actuator. If the width of the hot arm increased, the current density decreased, and the flexural rigidity of the hot arm increased. Both these parameters decreased the overall tip displacement in a direction perpendicular to the arm

length. The mechanical analysis of these electrothermal actuators showed that the crucial part in the bending of each arm structure was the portion connected to the anchors. The tip deflection can be further increased by reducing the cross section of each beam in correspondence of the anchors like the flexure portion in the cold arm. The modified structure named as design D is schematized in Figure 8.28.

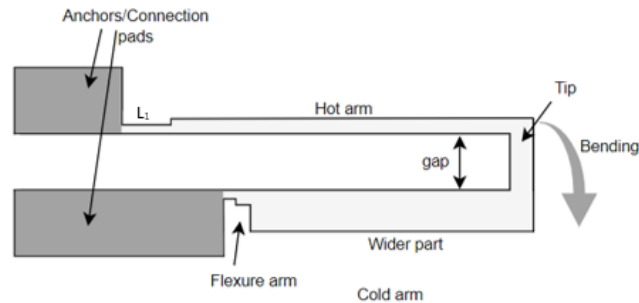


Figure 8.28. Schematic diagram of design D.

It is considered that the width of the thinner portion near anchors is equal to two third of the width of the hot arm. A smaller dimension will be more favorable. However, very thin structures will be hard to fabricate, handle, and vulnerable to melting given the use of large current density. Thus, the thinner portion is considered as 67% of the thickness of hot arm. First, the tip deflection as a function of length of the thinner part of the hot arm is considered and shown in Figure 8.29. The thinner portion of the flexure arm is considered as half the length of flexure arm due to its very small value. From the analysis, the optimal length of the thinner portion of hot arm (L_1) is $1/3$ of the length of hot arm (L_h).

The temperature distribution of this optimized design compared to the previous designs is shown in Figure 8.30a while the tip deflections of these designs is reported in Figure 8.30b. The average temperature of the hot arm was increased from design A to D, while the average temperature of the colder arm was decreased from design A to D. Thus, the overall temperature difference became more evident in design D and consequently the thermal expansion difference between the two arms and the overall tip displacement of the free end was higher in case D. The same can also be noticed from Figure 8.30b. The overall tip displacement was increased by 34% with respect to the displacement of design B working under similar conditions.

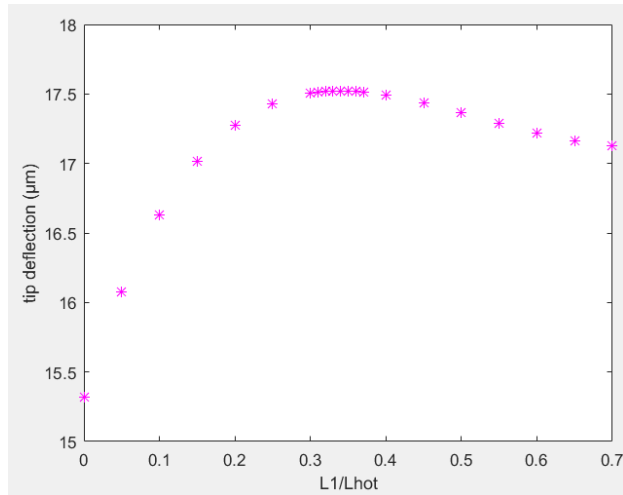


Figure 8.29. Tip deflection in function of length ratios of hot arm.

8.6.3. Optimized actuator-cantilever setup

From the analysis performed above, design D allowed a higher temperature difference between the hot and cold arm structures. Consequently, there was a higher bending of the tip in that case. The main purpose of this analysis was to obtain a higher cantilever excitation in the horizontal direction allowing the smaller axis of the ellipse described by the fiber tip to come close to a circle shape.

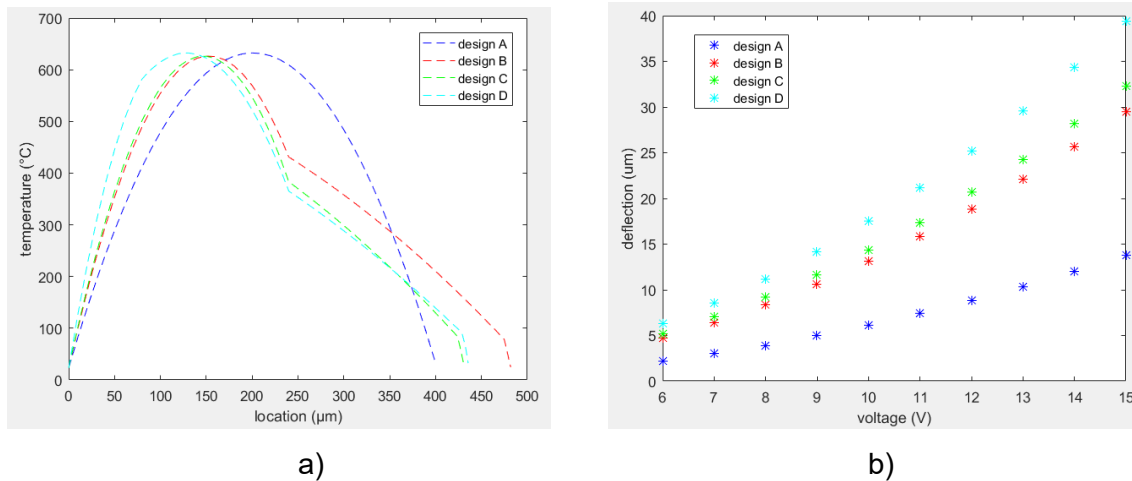


Figure 8.30. Performance of design D actuator compared to other designs: a) temperature distribution; b) tip deflection.

There are few samples prepared having the bridge shapes similar to that of a design D MEMS electrothermal actuator. A cantilever fiber was placed at the uplifted

bridge towards the hot arm as in schematics of Figure 8.12. In addition, a small portion of the 12 μm fiber was attached to the second half of the distal end of the cantilever, towards the colder arm side with the help of an epoxy. The pattern described by the free end of the cantilever tip at 20% duty cycle and 16V of input power is shown in Figure 8.31.

From Figure 8.31, there was an increase in the smaller diameter of the ellipse. As stated in the previous chapter, the area inside the ellipse can be imaged by changing the input power of the actuator, i.e., a decrease in the input power allowed a smaller excitation of the cantilever and consequently a smaller ellipse. However, altogether with the excitation, the average temperature of the bridge changed with the input power. This resulted in the fact that altogether with the change in the ellipse there was a continuous change in the center point of the ellipse as well. Thus, the ellipse was moving as the input power of the actuator was changed.

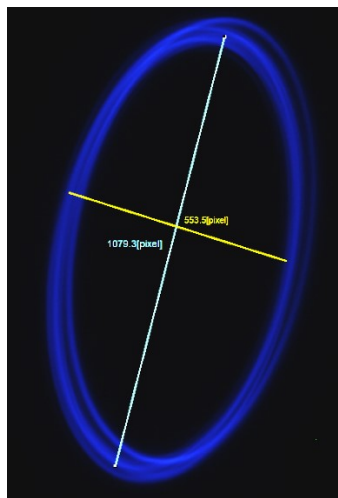


Figure 8.31. Front light image of the cantilever scan based on bridge having shape of design D.

Another possible approach to change the ellipse and sweep the area inside it is to change the excitation frequency around the resonance value by keeping the same input power. The change in the ellipse dimensions with the excitation frequency for two different samples is shown in Figure 8.32. The blue curves show the fiber tip displacement along the vertical direction, or the major axis of the elliptical shape described by the tip, while the red curves show the ellipse's minor axis performance with respect to the frequency. The two axes of the ellipse increase or decrease in linear fashion moving closer to or further away from the resonant frequency.

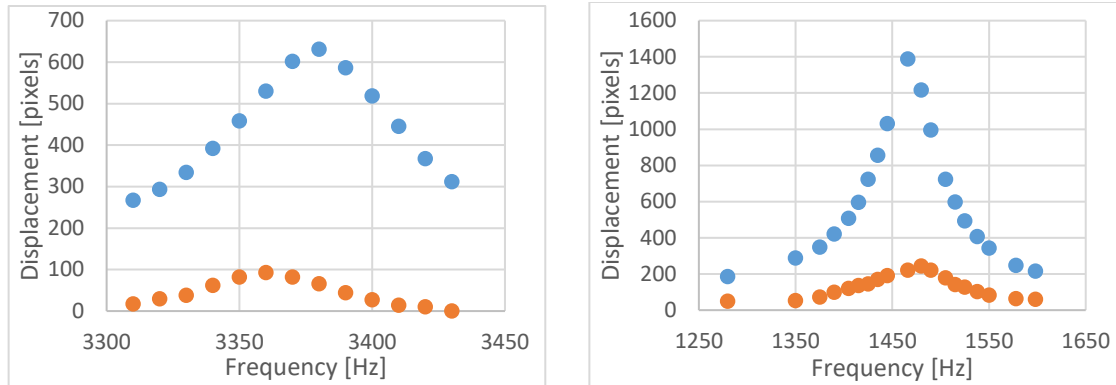


Figure 8.32. Tip displacement of the cantilever fiber with frequency change for two samples actuated by a bridge having shape similar to that of design D.

Design E

The design modification introduced in the last section allowed the fiber tip to move in a wider ellipse than with the original design. However, the minor axis of the ellipse was still much smaller than the major axis. A further modification in the actuator design was performed to resemble the pattern described by the fiber tip as a circle.

In the analyses performed for designs A, B, C, and D, the actuators consisted of two arm structures, and the current passes through both arms to have a closed circuit loop. Thus, the current passing through the cold arm caused the heating of that arm structure as well. It is possible to have a MEMS electrothermal actuator with more than two arm structures, where the current passes through at least two arms (called hot arms), and some additional arms with no current act passively as cold arms [271-273].

In our design, the dimensions of the bridge actuator needed to be minimized to reduce the amount of the inner cladding area covered by the bridge itself. Thus, this analysis was limited to a three-armed structure. It was also noted that the change in the flexure part of the cold arm structure in design D had very small impact on the device performance so it was neglected in further designs.

In a three-armed electrothermal actuator, it is possible to increase the temperature difference between the hot and cold arm structures using configuration shown in Figure 8.33, and possible to ground two arms together as in Figure 8.33a, allowing the current passing through the cold arm to be divided into two equal arms, i.e., small current density

in each of the colder arms. Like design B, this resulted in a smaller temperature through the cold arm. Actuators having such bridge shapes have been cut using the laser cutter and are shown in Figure 8.33b.

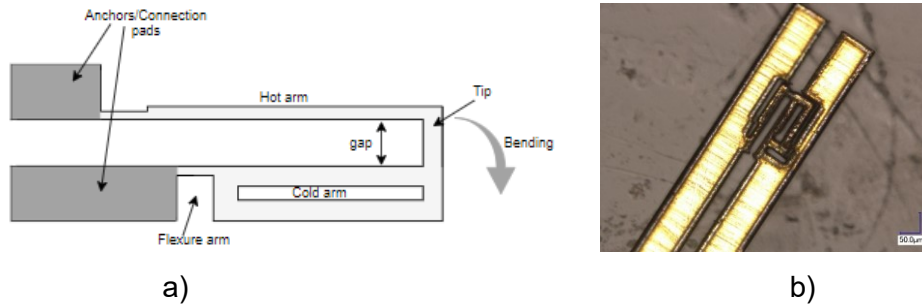


Figure 8.33. Design E having two cold arms connected at the base: a) schematic diagram; b) laser cut-out of the corresponding actuator.

In design E (Figure 8.33b), some samples were fabricated in combination with the asymmetrical cantilever. In this case, the asymmetric fiber portion was added towards the hot side of the actuator, as in Figure 8.34a, and the fiber tip follows a linear scan pattern (Figure 8.34b). Thus, the horizontal excitation generated by the asymmetry of the bridge canceled the out of plane motion caused by the asymmetry of the cantilever tip. In the design of Figure 8.34a, some additional fin structures were included on the side of the actuator to encourage heat dissipation. When the asymmetrical fiber was added towards the colder arm configuration, the fiber tip followed an elliptical path shown in Figure 8.34c.

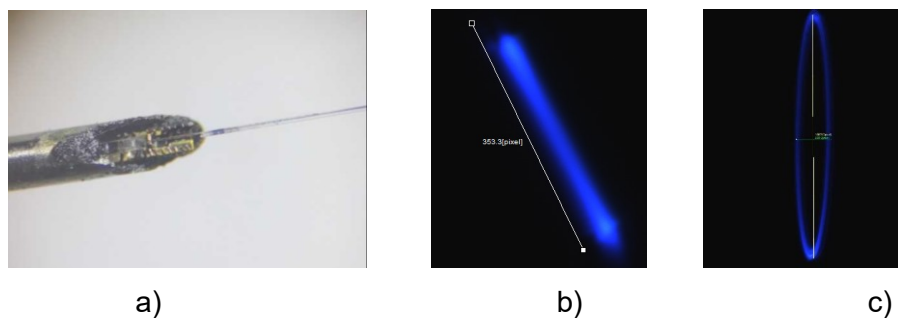


Figure 8.34. Sample with design E actuator configuration: a) cantilever-actuator assembly; b) scan performed by the fiber tip in case of asymmetric fiber facing hot arm; c) scan from fiber tip in case asymmetry towards the cold arm.

The asymmetry in the fiber tip motion was smaller than that of case D. It resulted from the fact that the flexural rigidity of the part connecting the two cold arms was higher

than that of Design D, so case “b” was analyzed and optimized in further design considerations.

It was possible to overcome this limitation by modifying the design as shown in Figure 8.35a, where one part of the cold arm was passive, and acts just as a fin to conduct heat from the two arms. The actuator pattern cut-out following this design is shown in Figure 8.35b.

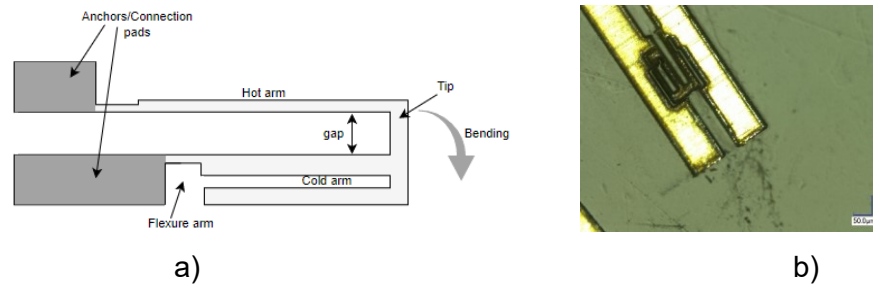


Figure 8.35. Modified version of design E having cold arm with a passive fin structure: a) schematic diagram; b) laser cut-out of the corresponding actuator.

One of the samples fabricated following this design in combination with an asymmetrical cantilever is shown in Figure 8.36a. Such a sample excited at a 50% duty cycle still showed an elliptical pattern, which became much wider in the case of smaller duty cycle. The fiber scan at a 15% duty cycle and at 12.4V input voltage is shown in Figure 8.36b.

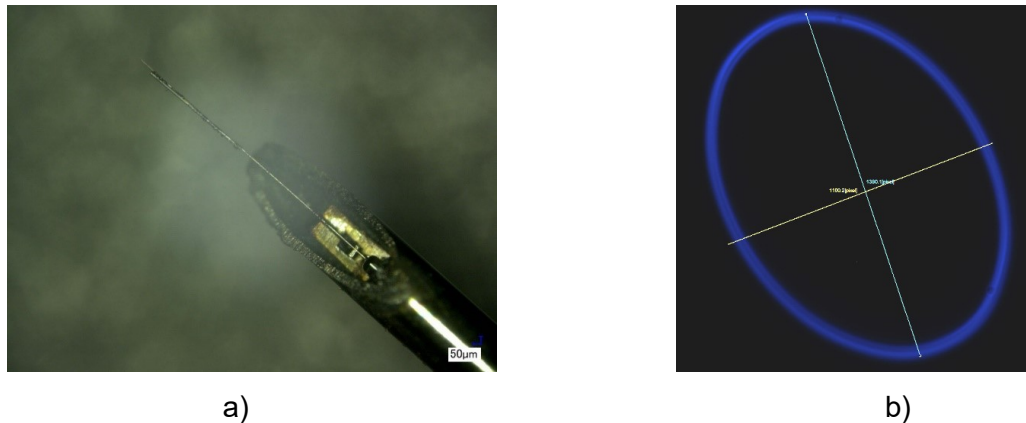


Figure 8.36. Sample with modified design E actuator configuration: a) cantilever-actuator assembly; b) scan from fiber tip in case asymmetry towards the cold arm.

8.7. 2D scan

As all the samples are handmade, the performance of each sample was different and affected the scanning pattern as well. Some samples generated a wider ellipse having a pattern close to that of a circle, while others had a scanning pattern more like an ellipse. The repeatability of a scanning pattern also varied among the samples and the driving power levels. All the samples showed a repeatable and stable behaviour if the driving power levels were considered safe enough to avoid the plastic deformation of the bridge material, i.e., the heat generated by the Joule effect was not causing displacement of the actuator surface which was not recoverable during the cooling phase. The samples were run under safe power levels for 5-10 minutes which was the typical time for the endoscopy procedure without having any degradation over time. At very high actuation power levels, the fiber tip started to become unstable causing the scanning pattern to drift while keeping the same frequency and input power, and the performance was not repeatable. It was mainly due to the plastic deformation of the brass which expanded beyond its reversible limit. Using the device under these conditions for a longer period of time, increased the average length of the bridge in time causing the fiber to bend more and break at the fixed end at certain point. Thus, to get a repeatable and stable scanning pattern, it was desirable to run the actuator at voltages not over 7.5 V for 50% duty cycle, and not over 15 V for 10% duty cycle.

The distal end of the cantilever fiber followed an almost circle shaped pattern as required, and a 2D scan was obtained using frequency sweeping. Using the optical bench setup shown in Figure 5.15, the sample was mounted on the 3D stage. In this preliminary setup of the final design, the light from the vibrating fiber tip was imaged using the camera. Using the function generator, the vibration frequency was manually changed using 7 V of input power and 50% duty cycle to detect the resonant frequency providing a large ellipse/circle. For one of the tested samples, the resonant frequency was 1.346 kHz, and the generated scan pattern at 13 V and 10% duty cycle is shown in Figure 8.37. At given actuation parameters, a frequency away from the resonant frequency was determined to be 1.220 kHz where the displacement of the fiber tip was almost zero.



Figure 8.37. Front view of cantilever scan for vibration at its resonant frequency.

Once the maximum and minimum frequency were manually determined, these values were fed into the variable frequency generation portion of the cantilever control code. In the case where the variable frequency was generated fast enough to overcome the value of the frame rate of the camera, it was possible to see the complete filled area of the scanning pattern as in Figure 8.38, where the major diameter of the generated ellipse was about $110\ \mu\text{m}$ while the minor diameter was about $90\ \mu\text{m}$. The light intensity changed within the scan area increasing from the periphery to the center of the scan area due to fact that the bent of the fiber tip increased with the tip displacement making the light out of focus at that point.

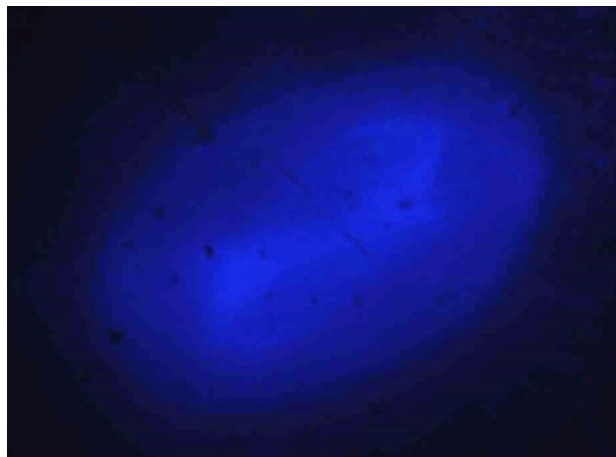


Figure 8.38. The scanning pattern from the fiber tip under the variable frequency scan.

8.8. Conclusions

The original proposed design of having a linear scan from the fiber tip and rotating the whole assembly to get a 2D scan required a complex system. The actuator and cantilever designs were altered to get a circular shaped scan from the distal end of the vibrating cantilever.

The principal modification in the actuator design consisted of optimizing the asymmetry between the two legs of the bridge structure allowing its free end to move in both horizontal and vertical directions. On the other hand, the cantilever tip was also made asymmetric by adding a piece of 12 μm fiber to the distal end of fiber. It is to be noted that the position of the asymmetry in the cantilever with respect to that of the actuator played a key role on the performance of the sample. A wide circular shaped scan was obtained by adding the asymmetrical fiber portion on the upper side of cantilever fiber and moved slightly towards the colder arm of the actuator.

Once a circular pattern was obtained, the 2D scan was realized by changing the excitation frequency near the resonant frequency.

Chapter 9.

Fabrication and testing of final assembled device

This chapter consists of the fabrication of the final prototype design based on the modifications described in previous chapters to obtain the optimal desired performance. In the second part of the chapter, the target object was scanned using the light coming from the vibrating fiber tip, and its image was reconstructed by collecting the reflected light within the device itself.

This chapter addresses OBJECTIVE 6 of the thesis: “Develop the final prototype catheter using a DCF as a cantilever and acquire image collecting the reflected light within the system itself”.

9.1. Introduction

The proposed dimensions of a sub-millimeter sized optical scanner determine some specifications for the design parameters. The key benchmark was the fact that the entire assembly needs to be encapsulated within a tube that is approximately 600 μm in diameter. Another key parameter was the tip displacement of the scanning fiber as it related to the image resolution and will be discussed later in the chapter. A higher tip displacement of the fiber tip resulted in a higher image resolution and increased field of view (FOV). Resonance was considered a key process enabling the high tip displacement of a vibrating cantilever at small actuation force/displacement. The project was based on the use of an electro-thermal actuator due to size limitations and higher force density at a given input power.

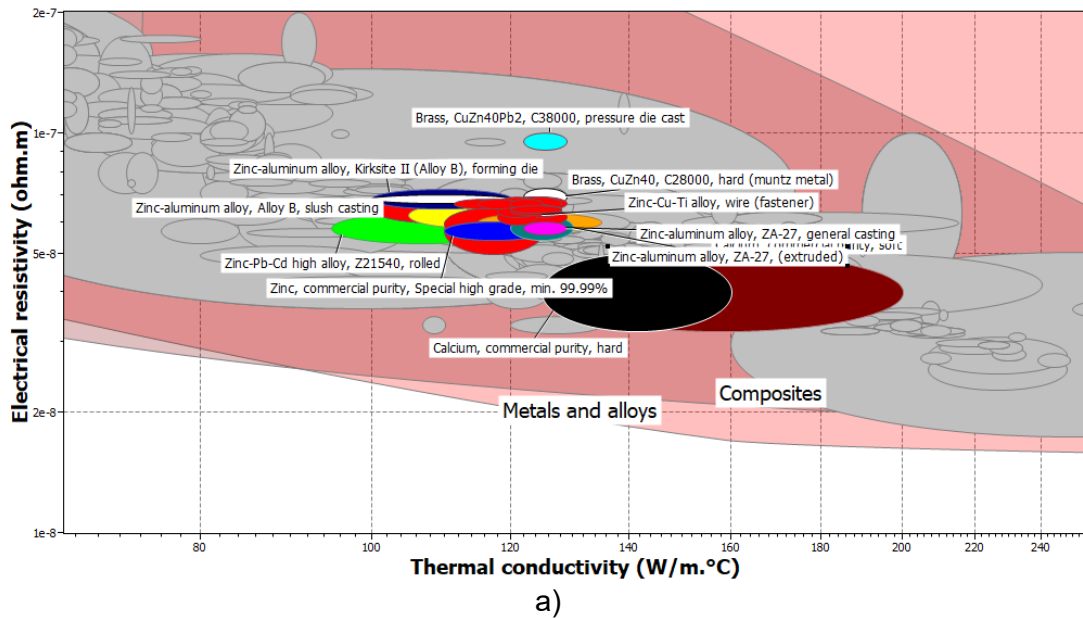
Another important design parameter was the frequency at which the fiber is vibrated. Considering the fiber was made of pure silica, Table 9.1 summarizes the resonance frequency as a function of cantilever fiber's length and diameter. The vibrating frequency was set to 1-2 kHz. This value resulted from a compromise based on the fact that a high frequency was required for in-vivo imaging, while it would be hard to dissipate heat within the small dimensions of the actuator. A 2 kHz first resonance mode frequency

estimated the cantilever length to be about 2-3 mm having a diameter of 10-12 μm as discussed in Chapters 4 and 5 in detail.

Table 9.1. Resonance frequency in Hz as a function of cantilever dimensions.

Diameter [μm] Length [mm]	10	12	15
1.00	8057.76	9669.31	12086.63
2.00	2014.44	2417.32	3021.66
3.00	895.31	1074.37	1342.96

Another key parameter in the device was the material needed to fabricate the actuator. As stated in Chapter 4 and [163], the key parameters considered in the material selection are: electrical resistivity, thermal conductivity, and coefficient of linear thermal expansion. Figure 9.1 shows different materials in “Granta: CES Selector” software package with their electrothermal material properties described above. Brass was selected to be the material for the actuator based on its better selection properties, ease of use and connection with the conducting wires.



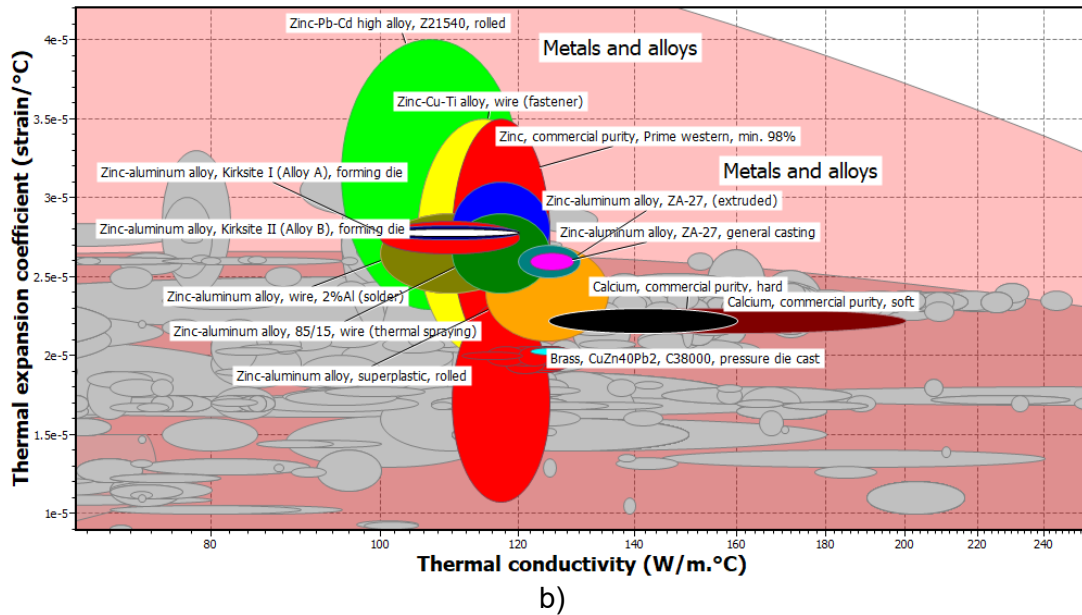


Figure 9.1. Material comparison in “Granta: CES Selector” software package based on thermal conductivity vs: a) electrical resistivity; b) thermal expansion coefficient.

Another important aspect of the device was FOV that can be imaged on the imaging plane. FOV highly depends on the tip displacement of the vibrating cantilever and the lens setup/assembly placed at the distal end of the device, as stated in Chapter 7. Simulations performed in Chapter 7 shows that a $\pm 100 \mu\text{m}$ cantilever displacement and the use of an off-the-shelf GRIN-IFRL-035-005-50 grin lens with $350 \mu\text{m}$ diameter provided a 38° FOV.

One of the other key parameters describing the performance of the device was the image resolution. The resolution of the image captured using an imaging device can be limited in terms of optical or sampling aspects described below.

9.1.1. Optical aspect of the resolution

The resolution defines the smallest resolvable feature imaged using an imaging system. In scanning fiber endoscopes, the resolution depends on the peak-to-peak scan amplitude and the core diameter of the fiber. In the case of the current DCF fiber used, the core size was $9 \mu\text{m}$ for a $\pm 100 \mu\text{m}$ cantilever tip displacement.

The resolution can be better estimated using the full width at half maximum (FWHM) of the light distribution coming out of the fiber. The FWHM from a single mode fiber can be calculated considering the Gaussian distribution of light. The core of the DCF, considered initially, acts as a single mode for 1550 nm (infrared) wavelength light source. In this case the visible light needs to be used for imaging, and it is better to consider either a custom made DCF having a core acting as single mode at a desired wavelength, or the cantilever made of a single mode fiber (460HP, Thorlabs) and a peripheric ring of multiple fibers to collect the reflected light.

460HP fiber has a core size of 2.5 μm and a mode field diameter (MFD) of 3.5 μm at 515 nm wavelength (green) light. MFD is a measure of the width of irradiation distribution, and in the Gaussian beam distribution of light is equal to the diameter of the Gaussian field where the light intensity is $1/e^2$. The light of a Gaussian beam varies as:

$$I(r) = I_0 e^{-2r^2/w^2} \quad (1)$$

Where I_0 is the light intensity at the center of the beam, r is the radial distance from the center of the beam, and w is the radius at which the light intensity is decreased to $1/e^2$ (also called Gaussian beam radius).

FWHM is the full width of the beam where the light intensity of the beam reduces to half. Thus,

$$0.5 = e^{-2\left(\frac{FWHM}{2}\right)^2/w^2} = e^{-FWHM^2/2w^2} \quad (2)$$

$$-2 \ln(0.5) = \frac{FWHM^2}{w^2} \quad (3)$$

$$FWHM = 1.1774 * w \quad (4)$$

For 460HP fiber, w is equal to 1.75 μm . Thus, the FWHM for such a fiber is 2.06 μm . Therefore, the resolution at the cantilever plane defined by the light distribution from the fiber (point spread function) is 2.06 μm .

The resolution at the tissue is reduced owing to the magnification of the lens system. In this case, a GRIN-IFRL-035-005-50 lens is mounted at the distal end of the fiber with a magnification of about 4.4x, the smallest resolvable feature will be about 9.06

μm . If the GRIN-IFRL-50-005-50 lens is used with an object working distance of $120 \mu\text{m}$, the magnification is about 2.9x, which makes the resolution to be about $5.97 \mu\text{m}$.

In a real system, the point spread function describing the distribution of light in a conjugate image plane will be aberrated by the optical system, increasing its size, and sacrificing resolution.

9.1.2. Sampling aspect of the resolution

Another limiting aspect of an imaging system is determined by the Nyquist criteria. It states that a sampling interval between the two adjacent samples is at least one-half of that of the spatial resolution to maintain the spatial resolution in the image. If the sampling occurs at an interval less than the value determined by the Nyquist criteria, the finer details with high spatial frequency will be lost causing sampling artifacts (or under sampling).

In the originally proposed linear scan, the assembly is proposed to rotate at 10 Hz. If the unidirectional scanning of $\pm 100 \mu\text{m}$ is implanted at scan rate of 1 kHz allowing to capture 50 image diameters per frame ($1000 \times 10/20$), it allows a radial resolution of 7.2° ($360/50$).

The design considerations analyzed in previous Chapters (4 to 8) allowed the distal end of the scanning fiber to be vibrated in resonance generating a circle shape pattern with the possibility to have a complete bi-dimensional scan by sweeping the vibrating frequency in a short range around the resonant value.

For sampling resolution of new scan patterns, it is best to consider the largest diameter circular scan as it will be the worst scenario. In a circular scan of $200 \mu\text{m}$ diameter at 1 kHz where a frequency sweep is performed at 10 Hz to sweep the area inside the circle, it allows the capture of 20 points along the diameter per frame. Thus, it has a radial resolution of $10 \mu\text{m}$.

These modifications were considered in the final design fabrication and are analyzed below in detail.

9.2. Fabrication and Packaging

The actuator in the final device is made up of 25 μm thick brass foil which was laser cut into the modified design pattern shown in Chapter 8. The asymmetric bridge structure was manually lifted, and the fiber was placed in the perpendicular direction with respect to the free end of the bridge.

The cantilever portion of the scanning fiber can be either fabricated using the heating and pulling method with the help of heat fusion splicer or using chemical wet etching by immersing the desired portion of the fiber in a buffer oxide etchant solution. From the analysis performed in Chapter 6, it was noted that the chemical etching enabled cantilever fabrication that maintained the continuity of the fiber core, which avoided the leakage of the light present in the case of first method. On the other hand, the interface surface did not show a perfect flat surface at the transitional region in the chemical etching method.

However, based on the analysis performed in Chapter 7, it was noted that the light collected through the inner cladding surface in the case of a perfect linear region is very small compared to the illumination light shone on the target sample. The signal to noise ratio was further decreased by the aberrations introduced by the lens system at the device tip as mentioned in the previous chapters. Moreover, the light leakage at the transitional region in the case of spliced cantilever, or a non-flat surface in the etched cantilever further decreased the signal to noise ratio. Moreover, in the modified actuator design, the fiber was placed perpendicularly with respect to the bridge structure, and as shown in Figure 9.2, the presence of the bridge structure blocked almost half of the inner cladding surface proposed to collect reflected light.

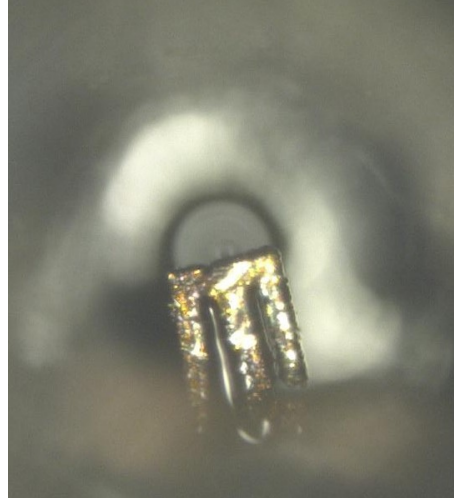


Figure 9.2. Front view of actuator-cantilever assembly.

Taking these findings into account and based on the resolution aspects performed above, a 460HP fiber with core size of $2.5\ \mu\text{m}$ was used for the cantilever fiber whose tip was fabricated using the chemical etching method, and the distal end of the cantilevered fiber was slightly melted to have micro-balled lens effect. These measures were considered to reduce the insertion losses in the fiber and have a more focused light on the target surface. The cantilevered fiber had an additional piece of $12\ \mu\text{m}$ fiber glued at its tip. Meanwhile, the backscattered reflected light from the target sample was collected using an external ring of multimode fibers.

To further enhance the heat dissipation from the actuating bridge area to the surrounding surface, experimentation was conducted to either cut a glass coverslip (Figure 9.3a) or diamond (Figure 9.3b) in the collar shape and place it near the bridge. However, the heat distribution around the bridge in both cases caused the bridge to melt easily. Thus, in the final assembly, the actuator and micro-cantilever fiber were assembled with the help of SU-8 collar structures as described in detail in Chapter 4.

The packaging steps of the sample fabrication are shown in detail in Figure 9.4. Like what was discussed in Chapter 4, the semi-circle collar structures were placed in the groove of the metal actuator (Figure 9.4a) and the upper collars were mounted on the SMF fiber (Figure 9.4b). A thin layer of epoxy was applied on both structures to fix them in place. The two parts were then connected using another layer of epoxy (Figure 9.4c). After the two parts were fixed, an additional piece of $12\ \mu\text{m}$ fiber was glued at the cantilever tip using epoxy (Figure 9.4d). After the curing of the epoxy, a thin layer of heat-cured

epoxy (EP17 HTND-CCM, MasterBond) was applied to the assembly which was then pushed inside the needle and cured (Figure 9.4e).

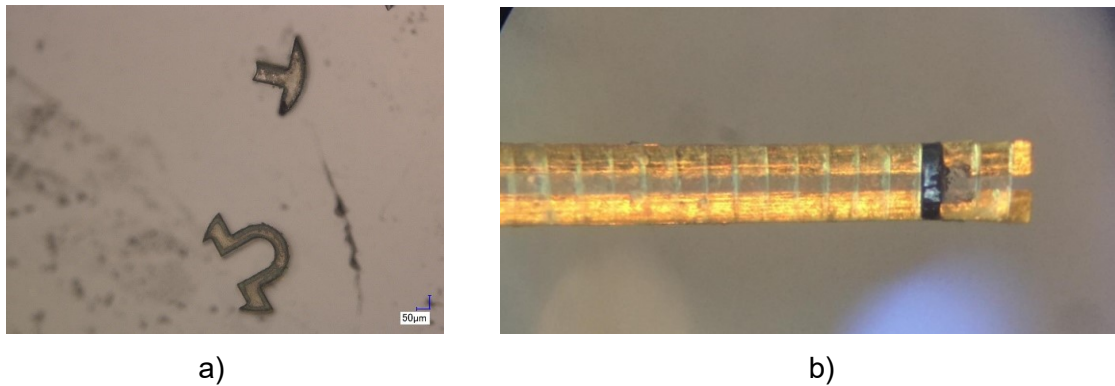


Figure 9.3. Collar structures made from laser cutting of: a) glass coverslip; b) diamond.

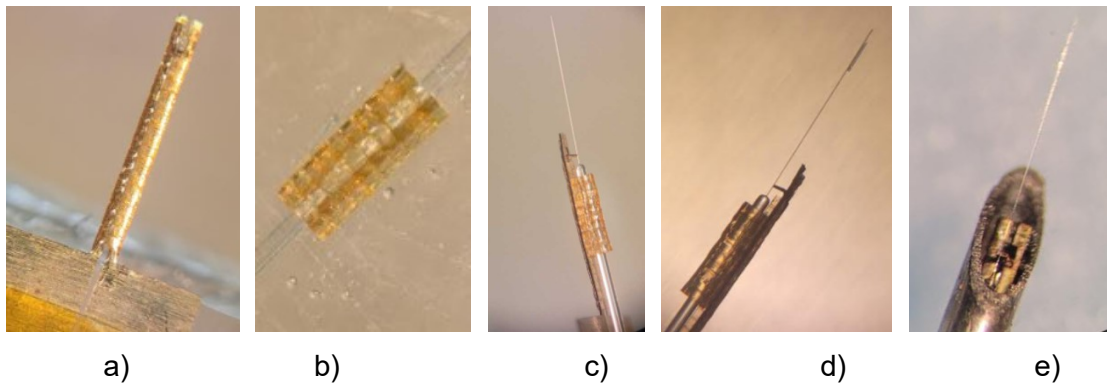


Figure 9.4. Packaging of the sample: a) semi-circle collars placed in the actuator groove; b) upper collars attached to the fiber; c) assembly of cantilever and actuator parts; d) an asymmetry is added to the cantilever tip; e) assembled device fixed inside the nitinol needle.

The schematic design of the final proposed packaged assembly is shown in Figure 9.5. As stated above in the final planned design, a single mode cantilevered fiber carried light from a laser connected to its proximal end through its core to the cantilever tip. The light leaving the micro-cantilever's tip was focused on the image/focal plane using the focusing GRIN lens. The backscattered reflected light was collected by the external multimode fibers placed at the periphery of the device in a ring structure placed at about 680 µm away from the lens surface towards the target sample.

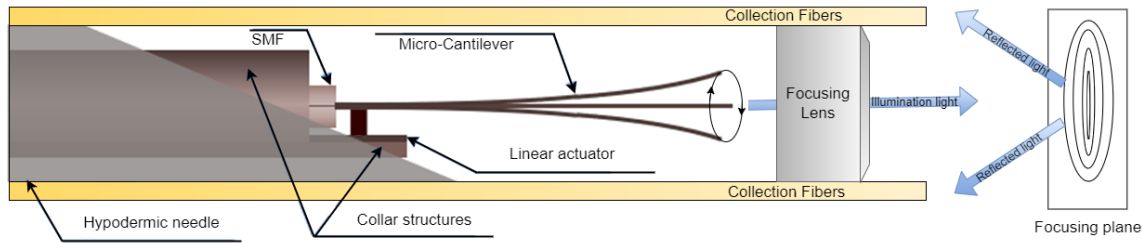


Figure 9.5. The schematic design of the final packaged assembly.

9.3. Testing Setup

The prototype samples were tested to evaluate the performance of their distal tip to a periodic input from the actuating bridge structure. Since all the samples were fabricated and assembled by hand, there were some deviations in the angle of the actuating bridge lifted manually, distance of the fixed end of the fiber relative to the actuating bridge, position of the fiber on top of the bridge, amount of epoxy applied to the sample, curing time, etc. Thus, the performance of each sample was different. As discussed in the previous chapter, these variations have an important impact on the performance of the sample.

The cantilever tip scanned the object in an elliptical/circular manner, while the continuous change in the frequency of vibration varied the diameter of the scanned circle. Thus, the sample was scanned in 2D in a spiral pattern. As stated above, each sample different from each other, so the resonant frequency of each sample was first monitored by manually changing the signal and analyzing the tip displacement as stated in Chapter 5.

A spiral scanning geometry was proposed to create a two-dimensional image. As discussed above, the cantilever scanned in a circular pattern (fast-axis of the scan) while the frequency change allowed it to scan across the circle (slow axis of the scan). The rate at which the actuation frequency was changed affected the resolution of the image. Altogether with the resonant frequency, the change in the circle diameters with the excitation frequency are also noted to generate diameter vs excitation frequency curves similar those reported in Figure 8.32.

This value of the resonant frequency with the range of variability of the frequency was assigned to the cantilever control program which sent the corresponding signal to the

DAQ board. The DAQ board was programmed to generate variable frequency signals to the actuator. The DAQ also converted the analog signal from the photodetector and converted it into digital form using an appropriate converter.

9.4. Future Proposed Imaging Setup

The imaging setup for evaluating the performance of the final proposed samples was like one performed earlier and reported in [24] and Chapter 5. As shown in Figure 9.6, the laser light from the vibrating fiber was scanned on the target sample. The backscattered reflected light was collected from the optical fibers placed at the periphery of the sample and was projected on the photo detector. The output from the detector was connected to a DAQ board which collected the analog light intensity from the detector. The data from the DAQ board was further processed in the cantilever control program to reconstruct the scanned image.

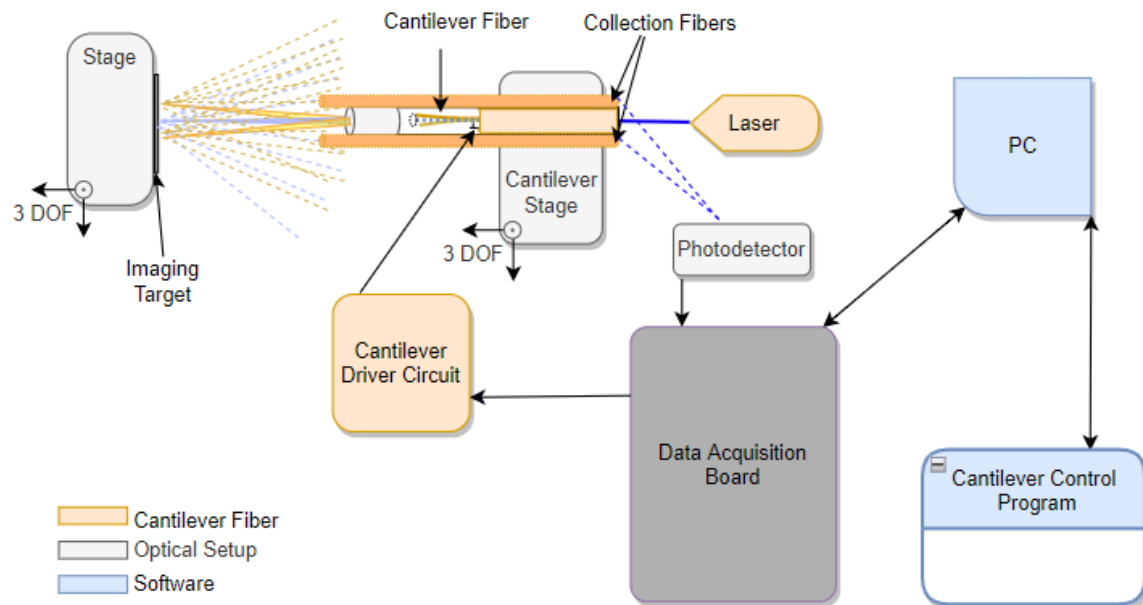


Figure 9.6. Schematic diagram of the proposed testing setup.

The digitization of the analog signal detected by the photodetector and the image interpolation curves to generate the final image are still under progress and can be developed following a similar path used in Chapter 5 for the image reconstruction.

Chapter 10.

Conclusion

The design of a sub-millimeter sized optical fiber scanner is presented in this thesis. The proposed work was the first to set the basis for the development of a sub-millimeter sized catheter for real time imaging of the small airways of the lung. It has the potential to provide new medical imaging technology that can increase the diagnostic yield of the peripheral lesions in the lungs, at the openings of pancreatic ducts, fallopian tubes, and other areas affected by pulmonary diseases.

The proposed scanner consisted of a vibrating optical fiber that carried the laser light to the target imaging area, and the backscattered reflected light was captured within the same device using a peripheric ring of more optical fibers. The desired vibratory motion of the scanning cantilevered fiber was obtained using an electro-thermal actuator which periodically excited the distal end of the scanning fiber to move. The proposed goal was evaluated by addressing the following objectives:

OBJECTIVE 1: Develop and configure a preliminary prototype using a novel thermal actuated cantilever able to meet the desired size requirements.

OBJECTIVE 2: Validate and test the developed prototype through experimentation and image the tip displacement of the cantilever fiber via an optical setup and reconstruct the radial scan from the light coming out from the tip of the Single Mode Fiber (SMF) cantilever.

OBJECTIVE 3: Fabricate the cantilever fiber minimizing the power leakage at the transitional zone between the fixed fiber portion and cantilever.

OBJECTIVE 4: Fabricate the cantilever using a Double Clad Fiber (DCF). Collect the reflected light signal in all cases via inner cladding and compute the signal to noise ratio (SNR).

OBJECTIVE 5: Design a rotary joint supporting optical and electrical signals or find alternative ways to avoid such connection by exciting the cantilever along two axes.

OBJECTIVE 6: Develop the prototype catheter using a DCF as a cantilever and acquire image collecting the reflected light within the system itself.

These objectives were addressed in Chapters 4 to 9 as follows:

The 1st objective was addressed in Chapter 4 by designing and prototyping optical scanners packaged in a hypodermic needle having a diameter of about 500 μm . This chapter elaborated on the overview of the design of an electro-thermal actuator made up of a 25 μm thin brass foil which was laser cut using an excimer laser in a pattern described in detail in Chapter 1. A bridge like structure was manually lifted 90° which expanded and contracted with periodic current passage due to the Joule heating effect. A 125 μm single mode fiber having a 2.5 μm core was connected to a 12 μm multimode fiber which was tapered down using a Vytran splicer where the controlled temperature and pulling of the fiber produced the desired diameter. The actuator and cantilevered fiber were assembled with the help of a series of SU-8 collars manufactured using the soft-lithography process. The two parts were joined together using epoxy such that the spliced region was about 100 μm apart from the uplifted bridge. A heat resistant epoxy was then applied on the entire assembly which was then pushed inside the hypodermic needle and cured.

The 2nd objective of validating and testing the prototype samples was met as described in Chapter 5. Mathematical models of the resonant vibration were briefly described in this chapter. The performance of the proposed design was simulated using COMSOL Multiphysics and ANSYS. The vibration response of cantilevered fiber was then imaged under a microscope for a sideview and using an optical setup for a front view. It was noted that the tip displacement of the fiber followed an elliptical path instead of a linear one when actuated in single direction due to the whirling effect generated from the nonlinear cross-coupling of the motion between two axes. Samples on this stage were moved in a single direction to get a line scan, and the imaging target sample was rotated to prove the concept of 2D imaging using this scanner.

The 3rd objective of fabricating cantilevered fibers with minimum power leakage was achieved in Chapter 6. The cantilevered fibers developed in Chapter 3 using the heating and pulling method required a separate fabrication of the thinner fiber and then its connection to the single mode fiber. Due to the non-perfect alignment of the cores of the two fibers, there was some leakage in correspondence to the connection area. In the original idea, it was proposed to use a double clad fiber in the scanner where the light from the laser source was transmitted to the sample area through its core, and the reflected light was captured through its inner cladding. In such a case, the leaked light acted as

noise in the reflected light collection signal causing blur and reduction of contrast in the image. Moreover, it required higher amount of light to be shone on the desired imaging tissue surface. This light leakage was avoided by developing a different cantilever fabrication method based on the modified chemical etching of the fiber in buffer oxide etchant solution which eroded the sides of the fiber to the desired dimensions. The tapering of the fibers during wet etching caused by the rising of etchant solution along the sides of the fibers on the dry side due to capillary effect was prevented by blocking the solution with a flexible membrane.

The 4th objective of fabricating the cantilever using a DCF and collecting the reflected light signal using inner cladding to compute the SNR was addressed in Chapter 7. First, the cantilever was fabricated using a double clad fiber with both splicing and tapering methods described in Chapters 4 and 6. The light was then transmitted through the central core of the stationary fiber and reflected light from a mirror surface was captured through the cladding and separated from the emitted light using a double clad fiber coupler. The light collection efficiency in both cases was noted to be very small. To evaluate the light collection efficiency in the case of the scanning fiber, and tissue surface as the target sample, Zemax simulations were performed. From the simulation results, only 0.5% of the emitted light was captured via the inner cladding. However, this amount emitted light was even less in real cases, due to aberrations introduced by the lens and by the presence of actuator which blocked some areas of the inner cladding. Moreover, the light leakage in the case of the cantilever fabricated using the spliced method, or nonperfect flat interface in the case of the etched cantilever reduced the actual amount of light captured via cladding. Thus, to better capture the reflected light, it was proposed to use a ring of multimode fiber at the periphery of vibrating cantilever.

The 5th objective of designing a rotary joint supporting optical and electrical signals or finding alternative ways to avoid such connections by exciting the cantilever along two axes was met in Chapter 8. Most of the current available hybrid fiber optic rotary joints permitting the continuity of electrical and optical connection of a fixed and rotating sides were available in dimensions in the centimeter range. There is no off-the-shelf available hybrid FORJ compatible with the size of the proposed scanner. Thus, the actuator was modified and optimized using mathematical equations and simulations performed in MATLAB to get the highest bi-directional actuation from a single actuator. Furthermore, the cantilever design was also altered by adding a small piece of additional fiber towards

the distal end of the fiber to one side. These changes allowed the cantilever tip to scan in a circular pattern.

The final objective 6, was addressed in Chapter 9 where the final design to get a bi-dimensional image was proposed. For white light imaging, and situations explored in Chapters 7 and 8, a SMF was chosen for the final design. The actuator and cantilever in this design were fabricated based on the analysis performed in previous chapters. The asymmetric cantilever and bridge structure in the actuator made the fiber tip move in a circular shaped pattern. A 2D scanning of the target sample was performed by changing the vibration frequency near the resonant frequency. The frequency offset from the resonance value caused the scanning circle to be small. Thus, the continuous change in frequency allowed the tip to move in a spiral manner. The reflected light was proposed to be collected using the external multimode fibers placed at the periphery of the scanning device in a ring-shaped pattern.

10.1. Future Work

The presented work provides a considerable contribution towards the proposed sub-millimeter sized endoscopic catheter head. All the samples currently tested were based on the fabrication of a few millimeters long probe device. However, an actual endoscopic catheter requires samples which are a few meters long to advance through the instrument channel of the bronchoscope to reach the target imaged area. Another possible feasibility risks include a potential temperature variation in the confined testing environment in the case of in-vivo testing which could highly impact the performance of the cantilever oscillation. In such a case, other methods of thermal compensation or heat dissipation could be employed, or a smaller amount of input power could be used. Another possible solution is to run the device intermittently giving an interrupted visualization of the imaging tissue avoiding overheating of the tissue or actuator itself.

The current system is working using the blue light laser source for direct light imaging based on the fiber used. It is possible to incorporate red, green, and blue lasers to get the reflected light colour image. Moreover, fluorescence imaging can be obtained in parallel by using a 50/50 beam splitter at the end of the collection fibers. A portion of the reflected light is forwarded to an avalanche photodiode for reflected light imaging, while using a fluorescence filter cube at place of 50/50 beam splitter, the fluorescent light signal

can be forwarded to a photo-multiplier tube for fluorescence imaging. It is also possible to use a Near infrared light source so that the light can penetrate deeper into the tissue and provide a high fluorescent signal when using exogenous contrast agents.

The different elements to develop the proposed scanner are evaluated in this thesis, while the final step to integrate all these elements is still under progress. In the future design, it is possible to incorporate the imaging collecting fibers at the periphery of the developed scanner. A more detailed image reconstruction program needs to be developed based on the changes to the scanner design introduced in Chapters 6 to 9.

It is also possible to develop a sideview scanner based on the proposed imaging device. A prism, mirror, or a reflecting surface can be mounted at the distal end of the device to bend the outgoing light at the desired angle. Moreover, the device in this case requires a transparent optical window on the side of the probe to allow the outgoing light to be transmitted on the target surface.

The final device requires an encapsulation protective sheath made up of bio-safe material like polyethylene terephthalate (PETE), or polyether block amide (Pebax). The minimum thickness of such tubes ranges from 20 μm to 50 μm . Thus, the final diameter of the device will be around 600 μm to 630 μm . The rigid length will be around 7mm which includes a 2.5 mm long actuator foil (without connection pads with wires), 2 mm of cantilever length, a 0.79 mm long GRIN lens, and estimated working distance of about 1.25 mm.

The imaging system requires testing at its various stages including on-the-bench testing, followed by testing in tubular structures having dimensions like those of smallest lung airways. Once such tests are performed well, it is possible to image some biologically relevant ex vivo tissues finally followed by an in-vivo imaging.

References

- [1] S. Coda and A. V. Thillainayagam, "State of the art in advanced endoscopic imaging for the detection and evaluation of dysplasia and early cancer of the gastrointestinal tract," *Clinical and Experimental Gastroenterology*, vol. 7, pp. 133-150, 2014.
- [2] J. Mannath and M. Banks, "Emerging technologies in endoscopic imaging," *F1000 Med Reports*, vol. 4, no. 3, 2012.
- [3] W. H. Organization, "Fact sheets Cancer," 12 09 2018. [Online]. Available: <https://www.who.int/news-room/fact-sheets/detail/cancer>. [Accessed 04 09 2019].
- [4] W. H. Organization, "Chronic obstructive pulmonary disease," 1 12 2017. [Online]. Available: [https://www.who.int/en/news-room/fact-sheets/detail/chronic-obstructive-pulmonary-disease-\(copd\)](https://www.who.int/en/news-room/fact-sheets/detail/chronic-obstructive-pulmonary-disease-(copd)). [Accessed 04 09 2019].
- [5] W. H. Organization, "<http://gco.iarc.fr/today/data/factsheets/cancers/13-Pancreas-fact-sheet.pdf>," 2018. [Online]. Available: <http://gco.iarc.fr/today/data/factsheets/cancers/13-Pancreas-fact-sheet.pdf>. [Accessed 04 09 2019].
- [6] W. H. Organization. [Online]. Available: <http://gco.iarc.fr/today/data/factsheets/cancers/25-Ovary-fact-sheet.pdf>. [Accessed 5 09 2019].
- [7] Y. Toyoda, T. Nakayama, Y. Kusunoki, H. Iso and T. Suzuki, "Sensitivity and specificity of lung cancer screening using chest low-dose computed tomography," *British Journal of Cancer*, vol. 98, no. 10, pp. 1602-1607, 2008.
- [8] P. Tummala, O. Junaidi and B. Agarwal, "Imaging of Pancreatic cancer: An overview," *Journal of Gastrointestinal Oncology*, vol. 2, no. 3, pp. 168-174, 2011.
- [9] V. R. Iyer and I. S. Lee, "MRI, CT, and PET/CT for Ovarian Cancer Detection and Adnexal Lesion Characterization," *American Journal of Roentgenology*, vol. 194, pp. 311-321, 2010.
- [10] R. S. Wiener, D. C. Wiener and M. K. Gould, "Risks of Transthoracic Needle Biopsy: How High?," *Clinical Pulmonary Medicine*, vol. 20, no. 1, pp. 29-35, 2013.
- [11] J. W. Memoli, J. P. Nietert and G. A. Silvestri, "Meta-analysis of Guided Bronchoscopy for the Evaluation of the Pulmonary Nodule," *Chest*, vol. 142, no. 2, pp. 385-393, 2012.

- [12] "Lung cancer fact sheet," Lung Cancer Fact Sheet, [Online]. Available: <https://www.lung.org/lung-health-and-diseases/lung-disease-lookup/lung-cancer/resource-library/lung-cancer-fact-sheet.html>. [Accessed 05 09 2019].
- [13] "Prognosis," Hirshberg foundation for pancreatic cancer research, [Online]. Available: <http://pancreatic.org/pancreatic-cancer/about-the-pancreas/prognosis/>. [Accessed 05 09 2019].
- [14] "Ovarian, Fallopian Tube, and Peritoneal Cancer: Statistics," Cancer.Net, 1 2019. [Online]. Available: <https://www.cancer.net/cancer-types/ovarian-fallopian-tube-and-peritoneal-cancer/statistics>. [Accessed 05 09 2019].
- [15] C. M. Lee, C. J. Engelbrecht, T. D. Soper, F. Helmchen and E. J. Seibel, "Scanning Fiber endoscopy with highly flexible, 1 mm catheterscopes for wide-field, full-color imaging," *Journal of biophotonics*, vol. 3, no. 5-6, pp. 385-407, 2010.
- [16] "Lung Cancer," Lung Cancer Canada, [Online]. Available: <https://www.lungcancercanada.ca/Lung-Cancer.aspx>. [Accessed 25 05 2022].
- [17] M. Kaur, P. M. Lane and C. Menon, "Endoscopic Optical Imaging Technologies and Devices for Medical Purposes: State of the Art," *Applied Sciences*, vol. 10, no. 19, pp. 6865:1-34, 2020.
- [18] X. Leng, W. Chapman, B. Rao, S. Nandy, R. Chen, R. Rais, I. Gonzalez, Q. Zhou, D. Chatterjee, M. Mutch and Q. Zhu, "Feasibility of co-registered ultrasound and acoustic-resolution photoacoustic imaging of human colorectal cancer," *Biomedical Optics Express*, vol. 9, no. 11, pp. 5159-5172, 2018.
- [19] J. Zhou and J. V. Jokerst, "Photoacoustic imaging with fiber optic technology: A review," *Photoacoustics*, vol. 20, pp. 100211:1-18, 2020.
- [20] R. Ubbink, L. J. D. van Dijk, D. van Noord, T. Johannes, P. A. C. Specht, M. J. Bruno and E. G. Mik, "Evaluation of endoscopic visible light spectroscopy: comparison with microvascular oxygen tension measurements in a porcine model," *Journal of translational medicine*, vol. 17, no. 1, pp. 65: 1-9, 2019.
- [21] D. A. Benaron, I. H. Parachikov, W.-F. Cheong, S. Friedland, B. E. Rubinsky, D. M. Otten, F. W. H. Liu, C. J. Levinson, A. L. Murphy, J. W. Price, Y. Talmi, J. P. Weersing, J. L. Duckworth, U. B. Hörtchner and E. L. Kermit, "Design of a visible-light spectroscopy clinical tissue oximeter," *Journal of Biomedical Optics*, vol. 10, no. 4, pp. 44005-44009, 2005.
- [22] J. A. Udovich, N. D. Kirkpatrick, A. Kano, A. Tanbakuchi, U. Utzinger and A. F. Gmitro, "Spectral background and transmission characteristics of fiber optic imaging bundles," *Applied Optics*, vol. 47, no. 25, pp. 4560-4568, 2008.

- [23] D. Scheffer, "Endoscopes use CMOS image sensors," *Vision Systems Design*, 30 07 2007. [Online]. Available: <https://www.vision-systems.com/home/article/16750278/endoscopes-use-cmos-image-sensors>. [Accessed 28 07 2020].
- [24] M. Kaur, M. Brown, P. M. Lane and C. Menon, "An Electro-Thermally Actuated Micro-Cantilever-Based Fiber Optic Scanner," *IEEE Sensors Journal*, vol. 20, no. 17, pp. 9877-9885, 2020.
- [25] L. V. Wang and H.-i. Wu, *Biomedical optics: principles and imaging*, New Jersey, USA: Wiley, 2007.
- [26] J. G. Fujimoto, C. Pitris, S. A. Boppart and M. E. Brezinski, "Optical Coherence Tomography: An Emerging Technology for Biomedical Imaging and Optical Biopsy," *Neoplasia*, vol. 2, no. 1-2, pp. 9-25, 2000.
- [27] A. M. Zysk and S. A. Boppart, "Optical Coherence Tomography," in *Optical Imaging and Microscopy: Techniques and Advanced Systems*, 401-436, Springer, 2007, pp. Heidelberg, Berlin.
- [28] C. Boudoux, *Fundamentals of Biomedical Optics: from light interactions with cells to complex imaging systems*, Montreal: pollux, 2017.
- [29] D. P. Popescu, L.-P. Choo-Smith, C. Flueraru, Y. Mao, S. Chang, J. Disano, S. Sherif and M. G. Sowa, "Optical coherence tomography: fundamental principles, instrumental designs and biomedical applications," *Biophysical Reviews*, vol. 3, no. 3, pp. 155-169, 2011.
- [30] Z. Qiu and W. Piyawattanametha, "MEMS Actuators for Optical Microendoscopy," *Micromachines*, vol. 10, no. 2, pp. 85: 1-18, 2019.
- [31] B. J. Kim, D. J. Irwin, D. D. Song, E. R. Daniel, J. D. Leveque, A. R. Raquib, W. L. Pan, G.-S. L. Ying, T. L. Aleman, J. L. Dunaief and M. L. Grossman, "Optical coherence tomography identifies outer retina thinning in frontotemporal degeneration," *Neurology*, vol. 89, no. 15, pp. 1604-1611, 2017.
- [32] B. Lumbroso, D. Huang, C. J. Chen, Y. Jia, M. Rispoli, A. Romano and N. K. Waheed, *Clinical OCT Angiography Atlas*, New Delhi, India: Jaypee Brothers Medical Publishers, 2015.
- [33] J. P. Cunha, R. Proença, A. Dias-Santos, R. Almeida, H. Águas, M. Alves, A. L. Papoila, C. Louro and A. Castanheira-Dinis, "OCT in Alzheimer's disease: thinning of the RNFL and superior hemiretina," *Graefe's Archive for Clinical and Experimental Ophthalmology*, vol. 255, no. 9, pp. 1827-1835, 2017.
- [34] S. A. Boppart, B. E. Bouma, C. Pitris, G. J. Tearney, J. G. Fujimoto and M. E. Brezinski, "Forward-imaging instruments for optical coherence tomography," *Optics Letters*, vol. 22, no. 21, pp. 1618-1620, 1997.

- [35] G. J. Tearney, S. A. Boppart, B. E. Bouna, M. E. Brezinski, N. J. Weissman, J. F. Southern and J. G. Fujimoto, "Scanning single-mode fiber optic catheter-endoscope for optical coherence tomography," *Optics Letters*, vol. 21, no. 7, pp. 543-545, 1996.
- [36] S. W. Paddock, T. J. Fellers and M. W. Davidson, "Introductory Confocal Concepts," *MicroscopyU*, [Online]. Available: <https://www.microscopyu.com/techniques/confocal/introductory-confocal-concepts>. [Accessed 23 06 2020].
- [37] L. Liu, E. Wang, X. Zhang, W. Liang, X. Li and H. Xie, "MEMS-based 3D confocal scanning microendoscope using MEMS scanners for both lateral and axial scan," *Sensors and Actuators A: Physical*, vol. 215, pp. 89-95, 2014.
- [38] D. L. Dickensheets and G. S. Kino, "Micromachined scanning confocal optical microscope," *Optics Letters*, vol. 21, no. 10, pp. 764-766, 1996.
- [39] K. C. Maitland, H. J. Shin, H. Ra, D. Lee, O. Solgaard and R. Richards-Kortum, "Single fiber confocal microscope with a two-axis gimbaled MEMS scanner for cellular imaging," *Optics Express*, vol. 14, no. 19, pp. 8604-8612, 2006.
- [40] I. W. Jung, D. Lopez, Q. Zhen and W. Piyawattanametha, "2-D MEMS Scanner for Handheld Multispectral Dual-Axis Confocal Microscopes," *Journal of Microelectromechanical Systems*, vol. 27, no. 4, pp. 605-612, 2018.
- [41] Cellvizio, "Cellvizio targeted biopsies," Mauna Kea Technologies, [Online]. Available: <https://www.maunakeatech.com/en/cellvizio/10-cellvizio-targeted-biopsies>. [Accessed 09 10 2020].
- [42] E. Laemmel, M. Genet, G. Le Goualher, A. Perchant, J.-F. Le Gargasson and E. Vicaut, "Fibered Confocal Fluorescence Microscopy (Cell-ViZio™) Facilitates Extended Imaging in the Field of Microcirculation," *Journal of Vascular Research*, vol. 41, pp. 400-411, 2004.
- [43] G. Li, X. Duan, M. Lee, M. Birla, J. Chen, K. R. Oldham, T. D. Wang and H. Li, "Ultra-Compact Microsystems-Based Confocal Endomicroscope," *IEEE transactions on medical imaging*, vol. 39, no. 7, pp. 2406-2414, 2020.
- [44] R. Li, X. Wang, Y. Zhou, H. Zong, M. Chen and M. Sun, "Advances in nonlinear optical microscopy for biophotonics," *Journal of Nanophotonics*, vol. 12, no. 3, pp. 033007:1-13, 2018.
- [45] D. W. Piston, T. J. Fellers and M. W. Davidson, "Multiphoton Microscopy," *MicroscopyU*, [Online]. Available: <https://www.microscopyu.com/techniques/multi-photon/multiphoton-microscopy>. [Accessed 23 06 2020].

- [46] J. Huang, N. Li, Q. Wang, Y. Gu and P. Wang, "A lysosome-targetable and two-photon fluorescent probe for imaging endogenous β -galactosidase in living ovarian cancer cells," *Sensors and Actuators B: Chemical*, vol. 246, no. C, pp. 833-839, 2017.
- [47] Z.-R. Liu, Y. Tang, A. Xu and W. Lin, "A new fluorescent probe with a large turn-on signal for imaging nitroreductase in tumor cells and tissues by two-photon microscopy," *Biosensors and Bioelectronics*, vol. 89, no. 2, pp. 853-858, 2017.
- [48] R. Kawakami, K. Sawada, Y. Kusama, Y.-C. Fang, S. Kanazawa, Y. Kozawa, S. Sato, H. Yokoyama and T. Nemoto, "In vivo two-photon imaging of mouse hippocampal neurons in dentate gyrus using a light source based on a high-peak power gain-switched laser diode," *Biomedical Optics Express*, vol. 6, no. 3, pp. 891-901, 2015.
- [49] T. S. Tkaczyk, "Endomicroscopy," in *Biomedical Optical Imaging Technologies: Design and Applications*, Heidelberg, Berlin, Springer, 2013, pp. 255-296.
- [50] P. J. Campagnola, M.-d. Wei, A. Lewis and L. M. Loew, "High-Resolution Nonlinear Optical Imaging of Live Cells by second Harmonic Generation," *Biophysics Journal*, vol. 77, no. 6, pp. 3341-3349, 1999.
- [51] H. Liu, W. Qin, Y. Saho, Z. Ma, T. Ye, T. Borg and B. Z. Gao, "Myofibrillogenesis in live neonatal cardiomyocytes observed with hybrid two-photon excitation fluorescence-second harmonic generation microscopy," *Journal of Biomedical Optics*, vol. 16, no. 12, pp. 126012:1-4, 2011.
- [52] B. F. Romeike, T. Meyer, R. Reichart, R. Kalff, I. Petersen, B. Dietzek and J. Popp, "Coherent anti-Stokes Raman scattering and two photon excited fluorescence for neurosurgery," *Clinical Neurology and Neurosurgery*, vol. 131, pp. 42-46, 2015.
- [53] T. T. Le, T. B. Huff and J.-X. Cheng, "Coherent anti-Stokes Raman scattering imaging of lipids in cancer metastasis," *BMC Cancer*, vol. 9, no. 1, pp. 42:1-14, 2009.
- [54] L. Wei, Y. Yu, Y. Shen, M. C. Wang and W. Min, "Vibrational imaging of newly synthesized proteins in live cells by stimulated Raman scattering microscopy," *Proceedings of the National Academy of Sciences*, vol. 110, no. 28, pp. 11226-11231, 2013.
- [55] L. v. Haasterecht, L. Zada, R. W. Schmidt, E. de Bakker, E. Barbe', H. A. Leslie, A. D. Vethaak, S. Gibbs, J. F. de Boer, F. B. Niessen, P. P. M. van Zuijlen, M. L. Groot and F. Ariese, "Label-Free stimulated Raman scattering imaging reveals silicone breast implant material in tissue," *Journal of Biophotonics*, vol. 13, no. 5, 2020.

- [56] S. Hu, K. Maslov and L. V. Wang, "Three-Dimensional Optical-Resolution Photoacoustic Microscopy," in *Biomedical Optical Imaging Technologies: Design and Applications*, Heidelberg, Berlin, Springer, 2013, pp. 55-77.
- [57] J. Yao and L. V. Wang, "Photoacoustic Microscopy," *Laser & Photonics reviews*, vol. 7, no. 5, 2013.
- [58] S. Hu and L. V. Wang, "Photoacoustic imaging and characterization of the microvasculature," *Journal of Biomedical Optics*, vol. 15, no. 1, pp. 011101:1-15, 2010.
- [59] E. W. Stein, K. Maslov and L. V. Wang, "Noninvasive mapping of the electrically stimulated mouse brain using photoacoustic microscopy," in *Proc. SPIE 6856*, San Jose, California, 2008.
- [60] Z. Xie, W. Roberts, P. Carson, X. Liu, C. Tao and X. Wang, "Evaluation of bladder microvasculature with high resolution photoacoustic imaging," *Optics Letters*, vol. 36, no. 24, pp. 4815-4817, 2011.
- [61] S. Hu and L. V. Wang, "Neurovascular Photoacoustic Tomography," *Frontiers in Neuroenergetics*, vol. 2, 2010.
- [62] S. A. Ermilov, T. Khampirad, A. Conjuteau, M. H. Leonard, R. Lacewell, K. Mehta, T. Miller and A. A. Oraevsky, " Laser optoacoustic imaging system for detection of breast cancer," *Journal of Biomedical Optics*, vol. 14, no. 2, pp. 024007:1-14, 2009.
- [63] K. Maslov, G. Ku and L. V. Wang, "Photoacoustic microscopy with submicron resolution," in *Proc. SPIE 7564*, San Francisco, USA, 2010.
- [64] L. V. Wang and S. Hu, "Photoacoustic tomography: in vivo imaging from organelles to organs," *Science*, vol. 335, no. 6075, pp. 1458-1462, 2012.
- [65] J. Chan, Z. Zheng, K. Bell, M. Le, P. H. Reza and J. T. W. Yeow, "Photoacoustic Imaging with Capacitive Micromachined Ultrasound Transducers: Principles and Developments," *Sensors*, vol. 19, no. 16, 2019.
- [66] C. Xu, W. Zipfel, J. B. Shear, R. M. Williams and W. W. Webb, "Multiphoton fluorescence excitation: New spectral windows for biological nonlinear microscopy," *Proceedings of the National Academy of Sciences of United States of America*, vol. 93, no. 20, pp. 10763-10768, 1996.
- [67] D. M. Hoffmann, K. Kuhnke and L. Kern, "Sum-frequency generation microscope for opaque and reflecting samples," *Review of scientific instruments*, vol. 73, no. 9, pp. 3221-3226, 2002.

- [68] A. Zumbusch, G. R. Holtom and S. X. Xie, "Three-Dimensional Vibrational Imaging by Coherent Anti-Stokes Raman Scattering," *Physical Review Letters*, vol. 82, no. 20, pp. 4142-4145, 1999.
- [69] P. Campagnola, "Second Harmonic Generation Imaging Microscopy: Applications to Diseases Diagnostics," *analytical Chemistry*, vol. 83, no. 9, pp. 3224-3231, 2011.
- [70] F. Ganikhanov, S. Carrasco, S. X. Xie, M. Katz, W. Seitz and D. Kopf, "Broadly tunable dual-wavelength light source for coherent anti-Stokes Raman scattering microscopy," *Optics Letters*, vol. 31, no. 9, pp. 1292-1294, 2006.
- [71] J. W. Baik, J. Y. Kim, S. Cho, S. Choi, J. Kim and C. Kim, "Super Wide-Field Photoacoustic Microscopy of Animals and Humans In Vivo," *IEEE Transactions on Medical Imaging*, vol. 39, no. 4, pp. 975-984, 2020.
- [72] J. P. Powers, *An introduction to fiber optic systems*, Chicago: Irwin, 1997.
- [73] M. Kaur, P. M. Lane and C. Menon, "Scanning and Actuation Techniques for Cantilever-Based Fiber Optic Endoscopic Scanners—A Review," *Sensors*, vol. 21, no. 1, pp. 251:1-38, 2021.
- [74] A. Ghatak and K. Thyagarajan, "Optical Waveguides and Fibers," in *Fundamentals of Photonics*, SPIE, 2008, pp. 249-261.
- [75] W. Gobel, J. N. Kerr, A. Nimmerjahn and F. Helmchen, "Miniaturized two-photon microscope based on a flexible coherent fiber bundle and a gradient-index lens objective," *Optics Letters*, vol. 29, no. 21, pp. 2521-2523, 2004.
- [76] L. Huang and U. L. Oesterberg, "Measurement of cross talk in order-packed image fiber bundles," in *Proceedings of SPIE*, 2536, San Diego, 1995.
- [77] B. A. Flusberg, E. D. Cocker, W. Piyawattanametha, J. C. Jung, E. L. M. Cheung and M. J. Schnitzer, "Fiber-optic fluorescence imaging," *Nature Methods*, vol. 2, no. 12, pp. 941-950, 2005.
- [78] J. Shao, W.-C. Liao, R. Liang and K. Barnard, "Resolution enhancement for fiber bundle imaging using maximum a posteriori estimation," *Optics Letters*, vol. 43, no. 8, pp. 1906-1909, 2018.
- [79] M. Dumripatanachod and W. Piyawattananmetha, "A Fast Depixation Method of Fiber Bundle Image for an Embedded System," in *8th Biomedical Engineering International Conference*, Pattaya, Thailand, 2015.
- [80] A. Shinde, S. M. Perinchery and M. V. Matham, "Fiber pixelated image database," *Optical Engineering*, vol. 55, no. 8, pp. 083105:1-6, 2016.

- [81] K. Vyas, M. Hughes, B. G. Rosa and G.-Z. Yang, "Fiber bundle shifting endomicroscopy for high-resolution imaging," *Biomedical Optics Express*, vol. 9, no. 10, pp. 4649-4664, 2018.
- [82] K.-B. Sung, C. Liang, M. Descour, T. Collier, M. Follen and R. Richards-Kortum, "Fiber-Optic Confocal Reflectance Microscope With Miniature Objective for In Vivo Imaging of Human Tissues," *IEEE Transactions on Biomedical Engineering*, vol. 49, no. 10, pp. 1168-1172, 2002.
- [83] J. Knittel, L. Schnieder, G. Buess, B. Messerschmidt and T. Possner, "Endoscope-compatible confocal microscope using a gradient index-lens system," *Optics Communications*, vol. 188, pp. 267-273, 2001.
- [84] P. M. Lane, S. Lam, A. McWilliams, J. C. Le Riche, M. Anderson and C. E. MacAulay, "Confocal fluorescence microendoscopy of bronchial epithelium," *J. of Biomedical Optics*, vol. 14, no. 2, pp. 024008:1-10, 2009.
- [85] A. Osdoit, F. Lacombe, C. Cave', S. Loiseau and E. Peltier, "To see the unseeable: confocal miniprobos for routine microscopic imaging during endoscopy," in *Proc. SPIE 6432, Endoscopic Microscopy II, San Jose (USA)*, 2007.
- [86] L. Giniunas, R. Juskaitis and S. Shatalin, "Scanning fiber-optic microscope," *Electronics Letters*, vol. 27, no. 9, pp. 724-726, 1991.
- [87] S. Kimura and T. Wilson, "Confocal scanning optical microscope using single-mode fiber for signal detection," *Applied Optics*, vol. 30, no. 16, pp. 2143-2150, 1991.
- [88] C. Pitris, B. E. Bouma, M. Shiskov, C. Boudoux and G. J. Tearney, "GRISM-based probe for spectrally encoded confocal microscopy," in *Proceedings of SPIE, Munich*, 2003.
- [89] D. Yelin, I. Rizvi, W. M. White, J. T. Motz, T. Hasan, B. E. Bouma and G. J. Tearney, "Three-dimensional miniature endoscopy," *Nature*, vol. 443, no. 7113, p. 765, 2006.
- [90] J. Zhao and H. Zeng, "Advanced spectroscopy Technique for Biomedicine," in *Biomedical Optical Imaging Technologies: Design and Applications*, Arizona, Springer, 2013, pp. 1-10.
- [91] Y. Choi, C. Yoon, M. Kim, T. D. Yang, C. Fang-Yen, R. R. Dasari, K. J. Lee and W. Choi, "Scanner-Free and Wide-Field Endoscopic Imaging by Using a Single Multimode Optical Fiber," *Physics Review Letters*, vol. 109, no. 20, pp. 203901:1-5, 2012.
- [92] J.-M. Yang, R. Chen, C. Favazza, J. Yao, C. Li, Z. Hu, Q. Zhou, K. K. Shung and L. V. Wang, "A 2.5-mm diameter probe for photoacoustic and ultrasonic endoscopy," *Optics Express*, vol. 20, no. 21, pp. 23944-23953, 2012.

- [93] W. Wei, X. Li, Q. Zhou, K. K. Shung and Z. Chen, "Integrated ultrasound and photoacoustic probe for co-registered intravascular imaging," *Journal of Biomedical Optics*, vol. 16, no. 10, pp. 106001:1-6, 2011.
- [94] I. N. Papadopoulos, S. Farahi, C. Moser and D. Psaltis, "Focusing and scanning light through a multimode optical fiber using digital phase conjugation," *Optics Express*, vol. 20, no. 10, pp. 10583-10590, 2012.
- [95] M. Sato, T. Kanno, S. Ishihara, H. Suto, T. Takahashi and I. Nishidate, "Reflectance Imaging by Graded-Index Short Multimode Fiber," *Applied Physics Express*, vol. 6, pp. 052503:1-3, 2013.
- [96] Y. Zhang, Y. Cao and J.-X. Cheng, "High-resolution photoacoustic endoscope through beam self-cleaning in a graded index fiber," *Optics Letters*, vol. 44, no. 15, pp. 3841-3844, 2019.
- [97] L. Fu, X. Gan and M. Gu, "Nonlinear optical microscopy based on double-clad photonic crystal fibers," *Optics Express*, vol. 13, no. 14, pp. 5528-5534, 2005.
- [98] D. Yelin, B. E. Bouma, S. H. Yun and G. J. Tearney, "Double-clad fiber for endoscopy," *Optics Letters*, vol. 29, no. 20, pp. 2408-2410, 2004.
- [99] L. Wang, H. Y. Choi, Y. Jung, H. B. Lee and K.-T. Kim, "Optical probe based on double-clad optical fiber fluorescence spectroscopy," *Optics Express*, vol. 15, no. 26, pp. 17681-17689, 2007.
- [100] J. Mavadia, J. Xi, Y. Chen and X. Li, "An all-fiber-optic endoscopy platform for simultaneous OCT and fluorescence imaging," *Biomedical Optics Express*, vol. 3, no. 11, pp. 2851-2859, 2012.
- [101] J. Xi, Y. Chen, Y. Zhang, K. Murari, M.-J. Li and X. Li, "Integrated multimodal endomicroscopy platform for simultaneous en face optical coherence and two-photon fluorescence imaging," *Optics Letters*, vol. 37, no. 3, pp. 362-364, 2012.
- [102] A. L. Buenconsejo, G. Hohert, M. Manning, E. Abouei, R. Tingley, I. Janzen, J. McAlpine, D. Miller, A. Lee, P. Lane and C. MacAulay, "Submillimeter diameter rotary-pullback fiber-optic endoscope for narrowband red-green-blue reflectance, optical coherence tomography, and autofluorescence in vivo imaging," *Journal of Biomedical Optics*, vol. 25, no. 3, pp. 032005:1-7, 2020.
- [103] X. Liu, M. J. Cobb, Y. Chen, M. B. Kimmey and X. Li, "Rapid-scanning forward-imaging miniature endoscope for real-time optical coherence tomography," *Optics Letters*, vol. 29, no. 15, pp. 1763-1765, 2004.
- [104] H.-C. Park, Y.-H. Seo, K. Hwang, J.-K. Lim, S. Z. Yoon and K.-H. Jeong, "Micromachined tethered silicon oscillator for an endomicroscopic Lissajous fiber scanner," *Optics Letters*, vol. 39, no. 23, pp. 6675-6678, 2014.

- [105] G. Huang and Z. Ding, "Rapid two-dimensional transversal scanning fiber probe for optical coherence tomography," in *Proceeds of SPIE 6429*, California, 2007.
- [106] Z. Liu, L. Fu, F. Gao and X. Zhang, "Design and implementation of 2-D endoscopic optical fiber scanner," in *Proceedings of SPIE 7280*, Wuhan, 2009.
- [107] G. Li, H. Gao, A. Zhou and Z. Liu, "Endoscope two dimensional scanning fiber probe and the driving method," in *Proceedings of SPIE 8199*, Beijing, 2011.
- [108] F. Akhoundi, Y. Qin, N. Peyghambarian, J. K. Barton and K. Kieu, "Compact fiber-based multi-photon endoscope working at 1700nm," *Biomedical Optics Express*, vol. 9, no. 5, pp. 2326-2335, 2018.
- [109] S. Kretschmer, J. Jager, S. Vilches, C. Ataman and H. Zapper, "A bimodal endoscopic imager in a glass package," *Journal of Micromechanics and Microengineering*, vol. 28, no. 10, pp. 105009:1-8, 2018.
- [110] A. Rajiv, Y. Zhou, J. Ridge, P. G. Reinhall and E. J. Seibel, "Electromechanical model based design and testing of fiber scanners for endoscopy," *Journal of Medical Devices*, vol. 12, no. 4, pp. 041003:1-8, 2018.
- [111] T. Wu, Z. Ding, K. Wang, M. Chen and C. Wang, "Two-dimensional scanning realized by an asymmetry fiber cantilever driven by single piezo bender actuator for optical coherence tomography," *Optics Express*, vol. 17, no. 16, pp. 13819-13829, 2009.
- [112] A. D. Aguirre, P. R. Herz, Y. Chen, J. G. Fujimoto, W. Piyawattanametha, L. Fan and M. C. Wu, "Two-axis MEMS Scanning Catheter for Ultrahigh Resolution Three-dimensional and En Face Imaging," *Optics Express*, vol. 15, no. 5, pp. 2445-2453, 2007.
- [113] J. M. Zara, S. Yazdanfar, K. D. Rao, J. A. Izatt and S. W. Smith, "Electrostatic micromachine scanning mirror for optical coherence tomography," *optics Letters*, vol. 28, no. 8, pp. 628-630, 2003.
- [114] K. H. Kim, B. H. Park, G. N. Maguluri, T. W. Lee, F. J. Rogomentich, M. G. Bancu, B. E. Bouma, J. F. de Boer and J. J. Bernstein, "Two-axis magnetically-driven MEMS scanning catheter for endoscopic high-speed optical coherence tomography," *Optics Express*, vol. 15, no. 26, pp. 18130-18140, 2007.
- [115] J. Yao, T. Peng, B. Sun, H. Zhang, M. Zhao, B. Dai, H. Liu, G. Ding, R. Swada and Z. Yang, "A Single-Fiber Endoscope Scanner Probe Utilizing Two-Degrees-of-Freedom (2DOF) High-Order Resonance to Realize Larger Scanning Angle," *IEEE transactions on components, packaging and manufacturing technology*, vol. 9, no. 12, pp. 2332-2340, 2019.
- [116] Y.-H. Seo, K. Hwang and K.-H. Jeong, "1.65mm diameter forward-viewing confocal endomicroscopic catheter using a glip-chip bonded electrothermal MEMS fiber scanner," *Optics Express*, vol. 26, no. 4, pp. 4780-4785, 2018.

- [117] Y.-H. Seo, K. Hwang, H.-C. Park and K.-H. Jeong, "Electrothermal mems fiber scanner for optical endomicroscopy," *Optics Express*, vol. 24, no. 4, pp. 3903-3909, 2016.
- [118] Q. A. Tanguy, O. Gaiffe, N. Passilly, J.-M. Cote, G. Cabodevila, S. Bargiel, P. Lutz, H. Xie and C. Gorecki, "Real-time Lissajous imaging with a low-voltage 2-axis MEMS scanner based on electro-thermal actuation," *Optics Express*, vol. 28, no. 6, pp. 8512-8527, 2020.
- [119] J. Sun, S. Guo, L. Wu, L. Liu, S.-W. Choe, B. S. Sorg and H. Xie, "3D In Vivo optical coherence tomography based on a low-voltage, large-scan-range 2D MEMS mirror," *Optics Express*, vol. 18, no. 12, pp. 12065-12075, 2010.
- [120] C. Duan, Q. Tanguy, A. Pozzi and H. Xie, "Optical coherence tomography endoscopic probe based on a tilted MEMS mirror," *Biomedical Optics Express*, vol. 7, no. 9, pp. 3345-3354, 2016.
- [121] H. Li, K. R. Oldham and T. D. Wang, "3 degree-of-freedom resonant scanner with full-circumferential range and large out-of-plane displacement," *Optics Express*, vol. 27, no. 11, pp. 16296-16307, 2019.
- [122] T. Kobayashi, T. Matsunaga and Y. Haga, "Active Bending Electric Endoscope Using Shape Memory Alloy wires," in *New Trends in Medical and Service Robots: Assistive, Surgical and Educational Robotics*, Switzerland, Springer, Cham, 2016, pp. 131-139.
- [123] Y. Pan, H. Xie and G. K. Fedder, "Endoscopic optical coherence tomography based on a microelectromechanical mirror," *Optics Letters*, vol. 26, no. 24, pp. 1966-1968, 2001.
- [124] A. L. Polglase, W. J. McLaren, S. A. Skinner, B. Kiesslich, M. F. Neurath and P. M. Delaney, "A fluorescence confocal endomicroscope for in vivo microscopy of the upper- and lower-GI tract," *Gastrointestinal Endoscopy*, vol. 62, no. 5, pp. 686-695, 2005.
- [125] J. Wu, M. Conry, C. Gu, F. Wang, Z. Yaqoob and C. Yang, "Paired-angle-rotation scanning optical coherence tomography forward-imaging probe," *Optics Letters*, vol. 31, no. 9, pp. 1265-1267, 2006.
- [126] M. V. Sarunic, S. Han, J. Wu, Z. Yaqoob, M. Humayun and C. Yang, "Endoscopic Optical Coherence Tomography of the Retina at 1310 nm Using Paired-Angle-Rotating Scanning," in *Proceedings of SPIE*, San Jose, 2007.
- [127] J. K. Kim, J. W. Choi and S. H. Yun, "350-um side-view optical probe for imaging the murine brain in vivo from the cortex to the hypothalamus," *Journal of Biomedical Optics*, vol. 18, no. 5, pp. 050502-1:3, 2013.

- [128] P. H. Tran, D. S. Mukai, M. Brenner and Z. Chen, "In vivo endoscopic optical coherence tomography by use of a rotational microelectromechanical system probe," *Optics Letters*, vol. 29, no. 11, pp. 1236-1238, 2004.
- [129] C. M. Lee, J. E. Chandler and E. J. Seibel, "Wide Field Fluorescence Imaging in Narrow Passageways Using Scanning Fiber Endoscope Technology," *Proceedings of SPIE*, vol. 7558, no. 755806, pp. 1-10, 2010.
- [130] E. Z. Zhang and P. C. Beard, "A miniature all-optical photoacoustic imaging probe," in *Proc. SPIE 7899*, San Francisco, USA, 2011.
- [131] G. J. Tearney, M. E. Brezinski, B. E. Bouma, S. A. Boppart, C. Pitris, J. F. Southern and J. G. Fujimoto, "In Vivo Endoscopic Optical Biopsy with Optical Coherence Tomography," *Science*, vol. 276, pp. 2037-2039, 1997.
- [132] X. Li, C. Chudoba, T. Ko, C. Pitris and J. G. Fujimoto, "Imaging needle for optical coherence tomography," *Optics Letters*, vol. 25, no. 20, pp. 1520-1522, 2000.
- [133] D. Lorensen, X. Yang, R. W. Kirk, B. C. Quirk, R. A. McLaughlin and D. D. Sampson, "Ultrathin side-viewing needle probe for optical coherence tomography," *Optics Letters*, vol. 36, no. 19, pp. 3894-3896, 2011.
- [134] V. X. D. Yang, Y. Mao, N. Munce, B. Standish, W. Kucharczyk, N. E. Marcon, B. C. Wilson and I. A. Vitkin, "Interstitial Doppler optical coherence tomography," *Optics Letters*, vol. 30, no. 14, pp. 1791-1793, 2005.
- [135] P. R. Herz, Y. Chen, A. D. Aguirre, K. Schneider, P. Hsiung, J. G. Fujimoto, K. Madden, J. Schmitt, J. Goodnow and C. Petersen, "Micromotor endoscope catheter for in vivo, ultrahigh-resolution optical coherence tomography," *Optics Letters*, vol. 29, no. 19, pp. 2261-2263, 2004.
- [136] B. Paulson, S. Lee, Y. Kim, Y. Moon and J. K. Kim, "Miniaturized omnidirectional flexible side-view endoscope for rapid monitoring of thin tubular biostructures," *Biomedical Optics Express*, vol. 10, no. 5, pp. 2264-2274, 2019.
- [137] H.-C. Park, Y.-H. Seo and K.-H. Jeong, "Lissajous fiber scanning for forward viewing optical endomicroscopy using asymmetric modulation," *Optics Express*, vol. 22, no. 5, pp. 5818-5825, 2014.
- [138] E. J. Seibel, R. S. Johnston and C. D. Melville, "A full-color scanning fiber endoscope," *Optical Fibers and Sensors for Medical Diagnosis and Treatment Applications*, vol. 6083, 2006.
- [139] A. Acemoglu and L. S. Mattos, "Magnetic Laser Scanner for Endoscopic Microsurgery," in *IEEE International Conference on Robotics and Automation*, Singapore, 2017.

- [140] Y. Wang, M. Bachman, G.-P. Li, S. Guo, B. J. Wong and Z. Chen, "Low-voltage polymer-based scanning cantilever for in vivo optical coherence tomography," *Optics Letters*, vol. 30, no. 1, pp. 53-55, 2005.
- [141] K. H. Gilchrist, R. P. McNabb, J. P. Izatt and S. Grego, "Piezoelectric scanning mirrors for endoscopic optical coherence tomography," *Journal of Micromechanics and Microengineering*, vol. 19, no. 095012, p. 1:11, 2009.
- [142] Y. Pan, Z. Li, T. Xie and C. R. Chu, "Hand-held arthroscopic optical coherence tomography for in vivo high-resolution imaging of articular cartilage," *Journal of Biomedical Optics*, vol. 8, no. 4, pp. 648-654, 2003.
- [143] T. Wu, R. Pan, K. Cao, L. Zhang, J. Wang, Y. Lu, C. He and Y. Liu, "Side-viewing endoscopic imaging probe for swept source optical coherence," *Optics Communications*, vol. 467, p. 125596, 2020.
- [144] D. J. Inman, *Engineering Vibrations*, New Jersey: Pearson, 2014.
- [145] S. T. S. Holmstrom, U. Baran and H. Urey, "Mems Laser Scanners: A Review," *Journal of microelectromechanical systems*, vol. 23, no. 2, pp. 259-275, 2014.
- [146] E. C. Haight and W. W. King, "stability of Nonlinear Oscillations of an elastic Rod," *The Journal of the Acoustical Society of America*, vol. 52, no. 3B, pp. 899-911, 1972.
- [147] M. W. Hyer, "Whirling of a base-excited cantilever beam," *Journal of Acoustical Society of America*, vol. 65, no. 4, pp. 931-939, 1979.
- [148] M. J. Kundrat, P. G. Reinhall, C. M. Lee and E. J. Seibel, "High Performance Open Loop Control of Scanning with a Small Cylindrical Cantilever Beam," *Journal of Sound and Vibration*, vol. 330, no. 8, pp. 1762-1771, 2011.
- [149] L. Wu, Z. Ding and G. Huang, "Realization of 2D scanning pattern of a fiber cantilever by nonlinear coupling," in *Fifth International Conference on Photonics and Imaging in Biology and Medicine*, 2006.
- [150] D. R. Rivera, c. M. Brown, D. G. Ouzounov, I. Pavlova, D. Kobat, W. W. Webb and C. Xu, "Compact and flexible raster scanning multiphoton endoscope capable of imaging unstained tissue," *PNAS*, vol. 108, no. 43, pp. 17598-17603, 2011.
- [151] B. H. W. Hendriks, W. C. J. Bierhoff, J. J. L. Horikx, A. E. Desjardins, C. A. Hezemans, G. W. ' . Hooft, G. W. Lucassen and N. Mihajlovic, "High-resolution resonant and nonresonant fiber-scanning confocal microscope," *Journal of Biomedical Optics*, vol. 16, no. 2, pp. 026007:1-8, 2011.

- [152] X. Zhang, C. Duan, L. Liu, X. Li and H. Xie, "A non-resonant fiber scanner based on an electrothermally-actuated MEMS stage," *Sensors and Actuators A: Physical*, vol. 233, pp. 239-245, 2015.
- [153] H.-C. Park, X. Zhang, W. Yuan, L. Zhou, H. Xie and X. Li, "Ultralow-voltage electrothermal MEMS based fiber-optic scanning probe for forward-viewing endoscopic OCT," *Optics Letters*, vol. 44, no. 9, pp. 2232-2235, 2019.
- [154] T. Naono, T. Fujii, M. Esashi and S. Tanaka, "Non-resonant 2-D piezoelectric MEMS optical scanner actuated by Nb doped PZT thin film," *Sensors and Actuators A: Physical*, vol. 233, pp. 147-157, 2015.
- [155] J. Sawinski and W. Denk, "Miniature random-access fiber scanner for in vivo multiphoton imaging," *Journal of Applied Physics*, vol. 102, pp. 034701:1-8, 2007.
- [156] S. Moon, S.-W. Lee, M. Rubinstein, B. J. F. Wong and Z. Chen, "Semi-resonant operation of a fiber-cantilever piezotube scanner for stable optical coherence tomography endoscope imaging," *Optics Express*, vol. 18, no. 20, pp. 21183-21197, 2010.
- [157] U. Hofmann, J. Janes and H.-J. Quenzer, "High-Q MEMS Resonators for Laser Beam Scanning Displays," *Micromachines*, vol. 3, no. 2, pp. 509-528, 2012.
- [158] C. Vinegoni, S. Lee, P. F. Feruglio and R. Weissleder, "Advanced Motion Compensation Methods for Intravital Optical Microscopy," *IEEE Journal of Selected Topics in Quantum Electronics*, vol. 20, no. 2, pp. 83-91, 2014.
- [159] V.-F. Duma, K.-s. Lee, P. Meemon and J. P. Rolland, "Experimental investigations of the scanning functions of galvanometer-based scanners with applications in OCT," *Applied Optics*, vol. 50, no. 29, pp. 5735-5749, 2011.
- [160] K. Hwang, Y.-H. Seo, J. Ahn, P. Kim and K.-H. Jeong, "Frequency selection rule for high definition and high frame rate Lissajous scanning," *Scientific Reports*, vol. 7, no. 1, pp. 14075:1-8, 2017.
- [161] A. Kovacs, "Scanning strategies for imaging arrays," in *Proc. SPIE 7020*, Marseille, France, 2008.
- [162] M. Tekpinar, R. Khayatzadeh and O. Ferhanoglu, "Multiple-pattern generating piezoelectric fiber scanner toward endoscopic applications," *Optical Engineering*, vol. 58, no. 2, pp. 023101:1-6, 2019.
- [163] A. A. Ahrabi, M. Kaur, Y. Li, P. Lane and C. Menon, "An Electro-Thermal Actuation Method for Resonance vibration of a Miniaturized Optical-Fiber Scanner for Future Scanning Fiber Endoscope Design," *Actuators*, vol. 8, no. 21, pp. 1-18, 2019.

- [164] S. Yang and Q. Xu, "A review on actuation and sensing techniques for MEMS-based microgrippers," *Journal of Micro-Bio Robotics*, vol. 13, no. 1-4, pp. 1-14, 2017.
- [165] P. Zhang, "Sensors and actuators," in *Advanced Industrial Control Technology*, United Kingdom, Elsevier, 2010, pp. 73-116.
- [166] E. Pengwang, K. Rabenorosoa, M. Rakotondrabe and N. Andreff, "Scanning Micromirror Platform Based on MEMS Technology for Medical Application," *Micromachines*, vol. 7, no. 24, pp. 7020024: 1-29, 2016.
- [167] J. Emery, "Piezoelectricity," 04 03 1997. [Online]. Available: <http://stem2.org/je/piezoelc.pdf>. [Accessed 12 06 2020].
- [168] I. M. Bahadur and J. K. Mills, "A New Model of Hysteresis in Piezoelectric Actuators," in *International Conference on Mechatronics and Automation*, Beijing, China, 2011.
- [169] ThorLabs, "Piezoelectric Tutorial," [Online]. Available: https://www.thorlabs.com/newgrouppage9.cfm?objectgroup_id=5030. [Accessed 15 06 2020].
- [170] W. Liang, G. Hall, B. Messerschmidt, M.-J. Li and X. Li, "Nonlinear optical endomicroscopy for label-free functional histology in vivo," *Light: Science & Applications*, vol. 6, no. 11, p. e17082, 2017.
- [171] S. Vilches, S. Kretschmer, C. Ataman and H. Zappe, "Miniaturized Fourier-plane fiber scanner for OCT endoscopy," *Journal of micromachines and microengineering*, vol. 27, no. 10, p. 105015, 2017.
- [172] M. Mayyas, "Comprehensive Thermal Modeling of ElectroThermoElastic Microstructures," *Actuators*, vol. 1, no. 1, pp. 21-35, 2012.
- [173] L. Lin and M. Chiao, "Electrothermal responses of lineshape microstructures," *Sensors and Actuators A: Physical*, vol. 55, no. 1, pp. 35-41, 1996.
- [174] H. So and A. P. Pisano, "Electrothermal modeling, fabrication and analysis of low-power thermal actuator with buckling arm," *Microsystem Technologies*, vol. 21, no. 1, pp. 195-202, 2015.
- [175] R. A. Buser, N. F. de Rooij, H. Tischhauser, A. Dommann and G. Stauffert, "Biaxial scanning mirror activated by bimorph structures for medical applications," *Sensors and Actuators A: Physical*, vol. 31, no. 1-3, pp. 29-34, 1992.
- [176] H. Guckel, J. Klein, T. Christenson, K. Skrobis, M. Laudon and E. G. Lovell, "Thermo-magnetic metal flexure actuators," in *Technical Digest IEEE Solid-State Sensor and Actuator Workshop*, Hilton Head Island, SC, USA, 1992.

- [177] Q.-A. Huang and N. K. S. Lee, "Analysis and design of polysilicon thermal flexure actuator," *Journal of Micromechanics and Microengineering*, vol. 9, no. 1, pp. 64-70, 1999.
- [178] R. Hickey, M. Kujath and T. Hubbard, "Heat transfer analysis and optimization of two-beam microelectromechanical thermal actuators," *Journal of Vacuum Science & Technology A: Vacuum, Surfaces, and Films*, vol. 20, no. 3, pp. 971-974, 2002.
- [179] Q.-A. Huang and N. K. Lee, "Analytical modeling and optimization for a laterally-driven polysilicon thermal actuator," *Microsystem Technologies*, vol. 5, no. 3, pp. 133-137, 1999.
- [180] C.-C. Lee and W. Hsu, "Optimization of an electro-thermally and laterally driven microactuator," *Microsystem Technologies*, vol. 9, no. 5, pp. 331-334, 2003.
- [181] T. Moulton and G. K. Ananthasuresh, "Micromechanical devices with embedded electro-thermal-compliant actuation," *Sensors and Actuators A: Physical*, vol. 90, no. 1-2, pp. 38-48, 2001.
- [182] M. Lara-Castro, A. Herrera-Amaya, M. A. Escarola-Rosas, M. Vazquez-Toledo, F. Lopez-Huerta, L. A. Aguilera-Cortes and A. L. Herrera-May, "Design and Modeling of Polysilicon Electrothermal Actuators for a MEMS Mirror with Low Power Consumption," *Micromachines*, vol. 8, no. 7, pp. 203:1-19, 2017.
- [183] R. Venditti, J. S. H. Lee, Y. Sun and D. Li, "An in-plane, bi-directional electrothermal MEMS actuator," *Journal of Micromechanics and Microengineering*, vol. 16, no. 10, pp. 2067-2070, 2006.
- [184] Y.-H. Seo, K. Hwang, H.-C. Park and K.-H. Jeong, "Electrothermal mems fiber scanner with lissajous patterns for endomicroscopic applications," *Optics Express*, vol. 24, no. 4, pp. 3903-3909, 2016.
- [185] E. T. Enikov, S. S. Kedar and K. V. Lazarov, "Analytical Model for Analysis and Design of V-Shaped Thermal Microactuators," *Journal of Microelectromechanical Systems*, vol. 14, no. 4, pp. 788-798, 2005.
- [186] A. Baracu, R. Voicu, R. Muller, A. Avram, M. Pustan, R. Chiorean, C. Birleau and C. Dutescu, "Design and fabrication of a MEMS chevron-type thermal actuator," in *AIP Conference Proceedings 1646*, Thessaloniki, Greece, 2015.
- [187] L. Que, J.-S. Park and Y. B. Gianchandani, "Bent-Beam Electrothermal Actuators-Part I: Single Beam and Cascaded Devices," *Journal of Microelectromechanical Systems*, vol. 10, no. 2, pp. 247-254, 2001.
- [188] M. J. Sinclair, "A High Force Low Area MEMS Thermal Actuator," in *Inter Society Conference on Thermal Phenomena*, 2000.

- [189] S. Iqbal, A. A. Malik and R. I. Shakoor, "Design and analysis of novel micro displacement amplification mechanism actuated by chevron shaped thermal actuators," *Microsystem Technologies*, vol. 25, no. 3, pp. 861-875, 2018.
- [190] C. Guan and Y. Zhu, "An electrothermal microactuator with Z-shaped beams," *Journal of Micromechanics and Microengineering*, vol. 20, no. 8, pp. 85014:1-9, 2010.
- [191] E. Rawashdeh, A. Karam and I. G. Foulds, "Characterization of Kink Actuators as Compared to Traditional Chevron Shaped Bent-Beam Electrothermal Actuators," *Micromachines*, vol. 3, no. 3, pp. 542-549, 2012.
- [192] W.-H. Chu, M. Mehregany and R. L. Mullen, "Analysis of tip deflection and force of a bimetallic cantilever microactuator," *Journal of Micromechanics and Microengineering*, vol. 3, no. 4, pp. 4-7, 1993.
- [193] Q. A. A. Tanguy, S. Bargiel, H. Xie, N. Passilly, M. Barthe's, O. Gaiffe, J. Rutkowski, P. Lutz and C. Gorecki, "Design and Fabrication of a 2-Axis Electrothermal MEMS Micro-Scanner for Optical Coherence Tomography," *Micromachines*, vol. 8, no. 146, pp. 8050146: 1-11, 2017.
- [194] R. E. Pawinanto, J. Yunas, B. Y. Majlis and A. A. Hamzah, "Design and Fabrication of Compact MEMS Electromagnetic Micro-Actuator with Planar Micro-Coil Based on PCB," *Telkomnika*, vol. 14, no. 3, pp. 856-866, 2016.
- [195] J. W. Judy and R. S. Muller, "Magnetically Actuated, Addressable Microstructures," *Journal of Microelectromechanical Systems*, vol. 6, no. 3, pp. 249-256, 1997.
- [196] K. M. Joos and J.-H. Shen, "Miniature real-time intraoperative forward imaging optical coherence tomography probe," *Biomedical Optics Express*, vol. 4, no. 8, pp. 1342-1350, 2013.
- [197] B. Sun, R. Sawada, Z. Yang, Y. Zhang, T. Itoh and R. Maeda, "Design and Fabrication of Driving Microcoil with Large Tilt-Angle for Medical Scanner Application," in *2014 Symposium on Design, Test, Integration and Packaging of MEMS/MOEMS (DTIP)*, Cote D'Azur, France, 2014.
- [198] B. Sun, H. Nogami, Y. Pen and R. Sawada, "Microelectromagnetic actuator based on a 3D printing process for fiber scanner application," *Journal of Micromechanics and Microengineering*, vol. 25, no. 7, pp. 075014:1-8, 2015.
- [199] X. Lv, W. Wei, X. Mao, Y. Chen, J. Yang and F. Yang, "A novel MEMS electromagnetic actuator with large displacement," *Sensors and Actuators A: Physical*, vol. 221, pp. 22-28, 2015.
- [200] P. R. Barbaroto, L. O. S. Ferreira and I. Doi, "Micromachined scanner actuated by electromagnetic induction," in *Proc. SPIE 4902*, Stuttgart, Germany, 2002.

- [201] T.-L. Tang, C.-P. Hsu, W.-C. Chen and W. Fang, "Design and implementation of a torque-enhancement 2-axis magnetostatic SOI optical scanner," *Journal of Micromechanics and Microengineering*, vol. 20, no. 2, p. 025020, 2010.
- [202] B. D. Cullity and C. D. Graham, "Magnetostriction and the effects of stress," in *Introduction to magnetic materials*, New Jersey, USA, Wiley, 2009, pp. 241-273.
- [203] T. Bourouina, E. Lebrasseur, G. Reyne, A. Debray, H. Fujita, A. Ludwig, E. Quandt, H. Muro, T. Oki and A. Asaoka, "Integration of Two Degree-of-Freedom Magnetostrictive Actuation and Piezoresistive Detection: Application to a Two-Dimensional Optical scanner," *Journal of Microelectromechanical systems*, vol. 11, no. 4, pp. 355-361, 2002.
- [204] A. Garnier, T. Bourouina, H. Fujita, E. Orsier, T. Masuzawa, T. Hiramoto and J.-C. Peuzin, "A fast, robust and simple 2-D micro-opticalscanner based on contactless magnetostrictive actuation," in *Proceedings IEEE Thirteenth Annual International Conference on Micro Electro Mechanical Systems*, Miyazaki, Japan, 2000.
- [205] P. Pandojirao-Sunkojirao, S. M. Rao, P. C. Phuyal, N. Dhaubanjari and J.-C. Chiao, "A Magnetic Actuator for Fiber-Optic Applications," *International Journal of Optomechatronics*, vol. 3, no. 3, pp. 215-232, 2009.
- [206] D. Collard, H. Fujita, H. Toshiyoshi, B. Legrand and L. Buchailot, "Electrostatic Micro-actuators," in *Microsystems Technology: Fabrication, Test & Reliability*, London and Sterling, VA, Kogan Page Science, 2003, pp. 75-115.
- [207] T. Bourouina, H. Fujita, G. Reyne and M. E. Motamedi, "Optical scanning," in *MOEMS: micro-opto-electro-mechanical systems*, Bellingham, WA, SPIE, 2005, pp. 323-367.
- [208] C. Henri and L. Franck, "Fabrication, Simulation and experiment of a rotating electrostatic silicon mirror with large angular deflection," in *Proceedings IEEE Thirteen Annual International Conference on Micro Electro Mechanical Systems*, Miyazaki, Japan, 2000.
- [209] P. R. Patterson, D. Hah, M. Fujino, W. Piyawattanametha and M. C. Wu, "Scanning micromirrors: An overview," in *Proc. SPIE 5604*, Pennsylvania, 2004.
- [210] W. Piyawattanametha, R. P. J. Barretto, T. H. Ko, B. A. Flusberg, E. D. Cocker, H. Ra, D. Lee, O. Solgaard and M. J. Schnitzer, "Fast-scanning two-photon fluorescence imaging based on a microelectromechanical systems two-dimensional scanning mirror," *Optics Letters*, vol. 31, no. 13, pp. 2018-2020, 2006.
- [211] T. Izawa, T. Sasaki and K. Hane, "Scanning Micro-Mirror with an Electrostatic Spring for Compensation of Hard-Spring Nonlinearity," *Micromachines*, vol. 8, no. 8, pp. 240-1:13, 2017.

- [212] H. Schenk, P. Durr, D. Kunze, H. Lakner and H. Kuck, "A resonantly excited 2D-micro-scanning-mirror with large deflection," *Sensors and Actuators A: Physical*, vol. 89, no. 1-2, pp. 104-111, 2001.
- [213] N. R. Munce, A. Mariampillai, B. A. Standish, M. Pop, K. J. Anderson, G. Y. Liu, T. Luk, B. K. Courtney, G. A. Wright, I. A. Vitkin and V. X. Yang, "Electrostatic forward-viewing scanning probe for Doppler optical coherence tomography using a dissipative polymer catheter," *Optics Letters*, vol. 33, no. 7, pp. 657-659, 2008.
- [214] W. W. Huebsch, S. D. Hamburg and R. W. Guiler, "Aircraft morphing technologies," in *Innovation in Aeronautics*, Woodhead Publishing, 2012, pp. 37-55.
- [215] J.-S. Koh, "Design of Shape Memory Alloy Coil Spring Actuator for Improving Performance in Cyclic Actuation," *Materials*, vol. 11, no. 11, pp. 2324: 1-16, 2018.
- [216] J. Qiu, J. Tani, D. Osanai, Y. Urushiyama and D. Lewinnek, "High-speed response of SMA actuators," *International Journal of Applied Electromagnetics and Mechanics*, vol. 12, no. 1-2, pp. 87-100, 2001.
- [217] T. Ishii, "Design of shape memory alloy (SMA) coil springs for actuator applications," in *Shape Memory and Superelastic Alloys*, Woodhead Publishing, 2011, pp. 63-76.
- [218] S. Maeda, K. Abe, K. Yamamoto, O. Tohyama and H. Ito, "Active endoscope with SMA (Shape Memory Alloy) coil springs," in *Proceedings of Ninth International Workshop on Micro Electromechanical Systems*, Amsterdam, Netherlands, 1996.
- [219] Y. Haga, Y. Tanahashi and M. Esashi, "Small diameter active catheter using shape memory alloy," in *Proceedings MEMS 98. IEEE. Eleventh Annual International Workshop on Micro Electro Mechanical Systems. An Investigation of Micro Structures, Sensors, Actuators, Machines and Systems*, Heidelberg, Germany, 1998.
- [220] W. Makishi, T. Matunaga, Y. Haga and M. Esashi, "Active Bending Electric Endoscope Using Shape Memory Alloy Coil Actuators," in *The First IEEE/RAS-EMBS International Conference on Biomedical Robotics and Biomechanics*, 2006, 2006.
- [221] W. Liang, H.-C. Park, K. Li, A. Li, D. Chen, H. Guan, Y. Yue, Y.-T. A. Gau, D. E. Bergles, M.-J. Li, H. Lu and X. Li, "Throughput-Speed Product Augmentation for Scanning Fiber-Optic Two-Photon Endomicroscopy," *IEEE Transactions on Medical Imaging*, vol. 39, no. 12, pp. 3779-3787, 2020.
- [222] S.-P. P. Thong, M. C. Olivo, K.-W. Kho, K. Mancner, W. Zheng, M. R. Harris and K.-C. Soo, "Laser confocal endomicroscopy as a novel technique for fluorescence diagnostic imaging of the oral cavity," *Journal of Biomedical Optics*, vol. 12, no. 1, pp. 014007:1-8, 2007.

- [223] L. Li and Z. J. Chew, "Microactuators: Design and Technology," in Smart Sensors and MEMS, Elsevier Ltd, 2018, pp. 313-354.
- [224] M. Komeili and C. Menon, "Modelling a micro-cantilever vibrating in vacuum, gas or liquid under thermal base excitation," Mechanics Research Communications, vol. 73, pp. 39-46, 2016.
- [225] M. Komeili and C. Menon, "Analysis and Design of Thermally Actuated Micro-Cantilevers for high Frequency Vibrations using Finite Element Method," World Journal of Mechanics, vol. 6, pp. 94-107, 2016.
- [226] M. Komeilli and C. Menon, "Modelling the dynamic response of a micro-cantilever excited at its base by an arbitrary thermal input using Laplace transformation," Applied Mathematical Modelling, vol. 43, pp. 481-497, 2017.
- [227] M. Komeili and C. Menon, "Resonance vibration of a thermally-actuated optical fiber with arbitrary periodic excitation: Analysis and optimization," International Journal of Mechanical Sciences, vol. 123, pp. 287-296, 2017.
- [228] M. Komeili, A. A. Ahrabi and C. Menon, "Resonance Vibration of an optical fiber micro-cantilever using electro-thermal actuation," Journal of Mathematical Models in Engineering, vol. 3, no. 1, pp. 1-16, 2017.
- [229] M. Kaur, G. Hohert, P. M. Lane and C. Menon, "Fabrication of a stepped optical fiber tip for miniaturized scanners," Optical Fiber Technology, vol. 61, pp. 102436:1-8, 2021.
- [230] S. Chung and S. Park, "Effects of temperature on mechanical properties of SU-8 photoresist material," Journal of Mechanical Science and Technology, vol. 27, no. 9, pp. 2701-2707, 2013.
- [231] C.-P. Liang, J. Wierwille, T. Moreira, G. Schwartzbauer, M. S. Jafri, C.-M. Tang and Y. Chen, "A forward-imaging needle-type OCT probe for image guided stereotactic procedures," Optics Express, vol. 19, no. 27, pp. 26283-26294, 2011.
- [232] M. T. Myaing, D. J. MacDonald and X. Li, "Fiber-optic scanning two-photon fluorescence endoscope," Optics Letters, vol. 31, no. 8, pp. 1076-1078, 2006.
- [233] J. M. Ward, D. G. O'Shea, B. J. Shortt, M. J. Morrissey, K. Deasy and S. G. Nic Chormaic, "Heat-and-pull rig for fiber taper fabrication," Review of Scientific Instruments, vol. 77, no. 8, 2006.
- [234] J. T. Krause, C. R. Kurkjian and U. C. Paek, "Strength of fusion splices for fibre lightguides," Electronics Letters, vol. 17, no. 6, pp. 232-233, 1987.

- [235] C. R. Kurkjian, M. J. Matthewson and J. M. Rooney, "Effects of heat treatment and HF etching on the strength of silica lightguides," in Reliability of Optical Fiber Components, Devices, Systems, and Networks II, Bellingham, 2004.
- [236] "Vytran Filament Fusion Splicer," Thorlabs, [Online]. Available: https://www.thorlabs.com/newgrouppage9.cfm?objectgroup_id=9355. [Accessed 16 November 2020].
- [237] Y. Yuan, L. Wang, L. Ding and C. Wu, "Theory, experiment, and application of optical fiber etching," Optical Society of America, vol. 51, no. 24, pp. 5845-5849, 2012.
- [238] J. Bierlich, J. Kobelke, D. Brand, K. Kirsch, J. Dellith and H. Bartelt, "Nanoscopic Tip Sensors Fabricated by Gas Phase Etching of Optical Glass Fibers," Photonic Sensors, vol. 2, no. 4, pp. 331-339, 2012.
- [239] R. M. Chyad, M. Z. M. Jafri and K. u. Ibrahim, "Fabrication nano fiber optic by chemical etching for sensing application," Eng. & Tech. Journal, vol. 33, no. 6, pp. 994-1002, 2015.
- [240] J. S. Judge, "A Study of the Dissolution of SiO₂ in Acidic Fluoride Solutions," Journal of Electrochemical Society, vol. 118, no. 11, pp. 1172-1175, 1971.
- [241] H. Proksche and G. Nagorsen, "The Influence of NH₄F on the Etch Rates of Undoped SiO₂ in Buffered Oxide Etch," Journal of the Electrochemical Society, vol. 139, no. 2, pp. 521-524, 1992.
- [242] S. Verhaverbeke, I. Teerlinck, C. Vinckier, G. Stevens, R. Cartuyvels and M. M. Heyns, "The Etching Mechanisms of SiO₂ in Hydrofluoric Acid," The Journal of the Electrochemical Society, vol. 141, no. 10, pp. 2852-2857, 1994.
- [243] K. Osseo-Asare, "Etching Kinetics of Silicon Dioxide in Aqueous Fluoride Solutions: A Surface Complexation Model," Journal of the Electrochemical Society, vol. 143, no. 4, pp. 1339-1347, 1996.
- [244] B. Shvartsev, D. Gelman, I. Komissarov, A. Epshtein, D. Starosvetsky and Y. Ein-Eli, "Influence of Solution Volume on the Dissolution Rate of Silicon Dioxide in Hydrofluoric Acid," ChemPhysChem, vol. 16, no. 2, pp. 370-376, 2015.
- [245] H. Kikuyama, M. Waki, I. Kawanabe, M. Miyashita, T. Yabune, N. Miki, J. Takano and T. Ohmi, "Etching Rate and Mechanism of Doped Oxide in Buffered Hydrogen Fluoride Solution," Journal of The Electrochemical Society, vol. 139, no. 8, pp. 2239-2243, 1992.
- [246] V. Talla, "BOE Wet Etch of Silicon Dioxide," 08 05 2011. [Online]. Available: <https://labs.ece.uw.edu/cam/SOPs/BOE%20Wet%20Etching%20of%20SiO2%20SOP.pdf>. [Accessed 14 08 2020].

- [247] "Silicon Dioxide (SiO₂) Etchants," Transene Company, Inc., [Online]. Available: <https://transene.com/sio2/>. [Accessed 14 08 2020].
- [248] A. Foti, C. D'Andrea, F. Bonaccorso, M. Lanza, E. Messina, E. Messina, O. M. Marago, B. Fazio and P. G. Gucciardi, "A Shape-Engineered Surface-Enhanced Raman Scattering Optical Fiber Sensor Working from the Visible to the Near-Infrared," *Plasmonics*, vol. 8, pp. 13-23, 2013.
- [249] C. R. Helms and B. E. Deal, "Mechanisms of the HF/H₂O vapor phase etching of SiO₂," *Journal of Vacuum Science & Technology A*, vol. 10, no. 4, pp. 806-811, 1992.
- [250] H. K. Kuiken, "Etching: A Two-Dimensional Mathematical Approach," *Proceedings of the Royal Society of London. Series A, Mathematical and physical sciences*, vol. 392, no. 1802, pp. 199-225, 1984.
- [251] C. B. Shin and D. J. Economou, "Effect of Transport and Reaction on the Shape Evolution of Cavities during Wet Chemical Etching," *Journal of the Electrochemical Society*, vol. 136, no. 7, pp. 1997-2004, 1989.
- [252] Y. C. Lam, J. C. Chai, P. Rath, H. Zheng and V. M. Murukeshan, "A Fixed-Grid Method for Chemical Etching," *International Communications in Heat and Mass Transfer*, vol. 31, no. 8, pp. 1123-1131, 2004.
- [253] P. Rath, J. C. Chai, H. Zheng, Y. C. Lam and V. M. Murukeshan, "Modeling two-dimensional diffusion-controlled wet chemical etching using a total concentration approach," *International Journal of Heat and Mass Transfer*, vol. 49, no. 7, pp. 1480-1488, 2006.
- [254] P. Rath and J. C. Chai, "Modeling convection-driven diffusion-controlled wet chemical etching using a total-concentration fixed-grid method," *Numerical Heat Transfer, Part B: Fundamentals*, vol. 53, no. 2, pp. 143-159, 2007.
- [255] A. Ivanov, "Simulation of Electrochemical Etching of Silicon with COMSOL," in *Proceedings of the 2011 COMSOL Conference, Stuttgart, Germany, 2011*.
- [256] H. M. Presby, A. F. Benner and C. A. Edwards, "Laser micromachining of efficient fiber microlenses," *Applied Optics*, vol. 29, no. 18, pp. 2692-2695, 1990.
- [257] C. H. Chao, S. C. Shen and J. R. Wu, "Fabrication of 3-D Submicron Glass Structures by FIB," *Journal of materials Engineering and Performance*, vol. 18, no. 7, pp. 878-885, 2009.
- [258] Y. S. Fawzy, M. Petek, M. Tercelj and H. Zeng, "In vivo assessment and evaluation of lung tissue morphologic and physiological changes from non-contact endoscopic reflectance spectroscopy for improving lung cancer detection," *Journal of Biomedical Optics*, vol. 11, no. 4, pp. 044003(1-12), 2006.

- [259] Thorlabs, "2x2 Double-Clad Fiber Couplers," Thorlabs, [Online]. Available: https://www.thorlabs.com/newgrouppage9.cfm?objectgroup_id=8400. [Accessed 16 November 2020].
- [260] T. Maeda, N. Arakawa, M. Takahashi and Y. Aizu, "Monte Carlo Simulation of Spectral Reflectance Using a Multilayered Skin Tissue Model," *Optical Review*, vol. 17, no. 3, pp. 223-229, 2010.
- [261] C. Timar-Fulep, "How to model the human skin and optical heart rate sensors in OpticStudio," Zemax, 30 March 2021. [Online]. Available: <https://support.zemax.com/hc/en-us/articles/1500005579202-How-to-model-the-human-skin-and-optical-heart-rate-sensors-in-OpticStudio>. [Accessed 07 January 2022].
- [262] E. S. Barhoum, R. S. Johnston and E. J. Seibel, "Optical modeling of an ultrathin scanning fiber endoscope, a preliminary study of confocal versus non-confocal detection," *Optics Express*, vol. 13, no. 19, pp. 7548-7562, 2005.
- [263] M. J. Gora, M. J. Suter, G. J. Tearney and X. Li, "Endoscopic optical coherence tomography: technologies and clinical applications," *Biomedical Optics Express*, vol. 8, no. 5, pp. 2405-2444, 2017.
- [264] L. Eitel, "Electric slip rings," *Motion Control Tips*, 27 December 2018. [Online]. Available: <https://www.motioncontroltips.com/electric-slip-rings-5-things-to-know-about-brushes-voltage-drops-and-noise-mitigation/>. [Accessed 09 January 2022].
- [265] M. Technology, "MFO - Fiber Optic Rotary Joints," MOFLON, [Online]. Available: <https://www.moflon.com/mfo102.html>. [Accessed 10 March 2022].
- [266] C. E. T. Co., "Integrated Slip Ring For Endoscope Equipment," CENO, [Online]. Available: <http://www.sliprings360.com/fiber-optic-rotary-joint/integrated-slip-ring-for-endoscope-equipment.html>. [Accessed 11 March 2022].
- [267] C. S. Pan and W. Hsu, "An electro-thermally and laterally driven polysilicon microactuator," *Journal of Micromechanics and Microengineering*, vol. 7, pp. 7-13, 1997.
- [268] R. S. Chen, C. Kung and G.-B. Lee, "Analysis of the optimal dimension on the electrothermal microactuator," *Journal of micromechanics and microengineering*, vol. 12, no. 3, pp. 291-296, 2002.
- [269] C.-C. Lo, M.-J. Lin and C.-L. Hwan, "Modeling and analysis of electro-thermal microactuators," *Journal of the chinese Institute of Engineers*, vol. 32, no. 3, pp. 351-360, 2009.
- [270] S. M. Karbasi, M. Shamsirsaz, M. Naraghi and M. Maroufi, "Optimal design analysis of electrothermally driven microactuators," *Microsystem Technologies*, vol. 16, pp. 1065-1071, 2010.

- [271] C. Elbuken, N. Topaloglu, P. M. Nieva, M. Yavuz and J. P. Huissoon, "Modeling and analysis of a 2-DOF bidirectional electro-thermal," *Microsystem technologies*, vol. 15, no. 5, pp. 713-722, 2009.
- [272] L. Li and D. Uttamchandani, "Dynamic response modelling and characterization of a vertical electrothermal actuator," *Journal of Micromechanics and Microengineering*, vol. 19, no. 7, pp. 075014:1-9, 2009.
- [273] D. Yan, A. Khajepour and R. Mansour, "Modeling of two-hot-arm horizontal thermal actuator," *Journal of Micromechanics and Microengineering*, vol. 13, no. 2, pp. 312-322, 2003.